Experimentele en numerieke studie van poreuze stroming in stortsteengolfbrekers onder golfbelasting

Experimental and Numerical Study of Wave-Induced Porous Flow in Rubble-Mound Breakwaters

Dieter Vanneste

Promotor: prof. dr. ir. P. Troch
Proefschrift ingediend tot het behalen van de graad van
Doctor in de Ingenieurswetenschappen: Bouwkunde

Vakgroep Civiele Techniek
Voorzitter: prof. dr. ir. J. De Rouck
Faculteit Ingenieurswetenschappen en Architectuur
Academiejaar 2012 - 2013

UNIVERSITEIT
GENT

Experimentele en numerieke studie van poreuze stroming in stortsteengolfbrekers onder golfbelasting

Experimental and Numerical Study of Wave-Induced Porous Flow in Rubble-Mound Breakwaters

Dieter Vanneste

Promotor: prof. dr. ir. P. Troch
Proefschrift ingediend tot het behalen van de graad van
Doctor in de Ingenieurswetenschappen: Bouwkunde

Vakgroep Civiele Techniek
Voorzitter: prof. dr. ir. J. De Rouck
Faculteit Ingenieurswetenschappen en Architectuur
Academiejaar 2012 - 2013

UNIVERSITEIT
GENT

ISBN 978-90-8578-563-7
NUR 956
Wettelijk depot: D/2012/10.500/89

Universiteit Gent
Faculteit Ingenieurswetenschappen en architectuur
Vakgroep Civiele Techniek
Afdeling Weg- en Waterbouwkunde

Supervisor:

Prof. dr. ir. P. Troch

Research institute:

Ghent University
Faculty of Engineering and Architecture

Department of Civil Engineering
Coastal Engineering Division
Technologiepark 904
B-9052 Zwijnaarde, Belgium

Tel.: +32-9-264.54.89
Fax.: +32-9-264.58.37

Acknowledgement

Completing a PhD dissertation probably is a key point in one's professional life and provides a moment for reflection. Recalling those six years of research, I have experienced all kinds of feelings, from frustration to more fortunate moments and sometimes sheer joy - when quoting a famous cigar-smoking character of a particular television series from the 80's was never far away.

I will spare the reader though from more of such philosophical contemplations and dedicate this part to what it is meant for: give credit to a number of people who have contributed to this work, in all kinds of ways. I would like to express my gratitude to those people mentioned hereafter, in no particular order of importance.

A big thank you is extended to prof. Julien De Rouck, first of all for his invitation to join 'AWW'. Teaching and guiding students under his supervision was always very pleasant and instructive. I would like to recognize him for sharing his professional experience, which is difficult to find in a textbook.

I would like to acknowledge my PhD supervisor, prof. Peter Troch, for making me enthusiastic to proceed with his research, sharing his knowledge and finally giving me the confidence and freedom to pursue my own research ideas during the final years of this work.

I am indebted to dr. Markus Muttray, for performing and generously sharing the GWK tests which has been of key importance to this work. Furthermore I would like to thank dr. Andreas Kortenhaus for his hospitality and offering me complete freedom to explore the archives of the Leichtweiss Institute, which made me feel like a real treasure hunter.

I am extremely grateful to dr. Michael Barkhudarov, for his guidance and answers to my innumerable questions by e-mail, which helped me a lot. Thank you Michael, for the good times at the user meetings in Tübingen, Reims and Monza!

We are fortunate enough to have a very skilled technical staff at our department. I would explicitly like to mention Tom Versluys, for his assistance in developing the pressure recording system and efficient LabView programming. This work would definitely have been a lot harder without him. Furthermore, a big thank you goes to Herman Van der Elst, Sam Meurez and David De Rynck, for constructing the breakwater scale model and their smart solution-driven thinking.

A well-functioning secretariat makes things run a lot smoother in our department. Anny, Ludo, Ellen and Lien, thank you for taking care of the administrative and financial merry-go-round.

In those six years, almost an eternity in a university environment, a lot of colleagues have come, stayed and left. It has been a pleasure being surrounded by the following people in the working atmosphere: Jimmy, Hadewych, Leen D.V., Charlotte, Griet, Tinqui, Jonas, Willem, Kurt, Wim, Koen, Leen B., Pieter M., Florent, Mathias, Dennis, Johannes, Vicky, Jesus, Pieter R., Annelies, Matthias, Dieter M., Yvan, Ronny, Tom D.M., Kevin, Sieglien, Liesbet, Anke, Boudewijn, Serge, Wouter, Corneel, Hans, Amélie, Ken, Dries, Wim, Dogan, Philippe, Etienne.

I have been lucky enough with wonderful office mates, with whom I could share many moments of laughter, interesting discussions and sometimes frustration. Thank you Lander Victor and Tomas Van Oyen for your kindness and patience, in particular at those moments when I was not a very pleasant company. A special word of thanks goes to Giang Hoang Hong, for introducing me to the Asian way of life and for his generosity and hospitality during our trip to Vietnam.

Of course, equally important as one's professional well-being -if not more- is having the blessing of friendship and love. I am especially grateful to Stijn Vantieghem and Tim Bekaert for their *rock-solid* and *longstanding* friendship. Hopefully we can get back to our jogging and cycling trips again, either in Zürich or Kluisbergen, definitely some sweat will be shed! A big thank you also to Bram & Elisabeth, Lander & Zyrine, Fernando & Irene, Alex, Wim and all the cycling and rowing mates for the much needed get-aways, (exhausting) sport and cultural activities, (dinner) parties, travels, ...

I am indebted to my family. I want to thank my parents for their unconditional support and living-by-example. My brothers Mathias and Pieter-Jan and sister-in-law Lindsay, for making home such a pleasant place to return to.

Finally, one special person deserves the last word of thanks for her love, support and patience, especially in those last few months of this research. Thank you, Emily, for bringing so much happiness in my life!

Dieter Vanneste
Ghent, December 2012

Contents

Nomenclature

Roman Symbols (SI units)

Ac	acceleration number	$-$
a	Forchheimer coefficient, laminar contribution	sm^{-1}
a_{eq}	linearized hydraulic resistance coefficient	sm^{-1}
b	Forchheimer coefficient, turbulent contribution	s^2m^{-2}
c	Forchheimer coefficient, inertia contribution	s^2m^{-1}
$c_{k,i}(z)$	regression parameter in pore pressure calculation model equations	$-$
C	generic wave celerity	ms^{-1}
$C^i(f)$	gain of $H^i(f)$	$-$
CR	reflection coefficient, ratio between reflected and incident wave height	$-$
$CR(f)$	reflection coefficient, obtained in frequency domain	$-$
D	characteristic length	m
D_{50}	median sieve diameter	m
$D_{n,50}$	median nominal diameter or equivalent cube size $=(M_{50}/\rho_r)^{1/3}$	m
D_s	seepage length factor	$-$
dx	uniform cell dimension	m
dt	time step size	s
dt_p	piston time step	s
e	half the piston stroke	m
f	frequency	s^{-1}
f_N	Nyquist frequency	s^{-1}
f_s	piston sample frequency	s^{-1}
f_{sf}	filter sample frequency	s^{-1}
g	gravitational acceleration	ms^{-2}
h	generic water depth	m

Roman Symbols (SI units)

h^i	discrete Finite Impulse Response (FIR) filter response	m
$H^i(f)$	complex frequency FIR filter response	$-$
H	generic wave height	m
H_0	input wave height for wave generation	m
H_m	mean wave height, defined in time domain	m
H_{m0}	significant wave height, defined in frequency domain	m
$H_{m,inc}$	incident mean wave height, defined in time domain	m
I	hydraulic gradient	$-$
I_P	gradient of pore pressure height	$-$
J_f	number of coefficients in FIR filter	$-$
k	turbulent kinetic energy	m^2s^{-2}
k	wave number ($= 2\pi/L$)	m^{-1}
k'	internal wave number, defined in porous medium	m^{-1}
K	hydraulic conductivity	ms^{-1}
K_w	hydraulic conductivity of single-phase (water) flow	ms^{-1}
K_{aw}	hydraulic conductivity of two-phase flow	ms^{-1}
KC	Keulegan-Carpenter number	$-$
K_n	near-field Biesel transfer function	$-$
K_f	far-field Biesel transfer function	$-$
L	wave length obtained from linear dispersion	m
L_p	peak wave length corresponding with peak period T_p	m
L'	wave length defined in porous medium	m
L_{sponge}	length of zone for passive wave absorption	m
L_B	beat length of harmonic generation	m
M_{50}	mass of particle for which 50% of the granular material is lighter	kg
n	porosity	$-$
n_a	air fraction in two-phase flow	$-$
n_s	power in sponge function	$-$
p	pressure	Nm^{-2}
P	pore pressure height	Nm^{-2}
P_m	mean pore pressure height, defined in time domain	Nm^{-2}
P_{m0}	significant pore pressure height, defined from pressure spectrum	Nm^{-2}

Roman Symbols (SI units)

R	source term in RNG model	$\mathrm{m^2s^{-4}}$
Re	Reynolds number	–
Re_p	pore Reynolds number, based on pore velocity and size	–
S	mean rate of strain	s^{-1}
S_{ij}	rate-of-strain tensor	–
$S_\eta(f)$	wave energy density spectrum	m^2s
Sc	Schmidt number	–
S_0	piston stroke	m
t	time	s
T	generic wave period	s
T_p	peak wave period defined from wave spectrum	s
T_{0f}	filter duration	s
u^*	filtered x-component of measured velocity	ms^{-1}
u_i	velocity component ($i = x$,y,z)	ms^{-1}
u^s	seepage velocity	ms^{-1}
u^f	filter or discharge velocity	ms^{-1}
u^p	pore velocity	ms^{-1}
$u^\star$	shear or friction velocity	ms^{-1}
$u_{\parallel}$	fluid velocity component parallel to wall face	ms^{-1}
u^*_{ref}	correction signal for piston control velocity in active absorption	ms^{-1}
u^*	filtered x-component of measured velocity signal	ms^{-1}
w^*	filtered z-component of measured velocity signal	ms^{-1}
x_i	general Cartesian spatial coordinate	m
x	first Cartesian spatial coordinate	m
x_1	x-coordinate of velocity measurement location for active absorption	m
$x_s(z)$	x-coordinate of separation point between zone 1 and 2 in the pore pressure calculation model	m
$X(t)$	piston displacement	m
$X^*(t)$	corrected piston displacement in active absorption	m
y	second Cartesian spatial coordinate	m
z	third Cartesian spatial coordinate	m
z_1	z-coordinate of velocity measurement location for active absorption	m

Greek Symbols (SI units)

α	armour slope angle	$-$
α_F	shape coefficient in Forhheimer coefficient a	$-$
β_F	shape coefficient in Forhheimer coefficient b	$-$
γ_F	added mass coefficient in Forhheimer coefficient c	$-$
Δf_f	filter frequency interval	s^{-1}
Δt_f	filter time interval	s
δ_{ij}	Kronecker delta	$-$
δ	damping coefficient	$-$
δ'	damping coefficient	$-$
ϵ	turbulent dissipation rate	m^2s^{-3}
η	free surface elevation	m
$\overline{\eta}$	time-averaged free surface elevation	m
η_c	free surface elevation of wave crest	m
η_t	free surface elevation of wave trough	m
η^*	corrected free surface elevation in active absorption	m
μ	dynamic viscosity	Nsm^{-2}
μ_T	turbulent or eddy viscosity	Nsm^{-2}
ν	kinematic viscosity	m^2s^{-1}
ν_T	turbulent kinematic viscosity	m^2s^{-1}
κ	von Karman constant	$-$
κ_s	local free surface curvature	m^{-1}
$\kappa(z)$	dimensionless parameter in pressure calculation model	$-$
λ_L	Froude length scale	$-$
ω	pulsation $(= 2\pi/T)$	$rad\ s^{-1}$
ϕ	velocity potential	m^2s^{-1}
φ_f	phase shift in wave maker theory	rad
φ_c	phase angle at wave crest	rad
$\varphi^i(f)$	phase of $H^i(f)$	rad
ξ	surf similarity or breaker parameter	$-$
ρ	mass density	kgm^{-3}
ρ_r	apparent mass density of rock, depending on the degree of saturation	kgm^{-3}
σ	fluid surface tension coefficient	Nm^{-1}
σ'	relative standard deviation	$-$
$\sigma_\eta(f_i)$	discrete wave energy spectrum	m^2
$\sigma_x(f_i)$	discrete piston-displacement energy spectrum	m^2
τ	shear stress	Nm^{-2}
τ_w	wall shear stress	Nm^{-2}

FLOW-3D variables (SI units)

A_i	cell area fraction in $i(=x, y, z)$ direction	–
A_x	cell area fraction in x-direction	–
A_y	cell area fraction in y-direction	–
A_z	cell area fraction in z-direction	–
$AFR_{i,j,k}$	area fraction of right face cell (i, j, k)	–
$AFB_{i,j,k}$	area fraction of bottom face cell (i, j, k)	–
$AFT_{i,j,k}$	area fraction of top face cell (i, j, k)	–
ALPHA	weight factor in first-order momentum advection scheme	–
AUTOT	time step control flag	–
CFPK	multiplier used in F-packing algorithm	–
CON	multiplier in Courant-Friedrich-Lewy (CFL) stability constraint	–
δx_i	cell dimension in x-direction of cell (i, j, k)	m
δy_j	cell dimension in y-direction of cell (i, j, k)	m
δz_k	cell dimension in z-direction of cell (i, j, k)	m
δt	times step size	s
DTMAX	maximum allowable time step size	s
EPSI	user-defined convergence criterion in pressure-velocity equation solution	–
EPSADJ	convergence control option in pressure-velocity equation solution	–
F	fluid fraction or VOF function	–
FCLEAN	treshold in fluid fraction cleanup algorithm	–
F_d	porous media drag coefficient	s^{-1}
FUX(Y,Z)	discretized u-momentum flux in $x(y,z)$-direction	ms^{-2}
FVX(Y,Z)	discretized v-momentum flux in $x(y,z)$-direction	ms^{-2}
FWX(Y,Z)	discretized w-momentum flux in $x(y,z)$-direction	ms^{-2}
ICMPRS	flag for flow compressibility	–
IFVOF	flag for VOF advection scheme	–
IFVIS	flag for turbulence modeling option	–
IFVISC	flag for fluid viscosity option	–
IGMRES	flag for Generalized Minimal Residual (GMRES) pressure solver	–

FLOW-3D variables (SI units)

IMPADV	flag for implicit/explicit treatment of momentum advection	–
IMPADV	flag for implicit/explicit treatment of viscous stress	–
IORDER	flag for of momentum advection scheme	–
ITMAX	maximum number of pressure-velocity iterations	–
ITDTMAX	maximum number of pressure-velocity iterations before δt is reduced	–
$NF_{i,j,k}$	cell (i,j,k) flag label defining fluid configuration	–
ny	number of cells in y-direction	–
ROUGH	length scale defining wall roughness	m
TLEN	turbulent length scale	m
TWFIN	total simulation duration	s
$u_{i,j,k}$	x-direction velocity at right face of cell (i,j,k)	ms^{-1}
$v_{i,j,k}$	y-direction velocity at bottom face of cell (i,j,k)	ms^{-1}
$w_{i,j,k}$	z-direction velocity at top face of cell (i,j,k)	ms^{-1}
$UAR(L)$	advecting velocity in momentum flux term FUX	ms^{-1}
$V_{F_{i,j,k}}$	cell (i,j,k) volume fraction	–
VFC	averaged volume fraction $V_{F_{i,j,k}}$ in momentum flux term *FUX(Y,Z)*	–
VISX(Y,Z)	discretized viscous shear stress acceleration in x(y,z)-direction	$ms{-}2$
WSX(Y,Z)	discretized wall shear stress acceleration in x(y,z)-direction	$ms{-}2$

Subscripts

GWK	referring to GWK test
num	numerical
max	maximum
min	minimum
c	corresponding with wave crest
t	corresponding with wave trough
inc	incident
LC	Low Cut-off
HC	High Cut-off
$real$	realized
$theo$	theoretical
p	peak

Acronyms

1D	one-dimensional
2D	two-dimensional
3D	three-dimensional
ADI	Alternating Direction Implicit
CFD	Computational Fluid Dynamics
CFL	Courant-Friedrich-Lewy
DNS	Direct Numerical Simulation
FAVOR	Fractional Area/Volume Obstacle Representation
FIR	Finite Impulse Response
GCG	Generalized Conjugate Gradient
GMO	General Moving Object
GMRES	Generalized Minimal Residual
GWK	Grösser Wellenkanal, Hannover (Germany)
JONSWAP	Joint North Sea Wave Project
LANL	Los Alamos National Laboratory, New Mexico (USA)
LES	Large-Eddy Simulation
LWF	Large Wave Flume, Hannover (Germany)
MAC	Marker-And-Cell
MWL	Mean Water Level
NS	Navier-Stokes
PFEM	Particle Finite Element Method
PLIC	Piecewise-Linear Interface Calculation
RANS	Reynolds-Averaged Navier Stokes
RMB	Rubble-Mound Breakwater
RNG	ReNormalization Group
SOR	Successive-Over-Relaxation
SPH	Smoothed Particle Hydrodynamics
SWL	Still Water Level
TMA	TMA-spectrum, after three data sources used in its development (Texel, Marsen, Arsloe)
UG	Ghent University, Ghent (Belgium)
VARANS	Volume-Averaged Reynolds-Averaged Navier Stokes
VOF	Volume-of-Fluid

Samenvatting

Het ontwerpproces van waterbouwkundige structuren wordt vandaag de dag gekenmerkt door een groeiende complexiteit. De toenemende projectschaal en de veelheid aan functies die in een beperkte ruimte verenigd moeten worden zijn hier de belangrijkste oorzaken van. De uitdagende taak van de bouwkundig ingenieur in deze bestaat erin om de fysische processen die in de kustzone aangrijpen te vertalen naar een veilig, economisch en duurzaam ontwerp van de kustwaterbouwkundige structuur.

Een van de voornaamste hydrodynamische processen in het domein van de kustwaterbouwkunde betreft de golfinteractie met doorlatende structuren, waarvan de stortsteengolfbreker wellicht het meest belangrijke voorbeeld is. Het wetenschappelijk onderzoek op deze structuren wordt sinds geruime tijd voornamelijk uitgevoerd op basis van proeven op schaalmodellen. Pas in de laatste decennia kennen numerieke modellen (en dan voornamelijk modellen gebaseerd op de Navier-Stokes vergelijkingen voor vloeistofdynamica) een toenemend gebruik binnen de kustwaterbouwkunde.

Het huidig onderzoek situeert zich op het raakvlak van beide ontwerpmethodieken, waarbij experimenteel onderzoek toegepast werd in de validatie van een numeriek stromingsmodel voor golfinteractie met een stortsteengolfbreker.

Het eerste gedeelte van dit onderzoek spitst zich toe op experimenteel onderzoek. Het huidige praktisch rekenmodel, dat gebruikt kan worden voor de bepaling van de ruimtelijke verdeling van poriëndrukken in de kern van de golfbreker, werd grondig getoetst aan de meetresultaten van een grootschalig model. Aangezien blijkt dat het huidig rekenmodel teveel vereenvoudigingen bevat werd een verbeterd rekenmodel ontwikkeld.

Een niet-lineaire regressieanalyse werd uitgevoerd op de meetgegevens van een grootschalig model, en op basis hiervan werden nieuwe semi-empirische modelvergelijkingen opgesteld. De vergelijkingen voorspellen de golfgeïnduceerde poriëndrukken op basis van de invallende golfparameters. Hierbij wordt opgemerkt dat de regressieparameters tot op zekere hoogte afhangen van de specifieke geometrie van de structuur en materiaaleigenschappen.

Vervolgens werden experimentele meetgegevens uit een kleinschalig golfbrekermodel toegepast op het verbeterd rekenmodel. Dit levert verder inzicht in de algemene toepasbaarheid van de regressieparameters. De proeven op kleine schaal omvatten zeer gelijkaardige golfcondities als deze in de grootschalige proeven, waarbij eenzelfde helling van het zeewaartse talud aangehouden wordt. Bovendien wordt aandacht besteed aan de verschaling van de kernfractie van het model. Door toepassing van een verschalingsprocedure wordt ernaar gestreefd om het visceuze laminaire stromingsveld in het fijnkorrelig materiaal op een correcte manier weer te geven in het model. De validatie op basis van de metingen op het kleinschalig model bevestigen dat het nieuwe rekenmodel de ruimtelijke verdeling van poriëndrukken relatief nauwkeurig beschrijft. De verschillen in regressieparameters tussen beide modellen wijzen evenwel op een zekere invloed van de materiaaleigenschappen en mogelijk ook de laagdiktes van het zeewaartse talud. De vergelijking tussen beide experimentele meetgegevens toont aan dat stromingsweerstand van het kernmateriaal de grootste invloed heeft op de modelparameters. De drukverdeling op de deklaag en tussenlaag is minder onderhevig aan de specifieke materiaaleigenschappen, wat bevestigd wordt door een betere overeenkomst in regressieparameters afgeleid voor beide experimenten. De vergelijking tussen het bestaande en het nieuwe rekenmodel toont aan dat de golfgeïnduceerde poriëndrukken gevoelig nauwkeuriger voorspeld kunnen worden. Een directe toepassingsmogelijkheid van het verbeterde rekenmodel ligt in de verschalingsprocedure voor fijnkorrelig kernmateriaal in fysische schaalproeven.

In een tweede onderzoeksluik wordt een numeriek stromingsmodel gebaseerd op de Navier-Stokes vergelijkingen toegepast op het probleem van golfinteractie met een stortsteengolfbreker. Het voornaamste doel is het valideren van een state-of-the-art model op basis van van experimentele metingen op een representatieve grootschalige modelsectie.

Een efficiënte behandeling van het vrije stromingsoppervlak en stroming doorheen poreuze materialen zijn de voornaamste eisen waaraan het model moet voldoen om de vooropgestelde onderzoeksdoelstellingen te bereiken. Op basis van deze criteria werd het commercieel pakket FLOW-3D® geselecteerd.

Het numeriek model is echter niet uitgerust met een standaard golfgeneratiemethode met actieve golfabsorptie, een absolute noodzaak om langeduur-golfproeven uit te voeren in de numerieke golfgoot. Daarom wordt een golfschot van het piston-type in het numeriek model geïmplementeerd, waarbij gebruik gemaakt werd van bestaande technologie voor de aandrijving van het golfschot in de fysische golfgoot van de Afdeling Weg-en Waterbouwkunde (UGent).

De werking van het golfschot wordt in detail gevalideerd op basis van enkele weloverwogen gekozen golfcondities met verschillende karakteristieken, zowel in generatiemodus als in absorptiemodus. De resultaten tonen aan dat het meest eenvoudige (eerste-orde nauwkeurige) momentumadvectieschema volstaat om een nauwkeurige en stabiele werking van het numerieke golfschot te bekomen. De specificatie van de bemonsteringsfrequentie voor de aandrijving van het schot blijkt hierbij een van de belangrijkste numerieke parameters te zijn, die zorgvuldig gekozen dient te worden op basis van de gridresolutie en verwachte tijdstapgrootte. Richtlijnen om tot een optimale numerieke parameterinstelling te komen worden in deze studie vermeld.

In een laatste stap van dit onderzoek werden de grootschalige modelproeven (die o.m. aan de basis lagen van het verbeterde rekenmodel) uitgevoerd in de numerieke golfgoot. Gezien de aard van het bestudeerde probleem werd een tweedimensionale berekening uitgevoerd, waarbij de vloeistof als één fase voorgesteld wordt en de effecten van turbulentie in het domein buiten de golfbreker als verwaarloosbaar beschouwd worden.

De eerste stap in deze validatiestudie is een grondige verificatie van het invallende golvenveld. De analyse van de hydrodynamische processen die gepaard gaan met de poreuze stroming toont aan dat het numeriek model de golftransmissie en de effecten tengevolge van een langdurige cyclische golfbelasting relatief nauwkeurig reproduceert. De vergelijking tussen experimenteel en numeriek bepaalde poriëndrukken geeft tenslotte aan dat deze nauwkeurig berekend kunnen worden in het numeriek model, op voorwaarde dat de basisveronderstelling (éénfasestroming) voldaan is. In een beperkte zone nabij het vrij oppervlak worden duidelijke verschillen vastgesteld, die toegeschreven kunnen worden aan het ontstaan van een lucht-water mengsel en bijhorende toename in poreuze stromingsweerstand, een effect dat in de huidige simulaties nog niet gemodelleerd werd.

De mate van nauwkeurigheid die in deze validatiestudie bereikt wordt toont aan dat dergelijke numerieke modellen een waardevolle bijdrage kunnen leveren in het ontwerpproces van stortsteengolfbrekers en andere doorlatende kustwaterbouwkundige structuren.

Summary

The design of coastal structures in modern age has become increasingly complex, due to the growing scale of projects over the last decades and the multitude of functions competing for vital space in a often limited coastal area. The task of the coastal engineer in this matter is to provide a link between the physical processes acting within the coastal zone and the design of coastal structures. One of the important hydrodynamic processes in coastal regions is the interaction of water waves with permeable coastal structures such as a Rubble-Mound Breakwater. Research on these structures has been historically based on physical scale model testing, but the progress achieved in the last decade in numerical modeling of wave-structure interaction (mainly based on models using the Navier-Stokes equations) suggest these models will become increasingly important for the coastal engineer. The present work fits within the scope of better understanding the hydraulic processes involved in wave-induced porous flow and the impact of these processes on the design of permeable coastal structures. To this end, experimental and numerical research are combined in an integrated study.

In a first part of this research, the accuracy of the existing state-of-art practical calculation model for the attenuation of pore pressure height within the core of a typical Rubble-Mound Breakwater section has been verified against an extensive dataset of large-scale model pore pressure measurements. The results point to oversimplifications in the current model, affecting the predictive accuracy under varying wave conditions. Therefore, improvements to the calculation model have been proposed.

The model equations in the improved calculation method were derived from a nonlinear regression analysis and relate the wave-induced pore pressure height to a sea state defined by the relative water depth and wave height, corresponding with non-overtopping and nonbreaking wave conditions. The dimensionless regression parameters appearing in the model equations are considered to be dependent to a certain extent on the breakwater geometry (slope angle, layer thickness) and the specific material properties affecting the porous flow resistance.

Pore pressure measurements on a small-scale breakwater model have been applied to the newly-derived calculation model, in order to provide insight into the general applicability of the model regression parameters. The small-scale model tests consider similar wave conditions as in large-scale tests and moreover present an equal armour slope. In an effort to maintain Froude scale similarity of the porous flow in the small-scale breakwater core, the core material has been determined using a scaling procedure. The validation with the small-scale data proves that the model equations are capable of describing the variation of pressure height under varying wave conditions, but also reveals differences in the model parameters to a certain extent. More specifically, the comparison between both models learns that the regression parameters in the model equation for the reference pressures (along the interface between underlayer and core) are least susceptible to a change in layer thickness or material properties of the armour or underlayer. This can be explained since the mean value of the reference pressures along the core slope is determined to a large extent by the wave run-up on the breakwater slope, a phenomenon which is implicitly captured due to the incorporation of the relative incident wave parameters in the model equation. When moving inside the breakwater core, the influence of the hydraulic resistance of the core material on the pressure height attenuation increases. Consequently, an increased dependency of the model parameters on the specific material properties may be expected.

The improvement in accuracy achieved with the new calculation method has been demonstrated by comparison with the existing method for a selected number of cases. A particular application of the improved method may be found in the scaling procedure of finer core material in reduced-scale models, making the procedure more reliable in varying wave conditions.

A second part of this PhD research explores the application of Computational Fluid Dynamics (CFD) modeling based on the Navier-Stokes equations to the interaction of water waves with permeable coastal structures. The principal goal is to validate the capabilities of such a numerical model, specifically aiming to use a realistic large-scale model case and consider long-term transient effects in the wave-structure interaction.

Prerequisites to the applied model are an efficient simulation of free surface and porous media flow, two main characteristics dominating the problem of interest. A commercial state-of-the-art CFD code, FLOW-3D®, has been selected for this purpose.

The numerical model has no standard wave boundary with active wave absorption, which is crucial to simulate realistic long-duration wave tests resembling those in a physical wave flume. For that reason, an additional wave generating technique has been implemented in the code. A linear piston wavemaker with active absorption has been implemented, based on existing technology from the piston wavemaker operated in the laboratory of the department of Civil Engineering (Ghent University). The generation and absorption capacities of the implemented piston wavemaker have been thoroughly validated. Simulations of the piston wave generation with and without active absorption have shown that the best results, in terms of accuracy and stability, are obtained with the first-order upwind momentum scheme. Another important factor concerns the specification of the piston sample frequencies, which needs to be in accordance with the numerical time step and is thus governed by the mesh resolution. Guidelines to define optimal settings for different numerical parameters were established.

Finally, a realistic validation case of wave interaction with the large-scale model was carried out. Due to the nature of the studied problem (nonbreaking waves), the problem was simplified to two-dimensional laminar single-fluid flow in the clear-fluid region.

A first step of the validation consisted of a detailed comparison between numerical and experimental incident wave fields. The analysis on the wave-induced flow features learns that the numerical model well predicts the transmission of free surface elevation throughout the breakwater cross-section, and proves to capture the long-term transient effects of the fluid flow under cyclic wave loading. Finally, comparing the experimental and numerical spatial distribution of pore pressures, the model was found to accurately predict the pore pressure height, provided the flow is not affected by air entrainment. Air entrainment leads to higher porous flow resistance, resulting in larger discrepancies between measured and numerical pore pressures in a (limited) zone near the free surface in the core and on the breakwater slope.

In conclusion, the overall predictive accuracy obtained with this model proves its value as a design tool in support of the coastal engineer.

1 Introduction

1.1 General

Coastal regions typically accommodate large population densities and a multitude of activities, such as harbours, fisheries and areas for environmental and recreational use, often with a large economical or ecological value. In places where a natural defense against the destructive power of the sea is absent, people have sought for solutions by building 'artificial' coastal structures, in order to prevent flooding of the hinterland, shelter harbour areas or reduce shoreline or beach erosion.

The design of coastal structures in modern times has become increasingly complex, due to increasing project scales and the multitude of functions competing for vital space in coastal areas worldwide, facing an increased anthropogenic pressure due to urbanization and rapid population growth (Nicholls et al., 2007). In addition, the expected sea level rise due to climate change obliges to revisit the design safety of existing coastal structures. Optimum solutions need to be found for these complex matters, and the role of the coastal engineer herein is to provide a link between the physical processes acting in the coastal region and the management of the coastal region.

One of the important hydrodynamic processes in coastal regions is the interaction of wind-generated water waves[1] with coastal structures. In the example of dikes or breakwaters exposed to severe storm conditions, these surface gravity waves may cause overtopping. In case of (grass) dikes, the down-rush of water at the rear-side may cause unacceptable erosion. In harbours, wave penetration through the harbour entrance and wave transmission through permeable breakwaters sheltering the harbour area cause ship motions, which must remain limited. In the particular design

---

[1] Tidal currents are an equally important factor in the hydrodynamic boundary conditions but act indirectly through modification of waves or morphological processes. Since they do not directly interact with the coastal structure, they are not considered here.

and operation of coastal structures or elements such as dikes, breakwaters and (gravel) beaches, forces generated by water waves might cause failure of the structure as a whole or unacceptable damage to individual parts of it. In brief, the aforementioned examples illustrate the need to predict the impact of waves on the coastal structure in the design process.

1.2 Design of rubble-mound breakwaters

Typical examples of coastal structures are breakwaters, revetments and dikes. In general, revetments and dikes have an impermeable core, since the principal function of these structures is to protect low-lying areas against flooding. These coastal structures are usually built as a mound of fine materials like sand and clay, which can be regarded as impermeable. In contrast, the principle function of a breakwater is to dissipate wave energy by friction loss in the permeable body of the structure.

The subject of the present study is the most common type of breakwater: a Rubble-Mound Breakwater (RMB). Due to the large diversity in hydraulic and geotechnical boundary conditions and available construction materials worldwide, ample variations in breakwater design exist. Nevertheless, the geometry and composition of a RMB can be reduced to a typical trapezial cross-section, illustrated in Fig. 1.1.

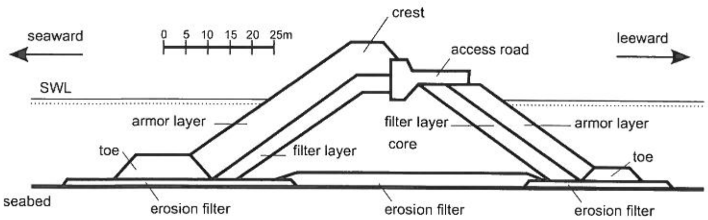

Figure 1.1: Typical cross-section of a (nonovertoppable) RMB (adapted from Troch, 2000).

The main part of the breakwater body, the *core*, is a mound of quarry run. The choice for a relatively fine material as quarry run is primarily based on economical considerations, besides its favorable properties of damping wave-induced flow and blocking sediment transport. The finer core material however will not remain stable under wave attack and is therefore protected by a layer of heavy armor stones on the seaward side. These armor units, either natural rock or artificial concrete units, are designed in weight and shape in order to remain stable or undergo a limited displacement when subject to the design wave conditions. A filter layer is placed between the armor and core, in order to prevent the finer core material being washed out through the voids of the armor layer. Toe constructions below the armor layers act as a foundation, providing geotechnical stability. Wherever needed, erosion filters between the seabed and the construction prevent erosion which could endanger the overall stability of the structure. The crest element on top of the core provides access to the breakwater.

The interaction between water waves and the RMB is characterized by a multitude of physical processes. As waves approach the structure, they undergo a nonlinear transformation in reduced water depth. This might lead to *wave breaking* either in front of the structure or on the armor slope. Alternatively, waves *run up* on the outer slope without breaking (*surging waves*). In either case, the result is a flow of water running up and down the breakwater slope, containing a certain amount of air. In this process, a part of the incident wave energy is *reflected* back toward the sea, where the interaction between the reflected and incident waves creates a partially standing wave field in front of the structure. The remainder of the wave energy which is not reflected is dissipated through friction losses on the slope and inside the armor layer or partially reflected on the interfaces between armor-filter and filter-core. What is left of the wave energy is then dissipated by friction losses of the *porous flow* in the core. Finally, only a small part of the wave energy reaches the rear side of the breakwater as *transmitted* waves. Depending on the crest level, the run-up on the armour slope might *overtop* and reach the leeward side of the breakwater via the crest and the leeward slope.

In conclusion, the external flow on the outer breakwater slope is governed by (i) the resulting wave field in front of the structure, (ii) the geometry of the structure, (iii) the roughness of the armour layer and (iv) the exchange of wave energy with the structure (inflow and outflow). The internal flow depends on the permeability of the structure, on its turn influenced by the material properties, air entrainment and inertia effects (Muttray, 2000). The internal and external flow are highly unsteady and dissimilar. In materials with larger voids (armor and filter layers) applied to design storm conditions, the internal flow is generally turbulent. In scale models however, the porous flow in the finer core material can exhibit both laminar and turbulent characteristics. Generally, two-phase flow arises due to air entrainment at the fluid interface, to an extent depending on the external flow.

The previous overview shows that the prediction of the hydraulic processes in wave-structure interaction, which are crucial in the design of a RMB, is not a straightforward task. The design of a RMB nowadays still heavily relies on physical scale model research, empirical design criteria and engineering practice, combining the expertise in different research areas such as coastal engineering, hydraulics, geotechnics, concrete and material research (Troch, 2000). For more details on the art in RMB design, the interested reader is referred to e.g. the Rock Manual (CIRIA et al., 2007) or the Coastal Engineering Manual (CECW-EH, 2011).

1.3 Motivation

Many permeable breakwaters have been successfully built to date, proving the value of the current design approach. However, in those particular cases where damage was reported, or even failure in load conditions less severe than design conditions, it often seems that the problems can be related to excessively large wave-induced pore pressures in the core (Harlow, 1980). This points to the important role of porous flow in the global interaction process of water waves with the structure, with implications on breakwater design. According to De Groot et al. (1994), the pore pressure distribution should be taken into account in the following design aspects:

- stability analysis of the breakwater slope, where failure might occur due to high pore pressures in the core and reduced wave pressures on the slope at the moment of maximum wave run-down;
- hydraulic stability of the armor units, influenced by pore pressures in the underlaying filter layer(s) and core;
- wave transmission, which is directly connected with wave-induced pore pressure oscillations and the resulting energy loss in the porous flow;
- wave run-up and overtopping, which are affected by the infiltration of the water in the slope, characterized by the porous flow in the armor and filter layer and the core;
- an optimized, economical design of filter layers in the presence of low pore pressure gradients;
- the occurrence of *set-up* in the breakwater, i.e. the rise of the phreatic water level due to the retention of water, a direct consequence of porous flow.

Although the internal flow field in a RMB seems to play an important role in the structure's response to wave loading, the phenomenon has not been the subject of many studies. Existing knowledge on this topic is rather limited and fragmental, compared to other design aspects, e.g. the design of the armor layer or the crest of the structure (a result of overtopping studies). This can be explained perhaps since coastal engineers have been relying mainly on physical scale model research for a long time. As such, global response parameters of the structure are studied and incorporated in design criteria, in contrast to the internal flow field, which is not readily available in a physical model. Whereas (pore) pressures can still be measured relatively easily in a physical model, in situ velocity measurements on the other hand are quite complex, particularly in porous media. Simple design criteria based on theoretical or empirical considerations are not likely however to provide an accurate description of the problem due to the stochastic nature of the wave-induced flow, the random character of the porous medium and the complexity of the specific breakwater geometry.

In view of the previous considerations, it is argued that often insufficient attention is paid to the internal flow field when designing permeable coastal structures. Since the link with the internal flow field is very often missing, it is difficult to obtain a fundamental understanding of the wave-structure interaction. One specific, yet important example which is highlighted here is the problem of scale effects in physical models at reduced scale (typically 1:30 to 1:60), where geometric (Froude) scaling causes an incorrect scaling of the laminar viscous flow in the breakwater core. Only a detailed view of the internal porous flow field can provide insight into the possible repercussions of scale effects on the research conclusions drawn from scale model tests.

In addition to physical modeling, the use of numerical modeling as a research tool for the coastal engineer is gaining importance. A growing number of numerical models for wave-structure interaction have been developed in the past decades, with increasing complexity and accuracy. In particular the advent of CFD models based on the Navier-Stokes (NS) equations has enabled the computation of flow fields with a sufficient level of detail and accuracy. In light of the previous concerns, the possibility of computing pressures and flow velocities inside a permeable coastal structure is regarded as a significant added value to the design process.

In the last decade, a growing use of NS models dealing with wave interaction with permeable structures can be observed. An overview of advances and the state of the art on this topic is included in Chapter 2. In order to become a reliable research tool for the coastal engineer, it is important however that these numerical models are well validated with experimental data. It is noticed that a validation making use of large-scale model data obtained from a realistic RMB structure (similar to Fig. 1.1), and focusing on long-term transient effects under cyclic wave loading is not well covered to date. The motivates one of the principal aims of this study.

The previous considerations reflect the need for a further investigation of the porous flow field in a typical multi-layered RMB. The present study aims to make a contribution to the design of these structures by combining experimental and numerical research in an integrated study. Concrete research goals are formulated hereafter.

1.4 Research objectives

The first research goal results from an experimental study on wave-induced pore pressures in a RMB core:

1. The existing calculation model for the spatial distribution of wave-induced pore pressures (Burcharth et al., 1999; Troch, 2000) is based on a limited number of large-scale model and prototype data, and needs further investigation. Using a more extensive data set resulting from experiments in the large wave flume in Hannover (Muttray, 2000) and a more detailed theoretical formulation, the practical calculation model will be extended to improve its accuracy under varying wave conditions.

In a second part of this research, the use of a NS-based CFD model for wave interaction with permeable coastal structures will be explored. The knowledge acquired in previous research (Troch, 2000) forms the starting point to select and employ a state-of-the-art numerical model with specific strengths of modeling free surface and porous media flow, the main elements which govern the problem of interest. In this context, two specific research goals are formulated:

2. The origin of the selected model is generic, rather than being specifically designed for coastal engineering applications. Therefore, an effective method for wave generation needs to be implemented and validated. This will allow to simulate realistic wave generation of long-duration tests, closely resembling the operation of a wavemaker used in laboratory testing.
3. Once the operation of the numerical wave flume has been established and validated, it requires validation. By using large-scale experimental data obtained from a typical multi-layered RMB, the aim is to bridge the current gap in validation studies for this type of numerical models.

1.5 Outline

A synopsis of relevant literature is included in Chapter 2, providing an overview of the state of the art on porous media flow modeling, experimental research on porous flow and numerical modeling of wave-structure interaction.

The use of experimental data obtained from scale model testing is one of the cornerstones of this research. Chapter 3 provides a detailed description of two test series, conducted on a physical model at large (1:5) and small (1:30) scale. The experimental data are used to establish an improved calculation method for the spatial distribution of pore pressures within the breakwater core, presented in Chapter 4.

In Chapter 5, the numerical framework to study wave-structure interaction is presented. The numerical model has been adapted with specific methods for wave generation. A description of the implementation and validation of the operation of the numerical wave flume is given in Chapter 6. This is followed by a validation study in Chapter 7, where the results of numerical simulations of large-scale model tests are presented.

Finally, research conclusions and perspectives for future research are provided in Chapter 8.

2 State of the art

Experimental and numerical research are combined in an integrated study in the present work. Naturally, acquired knowledge on wave interaction with permeable coastal structures forms the starting point. A synopsis of the current state of art is presented in this chapter, focusing on the three key aspects:

- an overview of theoretical concepts for porous media flow modeling, with particular attention to the incorporation of such a porous flow model in a generic numerical model for wave-structure interaction;
- an overview of acquired knowledge on the description of the porous flow field in a RMB, based on theoretical concepts and validated by experiments;
- the use of state-of-the art NS solvers to model wave interaction with permeable coastal structures.

2.1 Porous media flow

In the following, the general term *porous media* will be used when referring to different kinds of permeable material used in the construction of coastal structures. Under the definition of a porous medium is understood: solid materials with connected interstitial voids trough which fluid can flow.

A concept to describe the flow resistance in a porous medium is presented in this section, based on theoretical and experimental grounds. The porous media flow model concept will be of particular importance when applied in a numerical model for wave interaction with permeable structures (Chapter 5).

2.1.1 Stationary flow in porous media

Darcy (1856) was the first to obtain a solution for a specific type of porous media flow. Based on experimental work on groundwater flow, he experienced that the flow velocity in such case is proportional to the hydraulic gradient I:

$$u_i^f = KI = -\frac{K}{\rho g}(\frac{\partial p}{\partial x_i} + \rho g \delta_{ij}) \tag{2.1}$$

Eq. (2.1) is also known as the *law of Darcy*, an expression of the conservation of momentum for a laminar, stationary, incompressible fluid flow through a homogeneous, isotropic porous medium. In this equation, x_i denotes the independent spatial variable, ρ the fluid density, p the pressure and $g\delta_{ij}$ the gravity force. The *filter velocity* u_i^f, also referred to as *bulk* or *discharge* velocity is an average flow velocity, accounting for the total water flux across a well-defined cross section. The hydraulic conductivity of the flow through the porous medium is represented by the dimensional coefficient K. The conductivity depends both on the permeability of the porous medium (i.e. the configuration of the porous matrix) and the physcial properties of the fluid (density, viscosity). Various expressions for the hydraulic conductivity have been derived, see e.g. Bear (1972).

Considering purely horizontal (x-directional) flow and neglecting vertical accelerations, eq. (2.1) reduces to a one-dimensional equation:

$$I = -\frac{1}{\rho g}\frac{\partial p}{\partial x} = au^f \tag{2.2}$$

where a=K^{-1} and u^f the filter velocity in x-direction.

Eq. (2.2) is valid for laminar flow, i.e. when velocities and pore sizes are small. However, when velocities or pore sizes increase, a linear relationship between flow resistance and flow velocity does not longer hold. In order to represent a stationary flow in coarse granular material, Forchheimer (1901) proposed to include a quadratic velocity term to eq. (2.2):

$$I = au^f + bu^f|u^f| \tag{2.3}$$

where a and b are dimensional coefficients, often referred to as *friction factors*. These factors are found to depend on the fluid viscosity, the flow regime and specific granular composition of the porous medium. It is of importance to notice that these coefficients are not constants but depend on the flow regime, which is characterized by the Reynolds (Re) number:

$$Re = \frac{uD}{\nu} \tag{2.4}$$

where u is a characteristic velocity, D a characteristic length scale and ν the kinematic fluid viscosity. The Re number is a measure representing the relative contribution of turbulent and laminar effects.

In order to identify the different characteristics and flow regimes in porous flow, Dybbs and Edwards (1984) performed experimental research on idealised porous structures consisting of plexiglass spheres in a hexagonal packing, and glass and plexiglass rods arranged in a complex, fixed three-dimensional (3D) geometry. Water and oil were used for the test. Laser anemometry and flow visualization were applied to characterize the flow regime. They identified four regimes, characterized by $Re_p = u^p D_p / \nu$, i.e. a Reynolds number related to the pore size D_p and the pore velocity u^p. The flow regimes are summarized in Table 2.1. For the experiments with smooth spheres, the transition zones between the different flow regimes are relatively narrow and easy to identify.

Table 2.1: Porous flow regimes (after Dybbs and Edwards, 1984)

Regime	**Re_p-range**	**Flow characteristics**
Darcy flow	Re_p<1-10	Flow dominated by viscous forces, velocity distribution determined by local geometry.
Forchheimer flow	1-10<Re_p<150	Development of an inertial 'core' flow outside the boundary layers, causing a nonlinear relation between pressure drop and flow rate. The steady nonlinear laminar 'core' flow enlarges in size with growing Re_p.
Unsteady laminar flow	150<Re_p<300	Transitional flow regime between inertial Forchheimer and fully turbulent flow. At $Re_p \approx 150$, the first laminar wake oscillations in the pores develop, growing to larger vortices at higher Re_p number.
Fully turbulent flow	300<Re_p	Highly unsteady and chaotic flow regime, qualitatively resembling turbulent flow.

Forchheimer (1901) proposed eq. (2.3) on experimental basis. This equation can also be derived from the basic equations of fluid flow, the well-known Navier-Stokes equations (see Chapter 5 for a detailed discussion). The derivation (see e.g. Burcharth and Andersen (1995)), is retaken here since it yields more insight into the applicability of the porous flow model in different flow conditions. The NS equations for momentum transport in fluid flow naturally provide the basis for a general description of fluid flow in a porous medium:

$$\frac{\partial u_i}{\partial t} + u_j \frac{\partial u_i}{x_j} = g\delta_{iz} - \frac{1}{\rho}\frac{\partial p}{\partial x_i} + \nu \frac{\partial}{\partial x_j}\left(\frac{\partial u_i}{\partial x_j} + \frac{\partial u_j}{\partial x_i}\right) \tag{2.5}$$

with the appropriate boundary conditions along the grain surfaces and the boundary of the space in question. In these equations, t and x_i are the independent time and space variables, u_i is the (microscopic or pore) fluid velocity and ν the fluid kinematic viscosity. For a one-dimensional stationary closed conduit flow ($u_x = u$), and using the definition of the hydraulic gradient eq. (2.2), eq. (2.5) reduces to:

$$I = \frac{1}{g} u \frac{\partial u}{\partial x} - \frac{\nu}{g} \frac{\partial^2 u}{\partial x^2} \tag{2.6}$$

Introducing U and D as a characteristic velocity and length scale, eq. (2.6) can be written in a dimensionally correct form:

$$I = \alpha_F \frac{\nu}{g} \frac{U}{D^2} + \beta_F \frac{1}{g} \frac{U|U|}{D} \tag{2.7}$$

Eq. (2.7) is identical in form to eq. (2.3). The coefficients a and b (or α_F and β_F) are treated as constants for a given fluid viscosity, a given geometrical matrix of the porous medium and a certain flow regime (see Table 2.1). Based on experimental evidence by Fand et al. (1987), Burcharth and Christensen (1991) proposed a representation of the porous flow according to Fig. 2.1, to be used for flow in irregular and graded materials. In the latter case, transition zones between flow regimes are likely to be blurred and difficult to identify, in contrast to flow through a porous medium consisting of smooth uniform spheres which led to the classification of flow regimes in Table 2.1.

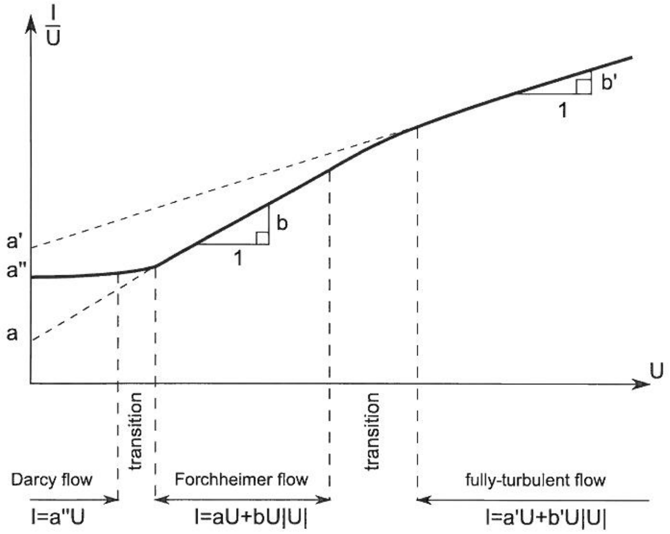

Figure 2.1: Representation of porous flow regimes based on the Forchheimer model eq. (2.3) (after Burcharth and Christensen, 1991).

In case of Darcy flow, also referred to as 'creeping flow', the velocities are small and the convective inertia term in eq. (2.6) can be neglected, leading to the following solution:

$$I = \alpha''_F \frac{\nu}{gD^2} U = a'' U \tag{2.8}$$

which is identical in form to eq. (2.2). This type of flow is not relevant for the coarser type of materials used in a RMB. When the velocities increase, the flow remaining stationary and laminar however, the perturbations of the flow paths in the porous medium introduce an additional pressure drop which is described by the nonlinear convective inertia term in eq. (2.6). Such a case corresponds with Forchheimer flow, and can be described by eq. (2.7).

With further increasing flow velocity, turbulence will occur. Theoretically, including this type of flow can be described with eq. (2.6), using the appropriate boundary conditions and fully resolving the dissipation of turbulent eddies at the smallest scales (see DNS, Chapter 5). The viscous term in fully turbulent flow can be neglected compared to the inertia term, so eq. (2.6) reduces to:

$$I = \beta'_F \frac{U^2}{gD} = b' U^2 \tag{2.9}$$

Obtaining a direct solution of the NS equations in case of turbulent flow in a porous medium is very complex, if not impossible in practice. Instead, it is more common to use a modeling approach to resolve turbulent phenomena. The derivation of the Forchheimer equation is retaken here for the so-called Reynolds-Averaged Navier Stokes (RANS) equations (see 5.3.3):

$$\frac{\partial \overline{u}_i}{\partial t} + \overline{u}_j \frac{\partial \overline{u}_i}{\partial x_j} = g\delta_{iz} - \frac{1}{\rho}\frac{\partial \overline{p}}{\partial x_i} + \frac{1}{\rho}\frac{\partial}{\partial x_j}\left[\mu\left(\frac{\partial \overline{u}_i}{\partial x_j} + \frac{\partial \overline{u}_j}{\partial x_i}\right) - \rho\overline{u'_i u'_j}\right] \tag{2.10}$$

where $\overline{u}_i$ denotes the ensemble averaged flow velocity component and u'_i the fluctuating velocity component, according to the Reynolds decomposition technique. In stationary, one-dimensional flow, eq. (2.10) reduces to:

$$I = \frac{1}{g}\overline{u}\frac{\partial \overline{u}}{\partial x} - \frac{\nu}{g}\frac{\partial^2 \overline{u}}{\partial x^2} + \frac{1}{g}\frac{\partial}{\partial x}\overline{u'^2} \tag{2.11}$$

Assuming that the velocity fluctuations u' in the Reynolds stress term vary proportionally to the velocity average $\overline{u}$, which can be represented by U, and taking D as a characteristic length scale, the Reynolds stress term has the same form as the convective term and can be merged into one term (Burcharth and Andersen, 1995). Since the laminar viscous term can be neglected in fully-turbulent flow, eq. (2.11) is then shown to reduce to eq. (2.9), representing the local convective acceleration and turbulent dissipation. The fact that the porous media model contains the dissipation by turbulence[1] is important when considering the application of a porous media model in a numerical model for wave-structure interaction (section 5.3.2).

Eqs. (2.8) and (2.9) represent two asymptotic expansions to the general Forchheimer equation eq. (2.7) for very small and very large Re numbers, respectively. Eq. (2.7) is often used to represent turbulent porous flow. In that case, the linear term is merely a fitting term without physical meaning[2], since viscous forces are deemed negligible. In order to represent fully-turbulent flow, e.g. in the core of structures at prototype scale, Burcharth and Andersen (1995) proposed a modified Forchheimer equation without the linear viscous term:

$$I = I_c + b'(u^f - u_c^f)^2 \; ; \; Re > Re_c = \frac{u_c^f D}{\nu} \tag{2.12}$$

where the critical lower limit for the turbulent flow region Re_c is in the range 300-600. I_c is computed from eq. (2.7) applying $u^f{=}u_c^f$.

With the aim of implementing a porous media model (eq. (2.7)) in a numerical model based on the NS equations, van Gent (1995) remarks that the coefficients α_F and β_F have to be determined for tests with sufficiently small convective terms. Otherwise, the presence of a large (macroscopic) convective term would increase the value of b, since the momentum needed to cause the acceleration would end up in the quadratic velocity term. Accordingly, the coefficient b derived from the experiment would not properly represent the porous flow resistance due to the local convective acceleration in the NS model.

2.1.2 Unsteady porous media flow

The Forchheimer equation eq. (2.3) is valid for stationary flow. An inertia term for unsteady flow was originally suggested by Polubarinova-Kochina (1962):

$$I = au^f + bu^f|u^f| + c\frac{\partial u^f}{\partial t} \tag{2.13}$$

where c, similar to a and b, is a dimensional coefficient. The coefficient c can only be applied to the local acceleration, which is usually dominating

---

[1] Referring to the turbulent dissipation in fully-developed unidirectional saturated stationary flow in a closed conduit. Turbulence due to air entrainment is not included in eq. (2.9).

[2] It is noticed moreover that a' is relatively small compared to $b'U$, hence the determination of a' from a linear regression analysis will be prone to a relatively large error.

over the convective accelerations (Burcharth and Andersen, 1995). In case of non-uniform flow with a considerable large-scale convective transport, an additional term needs to be included:

$$I = au^f + bu^f|u^f| + c\frac{\partial u^f}{\partial t} + \frac{1}{gn^2}u^f\frac{\partial u^f}{\partial x} \tag{2.14}$$

Several authors have presented a derivation for the inertia term in the extended Forchheimer eq. (2.13), based on the concept of *added mass*, the extra momentum needed for the acceleration of fluid volume in the presence of an obstacle. Gu and Wang (1991) and van Gent (1992) derived an expression for the inertia coefficient c on a theoretical basis:

$$c = \frac{1 + \gamma_F \frac{1-n}{n}}{ng} \tag{2.15}$$

where n is the porosity and γ_F the *virtual mass coefficient*, a nondimensional coefficient representing the effect of added mass. Burcharth and Andersen (1995) however argue the validity of eq. (2.15), since a pressure gradient acting on a fluid element in a porous medium was considered in the derivation of this equation. In reality, the pressure gradient acts on the entire sample of water and solids. Based on the analogy of flow trough a porous matrix containing cylindrical voids, they propose the following expression that is assumed to have a stronger physical basis:

$$c = \frac{1 + \gamma_F \frac{1-n}{n}}{g} \tag{2.16}$$

The analogy with the Morison equation for oscillatory flow around cylindrical structures suggests that both coefficient b and c depend on the flow characteristics and the composition of the granular matrix (i.e. porosity and the surface roughness of the individual grains in the porous medium). Strictly speaking, the coefficients b and c in eq. (2.13) are thus not to be considered as constants but are instantaneous values. In engineering practice however, the coefficients are taken as constants depending on a characteristic Reynolds and Keulegan-Carpenter number (KC) number, the latter being a representation of the ratio between the turbulence and inertia effects.

van Gent (1995) performed a detailed experimental study on the effect of inertia in oscillatory flow tests. In particular for low KC numbers, the value of the friction coefficient b in oscillatory flow was found to increase, compared to the value in stationary flow. A formulation of b including the KC number was proposed:

$$b = \beta_F \left(1 + \frac{7.5}{KC}\right) \frac{1-n}{n^3} \frac{1}{gD_{n,50}} \tag{2.17}$$

where β_F is the shape coefficient in stationary flow. The KC number is defined as:

$$KC = \frac{u^f_{max} T}{n D_{n,50}} \tag{2.18}$$

where u^f_{max} is the maximum filter velocity, T the period of the oscillatory flow and $D_{n,50}$ the median nominal grain size. The inertia coefficient c in eq. (2.15) was found to increase with a parameter Ac accounting for the acceleration:

$$\gamma_F = 0.85 - \frac{0.015}{Ac} \ , \ Ac = \frac{u^f_{max}}{ngT} > \frac{0.015}{n/(1-n) + 0.85} \tag{2.19}$$

Whereas the assumption of time invariant coefficients b and c might seem reasonable for a cyclic flow, Burcharth and Andersen (1995) question to which extent such an approach is valid for a random wave-induced flow.

2.1.3 Effects of anisotropy and inhomogeneity

The previous concepts were derived assuming an isotropic porous medium. In an anisotropic porous medium, the hydraulic resistance changes with flow direction. Porous media consisting of stones more likely tend to have the longest axis of the stones aligned horizontally (normal to the gravity force), and the smallest axis vertically. As a result, the hydraulic resistance in the vertical direction is larger than in the horizontal direction.

van Gent (1995) proposed a relatively simple correction to the β_F coefficient, including the aspect ratio and the relative orientation of the flow with respect to the longest stone axis. This correction however, was not verified experimentally.

The intrinsic inhomogeneity of the granular material (i.e. the stone grading) is incorporated in the expressions of a and b through the porosity and characteristic stone diameter. Naturally, differences in characteristics at macroscopic scale cannot be implemented in one single set of porous media parameters.

2.1.4 Effect of air entrainment

Air entrainment due to turbulent mixing in the presence of a free surface leads to two-phase porous media flow. In this compressible flow, air bubbles can move independently from the main flow, remain stuck in the pores or move with the main flow. According to Barends (1980), the hydraulic conductivity K_{aw} of the porous medium for two-phase flow decreases for increasing air fraction n_a:

$$K_{aw} \approx K_w (1 - n_a)^3 \tag{2.20}$$

where K_w denotes the conductivity of single-phase flow. The air fraction n_a is defined as the ratio of air volume to the total volume of pore water and air.

Since the experimental flow tests are typically derived in a closed conduit, the effect of air entrainment is not incorporated in the porous media parameters derived from these tests. Hannoura and McCorquodale (1978, 1985) performed experimental research on two-phase porous media flow and concluded that the effect of air entrainment on the hydraulic conductivity depends on the flow direction relative to the movement of the air phase. They proposed the following modification to eq. (2.13):

$$I = \frac{a}{1-n_a}u^f + \frac{b}{(1-n_a)^2}u^f|u^f| + c_2\frac{\partial u^f}{\partial t} - n_a cos\Phi \tag{2.21}$$

where c_2 is obtained with eq. (2.15), replacing n by an effective porosity for two-phase flow: $(1-n_a)n$. Φ is defined as the angle of the flow direction of the air-water mixture relative to the movement of the air phase (i.e. the vertical direction).

2.1.5 Porous media flow parameters

A number of researchers developed expressions for the friction factors a and b in eq. (2.3), both using theoretical concepts (e.g. pipe flow analogy) or by performing laboratory tests on porous flow. For a (historical) background on this research, reference is made to e.g. Burcharth and Andersen (1995). It can be argued what kind of characteristic length scale D is to be used in eq. (2.7). Nonetheless, the concept of a hydraulic radius for a porous medium consisting of granular spheres is widely used. The hydraulic radius is then defined as the ratio of the pore volume to the pore surface area:

$$D = \frac{n}{N_k S_k} = \frac{dn}{6(1-n)} \tag{2.22}$$

where N_k is the number of spherical grains, O_k is the surface of a spherical grain and d the spherical grain diameter. Using the hydraulic radius as a characteristic length scale and introducing the filter velocity, which relates to the microscopic or pore velocity as $u = u^f/n$, eq. (2.7) is rewritten as:

$$I = \alpha_F \frac{(1-n)^2}{n^3}\frac{\nu}{gd^2}u^f + \beta_F\frac{1-n}{n^3}\frac{1}{gd}u^f|u^f| \tag{2.23}$$

where α_F and β_F are dimensionless factors which need to be determined experimentally, often referred to as *shape coefficients*. α_F depends on Re, the gradation and grain shape, and β_F on the same parameters plus the relative surface roughness of the grains.

A comprehensive overview of porous media parameters α_F, β_F and γ_F in eq. (2.23) or eq. (2.13) is given by Troch (2000). The review comprises the work published by various authors on different types of materials in laminar (Forchheimer) and fully- turbulent, steady and unsteady flow conditions. An important comment in this review concerns the size of tested materials. To the author's knowledge, no experimental values of shape coefficients (α_F,β_F,γ_F) are reported for larger stone diameters (D_{50}>0.10 m). Although β_F may be expected to show little variation in fully-turbulent flow, the lack of experimental data still induces some uncertainty when applying the porous media flow model at prototype scale.

Based on practical design values of porous media parameters in fully-turbulent flow, which is the most common flow type in permeable coastal structures, it can be shown (Troch, 2000) that the contribution of the linear (au^f) and inertia ($c\partial u^f/\partial t$) term in the total hydraulic resistance is very small compared to the quadratic term ($bu^f|u^f|$). In addition, the importance of an accurate determination of the porosity is stressed, since the friction factor b is much more sensitive to the porosity than the shape factor β_F or grain size D, due to the term $(1-n)/n^3$ in eq. (2.23).

2.2 Study of wave-induced porous flow

2.2.1 Analytical solutions based on potential flow theory

The only theoretical description of the interaction of water waves with a porous medium, which can be solved analytically, is provided by potential flow theory. Under this approach, the flow field is considered to be irrotational ($\nabla \times \vec{u} = 0$) and can be described by a velocity potential ϕ:

$$u_i^f = n\nabla\phi \tag{2.24}$$

A solution is derived for a homogeneous, rectangular porous medium on a flat bottom with water depth h, subject to a perpendicular incidence of small amplitude waves with wave height H and period T (Le Méhauté, 1957, 1958; Madsen, 1974; Sollit and Cross, 1972). Considering the previous assumptions, introducing a linearized hydraulic resistance and neglecting large-scale convective accelerations, the NS equations reduce to the following linearized non-stationary Bernoulli equation (Muttray and Oumeraci, 2005):

$$cn\frac{\partial\phi}{\partial t} + \frac{p}{\rho g} + a_{eq}n\phi = const. \tag{2.25}$$

Several authors have presented theoretical concepts for the linearized hydraulic resistance coefficient a_{eq}, see e.g. Madsen (1974); Sollit and Cross (1972). A concise overview on this topic is given by Muttray (2000).

A two-dimensional solution for the velocity potential ϕ fulfilling the specific boundary conditions at the bottom ($z = -h$) and the free surface ($z = 0$) was first presented by Biesel (1950) and Le Méhauté (1957, 1958). In this solution, a factor $exp(-\delta k'x)$ accounts for the exponential attenuation of wave height or pressure height along the direction of wave propagation (i.e. the horizontal x-axis). In this exponential factor, δ is a dimensionless damping coefficient (accounting for the damping rate) and k' the internal wavenumber ($k' = 2\pi/L'$, where L' is the wavelength inside the porous medium). Le Méhauté (1957, 1958) derived a set of dispersion equations for k' and δ.

The theoretical approach based on potential flow theory yields a relatively simple solution for the wave-induced porous flow in the breakwater core. However, this method will only provide accurate results when the flow field in the clear fluid region is not characterized by intensive wave breaking, when the influence of the wave reflection on the rear side of the breakwater is limited and when the linearized hydraulic resistance coefficient a_{eq} is effectively representing the bulk hydraulic resistance of the core material (Muttray, 2000). Furthermore, the theoretical solution assumes a simplified geometry of the structure, which does not account for energy dissipation and deformation of the flow field by a typical breakwater slope. The analytical solution moreover yields a damping rate δ which is independent from the vertical position below the free surface, in contrast to what has been observed in experiments (cfr. infra). It is clear that this theoretical approach will not yield accurate solutions in a realistic case of wave interaction with a complex RMB geometry.

2.2.2 Experimental research

Experimental research on wave-induced porous flow in a breakwater core is typically conducted by means of pore pressure measurements. According to the theoretical solution of Biesel (1950) and Le Méhauté (1957, 1958), the free surface elevation and pore pressure height inside a rubble mound breakwater decrease exponentially in the direction of wave propagation. Oumeraci and Partenscky (1990) presented the following expression for the damping of pore pressure height $P(x)$ in the breakwater core:

$$P(x) = P_0 exp(-\delta k'x) \tag{2.26}$$

where P_0 is the height of pore pressure oscillations at the interface between core and filter layer, and δ and k' the damping coefficient and internal wave number, respectively.

The attenuation of pressure height according to (2.26) has been verified by various researchers, e.g. Bürger et al. (1988), Oumeraci and Partenscky (1990) and Muttray et al. (1995, 1992), who all performed large-scale experiments in the Grösser Wellenkanal, Hannover (Germany) (GWK). Troch et al. (2002, 1998) conducted field measurements on the Zeebrugge breakwater (Belgium) and analyzed prototype data, experimental data and numerical results. Small-scale experiments were conducted by Hall (1991, 1992) who reported the occurrence of constant maximum water surface elevations in the seaward part of the breakwater core when subject to larger waves. This is possibly induced by 'internal wave overtopping', where the wave run-up on the breakwater core reaches the top of the core and causes a downward infiltration from the crest.

Two different approaches are distinguished to study the attenuation of pore pressure height along a horizontal section, depending on the specific core area under consideration. Figure 2.2 contains a definition sketch of the reference system. The first approach, used by Bürger et al. (1988) and Burcharth et al. (1999), considers the full breakwater core with the starting point ($x = zcotan\alpha$) of the horizontal section at a given depth $z = z'$ on the interface between filter layer and core.

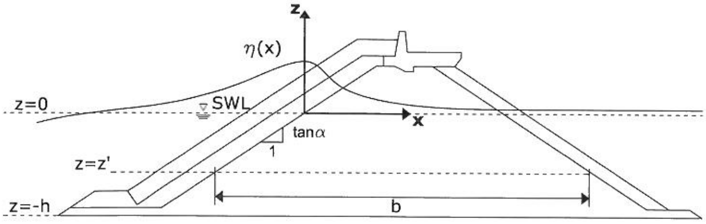

Figure 2.2: Definition sketch of the reference system used in the analysis.

The second approach proposed by Muttray and Oumeraci (2005) restricts the analysis of wave propagation to the part of the breakwater core where the water surface remains inside the core during the entire wave cycle. In this case, the analysis is limited to values of x larger than x_0, with x_0 corresponding to the point of maximum wave run-up on the core slope. This approach treats the wave transformation in the seaward part of the breakwater (i.e. the armour and filter layer and the seaward part of the core) and the wave propagation inside the core as two successive and separate processes. Using this assumption, the influence of the breakwater geometry on the pressure attenuation should be absent or strictly limited, and the latter should then only be affected by the hydraulic resistance of the core material.

Following the first approach, a practical calculation model was proposed by Burcharth et al. (1999) in order to assess P_0 and δ in eq. (2.26). From multiple experiments (e.g. Bürger et al. (1988), Oumeraci and Partenscky (1990)) and data from prototype measurements (Troch et al. (2002)), it was observed that the wave-induced pore pressure height at the interface between core and filter layer does not vary significantly along the core slope. Accordingly, a simple expression was proposed to predict the dimensionless 'reference pressure', i.e. the ratio between the dynamic oscillation of significant pressure height $P_{0,m0}/\rho g$ and the incident significant wave height $H_{m0,inc}$ at the breakwater toe:

$$\frac{P_{0,m0}}{\rho g H_{m0,inc}} \cong 0.5 \tag{2.27}$$

Burcharth et al. (1999) state that the rate of wave damping δ in the direction of wave propagation increases with increasing wave length (for equal wave height) and decreases with increasing wave height (for equal wave length). They moreover found δ to increase as the considered horizontal section moves closer towards the free surface. Based on the results from the experiments previously mentioned, the following empirical formula was proposed in order to complete the practical calculation model:

$$\delta = a_\delta \frac{\sqrt{n} L_p^2}{b H_{m0,inc}} \tag{2.28}$$

where n is the porosity of the core, b the total with of the considered horizontal section at depth $z = z'$ (see Figure 2.2) and $H_{m0,inc}$ and L_p are the significant wave height and peak wave length at the breakwater toe, respectively. A value for the dimensionless coefficient $a_\delta = 0.014$ was suggested, resulting from a linear regression analysis applied to the experimental δ values. The latter were obtained by curve fitting of the pressure recordings to eq. (2.26), assuming that the wave length inside the core can be approximated as $L_p^{'} \cong L_p/\sqrt{1.4}$. The accuracy of this calculation model, eqs. (2.27) and (2.27) will be further discussed in Chapter 4.

Following the second approach mentioned above, Muttray and Oumeraci (2005) derived a theoretical approach for the wave damping in the rear part of the breakwater ($x > x_0$). Different damping functions were established, based on the relationship between the hydraulic resistance (predicted with the Forchheimer equation eq. (2.3)) and the wave damping. Depending on the actual flow properties, the damping function takes a linear, quadratic or polynomial form. The theoretical solutions were validated with large-scale data obtained in the GWK flume and proved to describe the wave damping. However, an empirical correction was needed to compensate for deviations generated by simplifying assumptions such as the use of an averaged filter velocity and linearized dispersion equation.

2.3 Models based on the Navier-Stokes equations

The hydrodynamics of wave interaction with permeable structures are characterized by an ensemble of nonlinear three-dimensional processes, arising when surface water waves encounter an obstacle in their propagation, which can be either porous or solid. A numerical solution of such a problem is complex, due to the wide range of length scales which mark the different processes involved and their nonlinear interactions (del Jesus, 2011).

A multitude of *simplified*[3] approaches exist to model the fluid flow in wave-structure interaction. Regardless of the specific assumptions which lead to the simplified approach, their applicability is not general. The aim of the present study is to investigate the (nonlinear) wave-structure interaction with the highest possible accuracy and level of detail. For obvious reasons only a model based on the full NS equations will be suitable, since these equations (see Chapter 5 for a mathematical description) are the most general ones to describe fluid flow. They exactly represent the physical processes involved, from a microscopical point of view. Solutions need to be computed point by point and connected in the whole domain in order to obtain physically meaningful results.

All flow problems in coastal engineering exhibit a free surface, i.e. an interface between gas (air) and liquid (water). The much lower density of air with respect to the water [4] causes its inertia to be negligible compared to that of water. In this sense, the water moves independently, or freely, with respect to the air. The only influence of the air is induced by the pressure it exerts on the liquid surface and the effects of surface tension it possibly generates. The free surface is not explicitly incorporated in the model equations but rather acts as a boundary condition of the solution domain, which in addition is not fixed but moves and deforms under the action of the fluid. Numerical techniques have been specifically developed to deal with free surfaces.

A second important feature in the subject of study is the presence of a porous medium. Theoretically, a direct resolution of the NS equations inside the voids of the porous medium, without assumptions or simplifications of

---

[3] This term is used here to denote models which are not based on the full Navier-Stokes equations.

[4] The density of water is 998.21 kg/m at 20° Celsius. Compared to an air density of 1.20 kg/m under atmospheric pressure and the same temperature, the ratio of both densities is about 1:829.

any kind, should deliver the highest accuracy. Representing the exact nature of the highly complex porous matrix and the enormous computational cost (resulting from a very large variation in flow length scales) are true stumbling blocks however, which render the direction solution impossible to date. Instead, an engineering approach is used to represent the porous medium in the numerical model, making use of the concept of a porous media flow model (see section 2.1).

A synopsis of advances in NS solvers with applications in coastal engineering is presented hereafter.

2.3.1 Free-surface modeling

Basically two different approaches for free-surface modeling can be distinguished, commonly referred to as Lagrangian and Eulerian methods. Their classification is adopted from the frame of reference in which they are developed.

There are two main variations to the Lagrangian approach. In a first method, the grid is embedded in and moves with the fluid, which is probably the simplest means of defining and tracking a free surface. Several finite-element methods use this approach. The first applications in fluid dynamics go back to the early 1970's, see e.g. Hirt et al. (1970). A particular variation to the Lagrangian grid method is the Particle Finite Element Method (PFEM) method (Oñate et al., 2004), presenting a general formulation for solving fluid-structure interaction problems. A Lagrangian description is used to model the motion of grid nodes (particles) in both fluid and structure domains. Nodes are considered as particles which can freely move and even separate from the main fluid domain representing, for instance, the effect of water drops.

In a second branch of Lagrangian models, referred to as *(Lagrangian) particle methods*, the equivalents of grid points are fluid particles moving with the flow. The fluid particles are assigned a series of physical properties, mass being the most important one. An arbitrary number of particles constitute the free surface in this method. In a strict sense, it is not a free-surface modeling technique since the free surface is readily available in the meshfree method without further manipulation. An example of this kind of method with widespread use in coastal engineering is the Smoothed Particle Hydrodynamics (SPH) method.

The second class of free surface models are implemented in an Eulerian frame of reference, which is perhaps a more common way of representing the governing flow equations. The earliest numerical method devised for transient, free surface flow problems is the Marker-and-Cell (MAC) method (Harlow and Welch, 1965). This scheme is based on a fixed Eulerian grid of control volumes. The location of fluid within the grid is determined by a set of marker particles that move with the fluid, but otherwise have no volume, mass or other properties. Grid cells containing markers are considered occupied by fluid, while those without markers are empty (or void). A free surface is defined to exist in any grid cell that contains particles and that also has at least one neighboring grid cell that is void. Evolution of surfaces is computed by moving the markers with locally interpolated fluid velocities. Some special treatments are required to define the fluid properties in newly filled grid cells and to cancel values in cells that are emptied. In spite of its initial success, the method presents a number of drawbacks, e.g. a high computational cost due to the large number of particles required (Flow Science, 2012).

A last method discussed here is the Volume-of-Fluid (VOF) method based on the donor-acceptor approach first introduced by Hirt and Nichols (1981). This is an advection scheme for free-surface tracking employed in a considerable number of Eulerian NS solvers nowadays. The idea for this approach originated as a way to have the powerful volume-tracking feature of the MAC method without its high computational cost. In each grid cell (control volume), the fluid volume fraction within the cell is defined as a scalar quantity. Based on the amount of fluid in each cell, free surfaces can be located, as well as surface slopes and surface curvatures. The free surface can then be located in cells partially filled with fluid or between cells full of fluid and cells without fluid. First implementations of the VOF method suffered from the possibility of overfilling or over-emptying computational cells when volume fluxes are significant in all three directions and the time step size is close to the local Courant stability limit (Barkhudarov, 2004). These deficiencies were later remedied by introducing a Piecewise-Linear Interface Calculation (PLIC) scheme. Using the VOF method with PLIC is a contemporary standard. It is also used in the numerical model which will be further employed in this work. More details on this method are given in Chapter 5.

2.3.2 Porous media flow modeling

As mentioned before, it results to be impossible in practice to directly resolve the fluid flow in a highly complex, irregular and tortuous porous medium. A solution to this problem was presented by Sollit and Cross (1976), introducing the concept of *seepage velocity*. According to this simplifying approach, the real flow velocity inside the porous voids is replaced by an equivalent velocity over a continuous and microscopically homogeneous body. The flow that is confined to the interstitial voids is then distributed over the whole medium, neglecting the presence of the solid skeleton. This replacement avoids the need of a detailed representation of the voids. Their presence however is still accounted for by including macroscopic properties like porosity and permeability in the flow description. A consequence of this approach is the loss of flow details inside the porous medium. Furthermore, the porous medium properties are assumed to be time invariant, i.e. the porous medium is composed of a rigid skeleton that does not show any deformation under the action of the fluid flow.

Mathematically, the seepage velocity concept is a decomposition technique which resembles the Reynolds ensemble averaging technique for turbulent flows (see Chapter 5). The instantaneous (real) velocity u^* is split into three components:

$$u^* = u^s + u_s + u_t \tag{2.29}$$

where u^s is the seepage velocity and u_s and u_t are respectively spatial and temporal velocity fluctuations. The spatial fluctuations are due to geometrical irregularities of the porous matrix or boundary layers developing in the porous structure. The temporal fluctuations arise from unsteady flow features such as turbulent eddies in the pore holes. The same decomposition is applied to the pressure field.

The spatial and temporal fluctuations are locally defined and may present abrupt changes, while the seepage velocity represents the mean flow variation. In fact, the seepage velocity resembles the filter velocity u^f defined in section 2.1. The filter (or discharge) velocity is also an averaged porous flow velocity. However, it is averaged in a specific volume containing both fluid and solids, while the seepage velocity is defined as the average velocity of the fluid contained in the averaging volume. Both are related trough the porosity n of the porous medium:

$$u^f = nu^s \tag{2.30}$$

where n is the total volume of voids (accessible to the fluid) divided by the total volume of the porous medium considered.

If the instantaneous flow velocity in the NS equations is replaced by a decomposition according to eq. (2.29), time-averaging and volume-averaging operations are needed to eliminate the velocity fluctuations. Without specifying exact values for the averaging time interval and volume, Sollit and Cross (1976) state that the averaging time increment should be much smaller than the scale of macroscopic unsteadiness and that the averaging volume must contain a small but finite number of pores. Different approaches have been followed to implement the seepage velocity concept. Volume-Averaged Reynolds-Averaged Navier Stokes (VARANS) equations (Hsu et al., 2002; Slattery, 1999) and time averaging volume-averaged equations (de Lemos, 2006) are mentioned as two main approaches (del Jesus et al., 2012).

A review of existing VOF models applied in coastal engineering learns that there is not a unique method to incorporate a model for porous media flow. Mainly two different concepts in porous media flow modeling can be distinguished: (i) by applying volume-averaging techniques and (ii) by directly adding a porous drag term in the momentum equations[5]. It is moreover noticed that the specific approach to incorporate the porous media flow model is closely connected with grid composition and obstacle representation (see the difference between *body-fitted* meshes vs. *cut-cell* approach in Chapter 5).

Taking a closer look, it seems that the main difference between both approaches can be related to the treatment of turbulence in the porous media flow. Using the concept of seepage velocity and the Forchheimer drag model (eq. (2.3) or eq. (2.13)) provides a means to represent the flow losses in the numerical model in terms of an averaged macroscopic velocity. Since the derivation of the friction factors in the Forchheimer drag model is usually based on experimental measurements with saturated unidirectional flow in a closed conduit, only the flow losses included in such type of flow will be modeled. In this respect, these flow losses are to be considered as flow losses arising at *microscopic* scale (i.e. inside the pores), involving turbulent fluid shear stresses due to the geometrical structure of the individual grains inside the porous skeleton (inertial dispersion) and discrete shear and pressure forces acting onto the fluid along the external surfaces of the grains. *Macroscopic* flow losses due to velocity gradients over a larger length scale, in a specific flow pattern that is induced mainly by the macroscopic geometry of the porous medium do not correspond with the flow conditions which lead to the (extended) Forchheimer drag model.

Several authors (see e.g. Nakayama and Kuwahara (1999)) have worked on the modeling of macroscopic turbulence in porous media flow, using the seepage velocity concept. Applying volume-averaging to the RANS equations, a decomposition based on Reynolds-averaged quantities $\overline{q}$ (i.e. pressures or velocities) is performed, splitting the instantaneous value q into a volume-averaged component $\langle\overline{q}\rangle^f$, a turbulent ($q'$) and a spatial fluctuation (q''):

$$q = \langle\overline{q}\rangle^f + q' + q'' \tag{2.31}$$

In this way, the usual RANS equations are retrieved, with additional terms due to the volume-averaging process. The latter terms are then lumped into a macroscopic drag term according to eq. (2.3) or eq. (2.13), because they represent the aforementioned microscopic flow losses. In the reviewed models, the control volumes are identical to the cell volumes, turning the volume-averaged cell-based quantities into regular cell-based quantities. In this way, the VARANS approach become equivalent to the approach where a porous drag term is directly incorporated into the momentum equations.

---

[5] The presence of a porous medium should also be included in the mass continuity and kinematic free-surface boundary condition (if applicable), see Chapter 5.

The only possible difference between both approaches then stems from the turbulent shear stress term, which under the VARANS approach can be explicitly modeled inside porous media. Reference is made e.g. to del Jesus (2011), who applied volume-averaging to two different turbulence models: the k-ϵ model[6] and the SST model (Menter, 1994). The closure terms in the k-ϵ model are based on the work of Nakayama and Kuwahara (1999). It is noticed that this macroscopic turbulence model and closure terms were derived for fully-saturated flow. A validation study for two-phase flow has not been reported, to the author's knowledge. Experiments have shown (Hannoura and McCorquodale, 1985) that air entrainment causes a considerable reduction of the hydraulic conductivity, which is likely due to noticeable changes in the physical processes involved in two-phase turbulent porous media flow, e.g. the transport of air bubbles and possible blockage of pore holes.

Even within the VARANS approach differences are noticed in the formulation of the model equations (del Jesus, 2011). In this respect, it is important to recognize that an interface between the clear fluid and a porous obstacle, or between porous obstacles with different hydraulic conductivity, may introduce sharp variations in the flow field. In some volume-averaging approaches, matching conditions for velocity and shear stresses are imposed at these kind of interfaces, see e.g. de Lemos and Pedras (2001). In the model developed by del Jesus (2011), the prescription of such matching conditions is avoided by deriving one single set of equations applicable in both the clear fluid and porous medium. In the equations, the porosity function is included inside the spatial derivatives in the conservation equations, in order to correctly represent the interfaces appearing at the transition between clear fluid and porous media or between porous media with different characteristics. In the model used further in this work, which uses a cut-cell approach, the presence of such interfaces is automatically satisfied by inclusion of cell-based area and volume fraction functions in the conservation equations.

2.3.3 Applications in coastal engineering

In the last decade, many efforts have been made in developing and validating numerical models to study wave interaction with (permeable) coastal structures. Among the methods based on the NS equations previously mentioned, to the author's knowledge, it appears that two methods are nowadays widely used within the field of coastal engineering: the SPH method and Navier-Stokes solvers based on the VOF method.

The first attempts to model free-surface flows with the SPH method

---

[6] see Chapter 5

were carried out by Monaghan (1994). Ever since, the method has known an increasing number of applications in the field of coastal engineering. A general introduction on the application of SPH in wave modeling is given e.g. by Dalrymple and Rogers (2006). The method has already been applied to wave interaction with permeable coastal structures, see e.g. Shao (2010) who presented a two-dimensional model for wave interaction with a permeable structure. Although the SPH method shows a remarkable development in recent years, it is relatively new in coastal engineering. The validation of these models in wave interaction problems with permeable structures is still very limited. Consequently, this kind of method has not been considered for further use in the present study.

The first application of Eulerian NS solvers using the VOF method in coastal engineering is probably to the account of Austin and Schlueter (1982), who used the SOLA-VOF code (Nichols et al., 1980) to determine the flow field in a porous armour layer in a simplified rectangular breakwater section. Several successor codes have been developed subsequently from SOLA-VOF, extending the original method to a wider range of applications. A historical overview of key developments in VOF models used in the field of coastal engineering is given by Troch and De Rouck (1999), who also presented a model called VOFbreak[2]. The model was derived from SOLA-VOF and modified with some improvements and fixes in the donor-acceptor algorithm used in the VOF method. A Dirichlet-type wave boundary condition with active absorption was implemented and the governing equations were extended with the Forchheimer resistance terms to represent porous media flow. The numerical model was validated with a number of experimental data sets, derived from physical scale model testing and prototype measurements on the Zeebrugge breakwater (Belgium).

One of the successor codes of SOLA-VOF, called RIPPLE (Kothe et al., 1994) was modified with a k-ϵ turbulence model by Liu and Lin (1997) to simulate breaking waves. Wave generation boundary conditions were moreover implemented in this two-dimensional model, called COBRAS (Cornell BReaking waves And Structures). In an evolution of this model, Liu et al. (1999) included a porous media flow model by volume averaging the RANS equations according to the seepage velocity concept (cfr. supra). Hsu et al. (2002) further developed the model in order to account for turbulence inside the porous medium, based on the turbulence closure model presented by Nakayama and Kuwahara (1999). The model was applied in a 2D study of a composite breakwater.

Further development of COBRAS, adopted in COBRAS-UC, include the implementation of wave generation boundaries for simulation of sea states (Losada et al., 2008). This model has been successfully validated in a number of cases, e.g. for a low-mound breakwater (Lara et al., 2008), for a study of structure stability (Guanche et al., 2009) and for wave transformation on a barred beach (Torres-Freyermuth et al., 2010).

The previous models were limited to 2D flow. Hur et al. (2008) presented a numerical model to analyze 3D wave diffraction and transmission on a composite breakwater. This model does not apply volume-averaging of the NS equations but includes area and volume fractions in the momentum equations to represent the geometry of the porous structure, modeling the porous media flow resistance with a drag term. More recently, del Jesus et al. (2012) presented IH3VOF, a model for 3D wave interaction with permeable structures. The model makes use of the VARANS concept to simulate turbulent two-phase flow in porous media.

2.4 Conclusions

The literature review presented in this chapter has identified the advances in the field and current state of knowledge in three key aspects of the present study. Firstly, an overview on the theoretical concept to describe porous media flow was presented. The basic equation for steady porous media flow was first presented by Forchheimer (1901). This equation was later extended to unsteady flow. Furthermore, variations to the equation have been proposed to describe fully-turbulent and two-phase porous media flow. The Forchheimer model is based on experimental calibration of dimensional coefficients. A synopsis of porous media parameters derived from experimental flow tests performed by various authors is given by Troch (2000).

A second aspect of th literature review deals with the description of the porous flow field in permeable coastal structures, with special attention to RMB structures. An analytical solution for wave-induced flow in porous media is obtained with potential flow theory. It provides a theoretical basis for the description of the attenuation of flow motions within the porous medium, according to a negative exponential function. The assumptions in this approach however, simplifying the geometry of the porous structure and considering irrotational flow, render this method unsuitable for cases where the real solution to the problem is marked by a high degree of nonlinearity.

Several researchers have confirmed an exponential decay of surface elevation and pore pressure height in the core of a RMB, by means of experiments on physical scale models and prototype measurements. As a result, a practical calculation method was proposed (Burcharth et al., 1999) from which the wave-induced pore pressures can be related to the incident wave parameters in a straightforward manner. Muttray (2000) derived damping functions for the wave height attenuation within the core, based on experiments from a large scale model in the GWK flume. In this approach however, the influence of the breakwater slope on the spatial distribution of pore pressures was excluded. It is remarked that the latter large-scale tests provide an excellent basis for further research.

Finally, the advances in the development of numerical solvers based on the NS equations are discussed, which naturally provide the most accurate solutions for the wave-induced porous flow field in coastal structures. The most widespread models for coastal engineering applications are models based on the VOF approach, providing a computationally efficient method for free-surface tracking. To represent porous media flow, use is made of the seepage velocity concept, which can be implemented either by volume-averaging of the NS equations or by incorporation of a porous drag term in the momentum equations. In practice however, it turns out that both methods are equivalent.

The review of a selected, not exhaustive, number of 2D and 3D models based on the VOF method proves the value of these models in predicting wave interaction with permeable structures. To the author's knowledge however, the validation studies are typically limited to simplified cases on a reduced scale. This motivates the need for a thorough validation using large-scale data from a realistic multi-layered RMB, with inclusion of long-term transient effects under cyclic wave loading.

3 Physical scale model tests

3.1 Introduction

In the previous chapter, the large-scale tests performed by Muttray (2000) in the large wave flume (GWK) in Hannover have already been highlighted. This data set is probably unique in its kind and provides an excellent basis for fundamental research on wave-induced porous flow in a RMB, for a number of reasons:

- the large scale (1:5), excluding possible effects due to incorrectly scaled laminar porous flow in the core;
- a very extensive and accurate monitoring of pore pressures and surface elevations;
- an accurate determination of the porous media flow characteristics of the breakwater materials;
- a broad variation in regular and irregular wave conditions;

It is deemed useful to provide a concise description of the GWK model tests in the present chapter, since the work developed further on will heavily rely on the results obtained by these model tests. A synopsis of available information is presented hereafter, provided in the manuscript of Muttray (2000). For further details on the experimental setup not included here, reference is made to Muttray (2000) or Muttray and Oumeraci (2005).

In addition, a second experimental setup is presented, performed by the author in the wave flume of Ghent University (Belgium), hereafter referred to as the UG model. The tests concern pore pressure measurements on a smaller scale model (1:30), with a distorted core fraction in order to maintain Froude scale similarity. In the next chapter, the results of the small-scale and the large-scale model tests will be jointly used in the development of an improved calculation model for the wave-induced pore pressure distribution in the breakwater core.

3.2 Large-scale GWK model tests

3.2.1 Wave flume layout

A sketch depicting the layout of the wave flume is given in Fig 3.1, including a definition of the reference system. The wave flume has a total length of 300 m. A 100 m long, 1:50 foreshore slope makes the transition between flume beds near the paddle (the *far-field*) and breakwater model (the *near-field*). The start point of the foreshore is located at a distance of 133.95 m from the paddle in its initial position ($x = 0$ m). The foreshore continues in a 2 m thick sand layer on which the breakwater model is constructed. The sand has an average grain size D_{50}=0.22 mm and a hydraulic conductivity of $2.6 * 10^{-6}$ m/s. Muttray (2000) reports some erosion of the sand bottom in the vicinity of the slope toe and the toe of the breakwater, which has been considered when determining the local water depth at the breakwater toe. A 1:6 impermeable asphalt dike is positioned at the end of the flume ($x = 250.07$ m) as a spending beach. The toe of the breakwater (the point closest to the wave paddle) starts at 243.95 m from the piston.

The GWK wavemaker operated in the tests consists of a wave piston, combined with an upper rotating flap. The system is equipped with an active absorption system (Schmidt-Koppenhagen et al., 1997). The maximum piston stroke is ± 2.0 m , superimposed by upper flap movements of ± 10 degrees. An empirically corrected trochoidal wave profile is applied in case of regular waves, in order to enhance the stability of the wave train (Muttray, 2000).

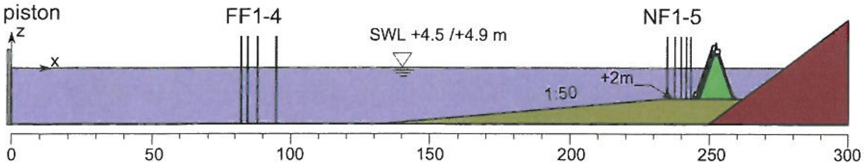

Figure 3.1: Layout of the GWK flume with indication of far-field (FFx) and near-field (NFx) wave gauges. Dimensions in m (stretched in vertical direction).

3.2.2 Breakwater model

A detailed view on the breakwater cross section is given in Fig 3.2. The breakwater consists of an Accropode armor layer (slope 1:1.5), filter layer, gravel core, toe protection and crest wall. The material specifications, adopted from Muttray (2000), are summarized in Table 3.1. Fig. A.1-A.4

in Appendix A shows the different parts of the breakwater model.

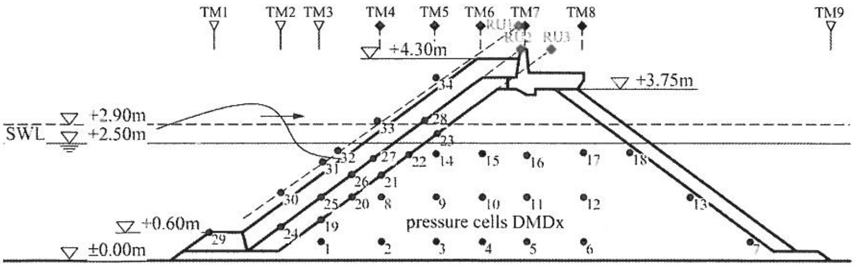

Figure 3.2: Cross section of the GWK breakwater model, with indication of pressure (DMDx), run-up (RUx) and wave gauges (TMx). Figure adapted from Muttray (2000).

Table 3.1: Properties of geometry, materials and porous flow conditions related to the GWK breakwater model.

	armour	**toe**	**underlayer**	**core**
type	Accropode	basalt rock	quarry rock (80/150 mm)	gravel (22/56 mm)
layer thickn. [m]	0.60	0.40	0.40/0.30	N/A
M_{50} [kg]	40	80	1.95	0.079
$D_{n,50}$ [m][1]	0.257	0.300	0.090	0.031
$D_{n,85}/D_{n,15}$ [-]	-	-	1.58	1.74
aspect ratio [-][2]	1	-	2.6	2
n [-]	0.510	0.450[3]	0.394	0.388
α_F [-][4]	305	305	305	1007
β_F [-][4]	1.27	1.27	1.27	0.63
γ_F [-][5]	0.52	0.43	0.43	0.00
Re [6]	$(5.0-10.1).10^5$	$(6.7-13.3).10^5$	$(1.4-2.7).10^5$	$(2.4-25.6).10^3$
KC [-][6]	23-153	22-148	51-338	8-226

[1] $D_{n,50} = (M_{50}/\rho_r)^{1/3}$, ρ_r is the apparent rock mass density

[2] max. length divided by min. distance between parallel lines through which the particle would pass (CIRIA et al., 2007)

[3] hypothetical value

[4] according to a and b in eq. (2.23), based on $D_{n,50}$

[5] according to c in eq. (2.15)

[6] corresponding with GWK wave tests (Muttray, 2000)

3.2.3 Instrumentation

Different aspects of the the wave motion on the breakwater slope were measured, including wave run-up, pressure distribution on the slope and water surface elevations. The wave propagation inside the structure was determined by wave gauges (TMx) installed inside the core and by wave run-up gauges (RUx) at the boundaries of the different layers. The pore pressures were measured by pressure transducers (DMDx) inside the core (at three different levels) and along the boundaries of the different layers. The location of the measuring devices at and inside the breakwater are indicated in Fig. 3.2. A full list of all measuring devices with exact position is included in Table A.1 in Appendix A. All data were recorded at 40 Hz.

3.2.4 Hydraulic boundary conditions

The hydraulic boundary conditions are summarized in Table 3.2. An important aspect of the wave conditions concerns the choice of Still Water Level (SWL) and wave height. To avoid downward infiltration into the breakwater core from the crest of the breakwater, wave overtopping conditions were excluded from the tests. For the given breakwater slope ($cot\alpha = 1.5$), the employed ranges of waves steepness result in nonbreaking (surging) wave conditions, since values of the breaker parameter ξ are larger than 2-3 (EurOtop, 2007). Ranges of ξ are included in Table 3.2. ξ is defined by eq. (3.1a) or eq. (3.1b), for regular and irregular waves respectively:

$$\xi = \frac{tan\alpha}{\sqrt{H_m/L_0}} \tag{3.1a}$$

$$\xi = \frac{tan\alpha}{\sqrt{2\pi H_{m0}/(gT^2_{m-1,0})}} \tag{3.1b}$$

where $T_{m-1,0} = m_{-1}/m_0$ is a spectral wave period, defined as the ratio of the first negative to the zero$^{\text{th}}$ moment of the variance spectrum of incident waves at the toe of the structure. H_m or H_{m0} refer to the incident mean or significant wave height at the toe of the breakwater in case of regular and irregular waves, respectively. It is noticed that in a limited number of irregular waves tests, the wave front of the steepest waves might becoming unstable and show a light form of wave breaking, as reported by Muttray (2000).

Table 3.2: Hydraulic boundary conditions in GWK tests.

	regular waves	irregular waves
wave spectrum	N/A	TMA[1]
water depth h [m][2]	2.5/2.9	2.5/2.9
H_{inc}/h [−][2]	0.08 - 0.48	0.08 - 0.38
kh [−]	0.32 - 1.45	0.32 - 1.45
ξ [−]	3.2 - 15.7	3.3 - 13.6

[1] Hughes (1984)
[2] at breakwater toe

3.3 Small-scale UG model tests

3.3.1 Wave flume layout

The experimental research (Vanneste and Troch, 2010) was conducted in the wave flume of Ghent University, which is 30 m long, 1.2 m high and 1 m wide. A sketch depicting the layout of the wave flume is included in Appendix B (Fig. B.1), including a definition of the reference system. Waves are generated with a piston wavemaker with active wave absorption (Troch, 2000), using the feedback of surface elevations of 2 wave gauges in the vicinity of the piston face. A 4.4 m long, 1:20 impermeable foreshore slope makes the transition between flume beds near the paddle and the breakwater model. The start point of the foreshore is located at a distance of 6.4 m from the paddle in its initial position ($x = 9.36$ m). The foreshore continues in a 0.29 m thick screed layer on which the breakwater model is constructed. A void of 0.05 m width below the foreshore connects the 'seaward' and 'landward' sides, allowing the recirculation of transmitted water. A gravel spending beach is constructed at the end of the wave flume. The toe of the breakwater (the point closest to the piston) starts at 17.54 m from the piston ($x = 20.5$ m).

3.3.2 Breakwater model

The breakwater model is based on the existing design of a low-crested breakwater built for the new port entrance in Ostend (Belgium) constructed in 2010-2012. The model cross section was scaled at 1:30 and slightly modified in the framework of the present research. In particular, the crest level was raised to 0.20 m above SWL to avoid overtopping in the applied wave conditions (see section 3.3.4). The experimental set-up consisted of a rubble-mound breakwater with a multi-layered cross section consisting of armour layer (slope 1:1.5), underlayer, core and toe protection (see Fig. 3.3). Three different types of armour layers were used : HARO units, Antifer units and coarse gravel. Material specifications are summarized in Table 3.3.

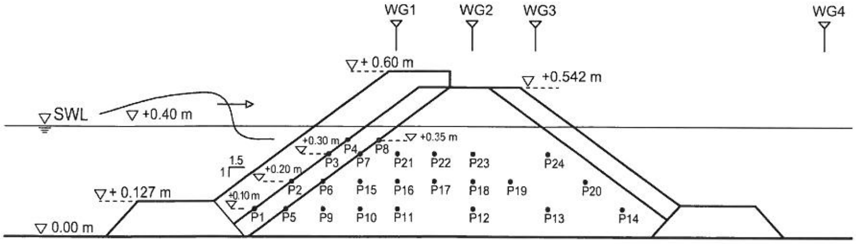

Figure 3.3: Cross section of the UG breakwater model with indication of pressure (Px) and wave gauges (WGx).

A point of particular interest concerns the scaling of the core material. In order to avoid a possible incorrect representation of the porous flow in the breakwater core, the size of the core material was determined by a scaling procedure according to Burcharth et al. (1999). The application of the scaling procedure assumes the knowledge of the hydraulic properties of the rock material. Therefore, a literature review of tested rock gradings was carried out, resulting in the selection of stone sample 'test 2' (5-25 mm) from the report of Burcharth and Christensen (1991). This means that the core material has been scaled with a larger scale (1:19) than the geometrical model scale (1:30).

Using the available sieves in the laboratory, this stone fraction 'test 2' was reconstructed to match the original sample as far as possible. The shape class of a representative sample taken from the stone material was determined according to the method specified by CIRIA et al. (2007). Details are given in Fig. B.3 in Appendix B.

Since it is important to have an accurate value for the porosity in the scaling procedure, measurements on the core material were carried out both in a recipient and 'in situ'. The latter method is performed on the material as built in the wave flume. A procedure has been elaborated to measure the porosity, by first weighing the amount of stones in well-determined volume in saturated surface dry conditions, followed by measuring the mass of water added to a control volume. Subsequently measuring the bulk volume occupied by the stones with a surface profiler, the porosity could then be determined. By measuring the bulk volume before and after compactation under wave loading, possible variations in the porosity could be detected. The stone density required in the previous procedure was measured from a representative sample in saturated surface dry conditions.

Table 3.3: Properties of geometry, materials and porous flow conditions related to the UG breakwater model.

	Armor			Filter	Core
type	HARO	Antifer	gravel (35/50 mm)	gravel (25/40 mm)	crushed rock (5/25 mm)
layer thickn. [m]	0.115	0.102	0.115	0.07	N/A
M_{50} [kg]	0.542	0.330	0.139	0.063	0.005
D_{50} [m]	0.070	0.060	0.043	0.033	0.0138
D_{85}/D_{15} [-]	N/A	N/A	1.18	1.37	1.84
aspect ratio [-]	N/A	N/A	-	-	2.3
n [-]	-	-	-	-	0.407[1]
α_F [-][2,3]	-	-	-	-	1053
β_F [-][2,3]	-	-	-	-	3.45
Re [-] [3,4]	-	-	-	-	182-1767

[1] experimental measurement in UG flume

[2] according to a and b in eq. (2.23), based on D_{50}.

[3] derived from stationary flow test (Burcharth and Christensen, 1991)

[4] valid range derived from experimental flow tests

3.3.3 Instrumentation

In total, 24 pressure gauges (Px) were installed to measure pore pressures on the filter and core slope and inside the core of the breakwater. The positions of the pressure gauges are indicated in Fig. 3.3. The sensors are placed in 3 levels, separated 0.10 m from each other, the lowest level at a distance of 0.10 m above the local seabed. The pressure transducers measure absolute pressures, resulting in high-precision measurement.

The water movement inside the breakwater core was measured with three wave gauges (WGx, see Fig. 3.3), protected by a perforated plastic pipe. One wave gauge (WG4) at the rear of the structure was used to measure wave transmission. Pictures showing the measurement instrumentation and the test facility are shown in Fig. B.4 and B.5 in Appendix B.

A full list of all measuring devices with exact position is included in Table B.1 in Appendix B. All data were sampled at 40 Hz.

3.3.4 Hydraulic boundary conditions

The hydraulic boundary conditions are summarized in Table 3.4. A constant water depth of 0.4 m was used. The test program consisted of regular and irregular wave trains. As in GWK tests, the wave heights and periods were chosen in accordance with the crest level in order to avoid wave overtopping. The range of wave heights for the regular waves varied between 0.02 and 0.10 m. Wave periods ranged between 1.09 and 2.6 s. Irregular wave are generated according to a JONSWAP spectrum (γ=3.3), with significant wave heights from 0.06 to 0.10 m and peak periods from 1.3 to 2.6 s. The length of both regular and irregular wave trains determined to include at least 500 waves. This provided a sufficient duration to eliminate transient effects in the pressure recordings and to track the potential water level set-up in the breakwater core.

During tests, no explicit wave breaking on the breakwater slope was observed, in accordance with the wave conditions from the tests series. Only the largest waves in the tests with irregular waves are situated in the transition zone between breaking and nonbreaking (ξ between 2 - 3), and might be associated with a mild form of wave breaking. Ranges of the breaker parameter ξ are given in Table 3.4.

Table 3.4: Hydraulic boundary conditions in UG model.

	regular waves	**irregular waves**
wave spectrum	N/A	JONSWAP (γ=3.3)[1]
water depth h [m][1]	0.4	0.4
H_{inc}/h [-][1]	0.04 - 0.28	0.17 - 0.28
kh [-]	0.51 - 1.50	0.51 - 1.16
ξ [-]	2.7 - 16.0	3.1 - 6.7

[1] Joint North Sea Wave Project (JONSWAP), Hasselmann et al. (1973, 1976)

[2] at breakwater toe

4 An improved pore pressure calculation model

4.1 Introduction

A relatively simple practical calculation method (Burcharth et al., 1999) can be used to determine the pore pressures in the core of a RMB, if the incident wave parameters at the toe of the structure are known. As will be shown further however, this method seems too simplistic to capture the variation in spatial distribution of pore pressures when the incident wave conditions vary significantly. This shortcoming is the main motivation to search for an improved calculation model, valid in a broad range of wave conditions, however limited to nonbreaking conditions in the present study.

The derivation of new empirical formulae to describe the pore pressure distribution is based on the results from large-scale model tests in the GWK flume, performed by Muttray (2000). The tests have been fully re-analyzed in detail in the present study. It is mentioned that the breakwater geometry tested by Muttray shows only minor differences to the geometry tested by Bürger et al. (1988) and Oumeraci and Partenscky (1990). It can be regarded as an optimization of the latter tests which were used to derive the calculation method (eqs. (2.27) and (2.28)).

In this chapter[1], a new approach is proposed to determine the distribution of pore pressure height inside the breakwater core, based on one single set of large-scale tests. In order to ensure the general applicability of the new calculation model, it is in addition verified using measurements from the small-scale UG model described in the previous chapter.

---

[1] The chapter is adapted from a paper published in Coastal Engineering (Vanneste and Troch, 2012).

4.2 Derivation of a new calculation model

The combination of equations (2.26), (2.27) and (2.28) yields a practical calculation model to estimate the pore pressure attenuation within the full breakwater core. Nevertheless, the derivation of this calculation model was initially based on a very limited number of large-scale model tests. A reanalysis by Troch et al. (2002), using the results of an extended number of GWK tests and prototype measurements, confirmed the applicability of the calculation model, but also revealed an increased scatter compared to the results from the original regression analysis by Burcharth et al. (1999). Moreover, the application of equations (2.27) and (2.28) on the complete set of experimental data from GWK tests has shown that the accuracy of the present model is poor under varying wave conditions (see further, Fig. 4.16). The previous considerations question the statistical validity of the existing calculation model equations, and give cause to search for improvements in both model formulation and accuracy.

4.2.1 Methodology

In the following, the term 'pore pressure' refers to the excess pore water pressure which is solely induced by wave action. The term '(pore) pressure height' (P) is used in the same way as for water waves to designate the height of the pressure fluctuations. The recorded pressure time series are processed in a similar way as the surface elevations. In experiments with regular waves, the pressure variation is characterized by the mean pressure height P_m, whereas for irregular waves a significant pressure height P_{m0} is obtained from the pressure variance spectrum.

Of both approaches that can be used to examine the pressure attenuation mentioned previously in section 2.2.2, the one considering the full breakwater core will be the most relevant for practical applications. The widely-used assumption of an exponential decay of pore pressure height in the direction of wave propagation (x-direction) according to eq.(2.26) will be used to describe the evolution of the measured pore pressure height in the core.

However, a concern rises when applying eq.(2.26) to a horizontal section with starting point at the interface between core and filter layer, since a significant deviation is observed between the theoretical exponential decay of pore pressure height and the actual measured decay. The deviation is observed in a limited region near the seaward breakwater slope, as illustrated in Fig. 4.1, showing the attenuation of pressure height along 3 sections in the breakwater core. The distance along each section at a certain depth z is represented by a local coordinate in horizontal direction with origin at the intersection between core and filter layer: $x' = x - zcotan\alpha$.

In the bottom and middle section, the rate of pressure height decay initially is small (or even negative in some tests) in a limited zone near the slope, followed by an accelerated decrease. The deviation from the theoretical exponential decay is most probably caused by the wave infiltration processes that take place in the lower part of the seaward slope, since the deviation is most pronounced on a horizontal section near the bottom, and virtually absent on a section close to the free surface. The observed deviation is more pronounced for regular waves, when compared to wave spectra.

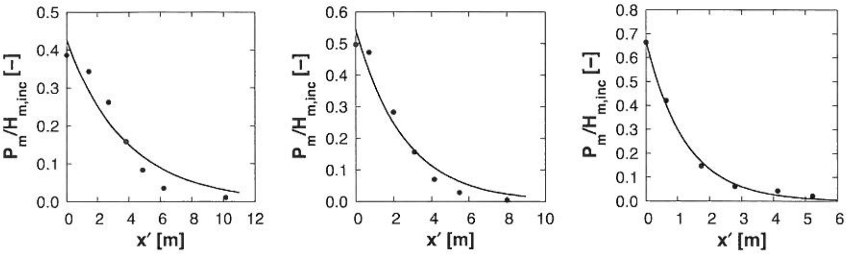

(a) (b) (c)

Figure 4.1: Attenuation of dimensionless pore pressure height at (a) bottom section ($z/h = -0.86$), (b) middle section ($z/h = -0.53$) and (c) top section ($z/h = -0.22$), GWK tests with regular waves ($H_{m,inc}$=0.222 m, T=3 s). Experimental values (dots) versus exponential fitting (line).

Given the deviation between the observed and theoretical attenuation of pore pressure height according to eq. (2.26), a new approach is proposed in order to describe the pressure height attenuation. The considered section at depth z is divided in two regions: (i) **zone 1**, near the seaward slope, where the decay of pressure height does not match an exponential function, and (ii) **zone 2**, where the use of an exponential function results in a accurate description of the pore pressure height evolution. Hereafter, empirical model equations are derived to describe the evolution of $P(x, z)$ within the breakwater core. The equations will be derived in three consecutive steps, in order to describe (i) the reference pressures on the interface between core and filter layer (at $x = zcotan\alpha$, see Fig. 2.2), (ii) the pressure gradient in zone 1 and (iii) the pressure attenuation in zone 2, according to an exponential pressure decay.

4.2.2 Reference pressures at the interface core-filter layer

The pore pressure P_0 along the interface between core and filter layer is represented hereafter by the so-called dimensionless *reference pressure*, i.e. the ratio between the dynamic pressure height oscillation $P_0/\rho g$ [mwc] and the incident wave height H_{inc} (=H_m or H_{m0}) at the toe of the breakwater. The reference pressures are measured by gauges on the interface between core and filter layer, see Table 4.1 and Fig. 3.2. In some test cases with a large incident wave height, it was observed that the pressure gauges DMD22 and DMD23 close to SWL are running dry under the passage of a wave trough. Such tests were eliminated from the final results.

Table 4.1: Positions of the pressure gauges on the interface between core and filter layer, in the GWK and UG model.

GWK			**UG**	
gauge	**z/h [−] ($h = 2.5\ m$)**	**z/h [−] ($h = 2.9\ m$)**	**gauge**	**z/h [−] ($h = 0.4\ m$)**
DMD19	-0.65	-0.70	P5	-0.75
DMD20	-0.46	-0.53	P6	-0.50
DMD21	-0.27	-0.37	P7	-0.25
DMD22	-0.10	-0.22	P8	-0.13
DMD23	+0.08	-0.07		

The reference pressures $P_0/\rho g H_{inc}$ will be affected by (i) the wave run-up on the armour slope and (ii) the hydraulic resistance of the armour and filter layer. The wave run-up on the armour slope is responsible for the spatial variation of the pressure height along the armour slope, whereas the hydraulic resistance of the armour and filter layer causes a difference between the pressure heights and the armour and core slope. This is illustrated in Fig. 4.2, showing the variation of the dimensionless pressure heights along the armour and core slope. The pressures on the armour slope are indeed governed by the wave run-up, and more specifically the wave length, since only very limited differences are observed between reference pressures associated with the two wave heights shown. The pressure variation on the core slope shows a different image. In this case, the variation along the core slope is much more limited since the increase of pressure height towards SWL is significantly reduced. The influence of the hydraulic resistance of the armour and filter layer becomes apparent in the deviation observed between tests with different incident wave height. This deviation is largest in the upper part of the slope ($-0.5 < z/h < 0$). The larger energy dissipation associated with increasing wave height is accounting for the deviation between tests with different wave height. The mean value of P_0 however is still strongly influenced by the wave run-up on the armour slope.

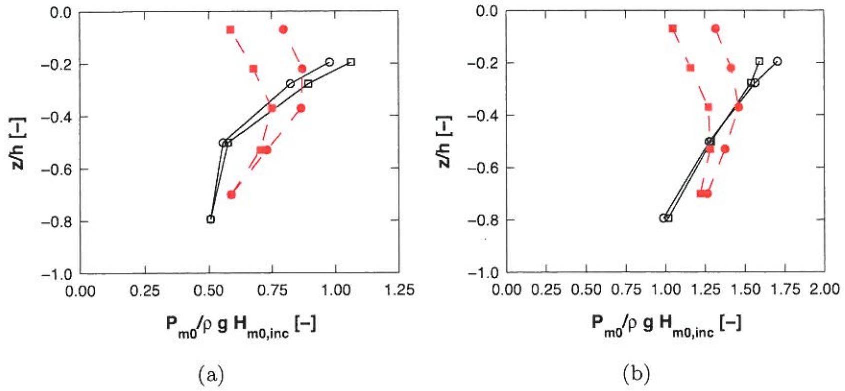

Figure 4.2: Variation of reference pressures along the armour slope (black solid) and core slope (red dashed): for GWK tests with (a) short waves (T_p=4 s, $kh = 0.98$) and (b) long waves (T_p=8 s, $kh = 0.44$). Both cases contain 2 wave heights: $H_{m0,inc} \approx 0.25$ m (circles) and $H_{m0,inc} \approx 0.7$ m (squares).

The prediction formula aimed for, capable of describing the variation of reference pressures on the core slope needs to: (i) represent the influence of the wave run-up (mainly affected by the wave length) and (ii) account for the flow losses due to the hydraulic resistance of the armour and filter layer. Concerning the latter, it appears impossible to express the influence of the hydraulic resistance by means of specific material properties (eg. porosity, grading, average stone size, porous flow characteristics), the thickness, the number of layers or any other property related to the breakwater geometry; not only from a practical point of view, but also since none of these parameters have been varied during the tests. Alternatively, the effect of the hydraulic resistance can be incorporated in the formula by including the variation of P_0 with varying incident wave height H_{inc}, as observed in Fig. 4.2.

The previous considerations imply that a prediction formula for the dimensionless reference height $P_0/\rho g H_{inc}$ will contain a dimensionless parameter accounting for the effect of the wave length (the relative water depth kh) and the wave height (the relative incident wave height H_{inc}/h). A detailed study was performed on the individual impact of the relative water depth and incident wave height on the reference pressure. This has resulted in the following empirical prediction formula, which is considered to a good compromise between model simplicity and predictive accuracy:

$$\frac{P_0(z)}{\rho g H_{inc}} = exp(c_{1,1}(z) - c_{1,2}(z)kh - c_{1,3}(z)H_{inc}/h) \tag{4.1}$$

where $c_{1,i}(z)$ $(i = 1..3)$ are dimensionless parameters resulting from a non-linear regression analysis performed on the pressure measurements, shown in Fig. 4.3. The lowest pressure gauge along the core slope is DMD19 (Table 4.1). The minimum value of z/h attains -0.7 in this case. In order to fill up the gap between z/h -0.7 and -1, a virtual measuring point on the core slope is added at the same vertical position as DMD1. The pressure height at this location is approximated by taking the average of the pressure heights measured by DMD24 and DMD1. Tests with different water depths were treated jointly in this analysis.

The regression parameters $c_{1,i}(z)$ in eq. (4.1) account for the spatial variation of the reference pressure along the core slope, induced by the wave run-up and the hydraulic resistance of the armour and filter layer. Theoretically, the parameters $c_{1,i}(z)$ are coupled with the specific properties of the GWK model, since the latter affect the run-up and hydraulic resistance (i.e. the front slope angle, layer thicknesses and material properties of armour and filter layer). The general applicability of the regression parameters will be discussed further.

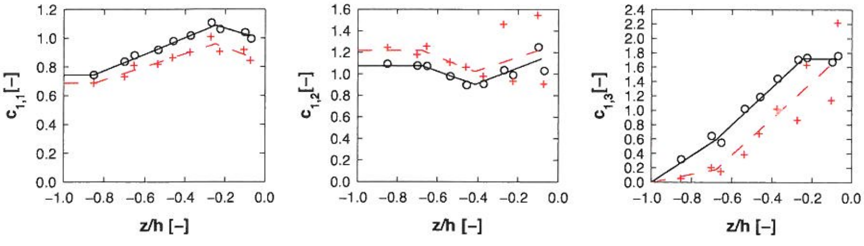

(a) (b) (c)

Figure 4.3: Dimensionless regression parameters (a) $c_{1,1}(z)$, (b) $c_{1,2}(z)$ and (c) $c_{1,3}(z)$ in eq. (4.1), for regular (black circles) and irregular (red crosshairs) wave tests. Piecewise linear approximations to $c_{1,i}(z)$ for regular (black solid) and irregular (red dashed) waves according to Table 4.2.

Of all the three regression parameters $c_{1,i}(z)$, the largest variation with depth z/h is observed for $c_{1,3}$. In Fig. 4.3(c), $c_{1,3}$ almost linearly increases from 0 to approximately 1.7 near SWL. This implies that the effect of the wave height will be most pronounced in the upper region of the core slope close to the free surface, an indication that the pressure attenuation in this region is mainly due to the hydraulic resistance[2]. Moreover, in the same zone near SWL ($z/h > -0.3$) and in case of irregular wave tests, the parameters $c_{1,2}$ and $c_{1,3}$ show a considerable variation between tests with different water depth (2.5 and 2.9 m). A comparison of the measured surface elevations and pore pressures did not reveal however any clear physical differences between tests with different water depth. This fact, together with the much more limited variation in case of regular wave tests, suggests that the scatter in $c_{1,2}$ and $c_{1,3}$ is an outcome of the regression analysis itself. Since larger values of $c_{1,2}$ are combined with smaller values of $c_{1,3}$, a certain correlation appears between the relative water depth and incident wave height in eq. (4.1), in case of irregular wave tests.

In order to employ eq. (4.1) in a practical calculation model, the variation of the different parameters $c_{1,i}(z)$ is approximated by a piecewise linear function with relative depth z/h, as shown in Fig. 4.3. In the aforementioned cases where values of $c_{1,i}$ vary noticeably between tests with water depth, the approximated value for a given pressure gauge is taken as the average value of both tests. Characteristic points which determine the piecewise linear approximation for $c_{1,i}(z)$ parameters are specified in Table 4.2.

Table 4.2: Characteristic model values of $c_{1,i}(z)$ [-] in eq. (4.1).

	Regular waves			**Irregular waves**		
z/h [$-$]	$c_{1,1}$	$c_{1,2}$	$c_{1,3}$	$c_{1,1}$	$c_{1,2}$	$c_{1,3}$
-1.00	0.74	1.07	0.00	0.69	1.22	0.00
-0.85	0.74	-	-	0.69	1.22	-
-0.68	-	1.07	0.60	-	1.22	0.18
-0.42	-	0.90	-	-	1.02	-
-0.25	1.09	-	1.72	0.96	-	-
-0.09	-	-	-	0.88	1.23	1.68
-0.08	1.02	1.14	1.72	-	-	-

Fig. 4.4(a,b) show the comparison between the reference pressures and values predicted by eq. (4.1), for regular and irregular waves, respectively. Parameters $c_{1,i}(z)$ according to Table 4.2 are employed to establish Fig. 4.4. The use of the approximated $c_{1,i}(z)$ values instead of the exact values determined in the regression analysis has only a minor impact on the prediction accuracy. The results in Fig. 4.4 show that eq. (4.1) is able to predict the reference pressures with good accuracy: a relative standard deviation (σ') between measured and predicted values of 6.5% is obtained in case of irregular waves, a slightly higher value of 8.4% is obtained in case of regular waves tests.

---

[2] Note that a pressure reduction due to air entrainment will be most pronounced near the free surface.

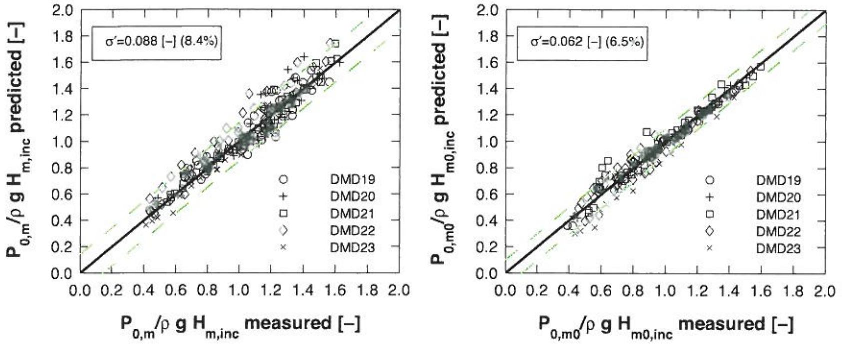

(a) (b)

Figure 4.4: Measured (GWK) vs. predicted values of reference pressure $P_0/\rho g H_{inc}$, for (a) regular and (b) irregular waves. Predicted values by eq. (4.1) with $c_{1,i}(z)$ according to Table 4.2; 90 % confidence interval in green dashed.

4.2.3 Pressure gradient in zone 1

The application of eq. (2.26) results in a poor description of the pressure height decay in zone 1, for this equation implies a decreasing rate of change of the gradient of pore pressure height I_P $(= -\partial(P/\rho g)/\partial x)$, whereas an increasing rate of change of I_P is generally noticed in zone 1. The transition between zone 1 and 2 will thus be marked by a rate of change of I_P equal to zero. The separation point $x_s(z)$ between zone 1 and 2 is obtained practically as the inflection point of the cubic spline fit through the measured pressure heights. A definition sketch of the proposed approach defining both zones is shown in Fig. 4.5.

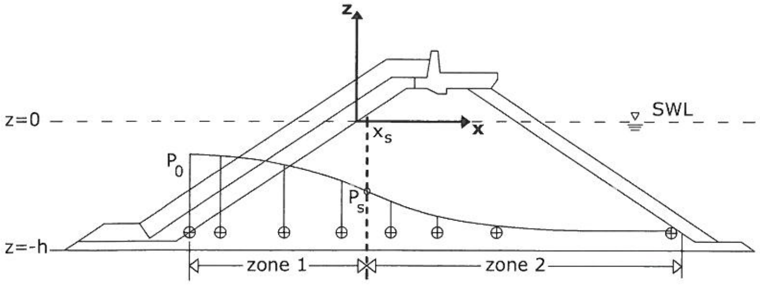

Figure 4.5: Definition of zone 1 and 2 in the breakwater core

In order to identify the x-coordinate $x_s(z)$ of the separation point, a dimensionless parameter $\kappa(z)$ is introduced:

$$\kappa(z) = \frac{x_s(z)}{z cotan \alpha} \tag{4.2}$$

Values of $\kappa(z)$ derived from the experiments are shown in Fig. 4.6. In tests with both regular and irregular waves with the smallest water depth employed (h=2.5 m), the attenuation of pressure heights measured by the upper row of pressure gauges is in accordance with an exponential decay starting from the interface core-filter, hence $\kappa = 1$. In other cases, κ (at a fixed depth z) varies significantly with varying wave length. In order to obtain a practical calculation model, the tests were divided in two groups, according to the wave length: (i) waves with small to medium-sized wave length ($kh \geq 0.5$) and (ii) long waves ($kh < 0.5$). In both groups, the value of $\kappa(z)$ used in the calculation model is approximated as the average of the κ-values of each section at depth z/h. Values of $\kappa(z)$ over the entire depth are then interpolated linearly in between the known model values, as shown in Fig. 4.6. The characteristic values which determine the practical piecewise linear approximation for $\kappa(z)$ are given in Table 4.3.

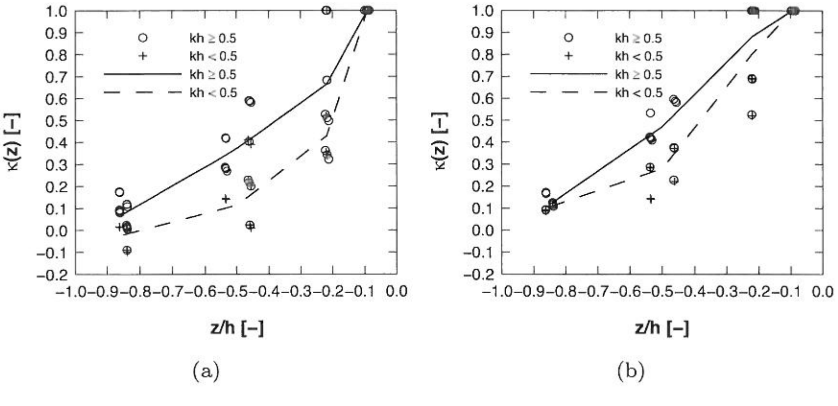

Figure 4.6: Experimental values of $\kappa(z)$ (circles and crosshairs) and piecewise linear approximations (solid and dashed lines), for tests with (a) regular and (b) irregular waves.

In Fig. 4.6, slightly smaller values of $\kappa(z)$ are observed in case of regular waves, compared to irregular waves. This is in agreement with the observation of a more pronounced deviation between the observed and theoretical attenuation of pressure height in case of regular waves. It is noticed, that the values of $\kappa(z)$ shown in Fig. 4.6 are determined for a fixed slope $cotan\alpha = 0.5$. Logically, $\kappa(z)$ will increase with increasing slope angle, as the influence of the breakwater slope on the spatial variation of pore pressures diminishes. It is expected that employing the model values of $\kappa(z)$ in Fig. 4.6 in cases where the slope differs (moderately) will not result in a dramatic loss of accuracy when employing the model equations in zone 1 and 2, determined hereafter.

Table 4.3: Characteristic model values of $\kappa(z)$ [-]

	Regular waves		**Irregular waves**	
z/h [$-$]	$kh \geq 0.5$	$kh < 0.5$	$kh \geq 0.5$	$kh < 0.5$
-0.85	0.07	-0.02	0.12	0.11
-0.50	0.37	0.11	0.47	0.28
-0.22	0.66	0.43	0.88	0.80
-0.09	1.00	1.00	1.00	1.00

Rather than searching for a description of the evolution of pore pressure height in zone 1, the total pressure gradient $I_{P,1}$ over zone 1 ($zcot\alpha \leq x \leq x_i(z)$) will be studied. Considering a horizontal section at depth z, the reference pressure $P_0(z)$ (at $x = zcot\alpha$) and the pressure height $P_s(z)$ (at $x{=}x_s(z)$) are linked by the total pressure gradient $I_{P,1}(z)$:

$$P_s(z) = P_0(z) + \rho g I_{P,1}(z)[1 - \kappa(z)]zcotan\alpha \qquad (4.3)$$

The local pressure height $P(x, z)$ in zone 1 ($zcotan\alpha \leq x \leq x_i$) can be approximated by a linear interpolation between $P_0(z)$ and $P_i(z)$, using the total gradient $I_{P,1}(z)$:

$$P(x, z) = P_0(z) - \rho g I_{P,1}(z)[x - zcotan\alpha] \qquad (4.4)$$

It is clear that using the total pressure gradient $I_{P,1}(z)$ will deliver an underprediction of the measured pressure height $P(x, z)$ in zone 1, given the increasing rate of change of I_P starting from $x = zcotan\alpha$.

It is assumed that the decay of pressure height in zone 1 differs from the theoretical exponential decay as a result of the distortion of the flow field by the breakwater slope. Under this assumption, $I_{P,1}(z)$ will be affected jointly by the local hydraulic resistance of the core material and by the wave run-up on the breakwater slope. A study of the experimentally obtained pressure gradients $I_{P,1}(z)$ shows that they are dominantly governed by the incident wave height. The impact of the wave length (and implicitly, the impact of the wave run-up) is much less pronounced; it is however noticed that $I_{P,1}(z)$ increases with increasing wave period, an observation which is more pronounced in case of irregular waves. In the practical model developed hereafter, the tests are grouped according to the wave length, in the same way as in the derivation of $\kappa(z)$: $kh < 0.5$ and $kh \geq 0.5$.

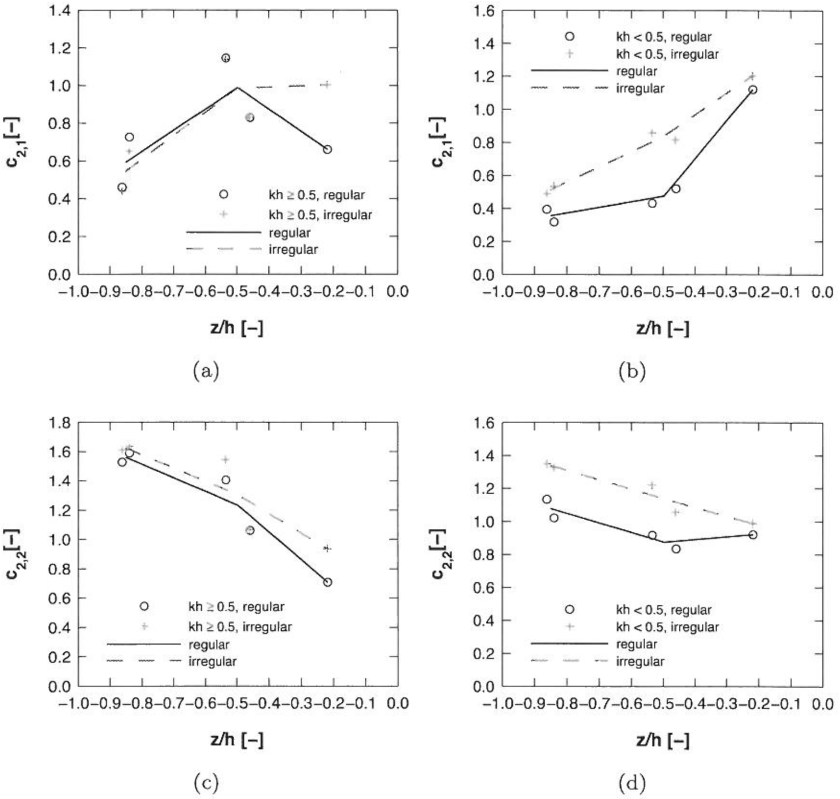

(a) (b) (c) (d)

Figure 4.7: Dimensionless regression parameters $c_{2,1}(z)$ and $c_{2,2}(z)$ in eq. (4.5), values obtained from regression analysis and piecewise linear approximations for regular and irregular wave tests: (a) $c_{2,1}(z)$ for $kh \geq 0.5$, (b) $c_{2,1}(z)$ for $kh < 0.5$, (c) $c_{2,2}(z)$ for $kh \geq 0.5$ and (d) $c_{2,2}(z)$ for $kh < 0.5$.

Similar as in eq. (4.1), no parameters related to the breakwater geometry or the hydraulic resistance of the core material will be included explicitly in the model equation to established. Instead, the pressure gradient $I_{P,1}(z)$ in zone 1 will calibrated in a non-linear regression analyis containing H_{inc}/h as the independent variable, since this parameter dominantly governs the measured values of $I_{P,1}(z)$. The following model equation proves to yield the best fit:

$$I_{P,1}(z) = c_{2,1}(z)(H_{inc}/h)^{c_{2,2}(z)} \tag{4.5}$$

where $c_{2,1}(z)$ and $c_{2,2}(z)$ are dimensionless parameters resulting from a non-linear regression analysis performed on the pressure measurements, shown in Fig. 4.7. In order to employ eq. (4.5) in a calculation model, the variation of the parameters $c_{2,1}(z)$ and $c_{2,2}(z)$ is approximated by a piecewise linear function over the depth z/h, as shown in Fig. 4.7. Characteristic points which determine this function are given in Table 4.4.

Table 4.4: Characteristic model values of $c_{2,i}(z)$ [-] in eq. (4.5)

	Regular waves				**Irregular waves**			
	$kh \geq 0.5$		$kh < 0.5$		$kh \geq 0.5$		$kh < 0.5$	
z/h [−]	$c_{2,1}$	$c_{2,2}$	$c_{2,1}$	$c_{2,2}$	$c_{2,1}$	$c_{2,2}$	$c_{2,1}$	$c_{2,2}$
-0.85	0.59	1.56	0.36	1.08	0.55	1.62	0.51	1.34
-0.50	0.99	1.23	0.48	0.88	0.98	1.31	0.84	1.14
-0.22	0.66	0.71	1.12	0.92	1.00	0.94	1.20	0.99

Fig. 4.8(a,b) show the comparison between experimental values of $I_{P,1}(z)$ and values predicted by eq. (4.5), for regular and irregular waves, respectively. Parameters $c_{2,i}(z)$ according to Table 4.4 are employed to establish Fig. 4.8. The use of the approximated values $c_{2,i}(z)$ has a minor impact on the prediction quality. Fig. 4.8 shows that pressure gradients $I_{P,1}(z)$ are predicted fairly accurately by eq. (4.1): a relative standard deviation of 13.5% is obtained in case of irregular and 17.7% in case of regular waves tests.

4.2.4 Pressure attenuation in zone 2

The observed attenuation of pore pressure height in zone 2 ($x > x_s$) results to be in good correspondence with the theoretical attenuation, given in eq.(2.26) and rewritten as:

$$P(x,z) = P_s(z)exp[-\delta'(z)k(x - x_s(z))] \tag{4.6}$$

According to eq.(4.6), the pore pressure height at position x ($x > x_s$) along a horizontal section of the breakwater core at depth z, is computed using the initial pressure height $P_s(z)$ (eq. (4.3)) and the damping coefficient $\delta'(z)$. Note the difference in notation between the damping coefficient δ' in eq. (4.6) and δ in eq. (2.26). Eq. (2.26) has been converted into eq. (4.6) in order to avoid any assumption regarding the internal wave number k', since it is impossible to determine k' directly with sufficient accuracy. Theoretically, k and k' are linked by a so-called 'seepage length

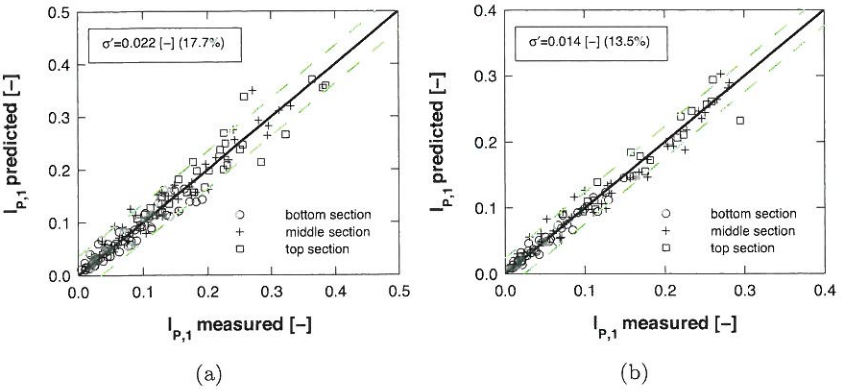

Figure 4.8: Measured (GWK) vs. predicted values of pressure height gradient $I_{P,1}(z)$ in zone 1, for (a) regular and (b) irregular waves. Predicted values by eq. (4.5) with $c_{2,i}$ according to Table 4.4; 90 % confidence interval in green dashed.

factor': $k'/k = \sqrt{D_s}$. This factor D_s accounts for seepage length as a result of the deviation of the flow path caused by the grains. In the approach of Burcharth et al. (1999), D_s is approximated as be 1.4, an empirical value for quarry rock material given by Le Méhauté (1957).

Experimental values of $\delta'(z)$ are obtained by a two-parameter non-linear regression analysis according to eq. (4.6), applied to the recorded pressure heights along a horizontal section. The analysis is performed at three different positions below SWL, indicated in Fig. 3.2. The following observations regarding the obtained values of $\delta'(z)$ apply:

- $\delta'(z)$ increases with decreasing vertical distance between the considered horizontal section and SWL;
- $\delta'(z)$ increases with increasing wave length, for a constant wave height;
- $\delta'(z)$ increases with increasing incident wave height for a constant wave period.

The first two observations are in agreement with what has been reported previously by various authors (see section 2.2.2). However, some ambiguity exists about the influence of H_{inc} on the damping rate. In particular, Burcharth et al. (1999) mention that the damping coefficient δ decreases with increasing wave height, which becomes visible in eq. (2.28) employed in the practical calculation model. In the present analysis, the effect of the

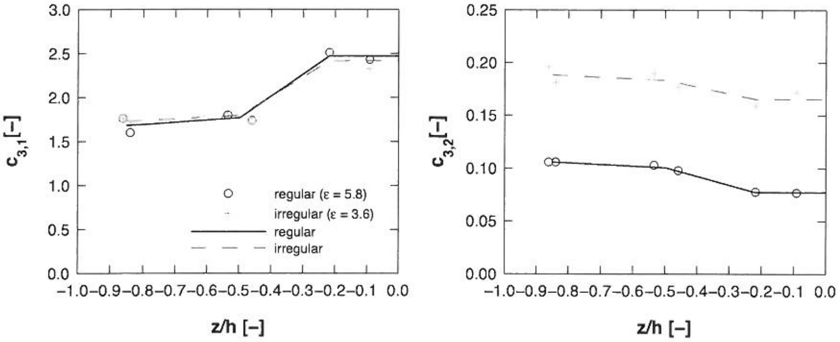

(a) (b)

Figure 4.9: Dimensionless regression parameters (a) $c_{3,1}(z)$ and (b) $c_{3,2}(z)$ in eq. (4.7), values obtained from regression analysis and piecewise linear approximations for regular and irregular wave tests.

incident wave height on $\delta'(z)$ is unmistakably clear, but however much less pronounced than the effect of the wave length.

Theoretically, the damping rate will be governed by both the porous flow characteristics of the specific core material (i.e. the porous flow coefficients a, b and c in eq. (2.13)) and the incident wave conditions that partially impose the filter velocities. In this empirical approach, it is aimed to establish a prediction formula for δ' that reflects the effect of the changing wave conditions (controlled by kh and H_{inc}/h) on the damping rate, but without explicitly incorporating the porous flow characteristics in the formula. Based on the previous findings from the experiments, eq. (4.7) is proposed to predict the damping rate:

$$\delta'(z) = c_{3,1}(z)(kh)^{-\epsilon c_{3,2}(z)}(H_{inc}/h)^{c_{3,2}(z)} \tag{4.7}$$

where $c_{3,1}(z)$ and $c_{3,2}(z)$ are dimensionless parameters resulting from a non-linear regression analysis performed on the pressure measurements. Analyzing the individual impact of the wave parameters on $\delta'(z)$ (the power of kh and H_{inc}/h in eq. (4.7)), it is noticed that the relative difference of the impact is approximately constant over the entire depth. Hence a fixed parameter ϵ is introduced in eq. (4.7), taken as the average value of the three horizontal sections. A value of 5.8 was obtained for ϵ in case of regular waves, compared to a value of 3.6 for irregular waves. The parameters $c_{3,1}(z)$ and $c_{3,2}(z)$, shown in Fig. 4.9, are clearly dependent on the depth z of the considered horizontal section, in agreement with the first observation from the tests, listed above. Given the considerations mentioned above, these parameters are partially determined by the porous flow characteristics. As observed in Fig. 4.9, values of $c_{3,1}(\mathrm{z})$ from regular and irregular wave tests are nearly identical over the entire depth. Values of $c_{3,2}(z)$ for irregular waves nearly double the values for regular waves. Equal values of H_{inc}/h thus lead to larger values of $\delta'(z)$ in case of regular waves, suggesting that the impact of the wave height on the damping coefficient is more pronounced for regular waves.

In order to employ eq. (4.7) in a calculation model, the variation of $c_{3,1}(z)$ and $c_{3,2}(z)$ with z/h is approximated by a piecewise linear function, shown in Fig. 4.9. Characteristic points which determine this approximation function are given in Table 4.5.

Table 4.5: Characteristic model values of $c_{3,i}(z)$ [-] in eq. (4.7)

	Regular waves		**Irregular waves**	
z/h [$-$]	$c_{3,1}$	$c_{3,2}$	$c_{3,1}$	$c_{3,2}$
-0.85	1.68	0.11	1.73	0.19
-0.50	1.77	0.10	1.79	0.18
-0.22	2.47	0.08	2.42	0.17
0.00	2.47	0.08	2.42	0.17

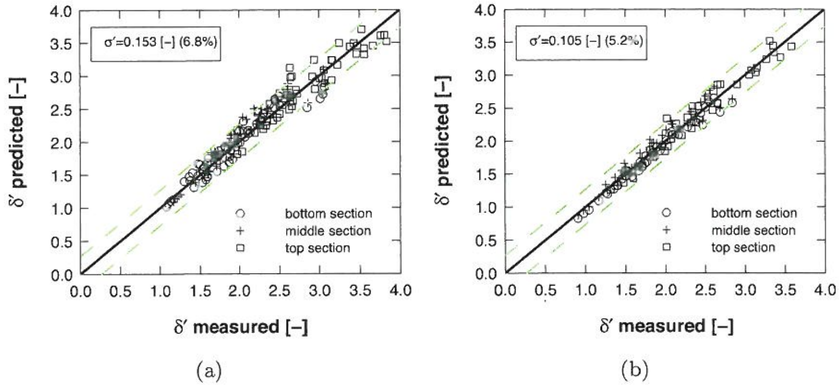

(a) (b)

Figure 4.10: Measured vs. predicted values of damping coefficient $\delta'(z)$ in zone 2, for (a) regular and (b) irregular waves. Predicted values by eq. (4.7), with $c_{3,i}(z)$ according to Table 4.5; 90 % confidence interval in green dashed.

Fig. 4.10(a,b) show the comparison between the damping coefficients obtained at the three different sections in the breakwater core, and values predicted by eq. (4.7), for regular and irregular waves, respectively. The parameters $c_{3,1}(z)$ and $c_{3,2}(z)$ according to Table 4.5 are employed to establish Fig. 4.10. The use of the approximated values $c_{3,i}(z)$ has a minor impact on the prediction quality. The results in Fig. 4.4 show that eq. (4.1) is able to predict the reference pressures with good accuracy: a relative standard deviation of 5.2% is obtained in case of irregular waves, a slightly higher value of 6.8% is obtained in case of regular waves tests.

4.3 Application to UG model data

In this section, the validity of the model equations derived in section 4.2 is verified with experimental results from similar tests on the small-scale physical model presented in Chapter 3, hereafter referred to as the UG model.

4.3.1 Reference pressures

Observations from tests with the 3 different types of armour layers do not show any significant differences regarding the reference pressures. Consequently, all results from UG tests with different armour layers were treated jointly in the analysis. A nonlinear regression analysis according to equation (4.1) has been applied to the measurements from pressure gauges P5 to P8 on the interface between core and filter layer (see Fig. 3.3 and Table 4.1). Fig. 4.11 shows the comparison between regression parameters $c_{1,i}(z)$ $(i = 1..3)$ determined from GWK and UG model tests, together with GWK piecewise linear approximations:

- values of $c_{1,1}(z)$ obtained from the UG model are slightly larger than GWK piecewise linear approximations for $z/h \leq -0.5$. The opposite is true for $z/h > -0.5$;
- values of $c_{1,2}(z)$ are very similar for $z/h \leq -0.5$, however they do not show an increasing trend towards SWL, as observed in GWK tests;
- values of $c_{1,3}(z)$ are very similar over almost the entire core slope, except for the pressure gauge $P8$ close to SWL. In case of regular waves, the underprediction of $c_{1,2}(z)$ is compensated by the overprediction of $c_{1,3}(z)$, indicating a certain interchangeability between both model parameters. In case of irregular waves, both $c_{1,2}(z)$ and $c_{1,3}(z)$ are overestimated by the GWK piecewise linear approximations.

Notwithstanding the use of eq. (4.1) with GWK piecewise linear approximations to $c_{1,i}(z)$ results in an increased prediction error, it still yields an acceptable approximation of the reference pressures. A relative standard deviation of 9.1% (compared to 5.4% using the exact regression parameters) and 8.5% (compared to 2.7%) is obtained for regular and irregular waves, respectively. The largest deviations between predicted and measured reference pressures are found for gauge P8 under irregular wave tests, due to the the aforementioned overprediction of both $c_{1,2}(z)$ and $c_{1,3}(z)$ by the piecewise linear approximations.

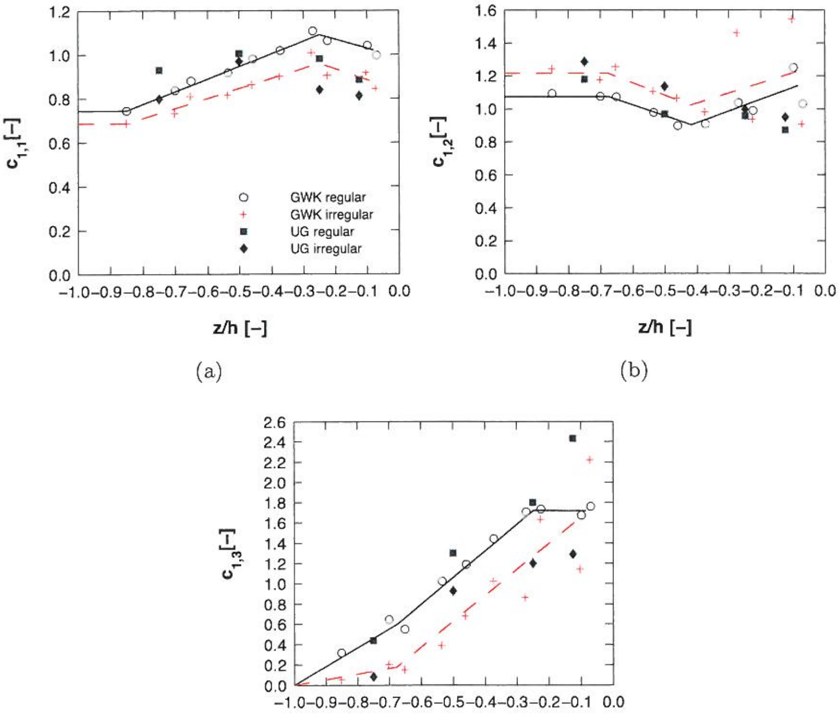

(a) (b)

(c)

Figure 4.11: Comparison between dimensionless regression parameters (a) $c_{1,1}(z)$, (b) $c_{1,2}(z)$ and (c) $c_{1,3}(z)$ in eq. (4.1), derived from UG and GWK model tests. Piecewise linear approximations to $c_{1,i}(z)$ for regular (black solid) and irregular (red dashed) waves according to Table 4.2.

Despite the different properties of the armour and filter layer employed in both model tests, only limited differences in model parameters $c_{1,i}(z)$ are observed in Fig. 4.11. This fact, together with the observation of virtually no differences between the three different armour types in the UG model tests, points to the probably limited effect of the hydraulic resistance and layer thicknesses on the reference pressures. It appears that eq. (4.1) - using the GWK piecewise linear approximation for $c_{1,i}(z)$ - is capable of predicting the reference pressures accurately in both GWK and UG model tests. This suggests that the prediction formula can be applied to other cases as well, where the breakwater geometry and material properties do not differ extremely. An important remark in this matter however concerns the influence of the breakwater slope angle. This parameter has been not varied in both model tests, so no conclusions can be drawn regarding its impact on the reference pressures.

4.3.2 Pressure gradient in zone 1

Values of $\kappa(z)$ are derived from the experiments in an identical way as for GWK tests. Similarly, the obtained value of $\kappa(z)$ shows a slight variation according to the wave length. In order to obtain a practical model approximation however, no distinction was made between tests with different wave length. All tests moreover fulfil the condition $kh \geq 0.5$, hence the same subdivision according to kh as in GWK tests is respected. The model approximations are taken as the average of each position z/h. Fig. 4.12 shows the $\kappa(z)$ values derived from UG tests, together with the piecewise linear approximations of both UG and GWK tests. It is observed that model $\kappa(z)$ values are slightly higher than in case of GWK tests, indicating a somewhat smaller effect of the breakwater slope on the pressure attenuation, however still very comparable.

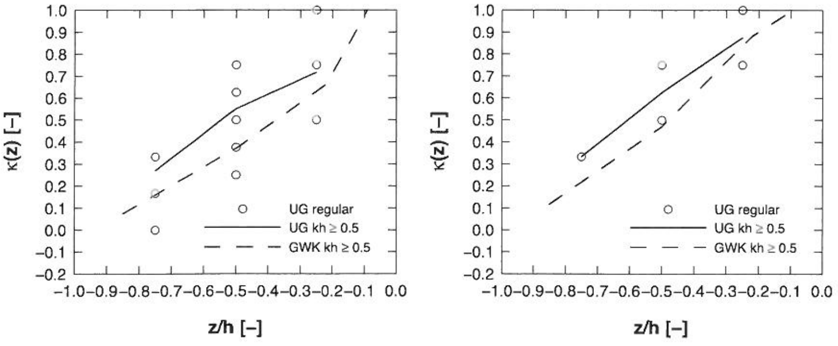

(a) (b)

Figure 4.12: Experimental $\kappa(z)$ values derived from UG tests and model approximations, for tests with (a) regular and (b) irregular waves.

Average pressure gradients $I_{P,1}(z)$ are derived from UG data, where the extent of zone 1 is determined using the GWK piecewise linear approximation for $\kappa(z)$. A regression analysis according to equation (4.5) yields the dimensionless regression parameters $c_{2,1}(z)$ and $c_{2,2}(z)$, shown in Fig. 4.13 together with data values and the piecewise linear approximation from GWK tests (for $kh \geq 0.5$):

- obtained values of $c_{2,1}(z)$ from the UG model show a much more limited variation with z compared to GWK values, and are generally smaller. Since $c_{2,1}(z)$ is the upper limit for $I_{P,1}(z)$ ($H_{inc}/h < 1$), this implies that lower pressure gradients $I_{P,1}(z)$ are measured in UG tests for larger values of relative incident wave height, compared to GWK tests;
- values of $c_{2,2}(z)$ show a better correspondence between UG and GWK model tests; indicating a similar rate of change of $I_{P,1}(z)$ with varying relative incident wave height.

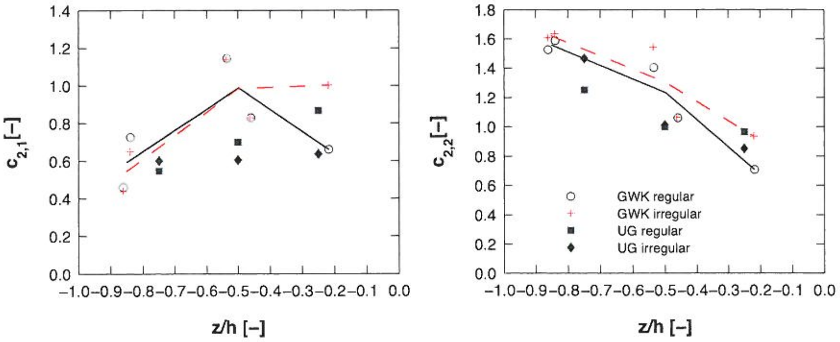

(a) (b)

Figure 4.13: Comparison between dimensionless regression parameters (a) $c_{2,1}(z)$ and (b) $c_{2,2}(z)$ in eq. (4.5), derived from UG and GWK model tests. Piecewise linear approximations to $c_{2,i}(z)$ for regular (black solid) and irregular (red dashed) waves according to Table 4.4 ($kh \geq 0.5$).

Applying eq. (4.5) with the GWK piecewise linear approximation for $c_{2,i}(z)$ increases the prediction error considerably, but still yields an acceptable approximation to $I_{P,1}(z)$. In case of regular waves, a relative standard deviation of 24.6% is obtained with the GWK piecewise linear approximations of $c_{2,i}(z)$, versus 18.9% using the exact regression parameters derived from UG tests. In case of irregular waves, the relative standard deviation attains 30.7% versus 18.1% using the exact regression parameters. The largest deviations (approx. 75% of the total error) between predicted and measured I_1-values are found for the top section (z/h=-0.25) with irregular wave tests, due to the overprediction of $c_{2,1}(z)$ by the GWK piecewise linear approximation.

It is likely to attribute the differences in $c_{2,i}(z)$ between both model tests to the difference in the hydraulic resistance of both core materials. Indeed, the reference pressures between both models are very comparable, and the pressure gradients $I_{P,1}(z)$ were found to be dominantly influenced by the incident wave height, imposing the local flow velocities. Notwithstanding the limited differences between $c_{2,i}(z)$, care should be taken when applying the model equation with the approximation function for $c_{2,i}(z)$ to a case where the hydraulic resistance of the core material differs considerably.

4.3.3 Pressure attenuation in zone 2

A comparison between UG and GWK tests of $\delta'(z)$ values obtained at the bottom section of pressure gauges is shown in Fig. 4.14. The values from UG tests are obtained with the GWK piecewise linear approximation to $\kappa(z)$. In case of UG tests with regular waves, no clear trend of decreasing $\delta'(z)$ with increasing kh is noticed in Fig. 4.14(a). The irregular wave tests in Fig. 4.14(b) on the other hand show a similar trend as in GWK tests. It is noticed that damping coefficients obtained in UG tests are clearly smaller than in GWK tests.

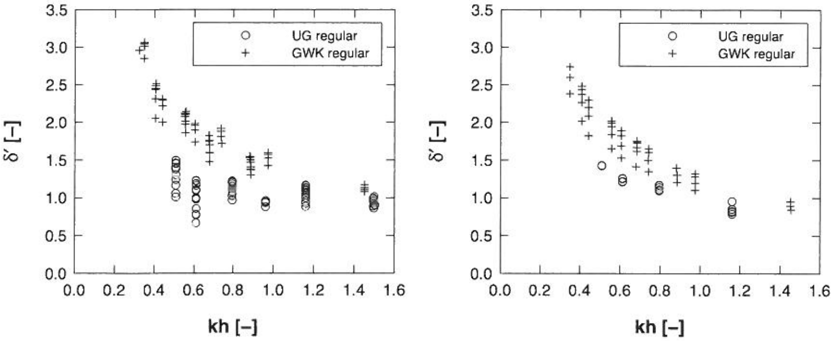

(a) (b)

Figure 4.14: Evolution of δ' (at bottom section) in function of kh, for (a) regular waves and (b) irregular waves.

In case of irregular waves, a value for ϵ equal to 3.7 is derived from the regression analysis (averaged over the three horizontal sections), compared to 3.6 in GWK tests. The regression parameters $c_{3,1}(z)$ and $c_{3,2}(z)$ show a similar trend over the depth z/h in Fig. 4.15, but are however significantly smaller than the GWK piecewise linear approximations. Using eq. (4.7) together with the exact regression parameters derived from UG tests delivers an accurate prediction of measured $\delta'(z)$: a relative standard deviation of 3.8 % is obtained. Using the GWK piecewise linear approximation to $c_{3,i}(z)$ clearly overpredicts the damping coefficient; the relative standard deviation rises to 37.1 %. In case of regular waves, a value of ϵ equal 1.6 is obtained, significantly smaller compared to the value of 5.8 obtained in GWK tests. The values of $c_{3,1}(z)$ are very comparable to the GWK values, but the discrepancy in $c_{3,2}(z)$ between UG and GWK tests is quite large, as seen in Fig. 4.15. Values of $c_{3,2}(z)$, together with a smaller ϵ of 1.7, reflect that the damping coefficient is not increasing as much with increasing wave length, as in GWK tests.

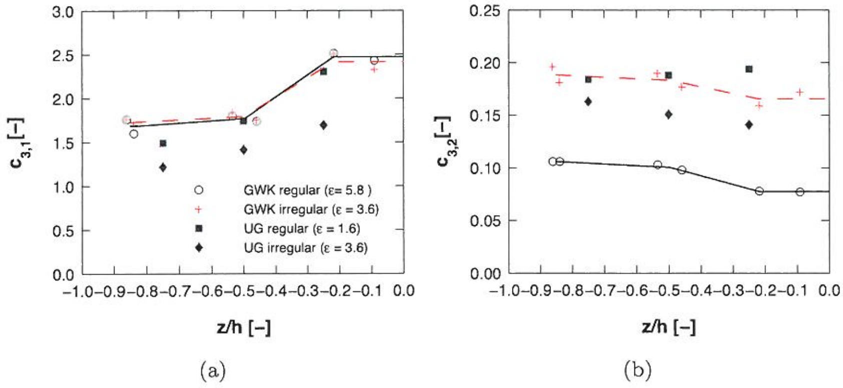

(a) (b)

Figure 4.15: Comparison between dimensionless regression parameters (a) $c_{3,1}(z)$ and (b) $c_{3,2}(z)$ in eq. (4.7), derived from UG and GWK model tests. Piecewise linear approximations to $c_{3,i}(z)$ for regular (black solid) and irregular (red dashed) waves according to Table 4.5.

The observed difference in $c_{3,i}(z)$ between UG and GWK tests probably points to the difference in flow resistance in both physical models. The flow resistance exerted by the core is smaller in the UG tests[3], the same observation was made for the pressure gradient $I_{P,1}(z)$ in zone 1.

It is noticed that the parameters ϵ, $c_{3,1}(z)$ and $c_{3,2}(z)$ in eq. (4.7) play a similar part as the porous flow coefficients a, b and c in eq. (2.13), by linking

---

[3] Note that a distorted scaling has been applied for the core fraction, according to the procedure by Burcharth et al. (1999).

the flow resistance properties of the specific core material to the governing flow conditions controlled by the relative water depth and incident wave height.

4.4 Comparison with the existing calculation method

The only practical calculation method at present (Burcharth et al., 1999) equally uses the hypothesis of an exponential attenuation of pore pressure height according to eq. (2.26). In this method, the reference pressures $P_{0,m0}/\rho g H_{m0}$ at the interface core-filter layer are considered to be independent of the position z/h below SWL, and moreover independent of the governing wave conditions. For practical use, an approximate value of 0.5 is proposed for the dimensionless reference pressure, according to eq. (2.27). The extensive analysis of the results from the large-scale GWK breakwater model in section 4.2.2 shows that this approximation is too coarse under various wave conditions. In cases of large wave run-up, the reference pressures attain values larger than 1, up to almost 2. Moreover, the spatial variation of the reference pressures along the interface is not negligible, as shown by the regression parameters $c_{1,i}(z)$ in Fig. 4.3.

At present, eq.(2.28) is the only empirical formula available to predict the damping rate δ in the direction of wave propagation starting from the interface core-filter layer. According to eq.(2.28), the damping rate is inversely proportional to the wave height. This is in conflict with the weakly positive correlation with the incident wave height observed in the present analysis.

Figure 4.16 shows the measured pressure heights along the middle section ($z/h = -0.54$) in the core of the GWK model. Four different irregular wave tests are shown, together with the attenuation of pressure height computed by the existing method (eqs. (2.26, 2.27, 2.28), Burcharth et al. (1999)) and by the method established in this work. In the latter, parameters $c_{k,i}(z)$ in equations (4.1), (4.5) and (4.7) are calculated with the piecewise linear approximations specified in Table 4.2, Table 4.4 and Table 4.5. Zone 1 and 2 are defined using the piecewise linear approximations to $\kappa(z)$, given in Table 4.3. Eq.(2.28) is computed using the assumption of $k'/k \cong \sqrt{1.4}$. In Figure 4.16, the calculation method of Burcharth et al. (1999) is employed once using eq. (2.27) for the reference pressure height and once using the measured value of the pressure height P_0 at the interface between core and filter layer.

Apart from the steepest waves in Fig. 4.16(a), the existing calculation model clearly overpredicts the damping of pore pressure height. In all cases, using eq. (2.27) implies a significant underestimation of the measured values. Employing the new prediction formulae clearly results in a more accurate prediction of the pore pressure height.

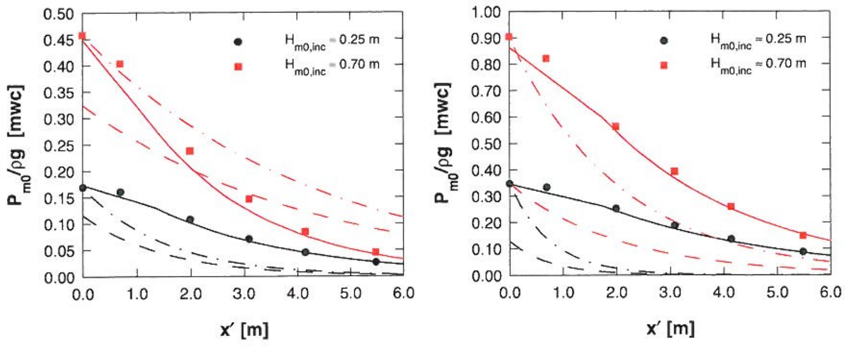

(a) (b)

Figure 4.16: Attenuation of pore pressure height in the GWK breakwater core (middle section, $z/h = -0.54$), for (a) short waves (kh=0.44) and (b) long waves (kh=0.98). Comparison between the new (solid line) and existing calculation model: eqs. (2.26, 2.27, 2.28) (dashed) and eq. (2.26, 2.28) with measured $P_{0,m0}$ (dash dot). Both cases contain 2 different incident wave heights: $H_{m0,inc} \approx 0.25$ and 0.70 m.

4.5 Application in the core scaling method

The core scaling method according to Burcharth et al. (1999) is based on the practical calculation model previously discussed, which is used to predict the locally varying pressure gradient within the core. Making use of eq. (2.3), pore velocities are derived to obtain the specific size of the core material, stating that Froude similarity should hold between the porous flow fields in prototype and in the model.

It is obvious that the improved calculation model derived in this work can be employed in this core scaling method, in order to improve the accuracy of predicted pressure gradients in varying wave conditions. A procedure for a core scaling method is given in Appendix C. The methodology is the same as in the method by Burcharth et al. (1999), but with slight a modification in the choice of averaging points to determine the characteristic pore velocity, based on the findings in this chapter.

4.6 Conclusions

Experimental pore pressure measurements in a large-scale rubble-mound breakwater model (Muttray and Oumeraci, 2005) have been re-examined in detail, leading to an improved practical calculation model for the attenuation of pore pressure height within the breakwater core. The new calculation model describes the evolution of the pore pressure height $P(x,z)$ along a horizontal section at position z with starting point at the interface between core and filter layer ($x = zcot\alpha$) indicated in Fig. 4.5. The reference pore pressure height at the interface is computed with eq. (4.1).

A new approach is suggested to deal with the deviation between the observed and theoretical exponential pressure height attenuation in the front zone of the breakwater core, dividing the considered section in two zones. $P(x,z)$ is computed with eq.(4.4) in zone 1 ($zcot\alpha \leq x \leq x_s$), with the total pressure gradient $I_{P,1}(z)$ given by eq.(4.5). In zone 2 ($x > x_s$), $P(x,z)$ is computed with eq.(4.6), using eq. (4.7) to predict the damping coefficient $\delta'(z)$. The point of separation $x_s(z)$ between zone 1 and 2 is computed using eq. (4.2), with values of $\kappa(z)$ specified in Table 4.3.

The empirical formulae in the calculation method were derived from a nonlinear regression analysis of the GWK data and provide the pore pressure height in the breakwater core for a sea state defined by the relative water depth and incident wave height, limited to non-overtopping and nonbreaking wave conditions in the present analysis. The regression parameters appearing in the formulae are considered to be dependent to a certain extent on the breakwater geometry and the specific material properties affecting the porous flow resistance.

The application of the calculation model to the small-scale pressure measurements provides insight into the general applicability of the regression parameters $c_{k,i}(z)$ in the prediction formulae. In the small scale model, the same wave conditions as in large-scale tests were used, and the breakwater model consists of the same front slope angle. In an effort to maintain Froude scale similarity of the porous flow, the core fraction of the small-scale model has been scaled with the procedure given by Burcharth et al. (1999).

The application to the small-scale data confirms that the prediction formulae are capable of accurately describing the measured evolution of pressure height under varying wave conditions, but also reveal differences in the model parameters $c_{k,i}(z)$ to a certain extent. The comparison between both models suggest that the parameters $c_{1,i}(z)$ in eq. (4.1) for the reference pressures are least susceptible to a change in layer thickness or material properties of the armour or filter. This can be explained since the mean value of the reference pressures along the core slope is determined to a large extent by the wave run-up on the breakwater slope. Since the latter is strongly influenced by the wave length (or kh) and by the wave height to a minor extent, the form of eq. (4.1) seems effective to represent the effect of wave run-up on the reference pressures.

When moving inside the breakwater core, the influence of the hydraulic resistance of the core material on the pressure height attenuation increases. This suggests that parameters $c_{2,i}(z)$ and $c_{3,i}(z)$, employed in the equations (4.5) and (4.7) respectively, will be dependent on the specific material properties to some extent. It is therefore suggested that further research is performed to investigate the susceptibility of the model parameters $c_{k,i}(z)$ to the specific breakwater properties, e.g. geometry, slope angle, layer thicknesses, core material properties.

A comparison between the existing calculation model (Burcharth et al., 1999) and the new model presented in this work shows a significant improvement in the prediction of pore pressure height, in a broad range of wave conditions. Accordingly, the improved calculation model contributes to making the core scaling method (Appendix C) more reliable in varying wave conditions, with due regard however for the limitations mentioned above.

5 Numerical framework

5.1 Introduction

An important characteristic of many coastal structures is that they are constructed of porous media, i.e. coarse granular material, rock or concrete units in variable sizes. An effective treatment of the flow in porous media is one of the main requirements in the numerical simulation of wave interaction with a RMB.

A second specific feature which characterizes the problem is the presence of a free surface. Different techniques for tracking and locating the free surface in NS solvers have been developed, as discussed in Chapter 2.

In the following chapter, the numerical framework is presented in which the present research has been carried out. The model equations and their numerical implementation are discussed, providing a background for the numerical study. In this discussion, the main features of the considered wave-structure interaction are emphasized: porous media flow and free surface modeling.

5.2 Motivation

From a scientific point of view, it is obviously preferred to have full access to the source code of the CFD model. There are a number of open source CFD codes available, e.g. OpenFOAM®[1] or TRUCHAS[2]. In general however, these models are not specifically developed for solving the fluid flow in wave-structure interaction, but encompass a wide variety of physical features such as electromagnetism, phase change, solid mechanics or heat transfer. It was not until very recently that an open source model specifically designed for coastal engineering applications has been released, called IHFOAM (Higuera et al., 2013). The model is based on OpenFOAM® and is still under

---

[1] www.openfoam.org

[2] telluride.lanl.gov

development. At present stage, it does not include porous media flow.

Even when disposing of a generic open source model, developing and validating a code requires a considerable amount of time and financial resources. In this respect, it was decided to employ a readily available, state-of-the-art commercial CFD model. There are a number of widely used commercial codes available, so the question rises which one is most suitable to address the research goals formulated in Chapter 1. The answer to that question is not straightforward, and probably a number of arguments can be used in favor of one or another specific model. After screening a number of available codes, the model FLOW-3D® was selected, developed by Flow Science Inc.[3]. This choice is mainly based on the following arguments:

- FLOW-3D is makes use of the VOF technique, developed by dr. C.W. Hirt and founder of Flow Science. The rigorous and efficient implementation of the VOF method is considered to be one of the main strengths of this particular model, providing an accurate and robust method for free surface tracking. In this respect, the numerical algorithm to evolve the shape and location of the free surface whilst maintaining its character as a discontinuity and the application of proper free surface boundary conditions are mentioned (Flow Science, 2012);
- the availability of customizable subroutines, providing some flexibility to the user to implement or adjust features to the model;
- the capability to model moving objects, which will be of importance to represent a piston wavemaker (cfr. infra);
- an efficient approach for grid generation and obstacle representation based on a cut-cell method, greatly reducing the amount of work on the users's part.

FLOW-3D is a multi-physics solver with options for a broad wide range of flow problems. The physical background of the model is presented hereafter, together with a description of the numerical implementation. The discussion is concentrated on the particular problem of wave interaction with a permeable structure.

5.3 Model equations

The following section presents the physical background of the numerical model. The basic equations are the fundamental equations for fluid dynamics, which reflect the conservation of mass and momentum. They are

---

[3] www.flow3d.com

presented here first in general form in a clear fluid region, i.e. in absence of obstacles of any kind. Next, the extension of the conservation equations with models for porous media flow and turbulence is presented. In addition to the conservation equations, the treatment of a free surface or fluid interface, in respectively single-fluid or two-fluid problems, forms one of the cornerstones of the model and deserves particular attention. Finally, a brief discussion is given on the initial and boundary conditions completing the specific problem setup.

5.3.1 Conservation equations

Mass cannot be created nor destroyed. The rate of accumulation of mass inside an infinitely small control volume has to be balanced by the net outflow of mass trough its boundaries:

$$\frac{\partial \rho}{\partial t} + \frac{\partial \rho u_i}{\partial x_i} = 0 \tag{5.1}$$

where ρ is the fluid density and $u_i (i = x, y, z)$ the Cartesian components of the velocity. Note the use of the Einstein summation convention. For an incompressible fluid eq. (5.1) reduces to

$$\frac{\partial u_i}{\partial x_i} = 0 \tag{5.2}$$

The conservation of momentum is based on Newton's second law, stating that the change in momentum in a control volume is due to the forces that act on that volume. The gravity force (acceleration g) is assumed to be the only acting body force. In differential form, the equation for an incompressible fluid reads:

$$\frac{\partial u_i}{\partial t} + u_j \frac{\partial u_i}{\partial x_j} = g\delta_{ij} - \frac{1}{\rho}\frac{\partial p}{\partial x_i} + \frac{1}{\rho}\frac{\partial \tau_{ij}}{\partial x_j} \tag{5.3}$$

where the terms on the left-hand-side of eq. (5.3) express the local and convective acceleration, equalized by the gravity force $g\delta_{ij}$ the pressure forces (p) and viscous accelerations (τ). The momentum equations (5.3), often referred to as the Navier-Stokes equations, describe the fluid motion with full consideration of nonlinear effects.

Eq. (5.3) is generally employed assuming that the shear stress τ_{ij} is proportional to the velocity gradient. A fluid with such properties is called Newtonian. When the fluid is incompressible, the shear stresses read:

$$\tau_{ij} = \mu \left(\frac{\partial u_i}{\partial x_j} + \frac{\partial u_j}{\partial x_i} \right) \tag{5.4}$$

with μ the dynamic viscosity.

5.3.2 Porous media flow model

In FLOW-3D, the porous medium flow resistance is modeled by inclusion of a drag term in the momentum equations, as discussed in section 2.3.2. Several drag models are available in the code to represent satured or unsatured porous media flow, including effects of capillary pressure. Coarse granular material is used in most coastal engineering applications, in which case the Forchheimer model is suitable (referred to as 'Reynolds number dependent drag' in FLOW-3D). Using this model, a drag term $F_d u_i$ is added to the right-hand-side of eq. (5.3), obtained by combination of eq. (2.3) and eq. (2.30):

$$F_d u_i = -g(anu_i + bn^2|u_i|u_i) \tag{5.5}$$

where $u_i = u_i^s$ are the velocity components solved in the momentum equation (5.3), representing the seepage velocity in the porous medium. $|u_i|$ is the norm of the (seepage) velocity vector and n the porosity. It is noticed that the inertial drag term in unsteady flow is neglected in eq. (5.5). The dimensional coefficients a and b were discussed in section 2.1.5. In FLOW-3D, the following formulation is used:

$$a = \alpha_F \frac{(1-n)^2}{n^3} \frac{\nu}{gD^2} \ , \ b = \beta_F \frac{(1-n)}{n^3} \frac{1}{gD} \tag{5.6}$$

where D is a characteristic grain size diameter (e.g. D_{50} or $D_{n,50}$) and α_F and β_F dimensionless shape coefficients.

It is noticed that the effect of macroscopic turbulence (see section 2.3.2) inside porous media is not considered in FLOW-3D. To the author's knowledge, no validation studies for coastal engineering applications have been reported that clearly identify the contribution of this term in the total flow loss inside porous media. It may be expected that macroscopic gradients of seepage velocity are intrinsically small, due to the averaging approach, and so will be the related turbulent flow losses. An exception may be found near the interfaces between clear fluid and porous medium or interfaces between porous media with different characteristics, where larger velocity gradients arise.

It is noticed that the presence of a porous medium does not only affect the equation for momentum conservation, but also the mass conservation equation and kinematic free-surface boundary condition. The specific numerical approach in FLOW-3D to satisfy these conditions will be treated in section 5.4.

5.3.3 Turbulence modeling

The most accurate approach for turbulence modeling, referred to as Direct Numerical Simulation (DNS), is to solve the Navier-Stokes equations with proper initial and boundary conditions, resolving the whole range of spatial and temporal scales of the turbulence, from the smallest dissipative scales up to the integral scale associated with the motions containing most of the kinetic energy. The computational cost of DNS is extremely high, even at low Reynolds numbers. Besides these constraints involving computational time and cost, it is even not desirable to apply DNS in cases where porous flow modeling is applied because of the volume-averaging approach.

When DNS is out of scope, turbulent effects are to be approximated in the model. Mainly two options are available: Large-Eddy Simulation (LES) and Reynolds-averaging of the Navier Stokes equations, which are both available in FLOW-3D. With LES, the basic idea is to directly compute all turbulent flow structures that can be resolved by the computational grid and approximate only those features that are too small to be resolved, using a subgrid scale model. Since a considerable amount of kinetic energy in the flow must be resolved, a high grid resolution is still needed. To allow the large flow structures to break up into smaller ones, the flow has to be simulated in three dimensions and time-accuracy has to be retained. Moreover, an energy-conserving discretization of the momentum convection is mostly needed in LES, in order not to dampen out resolved, turbulent fluctuations (Rauwoens, 2008). Because of these imperatives, and since the numerical simulations will be restricted to 2D in the following, LES is not explored further in this work.

The last approach for turbulence modeling treats the flow from a statistical point of view, restricting the description of turbulence to a subset of statistical properties, e.g. the mean value and (co-)variance of velocity components. The Reynolds decomposition technique leads to the so-called RANS equations, where an instantaneous flow variable q is separated into a mean (ensemble averaged) component $\overline{q}$ and a fluctuating component q'. In RANS, the breaking of large turbulent structures into smaller ones is not simulated, hence a 3D grid is not strictly necessary. In general, the requirements to the discretization are also less stringent, because of the relatively large importance of the turbulent model terms. The RANS equations for an incompressible fluid read:

$$\frac{\partial \overline{u}_i}{x_i} = 0 \tag{5.7a}$$

$$\frac{\partial \overline{u}_i}{\partial t} + \overline{u}_j \frac{\partial \overline{u}_i}{\partial x_j} = g\delta_{iz} - \frac{1}{\rho}\frac{\partial \overline{p}}{\partial x_i} + \frac{1}{\rho}\frac{\partial}{\partial x_j}\left[\mu\left(\frac{\partial \overline{u}_i}{\partial x_j} + \frac{\partial \overline{u}_j}{\partial x_i}\right) - \rho\overline{u_i' u_j'}\right] \tag{5.7b}$$

The shear stresses in eq. (5.7b) arise from momentum transfer at molecular level (viscous contribution) and from the fluctuating velocity field (turbulent contribution). The turbulent shear stresses $-\rho\overline{u_i' u_j'}$, often referred to as the Reynolds shear stresses, require additional modeling to close the RANS equation for solving. This has led to the creation of a number of turbulence models. In FLOW-3D, two types of two-equation turbulence transport models are incorporated: the standard k-ϵ and the ReNormalization Group (RNG) model. Both are highlighted briefly further on. It is of importance to mention that the application of the turbulence models is limited to the clear-fluid region, thus not within porous media.

The k-ϵ and RNG turbulence models, like many others, are based on the turbulent-viscosity hypothesis of Boussinesq (1877). This hypothesis, analogous to the stress-rate-of-strain relation of a Newtonian fluid, states that the Reynolds shear stresses are directly proportional to the mean rate of fluid deformation:

$$-\rho\overline{u_i'u_j'} = \mu_T\left(\frac{\partial\overline{u}_i}{\partial x_j}+\frac{\partial\overline{u}_j}{\partial x_i}\right)-\frac{2}{3}\rho k\delta_{ij} \tag{5.8}$$

where $\mu_T{=}\mu_T(x_i,t)$ is the dynamic eddy or turbulent viscosity which varies in space but is assumed to be isotropic however. k is the turbulent kinetic energy, defined as:

$$k = \frac{1}{2}\overline{u_i'u_i'} \tag{5.9}$$

Substitution of eq. (5.8) in eq. (5.7b) yields:

$$\frac{\partial\overline{u}_i}{\partial t}+\overline{u}_j\frac{\partial\overline{u}_i}{\partial x_j} = g\delta_{iz}-\frac{1}{\rho}\frac{\partial}{\partial x_i}\left(\overline{p}+\frac{2}{3}\rho k\right)+\frac{\partial}{\partial x_j}\left[\nu_{eff}\left(\frac{\partial\overline{u}_i}{\partial x_j}+\frac{\partial\overline{u}_j}{\partial x_i}\right)\right] \tag{5.10}$$

where

$$\nu_{eff}(x_i,t) = \nu+\nu_T(x_i,t) \tag{5.11}$$

is the effective kinematic viscosity, i.e. the sum of molecular (ν) and turbulent kinematic viscosity (ν_T). Equation (5.10) has the same appearance as the incompressible Navier-Stokes equation (5.3), with $\overline{u}_i$ and ν_{eff} in place of u_i and ν and with $\overline{p}+\frac{2}{3}\rho k$ as the modified pressure term.

Standard $k-\epsilon$ model

The standard k-ϵ model (Harlow and Nakayama, 1967; Launder and Spalding, 1974) consists of two transport equations, for the turbulent kinetic energy k and dissipation rate ϵ, respectively:

$$\frac{\partial k}{\partial t}+\overline{u_j}\frac{\partial k}{\partial x_j} = \nu_T\left(\frac{\partial\overline{u}_i}{\partial x_j}+\frac{\partial\overline{u}_j}{\partial x_i}\right)\frac{\partial\overline{u}_i}{\partial x_j}+\frac{\partial}{\partial x_j}\left[\left(\nu+\frac{\nu_T}{\sigma_k}\right)\frac{\partial k}{\partial x_j}\right]-\epsilon \tag{5.12a}$$

$$\frac{\partial\epsilon}{\partial t}+\overline{u}_j\frac{\partial\epsilon}{\partial x_j} = C_{\epsilon 1}\frac{\epsilon}{k}\nu_T\left(\frac{\partial\overline{u}_i}{\partial x_j}+\frac{\partial\overline{u}_j}{\partial x_i}\right)\frac{\partial\overline{u}_i}{\partial x_j}+\frac{\partial}{\partial x_j}\left[\left(\nu+\frac{\nu_T}{\sigma_\epsilon}\right)\frac{\partial\epsilon}{\partial x_j}\right]-C_{\epsilon 2}\frac{\epsilon^2}{k} \tag{5.12b}$$

where the terms are from left to right: local derivative, convective derivative, production, diffusion and dissipation. A dimensional analysis yields a definition of the turbulent viscosity, necessary to link the momentum equation (5.10) with the transport equations (5.12) :

$$\nu_T = C_\mu k^2/\epsilon \tag{5.13}$$

Standard values of the model constants in the $k-\epsilon$ turbulence model equations are:

$$C_\mu = 0.09, C_{\epsilon 1} = 1.44, C_{\epsilon 2} = 1.92, \sigma_k = 1.0, \sigma_\epsilon = 1.3 \tag{5.14}$$

RNG $k-\epsilon$ model

The RNG method, similar to the k-ϵ model, accounts for the effects of smaller scales of motion by applying a renormalization technique to the Navier-Stokes equations, see e.g. Yakhot et al. (1992). This method results in a modified form of the ϵ equation, attempting to account for different scales of motion through changes in the production term. This modification makes the RNG model more sensitive to flows having strong shear regions, due to the presence of the source term R:

$$\frac{\partial \epsilon}{\partial t} + \overline{u}_j \frac{\partial \epsilon}{\partial x_j} = C_{\epsilon 1} \frac{\epsilon}{k} \nu_T \left(\frac{\partial \overline{u}_i}{\partial x_j} + \frac{\partial \overline{u}_j}{\partial x_i} \right) \frac{\partial \overline{u}_i}{\partial x_j} + \frac{\partial}{\partial x_j} \left[\left(\nu + \frac{\nu_T}{\sigma_\epsilon} \right) \frac{\partial \epsilon}{\partial x_j} \right] - C_{\epsilon 2} \frac{\epsilon^2}{k} - R \tag{5.15a}$$

$$R = \frac{C_\mu \eta^3 (1 - \eta/\eta_0)}{1 + \beta \eta^3} \frac{\epsilon^2}{k} \tag{5.15b}$$

$$\eta = \sqrt{2 \overline{S}_{ij} \overline{S}_{ij}} \frac{k}{\epsilon} \tag{5.15c}$$

where $\overline{S}_{ij}$ is the mean-rate-of-strain tensor, defined for incompressible flow as:

$$\overline{S}_{ij} = \frac{1}{2} \left(\frac{\partial \overline{u}_i}{\partial x_j} + \frac{\partial \overline{u}_j}{\partial x_i} \right) \tag{5.16}$$

All constants (except β) appearing in eqs. (5.15) are derived explicitly in the RNG procedure. It is noticed that the source term according to eq. (5.15b) is an *ad hoc* model, not derived explicitly from RNG theory (Pope, 2000). Standard values of the model constants in the RNG model equations are:

$$\begin{gathered} C_\mu = 0.0845, C_{\epsilon 1} = 1.42, C_{\epsilon 2} = 1.68, \\ \sigma_k = 0.7194, \sigma_\epsilon = 0.7194, \eta_0 = 4.38, \beta = 0.012 \end{gathered} \tag{5.17}$$

Minimum dissipation rate and limits for turbulent scales

A particular numerical challenge of both the standard and RNG k-ϵ model is to limit the value of ϵ from below. In case eq. (5.12b) or (5.15a) yields values of ϵ close to zero, the turbulent kinetic energy should approach zero as well. If for numerical reasons this is not the case, this results in large, unphysical values of ν_T in eq. (5.13). Therefore, a minimal value for ϵ is defined as:

$$\epsilon_{min} = C_\mu \sqrt{\frac{3}{2}} \frac{k^{3/2}}{TLEN} \tag{5.18}$$

where TLEN is a maximum turbulent length scale. In FLOW-3D, this parameter can be defined by the user. Alternatively, a value of TLEN (varying in space and time) can be computed by the program. In the latter procedure, the lower bounds of the turbulent length (L_T) and time scales (T_T) are based on the Kolmogorov scales, whereas the upper bounds are based on the rapid distortion theory (Isfahani and Brethour, 2009):

$$L_{T,min} = 70\nu^{3/4}\epsilon^{-1/4} \tag{5.19a}$$

$$L_{T,max} = \frac{0.86}{C_\mu} \frac{\sqrt{k}}{S} \tag{5.19b}$$

$$T_{T,min} = 6\sqrt{\frac{\nu}{\epsilon}} \tag{5.19c}$$

$$T_{T,max} = \frac{0.35}{C_\mu} \frac{1}{S} \tag{5.19d}$$

where ν is the molecular kinematic viscosity and S the mean strain rate magnitude computed from the second invariant of the strain tensor S_{ij}.

The length scale L_T, subject to the limits given by eqs. (5.19a, 5.19b) is then replacing TLEN in eq. (5.18). The inverse of the time scale T_T, subject to the limits given by eqs. (5.19c, 5.19d), is used in the right-hand-side of eq. (5.12b) or (5.15a), where ϵ/k appears.

5.3.4 Free surface modeling

Different techniques for free surface modeling applied in NS models were discussed in section 2.3.1. FLOW-3D employs the VOF method (Hirt and Nichols, 1981), in which fluid configurations are defined in terms of a VOF function $F(x, y, z, t)$. The interpretation of the F function depends on how the fluid problem is being solved. Two options exist for the specific case of water in contact with air. In the first approach, referred to as *single-fluid modeling*, the air is not treated as a fluid but rather as a *void*, a region without fluid mass with a uniform reference pressure assigned to it. In the void, no fluid properties are transported, which means a considerable reduction of computational effort. In this case, F represents the volume fraction occupied by the fluid. Thus, fluid exists where $F = 1$, and void regions correspond to locations where $F = 0$. Averaged over a control volume, the value of F will be within the segment [0,1].

In *two-phase modeling*, when water and air are explicitly treated as two different phases, the F function represents the volume fraction of the incompressible phase (water), whereas the complementary region with volume fraction $1-F$ represents the compressible phase (air) that may have a constant density or a density computed from the fluid equation-of-state.

It is important to recognize that the F function is defined a discontinuous function in order to accurately track the free surface or two-fluid interface as a sharp interface. A prerequisite to the numerical implementation of the VOF method is to advance the fluid interface in time without destroying its character as a discontinuity. Moreover, it is necessary to impose proper boundary conditions at the free surface in single-fluid modeling.

5.3.5 Initial and boundary conditions

The model equations for momentum, turbulence and the free surface are partial differential equations, approximating the physics of the processes they model for every possible manifestation of the process of interest. In order to solve a specific problem, initial and boundary conditions are required.

Initial conditions specify the flow at the initial time step at every location in the computational domain. In case of waves propagating in a wave flume, the fluid at rest in the whole computational domain is a common and trivial initial condition, imposing a hydrostatic pressure distribution and a zero velocity-field. An initial reference pressure in the void or air region can be specified as well.

Boundary conditions represent the external factors acting in the specific flow problem through the boundaries of the domain. Hereafter, the boundary conditions for the momentum, turbulence and free-surface model equations are discussed.

Velocity

The velocity at the boundary will be affected by the type of boundary, which can be either solid or open. A solid boundary represents solid objects in the computational domain, such as the bottom or side wall of the flume, or any other object placed inside the domain. For a solid boundary, mainly two types of conditions apply:

1. no-slip condition : this condition states that on the solid boundary, there is no motion of the fluid relative to the solid

   $$u_i = v_{s,i} \tag{5.20}$$

   with v_s the velocity of the solid. This type of condition is valid for a viscous fluid ($\mu \neq 0$) and is used to model the flow in the boundary layer next to the rigid wall.

2. free-slip condition : this condition states that the tangential shear stress exerted by the solid is zero. In this case, the fluid velocity next to the solid boundary is only forced to match the normal velocity of the surface:

   $$u_i n_{s,i} = v_{s,i} n_{s,i} \tag{5.21}$$

   where $n_{s,i}$ are the components of the unit vector $\boldsymbol{n_s}$ normal to the solid surface, positive pointing outward.

An open boundary is a boundary through which fluid can enter or leave the domain. They are used to model the inflow of waves and/or currents or represent an outflow boundary at which waves or currents leave the domain without reflection. Multiple velocity boundaries are implemented in the code, going from a constant velocity (representing a current) to different types of linear and nonlinear wave boundary conditions. In case of a wave boundary, both the position of the free surface and velocity components at the boundary are specified according to the governing wave theory. More details on the wave boundary condition are given in section 6.2.3.

Pressure

Different pressure conditions exist, depending on the flow modeling type. In case of one-fluid flow, the pressure of the void region can be initialized to a value p_0 and stays constant during the computation.

In case of two-phase flow, where the water and air present in the domain are treated as two separate fluids, an initial pressure condition can be applied to the air region. This is generally the atmospheric pressure, acting as a reference to any other pressure in the flow. This condition is usually applied to the upper closure of the computational domain.

A pressure boundary condition can also be applied at the mesh boundary. In the specific case of a numerical wave flume however, this kind of boundary is not employed.

Free surfaces and fluid interfaces

At the free surface or fluid interface, the F function satisfies a kinematic boundary condition. Assuming the continuity of velocity, the free surface is ensured to be a material surface that always consists of the same particles[4]. In the absence of mass sources, the kinematic condition reads:

$$\frac{\partial F}{\partial t} + \frac{\partial}{\partial x_i}\left(F u_i\right) = 0 \tag{5.22}$$

In two-phase flow, a diffusion term is added to the right-hand side of eq. (5.22) to account for the turbulent mixing of both phases:

$$\frac{\partial F}{\partial t} + \frac{\partial}{\partial x_i}\left(F u_i\right) = \frac{\partial}{\partial x_i}\left(\frac{\nu_T}{Sc}\frac{\partial F}{\partial x_i}\right) \tag{5.23}$$

where Sc is the turbulent Schmidt number, a dimensionless number used to characterize fluid flows in which there are simultaneous momentum and mass diffusion-convection processes. It physically represents the relative thickness of the hydrodynamic layer and the mass-transfer boundary layer. The diffusion term with a simple gradient transport according to eq. (5.23) is only appropriate for homogeneous flows where the size of the energy-containing eddies is smaller than the distance over which the gradient varies appreciably (Shirani et al., 2006). For flows near the interface with inhomogeneous turbulence, a more appropriate model would include both gradient and convective transport terms, see e.g. Lumley (1975).

In case of single-fluid flow, the normal and tangential stress need to be specified as dynamic boundary conditions at the free surface, guaranteeing the continuity of stress components. The normal stress arises from the prescribed void pressure p_0 and the equivalent surface tension pressure. Denoting $\boldsymbol{n}$ as the unit normal on the free surface and n_i as the projection of $\boldsymbol{n}$ on the coordinate directions x_i, the continuity of the normal stress at the free surface boundary is written as:

$$p - \mu\left(\frac{\partial u_i}{\partial x_j} + \frac{\partial u_j}{\partial x_i}\right) n_i n_j = p_0 + \sigma \kappa_s \tag{5.24}$$

where σ is the fluid surface tension coefficient (in units of force per unit length) and κ_s the local free surface curvature.

For 3D problems, two unit tangential vectors t^k (k=1,2) are needed to define the local tangent plane on the free surface and t_i^k is defined as the projection of t^k on the coordinate directions x_i. The continuity of the tangential stress across the free surface is expressed as:

$$\mu\left(\frac{\partial u_i}{\partial x_j} + \frac{\partial u_j}{\partial x_i}\right) n_i t_j^k = t_j^k \frac{\partial \sigma}{\partial x_j} \tag{5.25}$$

---

[4] This only holds for a free surface that does not break up as it is the case under e.g. wave breaking.

In case of two-phase flow modeling, the contact region between water and air appears as an interface in the domain. The interface does not require the specification of a dynamic boundary condition since the solution at the interface comes out naturally of the equations of motion.

Turbulent model boundary conditions

Boundary conditions to the turbulence transport equations (5.12) and (5.15a) are to be specified either at a free surface, an in- and outflow or a solid boundary.

Advective fluxes of turbulent quantities into empty cells are set to zero since there is no fluid in those cells to either supply or receive the fluxed quantities. The same condition applies to an outflow condition. Mathematically, this takes the form of a null-flux condition:

$$\frac{\partial k}{\partial x_i} n_i = 0 \ , \ \frac{\partial \epsilon}{\partial x_i} n_i = 0 \tag{5.26}$$

At inflow boundaries, the turbulent kinetic energy k and dissipation rate ϵ must be specified:

$$k = k_0 \ , \ \epsilon = \epsilon_0 \tag{5.27}$$

At solid domain boundaries or internal obstacles where a no-slip condition is applied, contributions to the transport equation for k and ϵ need to be included, which arise from tangential wall shear stresses τ_w. Because the number of mesh points required to resolve all the details in the turbulent boundary layer would become prohibitively large in practical calculations, the flow is forced to match the *law of the wall* or *log-law*, which is an approximation for fully-developed, steady flow along a flat boundary:

$$u_{\|} = u^{\star} \left[\frac{1}{\kappa} ln \left(\frac{u^{\star} d}{\nu} \right) + 5 \right] \tag{5.28}$$

where $u_{\|}$ is the velocity component parallel to wall, κ is the von Karman constant and d the normal distance from the wall to the location where the velocity $u_{\|}$ is computed. The local *shear* or *friction* velocity $u^{\star}$ is defined from the wall shear stress τ_w as:

$$u^{\star} = \sqrt{\frac{\tau_w}{\rho}} \tag{5.29}$$

For eq. (5.28) to be valid, the point where $u_{\|}$ is calculated should fall within the turbulent log-law region. This is equivalent with the following restraint to the *viscous length scale* y^+ (Versteeg and Malalasekera, 1995):

$$30 < y^+ = \frac{u^{\star} d}{\nu} < 500 \tag{5.30}$$

For a high-Reynolds number, fully-developed flow, the boundary values of ϵ and k can be derived under the assumption of the logarithmic velocity profile (eq. (5.28)) and the turbulent viscosity hypothesis (eq. (5.8)). In the log-law region, it can be assumed that turbulent production and dissipation are in balance, and the boundary conditions for k and ϵ read (Pope, 2000):

$$k = \frac{(u^\star)^2}{\sqrt{C_\mu}} \; , \; \epsilon = \frac{(u^\star)^3}{\kappa d} \tag{5.31}$$

5.4 Implementation

In the previous section, the equations governing the physics of the wave-structure interaction problem have been described. Due to the nonlinear nature of the partial differential equations, analytical solutions are not readily available. For almost every particular problem of interest, predictions for flows have to be obtained by solving the equations with numerical methods.

In this numerical solution, the governing equations will be approximated by systems of algebraic equations. This requires a *discretization* of the equations, approximating continuous functions of time and space with a finite amount of information. The partial differential operators appearing in the governing equations express a variation in time and space. Due to their different character, they will be discretized in a different manner.

In the following, the numerical solution methods implemented in FLOW-3D are discussed. First, practical details are given on the mesh construction, the representation of obstacles and the allocation of flow variables. Next, the spatial discretization of the governing equations is treated, followed by a discussion on the time advancement of the discretized equations and the application of stability conditions to the time advancement.

Again, this discussion is organized with a focus on wave-structure interaction, paying special attention to the representation of porous media and free-surface tracking. Great part of the following is a synopsis based on the available information in the FLOW-3D manual (Flow Science, 2011). For details on the code not included here, reference is made to this manual.

5.4.1 Mesh generation and obstacle representation

Mesh generation involves the definition of a set of non-overlapping polygons (in 2D) or polyhedra (in 3D) which completely fill a well-defined domain in space. In FLOW-3D, the mesh is *structured*, meaning that the volume elements or *cells* are well ordered. The cells can be mapped on simple data structures in a structured mesh, using a simple scheme to label elements and identify neigboring cells. Both *Cartesian* and *cylindrical* meshes can be defined in FLOW-3D, and cell dimensions can be uniform or non-uniform.

One of the main benefits of a structured mesh is the ease of grid generation, with a minimal amount of information to be stored. One of the main drawbacks involves the representation of complex geometries. Unlike unstructured meshes, where general hexahedral cells can be used which conform with specified geometric shapes (a *body-fitted* mesh), the rectangular elements employed in a Cartesian mesh cannot accurately define complex geometric surfaces. The latter would have to be approximated by blocking out entire cells, leading to boundaries having discrete steps. These steps introduce flow losses and produce other undesirable effects.

In order to overcome this problem, obstacles are allowed to cut through the cells (*cut-cell method*). The latter method is referred to in FLOW-3D as the Fractional Area/Volume Obstacle Representation (FAVOR) method (Hirt and Sicilian, 1985). Curved obstacles, wall boundaries or other geometric features are embedded in the mesh by defining the fractional areas (A_i) and volumes ($V_{F_{i,j,k}}$) of the cells that are open to flow. The $V_{F_{i,j,k}}$ function is defined as the ratio of the open volume to the total volume in a mesh cell, and three A_i functions are defined as the ratio of the open area to the total area, at the three cell faces in the increasing cell-index direction.

The philosophy behind the cut-cell method is that the numerical algorithms are based a limited amount of information for each cell (each flow variable), so it would be inconsistent to use an excessive amount of information to define geometry (Flow Science, 2012). The cut-cell technique retains the simplicity of rectangular elements while representing complex geometric shapes at a level consistent with the use of averaged flow quantities within each volume element. Three area fractions and one volume fraction for each cell are stored, which is relatively little information compared with body-fitted grids.

Grids and geometry are free to be defined independently of one another, with very little time or effort on the part of a user. The work of computing the intersections between a grid and an obstacle description, is fully automized. This is a main advantage over unstructured grids, where the grid generation process is not completely automatic and may require considerable user interaction to produce grids with acceptable degrees of local resolution while at the same time having a minimum of element distortion.

An important point to recognize is that approximations of fluid-dynamic quantities are restricted to the open regions of cells in this cut-cell method. This restriction introduces the factors A_i and $V_{F_{i,j,k}}$ directly into the discrete approximations. For example, the flux of a quantity from one cell to another has the fractional area of the fluxing boundary that is open to flow as a multiplier. In general, the area and volume fractions are time independent, except when the moving obstacle model (GMO) is employed.

In spite of the aforementioned advantages of structured meshes in combination with a cut-cell method, some inconveniences exist as well. First of all, applying a local mesh refinement in a particular zone of interest is not possible in a structured mesh. This can be overcome by employing multiple rectangular meshes (*mesh blocks*) with different cell dimensions that are coupled at their boundaries (either adjacent to each other or nested in each other). However, in order to limit numerical approximation errors, restrictions exist to the maximum ratio of adjacent cell dimensions of different mesh blocks, and hence to the resolution increase achieved by adding one extra mesh block.

As a second drawback of the cut-cell method, it is important to recognize that it is limited by the resolution of the computational grid (Flow Science, 2011). This limitation is associated with the way area fractions are defined. For each cell face in a mesh, first it is determined which corners of the face are inside and which are outside of a defined geometry component:

- If all four corners of a cell face are inside the component, then the entire face is defined to be within the component.

- Similarly, if all corners lie outside, then the entire face is assumed to be outside the component.

- When some face corners are inside a component and some are outside, the area fraction generator computes the intersection of the component with the face edges. Area fractions are then computed from these intersection points assuming straight-line connections between intersection points within the face. The straight-line assumption introduces a small error in the fractional area when the component boundary is curved inside the cell. The approximation improves as the grid resolution is refined.

The implication of this face construction method is that any piece of a component extending across a cell face, but not including a corner of that face, is not recognized by the area fraction generator. For instance, a spherical subcomponent smaller than a mesh cell will not be recorded unless it covers at least one cell vertex. If the component surface has sharp edges then a multiple intersection is likely to occur, with the cell face intersecting more than one neighboring edge. In this case the corresponding cell edge is assumed to be either fully inside the object or fully outside it, leading to a representation error. The representation is improved as the mesh resolution is increased.

5.4.2 Arrangement of flow variables

With each cell there are associated local average values of all dependent variables. A *staggered* scheme is used to represent fluid velocities and pressures, illustrated in Figure 5.1: u-velocities and fractional areas A_x at the centers of cell-faces normal to the x-direction, v-velocities and fractional areas A_y at the centers of cell-faces normal to the y-direction, and w-velocities and fractional areas A_z at the centers of cell-faces normal to the z-direction. Pressures p, fluid fractions F, volume fractions $V_{F_{i,j,k}}$, area fractions A_i, densities ρ, turbulence quantities (k and ϵ), and viscosity μ are at cell centers.

The staggered arrangement is attractive because it maintains strong coupling between pressure and velocity and does not lead to spurious pressure oscillations, often referred to as the *checkerboard* problem. Furthermore, staggered arrangements do not require ad-hoc boundary conditions for the pressure, and can simultaneously conserve mass, momentum and kinetic energy for an inviscid flow (Harlow and Welch, 1965).

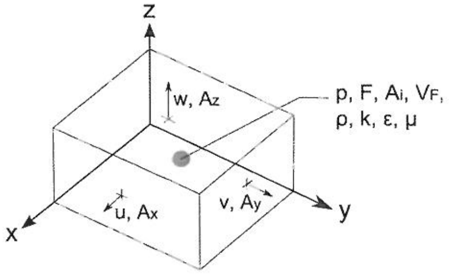

Figure 5.1: Location of variables in a mesh cell.

Before discussing the numerical solution method, some notes on the notation are given, adopted from the FLOW-3D user manual (Flow Science, 2011). The finite-difference, Cartesian mesh used for numerically solving the governing equations consists of rectangular cells of width δx_i, depth δy_j and height δz_k. The active mesh region has $IBAR$ cells in the x-direction labeled with the index i, $JBAR$ cells in the y-direction labeled with the index j, and $KBAR$ cells in the z-direction labeled with the index k. This region is surrounded by layers of fictitious or boundary cells used to set mesh boundary conditions. In total, there are $(IBAR + 2) * (JBAR + 2) * (KBAR + 2)$ cells in a complete mesh block.

A variable Q at the center of a cell (i, j, k) is denoted as $Q^n_{i,j,k}$, where the superscript n refers to the n-th time step value.

Velocities are located at the cell-faces, denoted as e.g. $u^n_{i,j,k}$ for the x-component located at the middle of the cell face between cells (i, j, k)

and $(i+1,j,k)$ at time level $n\delta t$. Fractional areas are denoted as $AFR_{i,j,k}$ (between cells (i,j,k) and $(i+1,j,k)$), $AFB_{i,j,k}$ (between cells (i,j,k) and $(i,j+1,k)$) and $AFT_{i,j,k}$ (between cells (i,j,k) and $(i,j,k+1)$).

When free surfaces or fluid interfaces are present, it is necessary to distinguish those cells that are empty, contain a surface, or are full of one fluid. By definition, a surface cell is a cell containing fluid #1 and having at least one adjacent cell (at $i \pm 1$, $j \pm 1$, $k \pm 1$), that is empty or full of fluid #2. A cell with an F value less than unity, but with no empty neighbor, is considered a full cell in single-fluid problems. A flag $NF_{i,j,k}$ is used to label the cells and also, in the case of surface cells, to indicate which neighboring cell lies in the direction of the inward normal to the surface. The flag values are indicated in Table 5.1. $NF_{i,j,k}$ is used to indicate the orientation of the surface between two fluids in an analogous manner.

Table 5.1: Definition of flag values $NF_{i,j,k}$

$NF_{i,j,k}$	**interpretation**
0	full or obstacle cell
1	surface ($i-1$ inward neighbor)
2	surface ($i+1$ inward neighbor)
3	surface ($j-1$ inward neighbor)
4	surface ($j+1$ inward neighbor)
5	surface ($k-1$ inward neighbor)
6	surface ($k+1$ inward neighbor)
7	cell undergoing cavitation
8	empty cell

5.4.3 Spatial discretization of momentum terms

The discretization of different terms in the momentum equation containing a spatial derivative is discussed in the following. Finite-difference approximations are formulated, based on Taylor series expansions of flow variables. The terms to be discretized are, from left to right in eq. (5.3): the momentum advection, pressure gradient and viscous shear stress.

In FLOW-3D, the viscous term $\partial\tau_{i,j}/\partial x_j$ refers to the internal viscous shear stress, i.e. away from solid boundaries. Wall shear stresses originating from solid boundaries with a no-slip condition are added separately in the momentum equation as force contributions. With the inclusion of fractional area functions A_i, vanishing at solid walls, it is then straightforward to apply the specific wall-boundary condition. The discretiation of the wall shear stress is also included in this discussion.

The discretization of the transport of turbulent quantities (advection-diffusion) is not treated here. More details on this topic can be found in the user manual (Flow Science, 2011).

Momentum advection : basic approach

In order to obtain finite-difference approximations to the advective fluxes, momentum control volumes are centered in each cell about the right face for x-momentum, the top face for y-momentum and the back face for z-momentum transport. For brevity's sake, the discussion is limited here to the transport of $u_{i,j,k}$-momentum in the x-direction. Figure 5.2 shows the control volume.

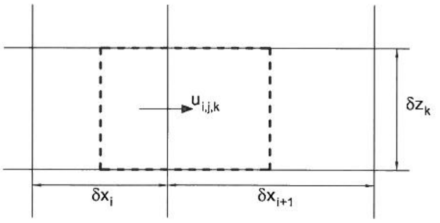

Figure 5.2: Control volume (dashed line) in (x,z)-plane used in finite-difference approximation for $u_{i,j,k}$-momentum (after Flow Science, 2011).

The advective fluxes can be written either conservatively ($\nabla \boldsymbol{uu}$) or nonconservatively ($\boldsymbol{u}\nabla\boldsymbol{u}$). The conservative approach is preferred, since it automatically ensures the conservation of momentum in the finite-difference approximations. In a non-uniform mesh however, the order of accuracy of the convective flux discretized in the conservative form is reduced by one, because the control volume is not centered about the position of the velocity component u_i at the cell face (Hirt and Nichols, 1981). In order to maintain at least first-order accuracy in a non-uniform mesh, the fluxes are approximated in a non-conservative form in FLOW-3D.

In the basic approach to the approximation of advection, a first-order upwind and centered-difference approximation are combined into a single expression with a parameter (ALPHA, α) that controls the relative amount of each. The approximation to the advection of u-momentum in x-direction, denoted as FUX, reads:

$$\begin{aligned}(FUX)_{i,j,k} \quad = \quad & \tfrac{1}{2VFC}\Big[(UAR - \alpha|UAR|)\left(\tfrac{\partial u}{\partial x}\right)_{i+1,j,k} \\ & +(UAL + \alpha|UAL|)\left(\tfrac{\partial u}{\partial x}\right)_{i,j,k}\Big]\end{aligned} \qquad (5.32a)$$

$$UAR = \frac{u_{i+1,j,k}AFR_{i+1,j,k} + u_{i,j,k}AFR_{i,j,k}}{2} \tag{5.32b}$$

$$UAL = \frac{u_{i,j,k}AFR_{i,j,k} + u_{i-1,j,k}AFR_{i-1,j,k}}{2} \tag{5.32c}$$

$$VFC = \frac{\delta x_i V_{F_{i,j,k}} + \delta x_{i+1} V_{F_{i+1,j,k}}}{\delta x_i + \delta x_{i+1}} \tag{5.32d}$$

where the velocity gradients in eq. (5.32a) are defined as:

$$\left(\frac{\partial u}{\partial x}\right)_{i,j,k} = \frac{u_{i,j,k} - u_{i-1,j,k}}{\delta x_i} \tag{5.33a}$$

$$\left(\frac{\partial u}{\partial x}\right)_{i+1,j,k} = \frac{u_{i+1,j,k} - u_{i,j,k}}{\delta x_{i+1}} \tag{5.33b}$$

UAR and UAL are the advecting velocities, averaged between the cell face velocity $u_{i,j,k}$ and the velocities at cells to the right and left of cell (i, j, k), respectively. Similar terms FUY and FUZ are developed for the advection of u in y- and z-direction respectively, as well as terms *FVX(Y,Z)* and *FWX(Y,Z)* for the advection of v- and w-momentum.

The basic idea underlying eqs. (5.32) is to weight the upstream quantity being fluxed more than the downstream value. The weighting factors are $(1+\alpha)$ and $(1-\alpha)$ for the upstream and downstream direction, respectively. The stream direction is determined by the sign of velocities UAR and UAL. When $\alpha = 0$, the approximation reduces to a centered-difference approximation that is spatially second-order accurate when the mesh is uniform. When $\alpha = 1$, the first-order, upwind discretization is retained.

The presence of an obstacle is directly taken into account by incorporation of the area functions in the advecting velocities and by the factor VFC, defined as the averaged volume fraction of both cells (i, j, k) and $(i + 1, j, k)$ surrounding $u_{i,j,k}$. It is noticed that the formulation of the advecting velocity in eq. (5.32a) is different from other formulations from predecessor codes (e.g. NASAVOF-2D, RIPPLE), where the advecting velocity is taken as the face velocity $u_{i,j,k}$. The formulation of eq. (5.32a) has the advantage however to reduce to a conservative approximation when the mesh is uniform.

Second-order approximation to momentum advection

The first-order upwind approximation yields stable results and has the property of *monotonicity*, which means that no new extrema are created and the value of a local minimum/maximum is non-decreasing/non-increasing in time. However, the upwind scheme also leads to high levels of numerical dissipation, causing sharp gradients of the convected quantity to be smoothed out in subsequent time levels. This may require a relatively high mesh resolution to obtain an accurate first-order solution. In such cases, it can be worthwhile to use higher-order schemes that are less prone to numerical dissipation. In FLOW-3D, two different second-order approximations methods are incorporated.

The essence of the first method is a double pass through the first-order advection subroutine in the code. In the first pass, the first-order downwind method is used with $\alpha = -1$. The resulting velocities are then stored in the arrays for the previous time velocities. The first-order calculations are then repeated, but this time with the upwind-differencing approximation ($\alpha = 1$). Finally, the results of the two calculations are averaged to give the desired second-order approximation to the new time-level velocities. The resulting approximation is second-order in time in general, and second-order in space in a uniform mesh. This algorithm is the least numerically diffusive of the three advection methods available in FLOW-3D. However, it does not possess the transportive property (monotonicity), which may lead to instabilities (*wiggles*) in the solution.

The other method is based on the second-order monotonicity-preserving upwind-difference method by Van Leer (1977). The higher-order discretization scheme consists of second-order polynomial approximations to the advected quantity, using a splitting method in which each coordinate direction is treated separately. The method is applicable to momentum advection as well as scalar quantities such as density, (turbulent) energy and fluid fraction. The method is briefly described here, limiting the discussion to the approximation of a variable Q advected in the x-direction. More details on the method are given by Bronisz and Hirt (1991).

To achieve a second-order accurate approximation in a non-uniform mesh, the approximation to the value fluxed through a cell-face, denoted as Q^*, needs to be third-order. The approach adopted by Van Leer (1977) is then to make polynomial approximations to the variable Q in function of h, the distance measured from the center of cell (i, j, k):

$$Q(h) = Q_i + Ah + \frac{1}{2}B\left(h^2 - 2hh_0 - \frac{1}{12}\delta x_i^2\right) + O(h^3) \tag{5.34}$$

where Q_i is the cell-centered value of Q, and A and B are defined in combination with h_0 such that:

$$\frac{\partial Q}{\partial h} = A + O(h^2) \ at \ h = h_0 \tag{5.35a}$$

$$\frac{\partial^2 Q}{\partial h^2} = B + O(h) \tag{5.35b}$$

h_0 is thus the location where A is a second-order approximation to the first derivative of Q.

The third-order accurate approximation to Q^* is obtained by integrating eq. (5.34) over the volume of the cell that is fluxed across the boundary in one time step δt, i.e. from $h = \delta x_i/2 - u_{i,j,k}\delta t$ to $h = \delta x_i/2$. If h_0 is carefully chosen, the approximation simplifies to:

$$Q^* = Q_i + \frac{A(1-C)\delta x_i}{2} \tag{5.36}$$

where Q_i is the cell-centered value and C is the CFL number $(u_{i,j,k}\delta t/\delta x_i)$. Eq. (5.36) holds exclusively for the location:

$$h_0 = \frac{(1-2C)\delta x_i}{6} \tag{5.37}$$

The coefficient A can easily be computed from two neighboring first derivatives by linear interpolation, provided these derivatives are second-order accurate. The latter can be achieved by computing the derivatives at the midpoints between Q_i locations; for example,

$$\left(\frac{\partial Q}{\partial x}\right)_{i+1/2} = 2\frac{Q_{i+1} - Q_i}{\delta x_{i+1} + \delta x_i} \tag{5.38}$$

is a second-order accurate first derivative of Q at the point between Q_i and Q_{i+1}. With this approach, the extension of the second-order, monotonicity-preserving method to non-uniform grids is straightforward.

To ensure monotonicity, it is necessary to restrict the value of the derivative A to twice the minimum magnitude of the centered Q-derivatives used in its computation (Van Leer, 1977):

$$A \leq 2min\left(\frac{dQ}{\delta x_i}, \frac{dQ}{\delta x_{i+1}}\right) \tag{5.39}$$

Furthermore, if Q_i is a local minimum or maximum value - that is, if the two centered derivatives appearing in the equation (5.39) are of opposite sign - then A is set to zero and the method reduces to a first-order upwind approximation.

Pressure gradient

Pressure is evaluated in the center of cell (i, j, k). The discretized form of the pressure gradient $-\frac{1}{\rho}\frac{\partial p}{\partial x_i}$ reads, e.g. in x-direction:

$$-\frac{1}{\rho}\frac{p_{i+1,j,k} - p_{i,j,k}}{\delta x_{i+1/2,j,k}} \tag{5.40}$$

In the notation of cell dimensions, the fractional subindex implies an averaging of neighboring cell dimensions, e.g. for the x-direction:

$$\delta x_{i+1/2,j,k} = \frac{\delta x_i + \delta x_{i+1}}{2} \quad , \; \delta x_{i-1/2,j,k} = \frac{\delta x_{i-1} + \delta x_i}{2} \tag{5.41}$$

Viscous shear stress

The term $\partial \tau_{ij}/\partial x_i$ in eq. (5.3), representing internal viscous shear (i.e. away from solid boundaries), is discretized using a standard second-order central-differencing scheme. For an incompressible fluid, the discretization in the x-direction reads:

$$\begin{aligned}(VISX)_{i,j,k} &= \tfrac{1}{\rho}\left(\frac{\partial \tau_{xx}}{\partial x} + \frac{\partial \tau_{yx}}{\partial y} + \frac{\partial \tau_{zx}}{\partial z}\right)_{i,j,k} \\ &= \tfrac{1}{\rho}\left(\frac{(\tau_{xx})_{i+1,j,k} - (\tau_{xx})_{i,j,k}}{\delta x_{i+1/2}} + \frac{(\tau_{yx})_{i,j,k} - (\tau_{yx})_{i,j-1,k}}{\delta y_j}\right. \\ &\quad \left. + \frac{(\tau_{zx})_{i,j,k} - (\tau_{zx})_{i,j,k-1}}{\delta z_k}\right)\end{aligned} \tag{5.42}$$

where the normal stress component is approximated in the cell center:

$$(\tau_{xx})_{i,j,k} = 2\mu_{i,j,k}\left(\frac{u_{i,j,k} - u_{i-1,j,k}}{\delta x_i}\right) \tag{5.43}$$

and tangential stress components at the vertices, e.g.:

$$(\tau_{yx})_{i,j,k} = \mu_{i,j,k}\left(\frac{u_{i,j+1,k} - u_{i,j,k}}{\delta y_{i+1/2}} + \frac{v_{i+1,j,k} - v_{i,j,k}}{\delta x_{i+1/2}}\right) \tag{5.44}$$

Similar terms $VISY$ and $VISZ$ are developed in y- and z-direction, respectively. In case a RANS turbulence model is used, the viscosity is evaluated as the effective viscosity according to eq. (5.11).

Due to the application of the porous media flow model, which includes the microscopic viscous shear, terms *VISX(Y,Z)* inside porous media are to be considered as macroscopic, related to gradients in seepage velocity.

Wall shear stress

The wall shear stresses are modeled assuming a zero relative tangential velocity on solid boundaries with the no slip-condition prescribed. It is important to remark that the approach in FLOW-3D, modeling the wall shear stresses as a separate term in the momentum equation, only holds for solid boundaries, since in that case the interface between the solid boundary and the fluid is resolved. Under the averaging approach (seepage velocity concept, see section 2.3.2), microscopic velocity gradients and resulting shear stresses at the interface between a porous medium and the clear fluid cannot be computed. Instead, all viscous and pressure forces are lumped into a flow loss term, described by the porous media flow model (Barkhudarov, 2012).

The wall shear acceleration for the w-velocity equation is derived here, denoted as WSZ. Terms $WSX(Y)$ are likewise obtained in the remaining directions. Wall shears influencing w can arise from any of the four wall areas located on x or y cell-faces surrounding $w_{i,j,k}$. For any one of these faces, if the fractional flow area A_i is less than unity, the remaining area fraction $(1 - A_i)$ is considered to be a wall on which a stress is generated.

If the flow is laminar, the acceleration due to tangential wall shear is proportional to the molecular viscosity μ and local velocity gradients, and can be approximated as:

$$\frac{1}{\rho}\frac{\partial}{\partial x}\left(\mu\frac{\partial w}{\partial x}\right) \tag{5.45}$$

For instance on an x-face to the right of $w_{i,j,k}$, the discretized approximation to eq. (5.45) reads:

$$(WSZ)_{i,j,k} = -\frac{2\mu_{i,j,k}}{\rho V_{F_{i,j,k}} AFT_{ijk}\delta x_i^2}\left[1 - \frac{(AFR_{i,j,k} + AFR_{i,j,k+1})}{2}\right](w_{i,j,k} - w_0) \tag{5.46}$$

where the velocity w_o is either zero or equal to the z-direction tangential velocity at a moving solid boundary. Because $w_{i,j,k}$ is located on the boundary between cells (i, j, k) and $(i, j, k + 1)$, an averaged value for the fraction area AFR is used. Similar stress components as in eq. (5.46) are evaluated at each of the four surrounding cell walls, and their sum is taken as the total stress WSZ.

For turbulent flows, a logarithmic velocity profile according to eq. (5.28) is assumed near the wall, which modifies the wall shear stress magnitude. Using the definition of the shear velocity eq. (5.29), the approximation to the wall shear acceleration reads:

$$(WSZ)_{i,j,k} = \frac{1}{V_{F_{i,j,k}}\delta x_i}\left[1 - \frac{(AFR_{i,j,k} + AFR_{i,j,k+1})}{2}\right](u_z^\star)^2 \tag{5.47}$$

Since the FAVOR method does not precisely locate wall locations within a cell, approximations must be introduced to find $u_{\|}$, $u^\star$ and d. For this purpose, the direction of the wall normal in the cell is first determined, and $u_{\|}$ is computed as the component of the cell-centered velocity parallel to the wall (relative to the wall velocity in the considered direction). The average distance to the wall (d_0) is estimated to be half of the cell width in the wall normal direction. That is, the triplet $(\delta x_i, \delta y_j, \delta z_k)$ is treated as a vector whose inner product with the wall normal is defined as the cell width in the normal direction. Finally, $u^\star$ is iteratively computed from eq. (5.28) in terms of $u_{\|}$ and d_0.

Both laminar and turbulent wall shear stresses at wall surfaces can be modified by defining a wall roughness, specified through the parameter ROUGH. The wall roughness length is incorporated into the usual shear stress calculations by adding to the molecular viscosity the product of ρ, ROUGH and u_i, the latter being the difference between the local fluid velocity and the wall velocity in the considered direction. For turbulent flow, the law-of-the-wall relation retains the same form as for a smooth wall, except the change in viscosity (i.e., from ν to $\nu+\text{ROUGH}*u_i$) automatically converts the logarithm dependence from a characteristic length scale defined by ν/u_i to the roughness length, when ROUGH is the larger of the two characteristic lengths.

5.4.4 Time advancement of conservation equations

The spatial discretization of the conservation equations results in a system of coupled ordinary differential equations with respect to time, in which pressure and velocity are the unknowns. In the following, the method to compute the equations one increment in time (δt) is discussed.

First, the discretized form of the conservation equations is given. In case of an incompressible fluid, the mass conservation eq. (5.2) reads:

$$\begin{aligned}\frac{AFR_{i,j,k}u^{n+1}_{i,j,k} - AFR_{i-1,j,k}u^{n+1}_{i-1,j,k}}{\delta x_i} &+ \frac{AFB_{i,j,k}v^{n+1}_{i,j,k} - AFB_{i,j-1,k}v^{n+1}_{i,j-1,k}}{\delta y_i} \\ &+ \frac{AFT_{i,j,k}w^{n+1}_{i,j,k} - AFT_{i,j,k-1}w^{n+1}_{i,j,k-1}}{\delta z_i} = 0\end{aligned} \tag{5.48}$$

Note that the presence of an obstacle, either solid or porous, is accounted for in eq. (5.48) by inclusion of the area fractions ($AFR_{i,j,k}$,$AFB_{i,j,k}$,$AFT_{i,j,k}$).

The momentum eqs. (5.3) for each direction read, with gravity (g) as the only acting body force:

$$\begin{aligned}\frac{u^{n+1}_{i,j,k} - u^{n}_{i,j,k}}{dt} &= -(FUX+FUY+FUZ)^{n}_{i,j,k} - \frac{1}{\rho}\frac{p^{n+1}_{i+1,j,k} - p^{n+1}_{i,j,k}}{\delta x_{i+1/2,j,k}} \\ &\quad + g_x + (VISX)^{n+1|n}_{i,j,k} - F_d u^{n+1}_{i,j,k} - (WSX)^{n+1}_{i,j,k}\end{aligned} \tag{5.49a}$$

$$\begin{aligned}\frac{v^{n+1}_{i,j,k} - v^{n}_{i,j,k}}{dt} &= -(FVX+FVY+FVZ)^{n}_{i,j,k} - \frac{1}{\rho}\frac{p^{n+1}_{i,j+1,k} - p^{n+1}_{i,j,k}}{\delta y_{i,j+1/2,k}} \\ &\quad + g_y + (VISY)^{n+1|n}_{i,j,k} - F_d v^{n+1}_{i,j,k} - (WSY)^{n+1}_{i,j,k}\end{aligned} \tag{5.49b}$$

$$\begin{aligned}\frac{w^{n+1}_{i,j,k} - w^{n}_{i,j,k}}{dt} &= -(FWX+FWY+FWZ)^{n}_{i,j,k} - \frac{1}{\rho}\frac{p^{n+1}_{i,j,k+1} - p^{n+1}_{i,j,k}}{\delta z_{i,j,k+1/2}} \\ &\quad + g_z + (VISZ)^{n+1|n}_{i,j,k} - F_d w^{n+1}_{i,j,k} - (WSZ)^{n+1}_{i,j,k}\end{aligned} \tag{5.49c}$$

where the terms $FU(V,W)X(Y,Z)$ and *VISX(Y,Z)* discussed in the previous section denote the convective fluxes and acceleration due to internal viscous shear, respectively. F_d is the porous drag coefficient according to eq. (5.5) and *WSX(Y,Z)* the acceleration due to wall shear stress.

The superscript $n+1|n$ relates to the time discretization scheme, which can be either implicit (evaluation at time level t^{n+1}) or explicit (at time level t^n). Convective fluxes are treated explicitly by default. Viscous shear stresses can be treated either explicitly or implicitly, upon judgment of the user which method is most suitable for solving the specific flow problem. Wall shear stresses are treated in an implicit way to avoid possible numerical instabilities arising in cells with large wall areas and small flow volumes. An implicit treatment is then no longer susceptible to the time step size. Since the wall shear terms are linear in flow velocities, their solution is straightforward.

Flow in porous media are modeled with a drag force proportional to the first power of the velocity, $F_d u_i$. For the applications with coarse granular media, the formulation according to eq. (5.5) is suitable. To compute a limit to the drag term for incompressible flow, it is necessary to treat the drag terms implicitly, not only in the momentum equations but also in the continuity equation. This is accomplished by using the velocity in the drag term at time level $n+1$ and algebraically solving the difference equation for the new velocity. The result is a division of all contributions to the new velocity by the term $(1+F_d\delta t)$. Keeping the effect of this extra term throughout all pressure/velocity adjustments then ensures that a balance between pressure gradient and drag forces can be achieved that also satisfies the continuity equation.

The major difficulty related to the time advancement of the discrete Navier-Stokes equations is that the mass-conservation equation does not contain an explicit time-derivative if the flow is incompressible. The incompressibility constraint rather acts as a kinematic constraint to the velocity field and couples pressure and velocity implicitly. The pressure can be considered as an auxiliary variable needed to maintain the incompressibility constraint. Fractional-step methods (Chorin, 1968) are without any doubt the most widespread technique to decouple the computation of the pressure from the advancement of the momentum equation. The advantage of such an approach is that the decoupled systems for p and u_i can be solved at a lower expense.

The basic idea of the fractional-step method is to isolate the pressure gradient from the other terms in the momentum equation and use it for the projection of the velocity field onto a solenoidal field. The several steps of this method include:

1. The *intermediate* velocities u_i^* are computed from the current-time (t^n) advective, pressure, and other accelerations:

$$\begin{aligned}\frac{u^*_{i,j,k} - u^n_{i,j,k}}{\delta t} &= -(FUX + FUY + FUZ)^n_{i,j,k} - \frac{1}{\rho}\frac{p^n_{i+1,j,k} - p^n_{i,j,k}}{\delta x_{i+1/2,j,k}} \\ &\quad + g_x + (VISX)^{*|n}_{i,j,k} - F_d u^*_{i,j,k} - (WSX)^*_{i,j,k}\end{aligned} \tag{5.50a}$$

$$\begin{aligned}\frac{v^*_{i,j,k} - v^n_{i,j,k}}{\delta t} &= -(FVX + FVY + FVZ)^n_{i,j,k} - \frac{1}{\rho}\frac{p^n_{i,j+1,k} - p^n_{i,j,k}}{\delta y_{i,j+1/2,k}} \\ &\quad + g_y + (VISY)^{*|n}_{i,j,k} - F_d v^*_{i,j,k} - (WSY)^*_{i,j,k}\end{aligned} \tag{5.50b}$$

$$\begin{aligned}\frac{w^*_{i,j,k} - w^n_{i,j,k}}{\delta t} &= -(FWX + FWY + FWZ)^n_{i,j,k} - \frac{1}{\rho}\frac{p^n_{i,j,k+1} - p^n_{i,j,k}}{\delta z_{i,j,k+1/2}} \\ &\quad + g_z + (VISZ)^{*|n}_{i,j,k} - F_d w^*_{i,j,k} - (WSZ)^*_{i,j,k}\end{aligned} \tag{5.50c}$$

   where terms with a superscript * are evaluated with intermediate velocities, i.e. implicitly. In case the viscous shear stresses are treated explicitly, solving for intermediate velocities is straightforward. In case they are treated implicitly, different solver algorithms (Jacobi iteration or an Alternating Direction Implicit (ADI) method) are used to solve for intermediate velocities u_i^*, depending on the pressure-velocity method in the next step (Yao, 2004). In case the GMRES solver is used (see next step), a Generalized Conjugate Gradient (GCG) algorithm is applied.

2. The 'new' velocity at time level $n+1$ is related to the intermediate one u_i^* through the following relationship:

$$\frac{u^{n+1}_{i,j,k} - u^*_{i,j,k}}{\delta t} = -\frac{1}{\rho}\frac{p'_{i+1,j,k} - p'_{i,j,k}}{\delta x_{i+1/2,j,k}} \tag{5.51a}$$

$$\frac{v^{n+1}_{i,j,k} - v^*_{i,j,k}}{\delta t} = -\frac{1}{\rho}\frac{p'_{i,j+1,k} - p'_{i,j,k}}{\delta y_{i,j+1/2,k}} \tag{5.51b}$$

$$\frac{w^{n+1}_{i,j,k} - w^*_{i,j,k}}{\delta t} = -\frac{1}{\rho}\frac{p'_{i,j,k+1} - p'_{i,j,k}}{\delta z_{i,j,k+1/2}} \tag{5.51c}$$

   where $p'_{i,j,k} = p^{n+1}_{i,j,k} - p^n_{i,j,k}$ represents the pressure change in each cell (i,j,k). Substitution of eqs. (5.51) into the mass continuity eq. (5.48) yields the *pressure-Poisson* equation (written here in differential form for the sake of brevity):

$$\frac{\partial(A_i u_i^*)}{\partial x_i} = \frac{\delta t}{\rho}\frac{\partial^2(A_i p')}{\partial x_i^2} \tag{5.52}$$

Basically two methods are incorporated in FLOW-3D in order to solve eq. (5.52). The first one, referred to as Successive-Over-Relaxation (SOR) uses a Newton type of relaxation process, adjusting the pressures on a cell-by-cell basis to enforce the mass conservation. A second method, using the GMRES algorithm, solves the linear system of eq. (5.52) simultaneously throughout the domain by an iterative technique (Brethour, 2009). In both algorithms, a convergence criterion is applied to the velocity divergence in each cell:

$$\left| \frac{\partial u_i}{\partial x_i} \right| \leq \text{EPSADJ} * 9.10^{-5} \delta t^{-1} \tag{5.53}$$

Convergence can be tightened optionally by setting EPSADJ to a value lesser than 1.0. It is also possible to supply a fixed value to the convergence parameter EPSI, which then replaces the right-hand-side in eq. (5.53) and makes the convergence criterion independent from δt.

3. After convergence is obtained, the velocities a time level $n + 1$ are corrected with the gradient of the new pressure p' using eqs. (5.51).
4. In a last step in fluid problems with a free surface or fluid interface, eq. (5.22) must be updated to give the new fluid configuration. The advection of other scalars (e.g. turbulence quantities) is also performed in this step. The next subsection discusses the time-advancement of fluid configuration into more detail.

Repetition of these steps will advance a solution through any desired time interval. At each step, suitable boundary conditions must be imposed at all mesh, obstacle, and free-surface boundaries. More details on the numerical implementation of these boundary conditions can be found in the user manual (Flow Science, 2011).

5.4.5 Time advancement of fluid configuration

For the general case of fluid flow in the presence of an obstacle, either porous or solid, the kinematic free-surface boundary condition eq. (5.22) needs to be discretized (written here in the absence of mass sources and considering flow without turbulent mixing in case of two-phase flow):

$$V_F \frac{\partial F}{\partial t} + \frac{\partial}{\partial x_i} \left(A_i F u_i \right) = 0 \tag{5.54}$$

The numerical solution to eq. (5.54) must prevent unphysical distortion of the free surface and preserve its sharpness (Barkhudarov, 2004). The original VOF advection method, which was developed for both single and two-fluid problems is based on the donor-acceptor approach first introduced by Hirt and Nichols (1981) and is referred to as the 'standard method' in FLOW-3D. Numerous enhancements have been made to the original algorithm to improve its accuracy and stability in complex one- and two-fluid flows with sharp interfaces. The standard method uses operator splitting and old time-level values of the F function to compute fluxes in three coordinate directions. The approach creates a possibility of overfilling or over-emptying computational cells when volume fluxes are significant in all three directions and δt is close to the local Courant stability limit (see section 5.4.6).

More recently developed methods, referred to as the 'unsplit' and 'split' Lagrangian method, are suitable for modeling both single and two-phase flow. The new advection methods have been developed to alleviate the aforementioned deficiencies of the standard algorithm. The fluid interface is reconstructed in 3D using a piecewise linear representation, where the interface is assumed to be planar in each control volume (or cell) containing the interface. The fluid volume bounded by the interface and cell faces is then moved according to the local velocity vector in a Lagrangian manner. Finally, the advected volume is overlaid back onto the Eulerian grid to obtain the new values of the fraction-of-fluid function. This combination of the Lagrangian and Eulerian methodology gives the new method its name. There is no difference in how the interface is reconstructed in both Lagrangian methods. The difference is only in how fluid is moved after the reconstruction. In the unsplit method, it is moved along the 3D velocity vector, while in the split method, it is moved first in x-direction, then in y-direction and finally in z-direction, with the interface being reconstructed after each step (Barkhudarov, 2012).

Generally, the two Lagrangian methods exhibit good accuracy in tracking sharp interfaces in complex three-dimensional motions. The split Lagrangian method typically produces lower cumulative volume error than the other methods, although the volume error may increase when this method is used together with the moving obstacle model. More details on the Lagrangian methods are given by Barkhudarov (2004).

When applying the free-surface boundary conditions and advection of the F function, it is necessary to determine an approximate direction normal to the free surface. The neighboring cell closest to the direction of the inward normal to the surface is recorded by specifying integer values of cell flags $NF_{i,j,k}$ (see Table 5.1). More details are provided in Flow Science (2011).

Methods are available code to suppress instabilities related to *misty* fluid regions, i.e. isolated fluid drops due to excessive splashing and free-surface breakup. The adjustment consists in artificially removing the fluid distribution in misty regions, for a cell (and all adjacent cells) with an F

value below the parameter FCLEAN, typically between 0 and 0.1. *Foaming* is another issue related to the extreme deformation of the free surfaces. In this case, an algorithm is available to eliminate the small voids in a flow with significant free-surface breakup. The algorithm, referred to as F-packing and only used in single-fluid flows, works by creating small negative divergences in internal fluid cells in which the fluid fraction is less than 0.99. The rate of F-packing is proportional to the coefficient CFPK. The default value is 1, when it is equal to 0 no packing will take place.

5.4.6 Stability conditions and time step control

The explicit schemes previously discussed need a limitation to the time step size δt in order to remain stable. Several criteria are applied to the maximum allowable timestep:

1. The fluid must not be permitted to flow across more than one computational cell in one time step. This advective transport depends not only on the velocity but also on the fractional area/volume open to flow. The basic stability condition is a modification to the CFL condition:

$$\delta t < \text{CON} * min\left(\frac{V_F\delta x_i}{A_x u}, \frac{V_F\delta y_j}{A_y v}, \frac{V_F\delta z_k}{A_z w}\right) \tag{5.55}$$

   The default value of CON amounts to 0.45 in case of incompressible flow. A cell with a large open face area and a small volume could restrict the time step to small values if there is significant flow in this cell. Should this happen, it can be determined by monitoring the mesh locations controlling the time step as printed in the output. In this case, it may be necessary to modify the mesh/obstacle arrangement. An algorithm is implemented in the code which automatically adjust these ratios by making small adjustments in volume fractions.

2. Free surfaces also introduce another type of stability condition associated with the propagation of surface waves. If an acceleration ACCN is applied to the fluid in a direction normal to the free surface (in this case ACCN$= g$, the gravitational constant), there can be surface waves with speeds of order $\sqrt{ACCN.h}$, where h is the depth of fluid or length of the wave. In practice, the cell size in the normal direction is used for h, together with an extra safety factor of 0.5 in the stability test. The actual condition is that surface waves should not propagate more than one cell in one time step. For example, if z is the normal direction to the surface and ACCZ is the normal acceleration, then the stability limit reads:

$$\delta t < 0.5 * \frac{min(\delta x_i, \delta y_j)}{\sqrt{\delta z_k ACCZ}} \tag{5.56}$$

Similar limits must be imposed in the x- and y-directions for each cell containing a free surface.

3. A linear analysis indicates that the time step must be further limited when a non-zero value of dynamic viscosity is used. This condition is

$$\delta t < 0.25 * max \left[RM \ \nu \left(\frac{1}{\delta x_i^2} + \frac{1}{\delta y_j^2} + \frac{1}{\delta z_k^2} \right) \right]^{-1} \tag{5.57}$$

   where RM is the maximum multiplier used on ν for all types of diffusional processes. The restriction physically means that no quantity should diffuse more than approximately one mesh cell in one time step. For safety, an extra factor of 0.5 has been incorporated in the right side of eq. (5.57) because the limit is otherwise marginal.

4. A last stability criterion regards the choice of parameter ALPHA in the first-order approximation of momentum advection. When ALPHA=1.0 is used, the previous stability conditions are sufficient. Generally, a value for ALPHA should satisfy the following condition:

$$\delta t * max \left(\frac{|u|}{\delta x_i}, \frac{|v|}{\delta y_j}, \frac{|w|}{\delta z_k} \right) < \text{ALPHA} \leq 1.0 \tag{5.58}$$

   If the first condition eq. (5.55) is fulfilled, eq. (5.58) implies that ALPHA is larger than CON.

The different options to control the evolution of δt are listed in Table 5.2 below.

Table 5.2: Time step control options

AUTOT	evolution of δt
0	constant
1	controlled by stability limit and number of pressure iterations
2	controlled by stability limit

If a constant time step is used (AUTOT=0), the initial value can be set by specifying δt, defaulted to TWFIN/100 (TWFIN being the total computation duration). However, the time-step size can also be changed, even if a constant value has been requested, when the fluid fraction advection exceeds an amount equal to twice the volume of the cell times the stability factor CON (or 0.85 times the volume of the cell if this is smaller). In this case the solution is returned to its state at the beginning of the cycle before continuing, and the cycle is repeated with the time step cut in half.

If AUTOT is set to 1, the code will adjust the time step to be as large as possible without violating stability conditions or exceeding the user-supplied maximum time-step size (DTMAX). δt will also be reduced when pressure iterations exceed corresponding nominal values that depend on the iteration options. Generally, the time step will float up or down with 5% changes per cycle unless a stability condition is violated, in which case a larger reduction may occur. The maximum number of pressure iterations before reducing the time step can be specified by means of the parameter ITDTMAX, defaulted to 10 when the GMRES pressure solver is used.

If AUTOT=2 is selected, the time step size will not be reduced if the number of pressure iterations exceeds a certain value. The number of pressure iterations per cycle is limited by ITMAX, defaulted to 100 for the GMRES pressure solver.

5.5 Conclusions

Prerequisites to a numerical model for wave interaction with permeable coastal structures are an effective treatment of the free surface and porous media flow. The CFD code FLOW-3D has been selected to this purpose. In this chapter, the basic model equations are discussed and a synopsis of their numerical implementation is provided, for a better understanding of the work developed subsequently.

FLOW-3D uses a cut-cell method for obstacle representation, together with structured rectangular grids and a staggered mesh topology. The philosophy behind this approach is to automize the grid generation process as far as possible. The definition of volume and area fraction functions enables a generalized approach for obstacle representation, applicable to both solid and porous obstacles.

Modeling of free-surface flows is achieved with the VOF method. In addition to the method based on the original donor-acceptor approach (Hirt and Nichols, 1981), more contemporary methods including a PLIC reconstruction scheme are available.

Flow in coarse granular media can be represented by a Forchheimer drag term in the momentum equations. The impact on the mass continuity and kinematic free-surface boundary condition is automatically fulfilled by the inclusion of volume and area fraction functions.

6 A numerical wave flume in FLOW-3D®

6.1 Introduction

FLOW-3D is a general multi-purpose CFD code. It has a standard wave boundary condition that enables the generation of regular and irregular surface gravity waves. However, to enable its operation as a numerical wave flume, the generation of stable long-duration test series of regular and irregular waves is indispensable. Hence, measures need to be taken to avoid re-reflection at the wave generation boundary, which would lead to an excessive increase of the total wave energy in the flume and disturb the desired incident wave field. Such a feature of the wave boundary condition is called *active absorption*.

The wave boundary condition that comes standard with the code however has no such technique for simultaneously absorbing the reflected waves. This compelled to develop additional techniques for wave generation. Because the code has a standard model for simulating moving objects, an interesting track consists of simulating the movements of a piston wavemaker, as it is employed in a physical wave flume. Existing techniques for controlling wavemakers with active absorption are well validated, and can be directly adopted in a numerical wave flume.

This chapter describes the implementation of a first-order piston wavemaker, which is the most simple type of wavemaker. First, details are given on the implementation of a control system for the piston motion. This is followed by an extensive set of validation tests, using wave conditions with varying nonlinearity. The specific objectives of the tests are to investigate the different parameters that can be selected in the numerical model, affecting the operation of the piston and the propagation of free-surface waves. In brief, the main objectives are to:

- validate the piston wave generation, paying special attention to the time-stability of long-duration wave simulations;
- validate the performance of the active wave absorption;
- identify the key numerical parameters controlling the operation of the piston and the simulation of progressive waves, and obtain optimal settings for those parameters.

6.2 Wave generation methods

The 2D Dirichlet wave boundary condition for regular and irregular waves that comes standard with FLOW-3D, prescribing surface elevations and velocity components at the mesh boundary, is probably the most efficient and widely-used method for numerical wave generation. However, the implementation in FLOW-3D does not include active wave absorption. Although it would be possible to extend the wave boundary condition with a method for active absorption, an alternative path is explored in this work, modeling the movements of a piston wavemaker. The main benefit of this approach is that the total amount of fluid within the wave flume is automatically preserved. This is generally not the case for a wave boundary condition, where a net inflow of fluid mass is retained over one wave period. Particularly for highly nonlinear waves and long test durations, the accumulation of fluid inflow might eventually cause a significant deviation from the initial water level, hence disturbing the hydraulic boundary conditions of the considered flume test. Additional corrections are often needed in order to compensate for the net inflow of fluid volume at the wave boundary.

In the following section, the implementation of a piston wavemaker for the generation of regular and irregular waves is presented, followed by a description of the active absorption method. A short description of the standard FLOW-3D wave boundary conditions is also included, since both wave generation methods will be jointly used in the validation tests.

6.2.1 Piston wavemaker

The piston wavemaker is implemented in FLOW-3D with the General Moving Object (GMO) model, which simulates rigid body motion. The motion of the piston will be prescribed, as for a *position-controlled* piston, a type of wave generator which is operated in many laboratories. Here, the most simple type of piston wavemaker is implemented, with a vertical face moving horizontally above the flume bed. The motion of the piston is assumed to be independent from fluid interaction.

Generation of regular waves

Biesel and Suquet (1951) provided the theoretical background in order to link a sinusoidal piston displacement $X(t)=esin(\omega t)$ to the surface elevation $\eta(x,t)$ of the progressive wave component generated by the piston:

$$\eta(x,t) = eK_f sin(\omega t - kx + \varphi_f) + eK_n sin(\omega t) \tag{6.1a}$$

$$K_f = \frac{4sinh^2(kh)}{sinh(2kh) + 2kh} \tag{6.1b}$$

$$K_n = \sum_{n=1}^{\infty} \frac{2sin^2(k_n h)exp(-k_n x)}{sin(k_n h)cos(k_n h) + k_n h} \tag{6.1c}$$

where e is half the piston stroke S_0, $\omega= 2\pi/T$ the pulsation frequency and k and k_n the wavenumbers obtained from the linear dispersion equations:

$$\omega^2 = kgtanh(kh) \tag{6.2a}$$

$$\omega^2 = -k_n gtanh(k_n h), n > 0 \tag{6.2b}$$

where k_n is the n^{th} real positive solution of eq. (6.2b). $K_n(k_n h)$ and $K_f(kh)$ are transfer functions for the near- and far-field, respectively. The first term in eq. (6.1a) describes a progressive wave with amplitude eK_f at large distance from the piston, the *far field* solution. The far-field surface elevation is shifted in phase with respect to the displacement of the wavemaker. In case of a piston wavemaker, φ_f equals $= \pi/2$.

The second term in eq. (6.1a) refers to the *near-field* solution or *evanescent modes* (Schäffer, 1996), representing a series of standing waves near the piston, in phase with the piston movement. They are caused by the difference between the velocity profile of the progressive wave and the uniform velocity profile created by the piston. The transfer function K_n contains a negative exponential factor to account for the decreasing amplitude of evanescent modes with increasing distance from the piston. In practice, the near-field solution can be discarded at a sufficient distance from the piston, e.g. 3 times the water depth h (Dean and Dalrymple, 1991). According to Frigaard et al. (1993), the disturbance from the near-field solution will be less than 1% of the far-field solution in a distance of approximately one to two wave lengths from the piston.

In order to generate a sinusoidal monochromatic progressive wave with wave height H and wave number k in a water depth h, the piston stroke $S_0 = 2e$ becomes:

$$S_0 = \frac{H}{K_f(kh)} \tag{6.3}$$

Limitations to the operation of the piston wavemaker exist. The limit of K_f in eq. (6.1b) tends to zero when kh approaches 0. Consequently, the piston stroke S_0 would need to become very large in order to generate long waves. Practical limitations, both in the physical and the numerical wave flume restrict the maximum allowable piston stroke, which renders the generation (and absorption) of long waves difficult.

The GMO model in FLOW-3D requires the prescription of the object velocity, which implies that piston *control velocities* rather than displacements need to be specified. A customizable subroutine *mvbvel_usr.f* is used to pass the velocities to the moving object, in order to generate the desired progressive wave field. Existing LabView® subroutines, used in the piston control software of the wave flume of the Civil Engineering Dept. (Ghent University) were modified to generate the file *piston_left.vel*, containing the horizontal piston velocities derived from the piston displacements. The sampling rate of piston control velocities are specified with the parameter f_s.

Generation of irregular waves

The methodology described in the previous section can equally be used to generate irregular waves. Here, the so-called *random phase method* is used (Tuah and Hudspeth, 1982), a deterministic method producing wave trains of finite durations which match the specified wave characteristics exactly.

Random waves are simulated in the frequency domain and subsequently transferred using a Fast Fourier Transfer (FFT) algorithm in order to obtain the time series of surface elevations η. The discrete amplitude wave spectrum corresponding to the target wave energy spectrum is combined with a random phase spectrum synthesized from a random number generator. The several steps to obtain the piston control signal include:

1. defining a target wave energy density spectrum $S_\eta(f)$, according to e.g. Pierson-Moskowitz (Pierson and Moskowitz, 1964) or JONSWAP (Hasselmann et al., 1976);
2. choosing the sample frequency f_s and spectral resolution N (half the number of Fourier components). This yields the frequency domain resolution $\Delta f = f_s/N$. The discrete wave energy spectrum $\sigma_\eta(f_i)$ is computed as:
$$\sigma_\eta^2(f_i) = S_\eta(i\Delta f)\Delta f \tag{6.4}$$
3. computing the discrete piston-displacement energy spectrum $\sigma_x(f_i)$:
$$\sigma_x^2(f_i) = \sigma_\eta^2(f_i)[K_f(k_i h)]^{-2} \ , \ i = 1..N \tag{6.5}$$

where the Biesel transfer function K_f is a function of the discrete wave number $k_i = k(f_i)$;

4. calculating the N complex Fourier coefficients $C = A + iB$ by picking a random phase φ_f between 0 and 2π, for all frequencies smaller than the Nyquist frequency $f_N = f_s/2$:

$$\begin{aligned} A_i &= cos(\varphi(f_i))\sqrt{\sigma_x^2(f_i)}/\sqrt{2} \\ B_i &= sin(\varphi(f_i))\sqrt{\sigma_x^2(f_i)}/\sqrt{2} \end{aligned} \tag{6.6}$$

   The N Fourier coefficients are mirrored to the Nyquist frequency f_N in order to obtain a hermitian Fourier Transform, i.e.:

$$C_{N+i} = C^*_{N-i+1} \ , \ i = 1..N \tag{6.7}$$

   where * denotes the complex conjugate;

5. applying the inverse Fourier transform and calculating the time series of the control signal $X(t)$ for the piston. The real part of the inverse Fourier transform is the time series, the imaginary part is zero because the Fourier transform is Hermitian.

In the same way as for regular wave generation, the piston displacements $X(t)$ are converted into piston control velocities, which are stored in the file *piston_left.vel*.

6.2.2 Active wave absorption

Methods for wave generation with active wave absorption were originally developed for physical wave flume experiments (Frigaard and Christensen, 1994). A velocity-meter based method for a VOF model with a Dirichlet wave boundary condition was presented by Troch and De Rouck (1999). A method based on the same principle is implemented here, with the necessary modifications to enable an operation in combination with a piston wavemaker.

Working principle

The principle of the active wave absorption is indicated in Fig. 6.1 and comprises two steps. Firstly, an on-line detection of velocities (u, w) at position (x_1,z_1) in front of the piston is performed. The measurement of these velocities enables the detection of the reflected wave field.

In a second step, a correction signal u^*_{ref} for the piston control velocity is computed, which will cancel out the reflected wave component propagating

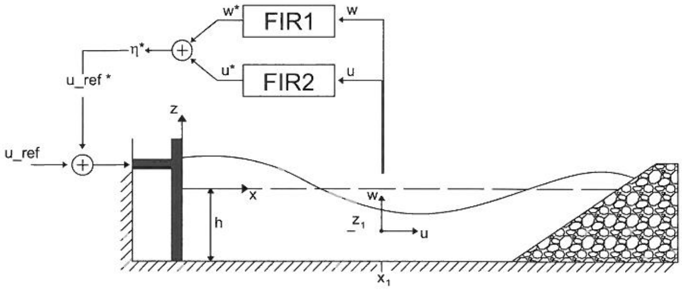

Figure 6.1: Definition sketch of active wave absorption system implemented in FLOW-3D.

towards the piston. The correction signal u^*_{ref} is determined from the two filtered velocity signals u^* and w^*. Digital FIR filters are used to compute a time-domain discrete convolution of the velocities (u, w) and the impulse response h^i (where i=u or w); e.g. for the u-velocity component:

$$u^*[n] = \sum_{j=0}^{J_f-1} h^u[j]u[n-j] \tag{6.8}$$

where J_f is the number of filter coefficients and $u^*[n] = u^*(n\Delta t_f)$ the filter output at time $t = n\Delta t_f$, with Δt_f the filter time interval. The impulse response $h^i(t)$ is determined from inverse Fourier transformation of the complex frequency response function $H^i(f)$, composed of a gain $C^i(f)$ and a phase $\varphi^i(f)$ (i=u or w):

$$Re(H^i(f)) = C^i(f)cos(\varphi^i(f)) \tag{6.9a}$$

$$Im(H^i(f)) = C^i(f)sin(\varphi^i(f)) \tag{6.9b}$$

The additional surface elevation $\eta^* = u^* + w^*$ to be generated in order to absorb the reflected wave is equal to $\eta_{-R} = a_R cos(\omega t + \varphi_R + \pi)$, which is the reflected wave component at the generation boundary, in opposite phase. The derivation of the gain $C^i(f)$ and a phase $\varphi^i(f)$ for a system with a wave boundary condition is given by Troch and De Rouck (1999):

$$C^u(f) = \frac{-sinh(kh)}{2\omega cosh(k(h+z_1))} \tag{6.10a}$$

$$C^w(f) = \frac{-sinh(kh)}{2\omega sinh(k(h+z_1))} \tag{6.10b}$$

$$\varphi^u(f) = \pi - kx_1 \tag{6.10c}$$

$$\varphi^w(f) = \pi - kx_1 + \pi/2 \tag{6.10d}$$

Applying the Biesel transfer function (eq. (6.1b)) and a phase shift φ_f converts η^* into a corrected piston displacement: $X^*(t) = K_f^{-1} a_R cos(\omega t + \varphi_R + \varphi_f + \pi)$. The time derivation of $X^*(t)$ yields the required correction signal for the control velocity u^*_{ref}, and is simply obtained by amplifying the velocity signal by ω and applying a phase shift $\varphi(f) = \pi/2$. This leads to the following expressions for the gain and phase defining the frequency response eq. (6.9):

$$C^u(f) = \frac{-sinh(kh)}{2K_f cosh(k(h+z_1))} \tag{6.11a}$$

$$C^w(f) = \frac{-sinh(kh)}{2K_f sinh(k(h+z_1))} \tag{6.11b}$$

$$\varphi^u(f) = \pi - kx_1 + \varphi_f + \pi/2 \tag{6.11c}$$

$$\varphi^w(f) = \pi - kx_1 + \pi/2 + \varphi_f + \pi/2 \tag{6.11d}$$

Design of digital filters

Inverse Fourier transformation of the theoretical complex frequency response function, denoted as $H^i_{theo}(f)$, delivers the theoretical impulse response $h^i_{theo}(t)$. In practice, a discrete number of filter coefficients is used:

$$h^i_{theo}[j] = J_f^{-1} \sum_{k=0}^{J_f-1} H^i_{theo}[k] exp(i2\pi kj J_f^{-1}) \tag{6.12}$$

where $h^i_{theo}[j] = h^i_{theo}(j\Delta t_f)$ is the discrete value of the theoretical filter coefficient at time $t = j\Delta t_f (j = 0..J_f - 1)$.

By using a finite number (J_f) of filter coefficients in the Fourier transformation, the filter response may deviate from the theoretical response for input frequencies not coinciding with one of the discrete filter frequencies. As a result, it is recommended to verify the filter performance for intermediate frequencies (i.e. between discrete theoretical filter frequencies) by means of an oversampling technique, particularly for the absorption of reflected wave spectra.

It is noticed that the number of filter coefficients J_f is virtually unlimited in a numerical model, since the filter convolution is not exectuted in real time as it is the case in a physical wave flume (see further). The parameters which define the filter design are:

- **the filter duration** T_{0f}, the most important parameter of the filter design. It defines the filter frequency interval $\Delta f_f = T_{0f}^{-1}$, which mainly determines the accuracy of the filter operation. In between discrete values of Δf_f, the realized filter response might deviate from the theoretical gain and phase. In case of regular waves, it is possible to achieve good performance when Δf_f is a multiple of T^{-1}, even with a limited frequency resolution. In case of irregular wave generation, the frequency resolution should be chosen as high as possible, yet in accordance with the length of the wave flume since the filter should have reached a 'steady state' when the reflected waves reach the wave piston:

  $$T_{0f} < 2L_{struct}/C \tag{6.13}$$

  where L_{struct} is the distance between the piston and the intersection point between SWL and tested structure, and C the wave celerity ($= L_m/T_m$ or L_p/T_p).

- for a given filter duration, the **number of filter coefficients** J_f defines the filter time interval $\Delta t_f = T_{0f}/J_f$ or the execution rate of the convolution eq. (6.8). Operation in a physical wave flume requires a real-time response of the piston to the reflected waves. This constrains the number of filter coefficients, since the calculation time of the convolution increases with J_f. Such a restriction does not exist in a numerical model, where the time step δt is advanced after the computation of the convolution has finished. This allows an arbitrary definition of the filter time step, a property that turns out to be very useful in the numerical simulations (see further). Analogous to the physical wave flume, the input control and the corrected control velocities are prescribed at equal time intervals Δt_f. A different execution rate of piston movements (f_s) and filter operation ($f_{sf} = \Delta t_f^{-1}$) is possible, but has not been considered in this study.

- the **cut-off frequencies** f_{LC} and f_{HC} define the frequency interval in which the realized frequency response of the filter should match the theoretical response as closely as possible. This interval corresponds to the interval wherein all the energy of the wave spectrum is concentrated.

- the **position** (x_1,z_1) of the point where velocities are detected. By changing x_1, a phase shift in the filter operation is applied. This can be useful to avoid high-amplitude filter components at the initial and final instant of the filter duration, which deteriorates the filter performance. The value of z_1 has little effect on the filter performance. Considering however that the active absorption method is based on linear wave theory, a sufficient distance with SWL should be respected ($> h/3$), in particular when absorbing nonlinear waves. This is due to the deviation from the linear velocity profile, which is largest near SWL. Hereafter, z_1 is always chosen equal to $-0.4h$.

The frequency response (eqs. (6.11)) shows one singularity in the gain $C^w(f)$ at $f = 0$ Hz. For high frequencies ($f > 2$ Hz), zero gain is prescribed to avoid quick transitions in the phase shift. A cosine taper is applied to the theoretical gain $C^i_{theo}(f)$ in order to obtain a gradual transition between zero gain and the theoretical value:

$$C^i(f) = 0.5C^i_{real}(f_{LC})(1 + cos\left(\frac{\pi f}{f_{LC}} + \pi\right) \; ; \; f \in [0; f_{LC}] \tag{6.14a}$$

$$C^i(f) = 0.5C^i_{real}(f_{HC})(1 + cos\left(\frac{\pi(f - f_{HC})}{5\Delta f_f}\right) \; ; \; f \in [f_{HC}; f_{HC} + 5\Delta f_f] \tag{6.14b}$$

Moreover, a tapering of the filter coefficients h^i can be applied to get a more stable digital filter. Existing LabView® code of the active absorption system operated in the wave flume of Ghent University has been adapted to the theoretical filter responses given by eqs. (6.11). In summary, the several steps in the design of the digital filter include:

1. selecting the filter duration T_{0f}, which should be chosen as large as possible to obtain the highest accuracy (certainly in case of irregular waves). An upper bound can be estimated from eq. (6.13);

2. selecting J_f, which determines the filter time interval and filter sample frequency f_{sf};

3. selecting f_{LC} and f_{HC} according to the generated wave period. In case of regular waves, a smaller frequency interval can be chosen, which simplifies the filter design. Care should be taken however that possible higher-order components in the reflected wave field arising from nonlinear interactions can be properly neutralized by the piston. It is recommended to take f_{HC} not smaller than $2T^{-1}$. In case of irregular waves, the interval $f_p/3 < f < 3f_p$ is generally respected. Choosing a value of f_{LC} slightly larger than the lower bound ($f_p/3$) can improve the filter performance, although the margin to adjust f_{LC} is limited due to the shape of the wave spectrum, which generally shows a steeper slope for $f < f_p$;

4. adjusting x_1 in order to achieve small (or zero) values of the filter coefficients at the initial and final instant of the filter duration. This can significantly improve the filter performance.

The control parameters defining the active wave absorption system are included in Table 6.1. They are implemented in the subroutine *mvbvel_usr.f*.

Table 6.1: Control parameters for active wave absorption.

parameter	**control option**
$paddle\_left$ (0 or 1)	(de)activate piston
awa (0 or 1)	(de)activate active wave absorption
$xpistonL$ [m]	position of the right face of the piston
$dx1$ [m]	distance between right piston face and measurement point
$zpos$ [m]	distance between SWL and vertical position of measurement point
$dpaddle$ [m]	water depth near piston
$f_s = f_{sf}$ [Hz]	sample frequency of piston velocities and filter execution rate

6.2.3 Wave boundary conditions

Linear and nonlinear wave boundary conditions are available in the standard version of FLOW-3D. Nonlinear waves can be generated with a wave boundary based on Fenton's Fourier Series method (Fenton, 1988; Rienecker and Fenton, 1981). In order to prevent the aforementioned problem of fluid accumulation through the wave boundary, the code provides a default option that eliminates the net volume influx through the wave boundary (IRMFLUX=1). Tests have shown however that the efficiency of this remedy is questionable, particularly for highly nonlinear waves.

Other wave boundary conditions that come standard with FLOW-3D enable the generation of cnoidal, solitary wave and random waves. Standard wave spectra included in the random wave generator are the Pierson-Moskowitz and JONSWAP spectrum. Additionally, it is also possible to employ a user-defined wave energy spectum. For further details on the implemented wave boundary conditions, the interested reader is referred to the FLOW-3D user manual (Flow Science, 2011).

6.2.4 Considerations with linear generation methods

Nonlinear regular waves propagating with constant form in intermediate or shallow water can be decomposed into free first harmonics and bound higher harmonics. A linear wave generation method, either a piston wavemaker or a wave boundary condition, does not include the natural bound higher harmonics. This leads to the release of parasitic higher harmonics which will propagate as free wave components. The superposition of the free and bound higher harmonics leads to a spatially varying wave amplitude. In a first estimate of the resulting surface elevation (Madsen and Sørensen, 1993), the second harmonic amplitude varies between 0 and 2 times the bound wave amplitude with a repetition or beat length L_B:

$$L_B = \frac{2\pi}{k_2 - 2k_1} \tag{6.15}$$

where k_1 and k_2 are the wave numbers corresponding to the free first and second bound harmonic, respectively. In this simplified description, subsequent sub- and superharmonic wave-wave interactions are neglected, as well as near-resonant triad interactions.

In the following, it will be verified whether and to which extent the piston wave generation is affected by harmonic generation.

6.3 Validation : 2D wave propagation over a horizontal bed

The propagation of 2D progressive nonbreaking waves over a horizontal bed is studied in detail in this section. Results obtained with the piston wavemaker will be compared with the nonlinear wave boundary and a theoretical solution based on Fenton's Fourier series theory. In a first step, a grid convergence study will be performed with the simplest spatial and time discretization options. Next, further testing of more advanced numerical options will be carried out. The goals of this study are to validate the operation of the piston wavemaker, to determine the numerical settings affecting the solution and to derive an optimal set of numerical parameters.

6.3.1 Test setup

The following study is limited to progressive waves. Reflection is prevented by constructing a wave flume with a sufficient length for the given test duration. Fig. 6.2 shows a definition sketch of the test setup. The initial piston position x_0 and flume length x_R are specified in Table 6.2. In case a wave boundary condition is used, the boundary coincides with $x = 0$. All other mesh boundaries are modeled as a free-slip condition.

Uniform cell dimensions are used throughout the entire study, using one single mesh block. Local mesh refinement by creating multiple mesh blocks is not considered. In this way, interpolation errors associated with block boundaries are avoided. The choice of uniform grid cells moreover delivers the highest possible accuracy. This higher accuracy originates from the way the governing equations are discretized (see Chapter 5), since in the evaluation of the change between quantities on either side of a cell, higher order terms then cancel by symmetry in uniform cells (Flow Science, 2011).

The moving piston is represented by a solid obstacle. Care must be taken that the edges of the box-shaped piston in initial position coincide

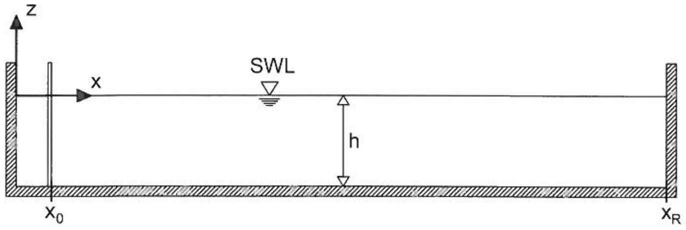

Figure 6.2: Definition sketch of the computational domain with indication of reference system.

with the cell edges. Otherwise, the FAVOR obstacle representation, which is limited by the mesh resolution, introduces discretization errors in the contact area between the bed and the piston, allowing fluid to 'leak' to the dry area behind the piston. Tests show that a minimum obstacle thickness of 2 cells is required, again to avoid leakage of fluid caused by discretization errors. Fig. 6.3 illustrates the initial position of the piston in the mesh. A tapering in the start and end of the piston movements is applied. In this way, surface elevations gradually build up or decrease, minimizing possible disturbances caused by excessive fluid acceleration.

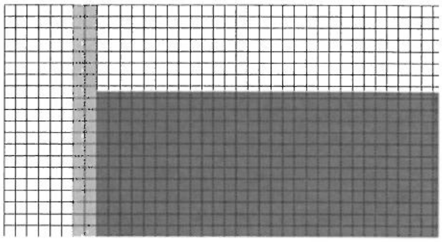

Figure 6.3: Initial position of the piston in the mesh.

Wave conditions are adopted from GWK tests, which are used in the validation study in Chapter 7. Four tests cases are selected (Table 7.2), in such way that practically the entire range of wave conditions is covered. Only regular waves are simulated at this stage, aiming to compare the results of surface elevations and velocity profiles with the linear and nonlinear wave theory.

Table 6.2: Definition of 2D wave propagation test cases.

case	h [m]	T [s]	H_0 [m]	L^1[m]	kh [-]	x_0[m]	x_R[m]	duration [s]
1	4.5	4.0	0.25	21.6	1.31	1.6	541.0	100
2	4.5	4.0	1.00	21.6	1.31	1.6	541.0	100
3	4.5	8.0	0.25	50.6	0.56	1.6	950.0	150
4	4.5	8.0	1.00	50.6	0.56	1.6	950.0	150

[1] according to linear wave theory

Test wave conditions are shown together with the limits of linear and nonlinear wave theories in Fig. 6.4. Theoretically, case 1 and 3 can be described by second-order Stokes wave theory, showing a mildly nonlinear character, close to linear waves. Waves in case 2 can be classified in between second- and third-order Stokes wave theory. Waves in case 4 exhibit the most pronounced nonlinear character, and are to be described by the fifth-order Stokes theory.

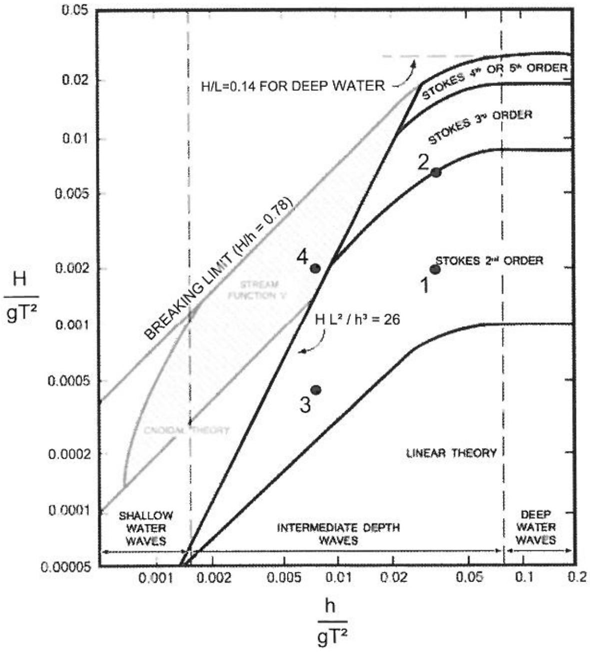

Figure 6.4: Location of wave conditions case 1 - 4 (Table 6.2) in diagram of wave theories (after Le Méhauté, 1976).

6.3.2 Basic grid convergence study

In the basic study, the first-order upwind momentum advection scheme will be employed. In this case, truncation errors are proportional to:

- the first power in time increment dt
- the first power in space increments dx, dy, dz if ALPHA $\neq 0$

Notwithstanding the first-order scheme generally shows good properties in terms of robustness and stability, it possibly produces larger numerical dissipation. In the grid convergence study, the consistency of the solution is verified by gradually reducing the cell dimensions. The aim of the convergence study is thus to verify whether and to what extent the simulations are sensitive to numerical dissipation. This dissipation can become visible in terms of wave height reduction and phase lag.

In the basic approach, an explicit treatment of convective terms and viscous stresses is applied. This imposes restraints to the time step size dt. Therefore, the time step control algorithm will be used, which automatically adjusts the time step size within the stability limits specified in 5.4.6. When using the piston wavemaker, the sampling frequency f_s of the piston control velocities should be chosen in accordance with the resulting time step. The impact of this parameter on the solution will be discussed hereafter. Unless otherwise stated, the piston sample frequency f_s employed in all test cases is 40 Hz.

Since the studied problem deals with progressive nonbreaking waves, the flow is assumed to be laminar. All computations are performed with the split Lagrangian VOF advection method. The standard donor-acceptor algorithm produces very similar results in terms of free surface motion, however also a considerably larger convective volume error. A list of relevant numerical parameter settings of the basic convergence study is given in Table 6.3. Other parameters not included in this table are set to default values. The solver executable *hydr3d* version 10.0.3 is used in all tests.

Case 1

Convergence is tested using 4 different cell sizes dx ranging between 0.4 and 0.05 m. Fig. 6.5 shows the results of surface elevations η and depth-profile of horizontal u-velocities under the passage of a wave crest and trough. Numerical results are plotted together with the theoretical solution obtained with Fenton's Fourier series method (Fenton, 2012).

Fig. 6.5(a,b) show the results obtained with the piston wavemaker at locations x=21.5 m ($\approx 1L$ from the piston) and x=146.5 m ($\approx 7L$ from the piston), respectively. The surface elevations correspond to an instant near the start of the wave train, after waves have fully built up and reached

Table 6.3: Parameter settings in basic convergence study.

Option	Setting	Parameter
fluid	fresh water (20° C), incompressible	ICMPRS=0
viscosity	Newtonian fluid	IFVISC=1
turbulence	laminar calculation	IFVIS=0
pressure solver	GMRES	IGMRES=1
	standard convergence criterion	EPSADJ=1
momentum advection	explicit	IMPADV=0
	first-order, upwind	IORDER=1, ALPHA=1
viscous stress	explicit	IMPADV=0
VOF advection	split Lagrangian method	IFVOF=6
F-packing	default	CFPK=1
time step control	automatic (stability and convergence)	AUTOT=1
maximum dt	default	DTMAX=10^{10} s

steady state. In order to enhance the comparison of surface elevations, a time synchronization of wave crests at t/T=0.5 is applied. The small phase lag between results is a consequence of a different time step size associated with different cell sizes.

Surface elevations and velocity profiles show very limited differences between runs with cell size dx 0.4 and 0.05 m. They are in almost perfect agreement with the theoretical solution. The comparison between locations at different distance from the piston points to spatially stable results.

Fig. 6.5(c,d) show the results obtained with the nonlinear wave boundary generation based on Fenton's Fourier series method. Again, good correspondence with the theoretical surface elevation and velocity profiles is obtained. However, slightly larger deviations from the theoretical solutions are noticed at further distance from the piston, as seen in Fig. 6.5(d).

The stability of surface elevations and velocities in time is further explored in Fig. 6.6, showing velocity profiles under the passage of a wave crest and trough at the beginning and end of the wave train, for cell size dx=0.05 m. Fig. 6.6(a,b) at respectively closer and larger distance from the piston, show that the surface elevations and velocities are stable, both in time and space. Fig. 6.6(c,d) show the same for the nonlinear wave boundary. At larger distance from the wave boundary, larger variations in surface elevation and velocity profile are noticed, albeit still limited.

The grid-dependency of the wave height is verified by calculating characteristic wave heights $H_{m,123}$ and $H_{m,456}$, obtained by averaging the mean wave height H_m in 3 locations x_i, indicated in Table 6.4. The obtained averages are specified in Table 6.5, expressed as the relative difference Δ

with H_0 ($= 0.25$ m), the value specified at the generation boundary:

$$\Delta = \frac{H_m - H_0}{H_0} \tag{6.16}$$

Limited differences in averaged H_m values are noticed between different cell sizes in Table 6.5. A more pronounced difference appears between H_{123} and H_{456}, showing a slight reduction of wave height with increasing distance from the piston or wave boundary. In all cases however, the obtained wave height is within a range of 6% of the target value (Table 6.5). It seems that the impact of the first-order momentum advection, and the expected numerical diffusion resulting from this approximation is limited. Even with the largest cell size tested (dx=0.4 m), a relatively accurate wave generation is achieved. However, tests with cell sizes larger than 0.4 m show increasing instabilities in surface elevations and velocities. A value of 0.4 m seems to be a practical upper limit for the cell size dx in this case.

Table 6.4: Positions x_i (in m) used in spatial averaging of H_m, case 1 and 2.

x_1	x_2	x_3	x_4	x_5	x_6
21.5	27	32.5	135.5	141	146.5

Table 6.5: Difference Δ [%] between target wave height H_0 (=0.25 m) and space-averaged H_m, case 1.

	piston		wave boundary	
dx [m]	Δ_{123}	Δ_{456}	Δ_{123}	Δ_{465}
0.40	-2.00	-3.68	-2.52	-4.50
0.20	-1.54	-4.79	-2.01	-4.79
0.10	-2.34	-5.35	-1.85	-4.63
0.05	-0.05	-3.12	-2.31	-4.69

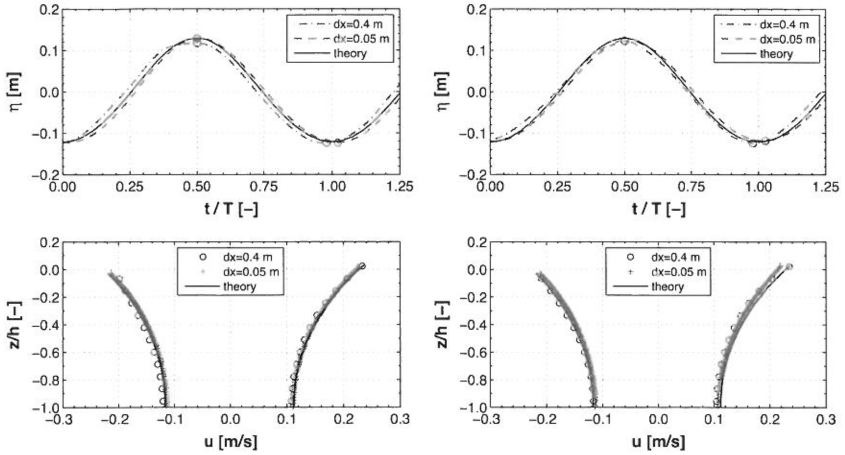

(a) Piston, x=21.5 m

(b) Piston, x=146.5 m

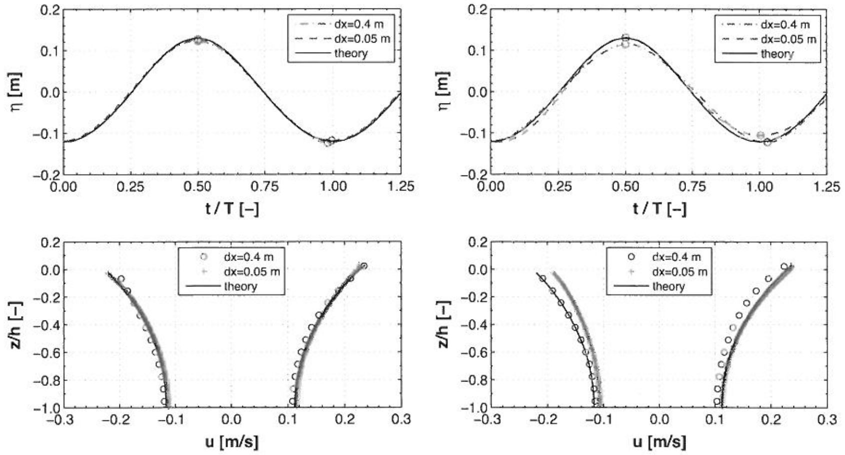

(c) Wave boundary, x=21.5 m

(d) Wave boundary, x=146.5 m

Figure 6.5: Close-up on surface elevation η and horizontal velocity $u(z)$ at an instant near the start of the wave train. Numerical results generated with the piston wavemaker and nonlinear wave boundary, at two different x-positions and for two different cell sizes dx, case 1.

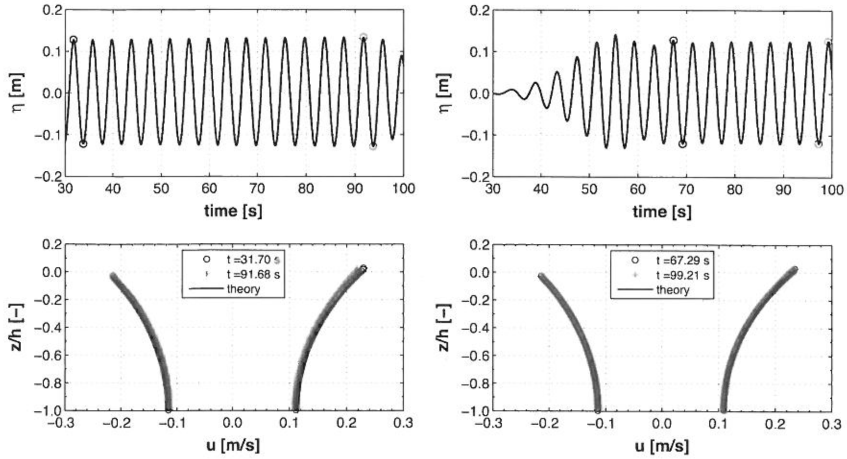

(a) Piston, x=21.5 m

(b) Piston, x=146.5 m

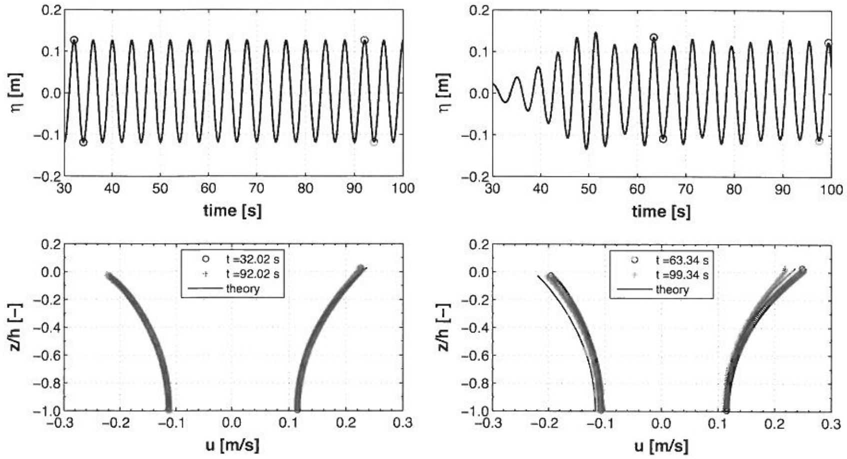

(c) Wave boundary, x=21.5 m

(d) Wave boundary, x=146.5 m

Figure 6.6: Verification of time-dependent stability of surface elevation η and horizontal velocity $u(z)$ generated by the piston wavemaker and nonlinear wave boundary, at two different x-positions, cell size dx=0.05 m, case 1.

Case 2

The spatial variability of surface elevations is checked first, as the nonlinear waves (see Fig. 6.4) might be affected by harmonic generation. The wave profiles resulting from both wave generation methods are plotted at several distances in between x=65 m ($\approx 3L$ from the wave boundary) and x=80 m in Fig. 6.7. The distance covered (15 m) is approximately equal to the theoretical beat length predicted by eq. (6.15). Given the very limited spatial variation of the wave profile in Fig. 6.7, it can be concluded that no significant harmonic generation occurs. Generally, good agreement is observed between the theoretical and numerical surface elevations.

The grid-dependency of the numerical solution is shown in Fig. 6.8, providing a detailed view of the surface elevation over one wave period, together with the corresponding horizontal velocities under the passage of a wave crest and trough. The surface elevations correspond to an instant near the start of the wave train, after waves have fully built up and reached steady state. In order to enhance the comparison of surface elevations, wave crests are synchronized at t/T=0.5.

Fig. 6.8(a,b) show the results obtained with the piston wavemaker at locations x=21.5 m ($\approx 1L$ from the piston) and x=146.5 m ($\approx 7L$ from the piston), respectively. The accuracy of the solution clearly improves with increasing mesh resolution. For cell size dx of 0.05 m, numerical results are in excellent accordance with the theoretical solution. The solution obtained with dx 0.4 m clearly suffers from numerical dissipation, to an increasing degree with increasing distance from the piston. Fig. 6.8(c,d) show similar results, yet obtained with the nonlinear wave boundary. Slightly larger deviations from the theoretical solution are noticed here.

In order to evaluate the time-dependent stability of the generated wave train, a large part of the total time series is shown in Fig. 6.9, together with depth-profiles of u-velocities corresponding with a crest and trough, at two instants near the beginning and the end of the wave train. The solution obtained with the piston wavemaker (dx=0.05 m) is shown in Fig. 6.9(a,b) at location x=21.5 m, and x=146.5 m, respectively. Clearly, a stable wave train is obtained, both in time and space. Fig. 6.9(c,d) show similar results, yet obtained with the nonlinear wave boundary. Again, as in case 1, the solution seems to show larger variability in time, when compared to the piston wavemaker.

Space-averaged values of H_m are given in Table 6.6, expressed as the relative difference with H_0 (=1.0 m). As expected, wave heights tend toward the target value when the mesh resolution increases. Simulations with cell sizes 0.40 and 0.20 m are clearly affected by numerical dissipation. In addition, a significant difference between H_{123} and H_{456} appears, showing a clear reduction of wave height with increasing distance from the piston or wave boundary. With a sufficient mesh resolution however, wave heights generated by the piston are within ± 2 % of the target value.

Table 6.6: Difference Δ [%] between target wave height H_0 (=1.0 m) and space-averaged H_m, case 2.

	piston		**wave boundary**	
dx [m]	$\mathbf{\Delta_{123}}$	$\mathbf{\Delta_{456}}$	$\mathbf{\Delta_{123}}$	$\mathbf{\Delta_{465}}$
0.40^1	-5.91	-14.60	-5.85	-14.67
0.20^1	+0.03	-5.34	+0.35	-8.84
0.10^1	+1.95	-3.54	-2.37	-6.13
0.05^2	+2.08	-1.65	-3.19	-4.49

[1] obtained with f_s=40 Hz,

[2] obtained with f_s=100 Hz

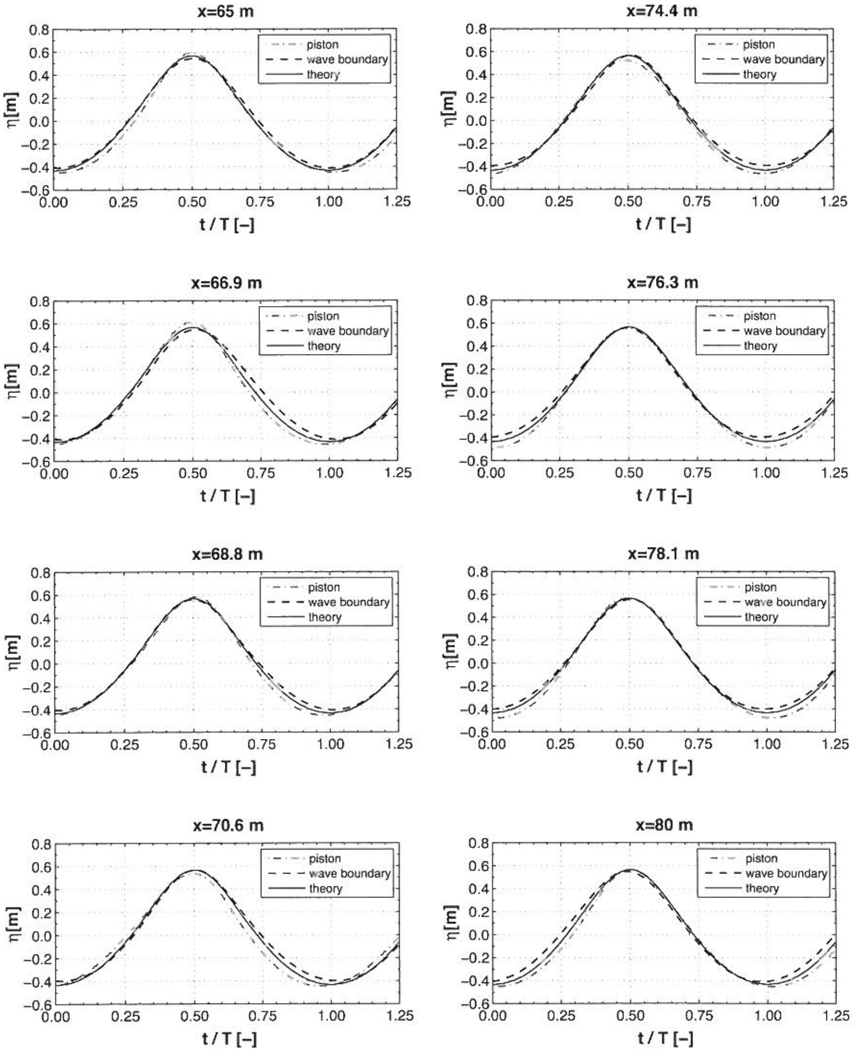

Figure 6.7: Variation of surface elevation η between x=65 and 80 m, corresponding with an instant near the end of the wave train, for test case 2. Numerical surface elevations obtained with piston wavemaker and nonlinear wave boundary condition (dx = 0.05 m), theoretical values with Fenton's Fourier series method.

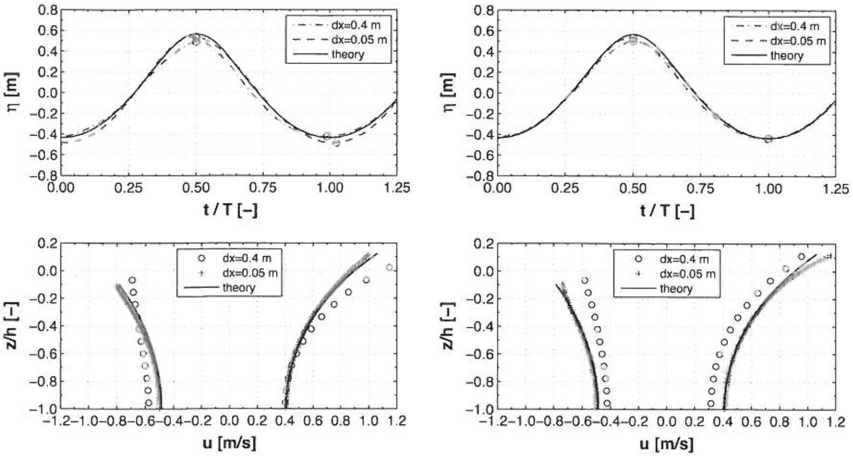

(a) Piston, x=21.5 m

(b) Piston, x=146.5 m

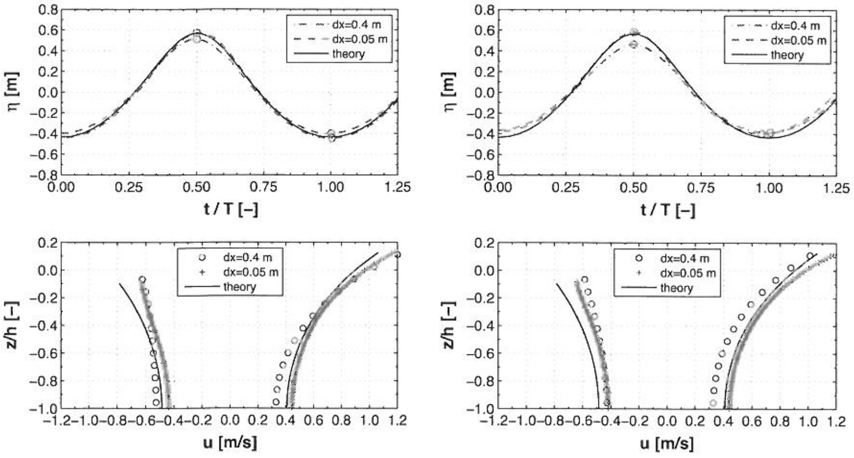

(c) Wave boundary, x=21.5 m

(d) Wave boundary, x=146.5 m

Figure 6.8: Close-up on surface elevation η and horizontal velocity $u(z)$ at an instant near the start of wave train. Numerical results generated with the piston wavemaker and nonlinear wave boundary, at two different x-positions and for two different cell sizes dx, case 2.

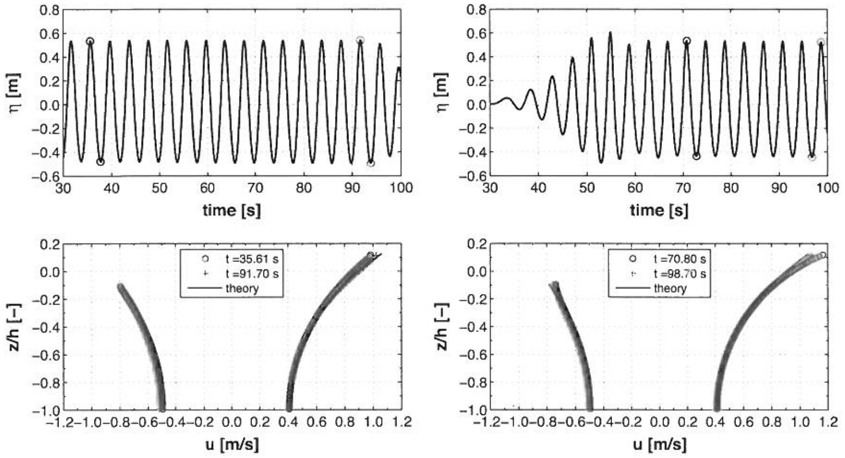

(a) Piston, x=21.5 m (b) Piston, x=146.5 m

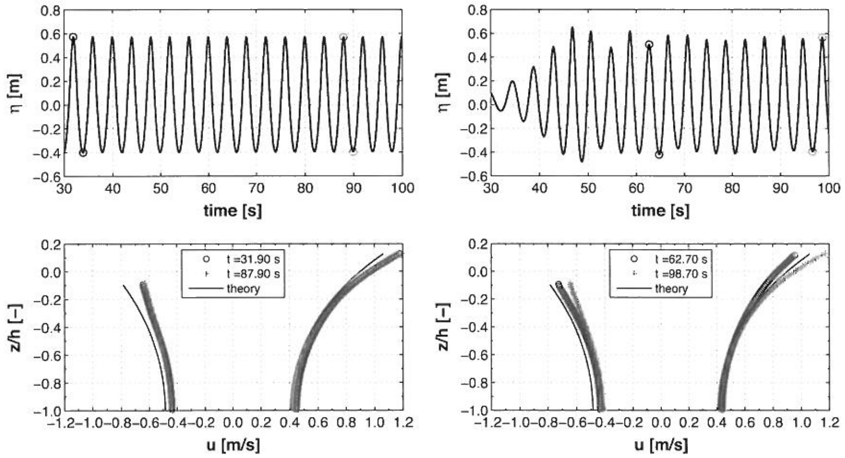

(c) Wave boundary, x=21.5 m (d) Wave boundary, x=146.5 m

Figure 6.9: Verification of time-dependent stability of surface elevation η and horizontal velocity $u(z)$ generated by the piston wavemaker and nonlinear wave boundary, at two different x-positions, cell size dx=0.05 m, case 2.

Case 3

Fig. 6.10 shows the surface elevation and velocity profiles in detail. No significant differences between both generation methods are observed. The comparison with the theoretical surface profile near the wave boundary in Fig. 6.10(a,b) shows a better correspondence compared to the surface elevation at further distance (Fig. 6.10(c,d)). It is noticed that the surface profile obtained with the wave boundary condition in Fig. 6.10(d)) shows a more pronounced asymmetry with respect to the vertical plane. Nonetheless, surface elevations and velocity profiles generally agree very well with the theoretical solution. The comparison between results obtained with dx=0.4 and 0.1 m indicate that convergence is already obtained with the lowest mesh resolution.

Fig. 6.11 shows a large part of the entire time series where velocity profiles are taken at instants corresponding with the start and end of the wave train. It can be concluded that the results are stable in time, for both wave generation methods.

Analogous to the previous cases, wave heights $H_{m,123}$ and $H_{m,456}$ are obtained by averaging the mean wave height H_m in 3 locations x_i, indicated in Table 6.7. Table 6.8 shows the space-averaged wave heights, expressed as the relative difference with H_0(=0.25 m). It is noticed that a larger wave height is obtained with the largest cell size ($dx = 0.4m$), in contrast to the previous cases. If numerical dissipation were to have an effect, it should decrease with increasing mesh resolution. One would then rather expect the wave height to increase with increasing mesh resolution. Deviations from the target wave height are limited however, within ± 5 %.

Table 6.7: Positions x_i (in m) used in spatial averaging of H_m, case 3 and 4.

x_1	x_2	x_3	x_4	x_5	x_6
51.0	63.5	76.0	253.5	266.0	278.0

Table 6.8: Difference Δ [%] between target wave height H_0 (=0.25 m) and space-averaged H_m, case 3.

	piston		wave boundary	
dx [m]	Δ_{123}	Δ_{456}	Δ_{123}	Δ_{465}
0.40	+0.36	-0.81	+0.12	+0.55
0.20	-1.89	-3.52	-0.80	-0.69
0.10	-2.32	-3.68	-1.76	-2.48
0.05	-1.12	-4.04	-3.21	-4.44

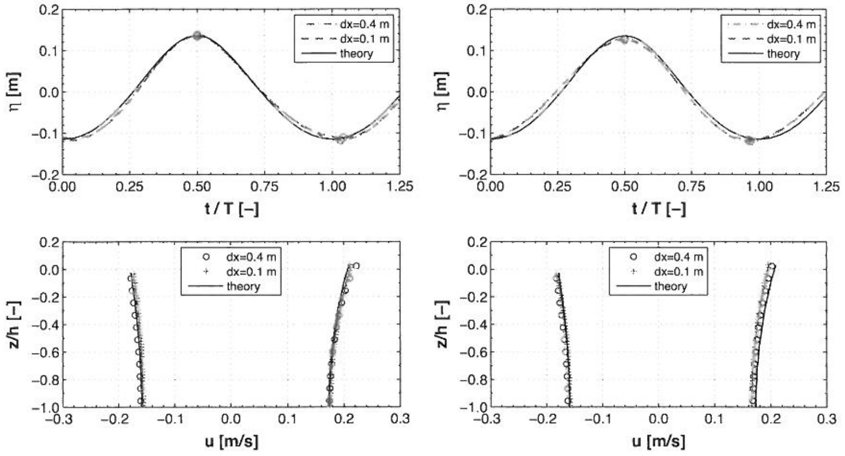

(a) Piston, x=51.0 m (b) Piston, x=278.0 m

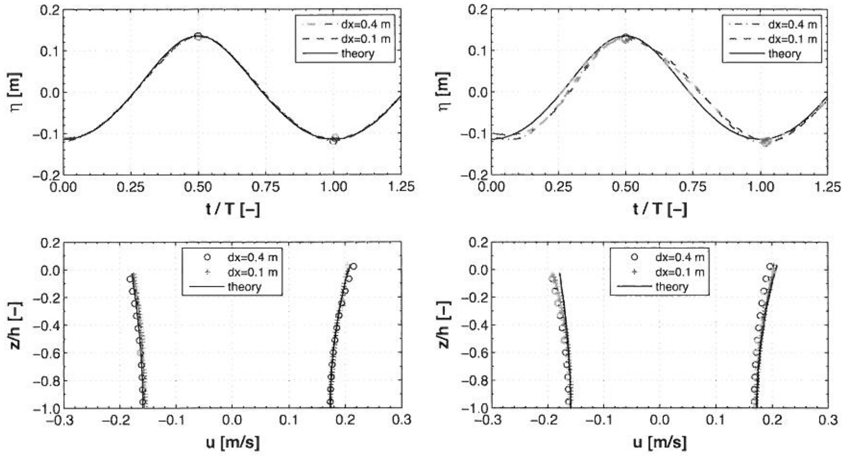

(c) Stokes V, x=51.0 m (d) Stokes V, x=278.0 m

Figure 6.10: Close-up on surface elevation η and horizontal velocity $u(z)$ at an instant near the start of the wave train. Numerical results generated with the piston wavemaker and nonlinear wave boundary, at two different x-positions and for two different cell sizes dx, case 3.

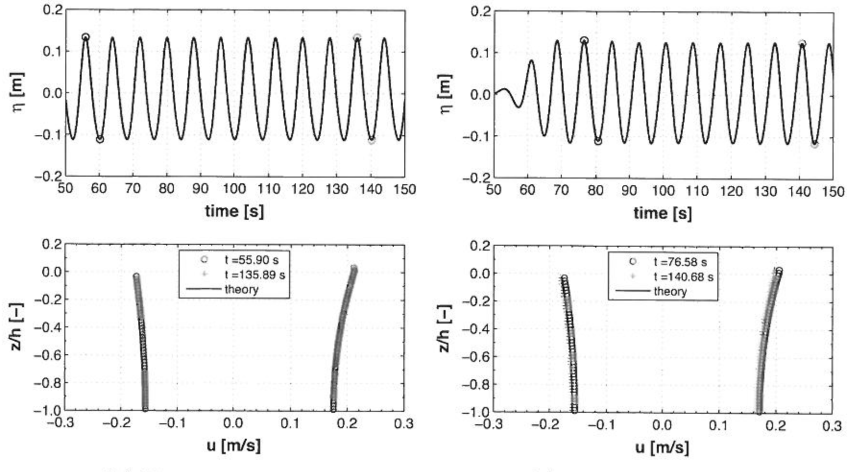

(a) Piston, x=51.0 m

(b) Piston, x=278.0 m

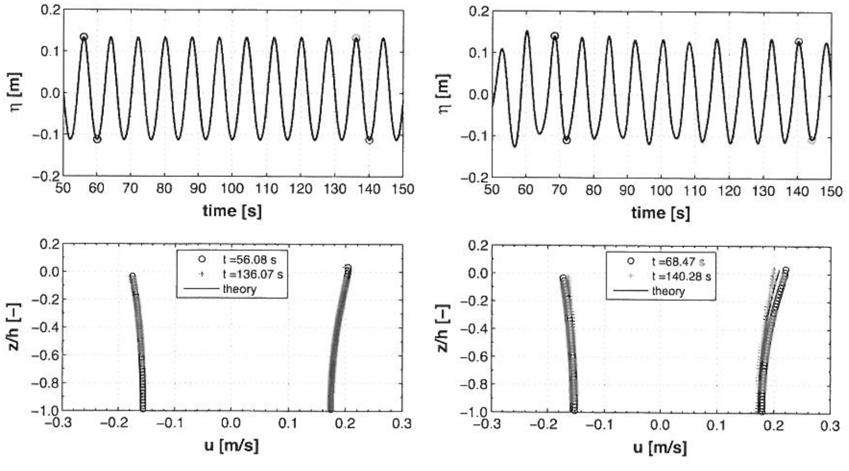

(c) Wave boundary, x=51.0 m

(d) Wave boundary, x=278.0 m

Figure 6.11: Verification of time-dependent stability of surface elevation η and horizontal velocity $u(z)$ generated by the piston wavemaker and nonlinear wave boundary, at two different positions x, cell size dx=0.10 m, case 3.

Case 4

Of all four test cases in Fig. 6.4, waves in case 4 exhibit the highest nonlinear character. The theoretical beat length according to eq. (6.15) amounts to 146 m, using the linear wave theory to approximate k_1 and k_2. Fig. 6.12 shows the free-surface elevation at eight different locations in between one beat length. Computations with dx=0.1 m are shown, obtained with the piston wavemaker and the nonlinear wave boundary condition. The comparison between different locations reveals a clear variation of surface elevation for the linear piston wavemaker. At some locations, secondary peaks in the trough appear. The spatial η-variation caused by the release of higher harmonics is not observed with the nonlinear wave boundary.

The surface profile generated by the piston wavemaker at location x=150 m is very similar to x=296 m, an indication that the repetition of the spatial variation corresponds well with the theoretical beat length predicted by eq. (6.15). The harmonic generation under linear piston generation results in larger wave heights compared to the waves generated by the nonlinear wave boundary, as indicated in Table 6.9.

Fig. 6.13 shows the velocity profile at different locations between x=150 m and x=241.2 m, obtained with the piston wavemaker. Notwithstanding the spatial variations in η, the wave train appears to be stable in time in each location. The velocity profiles corresponding with the passage of a crest and trough clearly deviate from the theoretical solution. The discrepancy between numerical and theoretical profiles of u-velocities increases when the local amplitude of the second harmonic reaches its maximum value, at approximately half the beat length. In Fig. 6.13(c), the sharp, peaked crest and flattened trough correspond with an increase in u-velocities near the free surface.

Table 6.9: Difference Δ [%] between target wave height H_0 (=1.0 m) and space-averaged H_m, case 4.

	piston		**wave boundary**	
dx [m]	$\mathbf{\Delta_{123}}$	$\mathbf{\Delta_{456}}$	$\mathbf{\Delta_{123}}$	$\mathbf{\Delta_{465}}$
0.20[1]	+15.63	+4.13	-1.72	-1.55
0.10[1]	+14.37	+3.41	-2.29	-1.60
0.05[2]	+11.67	+1.46	-2.60	-1.78

[1] obtained with f_s=40 Hz,
[2] obtained with f_s=100 Hz

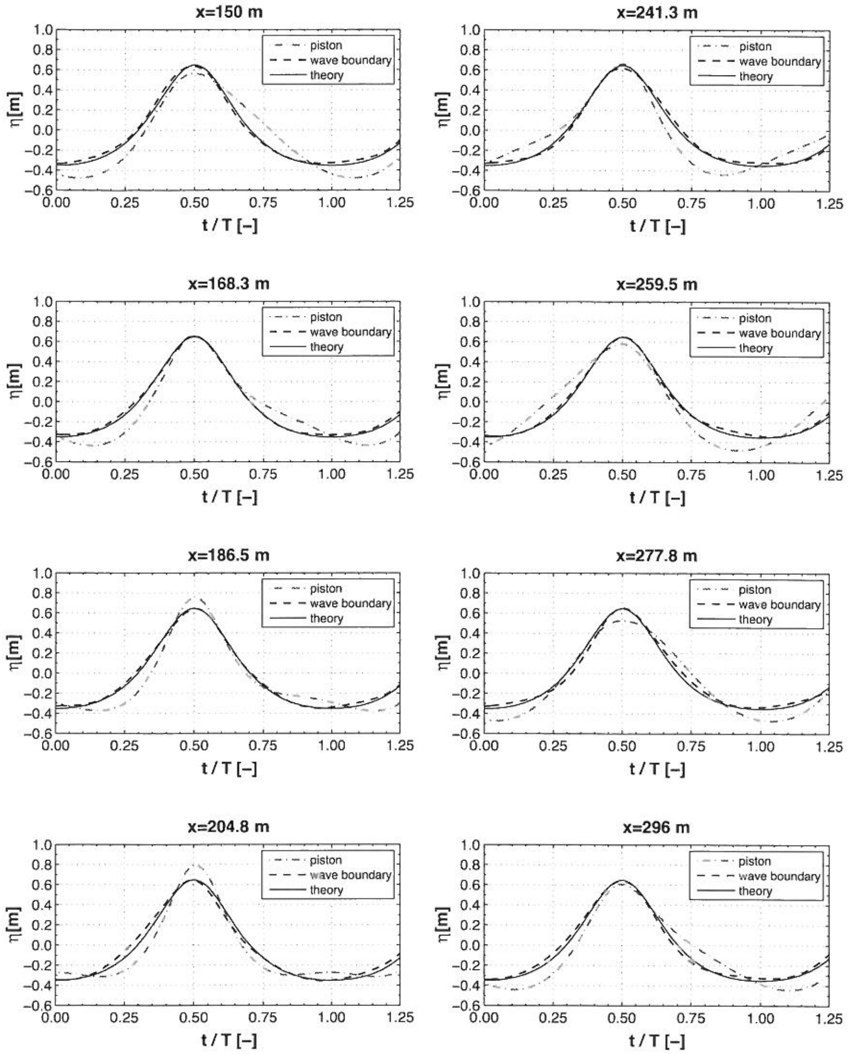

Figure 6.12: Variation of surface elevation η between x=150 and 296 m, corresponding with an instant near the end of the wave train, for test case 4. Numerical surface elevations obtained with piston wavemaker and nonlinear wave boundary condition ($dx = 0.10$ m), theoretical values with Fenton's Fourier series method.

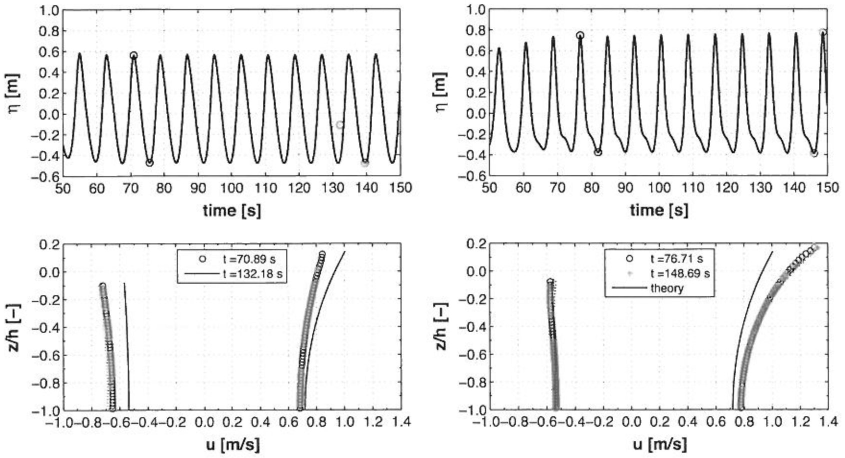

(a) x=150.0 m (b) x=186.5 m

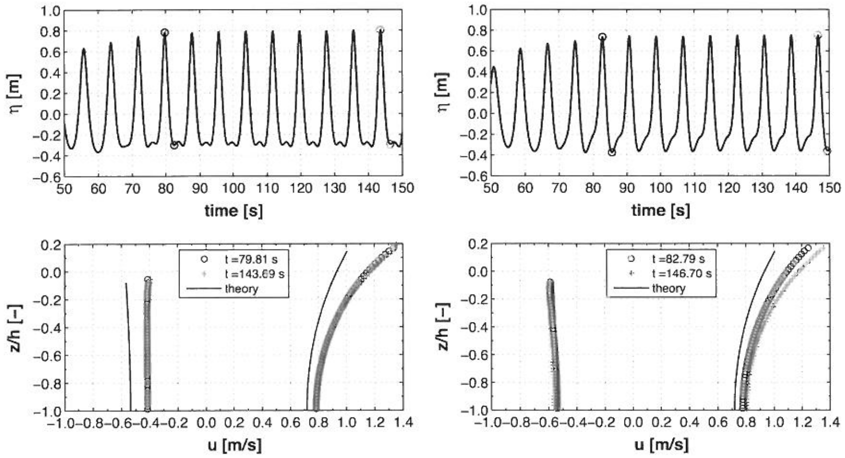

(c) x=204.8 m (d) x=223.0 m

Figure 6.13: Close-up on surface elevation η and horizontal velocity $u(z)$ generated by the piston wavemaker, at different locations x in between approximately half the beat length, cell size dx=0.1 m, case 4.

6.3.3 Further testing of numerical options

In the previous section, a first-order upwind discretization scheme for the momentum advection terms was used in all simulations. In the following it is tested whether a mixed first-order or second-order scheme yields better results in terms of computational accuracy and/or efficiency. A discussion on the time step control (section 5.4.6) is included in the following, since it appears that the time step evolution is closely connected with the spatial discretization of momentum advection.

Because of the larger wave height and absence of harmonic generation in case 2, this particular case will be used to illustrate the impact of the momentum discretization scheme and time step control on the solution. All results are obtained with piston wave generation, with f_s=40 Hz (unless otherwise stated).

Momentum advection approximations

A variation to the first-order upwind scheme consists of a mixture of upwind and centered differences (see 5.4.3) and is obtained by setting the weighting factor ALPHA to a value between 0 and 1. Liu and Lin (1997) suggest to take ALPHA in the range of 0.3 to 0.5. The impact of the weighting factor ALPHA is studied by comparing the standard upwind scheme (ALPHA=1) to a mixed scheme with ALPHA=0.3. Use is made of the automatic time step algorithm, determined by stability constraints and the number of pressure iterations (AUTOT=1).

Fig. 6.14 shows the impact of ALPHA on the time step size. Clearly, the mixed scheme results in a reduction of the time step size. In both cases, the advection in the x-direction is the restraining limit to the time step size. It is noticed that the value of ALPHA is smaller than the default value (0.45) of the CFL stability limit (section 5.4.6), hence eq. (5.57) yields the most stringent condition to the time step limit.

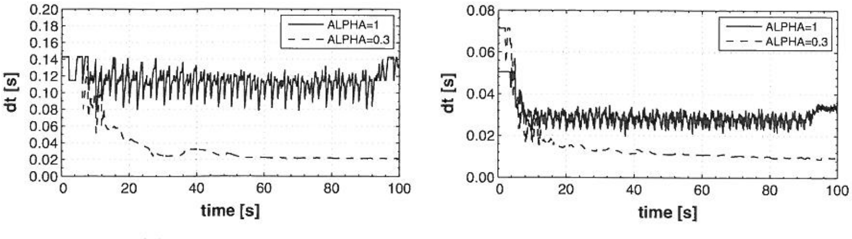

(a) dx=0.40 m (b) dx=0.10 m

Figure 6.14: Impact of ALPHA on time step size dt, case 2.

Surface elevations and corresponding velocity profiles under a passage of a crest and trough are shown in Fig. 6.15, at location x=146.5 m, taken at an instant corresponding to the start of the wave train. Comparison of results between different cell sizes in Fig. 6.15 show that the mixed scheme is more prone to numerical dissipation than the fully upwind scheme (ALPHA=1). In either case, a disturbance of the velocity profile near the free surface is noticed with the mixed scheme. This could be the result of the significant reduction in time step size.

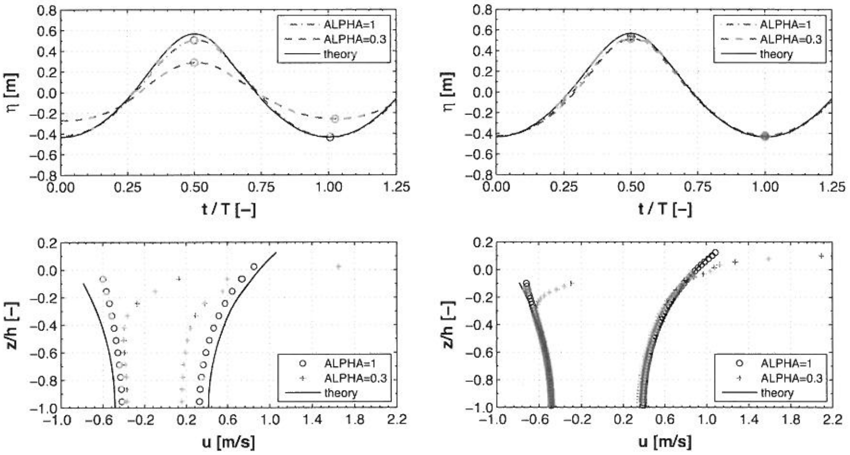

(a) dx=0.40 m (b) dx=0.10 m

Figure 6.15: Impact of ALPHA on surface elevation η and horizontal velocity $u(z)$, shown at x=146.5 m, at an instant near the start of the wave train, case 2.

In the previous section, simulations with the first-order upwind scheme proved to yield accurate results with limited numerical dissipation, when the mesh resolution is sufficiently high. It was noticed that a higher mesh resolution is needed for the cases with larger wave height. In the following, it is verified whether a second-order advection scheme yields higher accuracy for lower mesh resolutions. Both the regular (IORDER=2) and monotonicity-preserving (IORDER=3) second-order scheme are used.

Fig. 6.16 shows the impact of the momentum discretization on the time step size. A standard upwind differencing (ALPHA=1) is used in the first-order scheme. Employing the automatic time step control with both second-order schemes results in a significant reduction of the time step size in case of a relatively coarse grid (Fig. 6.16(a)). On a finer grid, all time step sizes result to be very similar (Fig. 6.16(b)).

Contrary to what one would assume, the second-order schemes do not

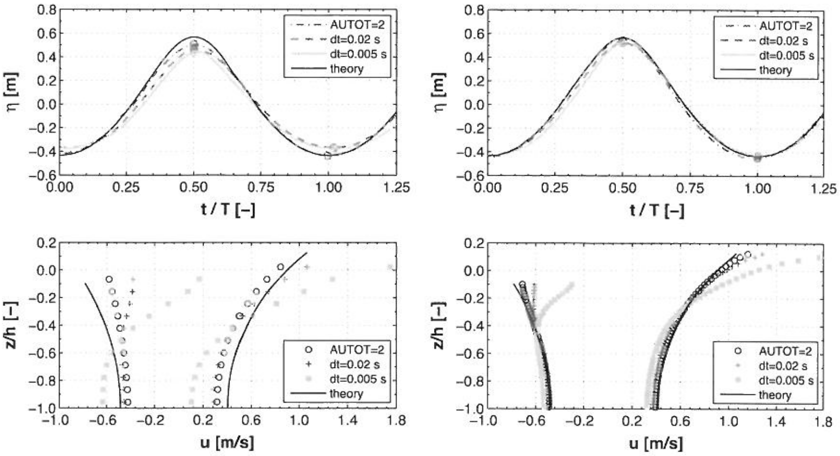

(a) dx=0.40 m, EPSI= $5 * 10^{-4}$

(b) dx=0.10 m, EPSI= $1 * 10^{-3}$

Figure 6.18: Impact of time step control and time step size dt on surface elevation η and horizontal velocity $u(z)$, shown at x=146.5 m, at an instant near the start of the wave train. Simulations case 2 with IORDER=1, ALPHA=1.

Selecting the piston sample frequency f_s

In this previous section, the rate f_s at which piston control velocities are specified was set to 40 Hz in all cases, except for the smallest cell size (dx=0.05 m). In fact, it is noticed that the piston time step $dt_p = f_s^{-1}$ should be chosen in accordance with the time step size dt resulting from the application of stability constraints. For instance, when dt_p is much larger than the realized time step, the input signal of the piston control velocities looks like a step function. Tests with different values of dt_p show that this can affect the surface elevation and particularly the u-velocities, which tend to show an increase (a *drift*) in a confined region near the free surface.

Table 6.10 contains time step sizes dt for different combinations of dx and dt_p, computed for test cases 1 and 2. The results in Table 6.10 indicate that the drift in u-velocity is connected with a relatively large ratio of and dt_p to dt. It is also noticed that the value of dt_p has a small impact on the resulting time step since the latter is being adapted by the automatic time step control algorithm, in order to properly resolve the movement of the GMO. Using a smaller piston time step dt_p generally results in a slightly larger time step dt.

Fig. 6.19 shows the impact of f_s on the surface elevations and velocity profiles in case 2, computed with different mesh resolutions. For cell sizes dx=0.2 and 0.1 m, the observed drift in u-velocity vanishes when dt_p is reduced. For the highest mesh resolution (dx=0.05 m) however, it seems that the drift is very limited, in spite of the large difference between dt_p and dt in case f_s=10 Hz. In Fig. 6.19, the deviations in the velocity profile reach till a depth of about $-0.4h$, which corresponds with the vertical position of the single-point velocity measurement in the active wave absorption procedure. If the disturbance grows beyond this point, it could affect the performance of the active wave absorption.

Table 6.10: Difference between dt_p and realized dt and indication of drift in $u(z)$, for case 1 and 2.

	case 1 (H_0 = 0.25 m)			**case 2 (H_0 = 1.0 m)**		
dx [m]	dt_p [s]	dt [s]	**drift?**	dt_p [s]	dt [s]	**drift?**
0.4	0.10	0.101	no	0.10	0.079 - 0.101	no
0.4	0.025	0.101	no	0.025	0.078 - 0.101	no
0.2	0.10	0.06 - 0.071	no	0.10	0.028 - 0.045	yes
0.2	0.025	0.071	no	0.025	0.045 - 0.065	no
0.1	0.10	0.010 - 0.051	yes	0.10	0.015 - 0.025	yes
0.1	0.025	0.046 - 0.051	no	0.025	0.025 - 0.033	no
0.05	0.10	0.015 - 0.031	yes	0.10	0.010 - 0.015	yes
0.05	0.025	0.028 - 0.032	no	0.01	0.012 - 0.017	no

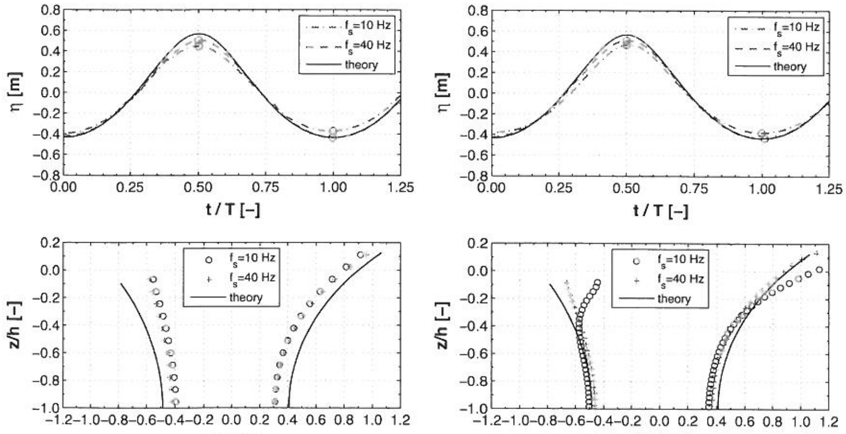

(a) dx=0.40 m (b) dx=0.20 m

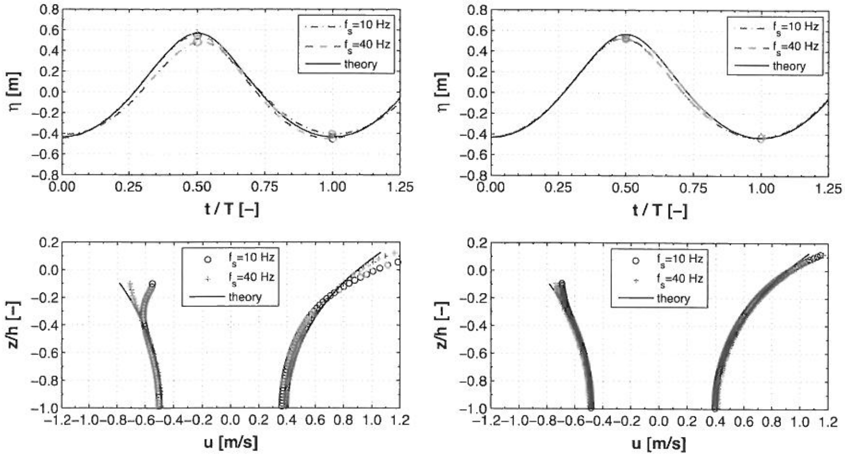

(c) dx=0.10 m (d) dx=0.05 m

Figure 6.19: Impact of f_s on surface elevation η and horizontal velocity $u(z)$ shown at x=146.5 m, at an instant near the start of the wave train. Simulations case 2 for different cell sizes dx.

6.3.4 Conclusions

The observations drawn from the simulation of progressive, 2D, nonbreaking waves over a horizontal bed lead to the following conclusions and recommendations:

- The previous test cases show that the minimum mesh resolution required for an accurate solution of surface elevations and velocities is mainly determined by the wave height. A minimum ratio H/dx of 0.5 to 1 appears sufficient when the wave height is relatively small (case 1 and 3). For larger waves, H/dx needs to be raised (to about 20 for case 2 and 4). The wavelength has a smaller impact on the required mesh resolution, though a minimum ratio L/dx about 50 to 100 seems reasonable. Note that uniform cell sizes dx were used in all simulations. A further optimization with nonuniform meshes is not undertaken in the present study;

- An accurate modeling of progressive waves can be achieved with the first-order upwind scheme, which has been shown to yield the most stable solutions. A comparison with higher-order momentum advection schemes does not indicate a larger numerical dissipation for the first-order method, even on relatively low mesh resolutions;

- The automatic time step control (AUTOT=1/2) provides the most efficient solution. A user-specified constant time step much below the implemented stability constraints can lead to deviations in the velocity profile near the free surface, and to a minor extent in the surface elevation. The critical minimum time step associated with the occurrence of a drift in near-surface velocities depends on the mesh resolution;

- A maximum piston time step dt_p should be selected, which should not largely exceed dt resulting from the automatic time step control. Otherwise, control velocities behave like a step-function which can affect the results. The sensitivity of the solution to the value of dt_p however is observed to be mesh-dependent and diminishes moreover with increasing mesh resolution. No specification of a maximum allowable time step size is needed when the piston operates in single generation mode (i.e. without active absorption).

6.4 Validation : long-duration wave test

2D wave propagation over a horizontal bed was modeled in the previous section, where zero wave reflection was obtained by constructing a long wave flume and a relatively short test duration (about 20 wave periods). In most wave flume studies however, the simulation of long-duration test series is required, e.g. in tests with irregular waves or tests where certain aspects of wave-structure interaction take a considerable number of wave cycles in order to fully establish; e.g. the wave-induced set-up of MWL in permeable structures.

In the following section, the stability in time of a long series of piston-generated waves (about 100 wave periods) is investigated. Tests in section 6.3.3 revealed that results can become unstable when the time step size is reduced. This is of particular importance, since a reduction of time step size is most likely to occur when waves interact with a structure. The following tests aim to the investigate the effect of a variable time step size on the long-term stability of the generated wave train, using the different momentum discretization schemes available in FLOW-3D.

6.4.1 Test setup

The simulation of an undisturbed progressive wave field with long duration in combination with a wave flume of limited length requires an adequate technique for absorbing the waves. The standard nonreflecting outflow boundary condition available in the code (a Sommerfeld-type condition) does not require additional space in the computational domain and therefore is the most efficient method in terms of computational cost. However, tests with this boundary condition show unacceptable degrees of reflection in most cases. Therefore, use is made of a passive absorption technique, a so-called *sponge* layer. The sponge is the numerical counterpart of an absorbing beach applied in a physical wave flume, where flow motions are gradually dampened out over a gentle slope, reducing the reflection as much as possible.

Fig. 6.20 presents the setup of the numerical flume, with indication of the piston and the sponge. In FLOW-3D, the sponge has been implemented in the customizable subroutine *qsadd.f*, by gradually damping the individual fluid velocity components (u, v, w) over a distance L_{sponge} toward zero values at $x = x_R$. The mathematical description of the sponge takes the form of a

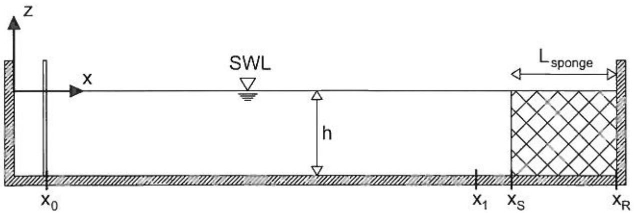

Figure 6.20: Definition sketch of the computational domain for long-duration wave test.

power function[1], which e.g. for the u-velocity reads as:

$$u^*(x_i) = u(x_S)\left[1 - \left(\frac{x_i - x_R + L_{sponge}}{L_{sponge}}\right)^{n_s}\right] \tag{6.17}$$

where $u^*(x_i)$ and $u(x_s)$ are the velocity components at position x_i and x_s, respectively ($x_S \leq x_i \leq x_R$). The power n_s in eq. (6.17) determines the shape of the sponge function. Tests with the sponge function eq. (6.17) indicate a recommended value of n_s between 3 and 7. Additionally, the absorption performance improves with increasing the sponge length L_{sponge}. Tests with varying sponge lengths show that a minimum sponge length of about one wave length is required to achieve acceptable absorption (i.e. CR<0.20). A sponge length of about $3L$ provides optimum results in terms of absorption capacity and computational cost. For smaller sponge lengths, a smaller value of n_s in eq. (6.17) yields better absorption. For larger L_{sponge} ($> 2L$), the value of n_s has a limited impact on the absorption performance.

As in section 6.3.3, case 2 will be employed as a reference case in the following tests. Waves are generated using the piston wavemaker in single generation mode. All simulations are performed with dx=0.1 m and f_s=40 or 100 Hz (depending on dt). A fixed sponge length of 64.8 m ($\approx 3L$) is used, with n_s=3. A wave flume with length 108 m ($\approx 5L$) is constructed between the initial piston position x_0 and the starting point x_S of the sponge.

6.4.2 First-order upwind momentum advection

Tests are run with a constant time step size of 0.3 and 0.15 s, set by AUTOT=0. A value of 0.3 s closely corresponds to the smallest time step size resulting from the automatic time step control (AUTOT=2). Fig. 6.21 shows the resulting surface elevations and velocity profiles at a location $x_1 = 100$

---

[1] Other formulations of the damping function than eq. (6.17) exist (e.g. elliptic or cosine functions) but are not tested here.

m, near the end of the wave flume. The reduced time step size clearly leads to a dissipation of incident wave height, shown in detail in Fig. 6.21(b). The dissipation increases with time but apparently stabilizes after about 200 s. The reduction of wave height corresponds with a drift of velocity in Fig. 6.21(d): in the lower half of the cross section, a decrease of horizontal velocities occurs, whereas an increase is noticed in the upper half.

It is known that a reduction in time step size increases the numerical dissipation in the first-order upwind scheme, since the diffusive error ϵ_{diff} for e.g. a flow with velocity u in the x-direction is proportional to:

$$\epsilon_{diff} \propto \left(1 - u\frac{dt}{dx}\right) \tag{6.18}$$

Tests with increasing mesh resolution do not yield significant improvement in the velocity profile. It is thus unlikely that the increase in velocity observed in Fig. 6.21(d) is caused by numerical diffusion, since a diffusive effect should decrease noticeably with increasing mesh resolution. It can only be concluded that a plausible argument is still lacking at the moment, explaining for the erroneous behavior of the first-order upwind scheme in case the time step size is reduced considerably below the stability limit resulting from the automatic time step control.

6.4.3 Second-order momentum advection

A drawback of the second-order momentum advection is a reduced lower stability compared to the upwind scheme, manifesting as spurious velocities near the free surface. The local increase of velocity causes a reduction of dt, due to the application of the CFL stability constraint. The following tests with the second-order schemes are therefore run with AUTOT=2 and the specification of DTMAX.

Fig. 6.22 shows the resulting surface elevations and velocity profiles at x_1. A detailed view on the surface elevations shows that a reduced DTMAX leads to slightly larger wave heights. However, both simulations show excellent time-stability. The velocity profiles in Fig. 6.22(c,d) remain stable and agree very well with the theory, except for the spurious velocities near the free surface.

6.4.4 Second-order monotonicity preserving momentum advection

Similar tests are performed as with the second-order scheme. Fig. 6.23 shows that this algorithm does not yield stable results, in spite of the methodology applied in the algorithm which aims for enhanced stability.

6.4.5 Impact of spatial discretization

In an attempt to further explore the instable behavior of the first-order upwind scheme, the influence of the grid is investigated. Therefore, the simulation with dt=0.015 s, which showed to become unstable, is repeated with the number of cells ny in transversal direction increased to 2 and 4.

Fig. 6.24 shows the resulting surface elevations and velocity profiles of both simulations. Small differences are observed between different values of ny. However, both simulations with ny equal to 2 and 4 do not exhibit the damping of wave height and drift in fluid velocities, associated with the time step reduction with ny=1 (Fig. 6.21). This suggests that other factors than numerical diffusion are causing the instability under a reduction of time step size.

The slight deviations in the velocity profiles in Fig. 6.24(c,d) are most probably caused by disturbances in the transversal direction, as shown in Fig. 6.25. Theoretically, the velocity component v should be zero over the entire fluid depth for a purely 2D flow. Disturbances in the v-profile are small, limited to about 5% of the u-profile, but seem to increase with time.

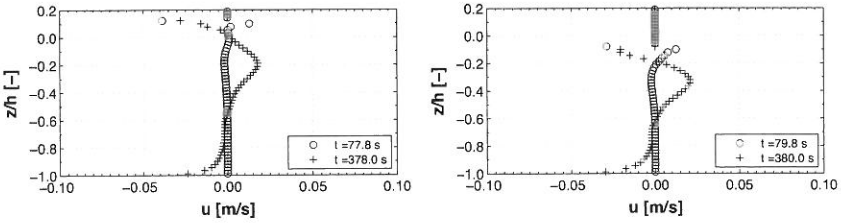

(a) crest (b) trough

Figure 6.25: Cross-direction v-velocity profile, shown at $x = x_1$ and half the cross section width (y=0.2 m). Velocity profiles corresponding with the passage of (a) crest and (b) trough, corresponding with the start and end of the wave train. Simulations case 2 with dx=0.1 m, ny=4, IORDER=1, ALPHA=1, AUTOT=2, DTMAX=0.015 s, EPSI= $1 * 10^{-3}$.

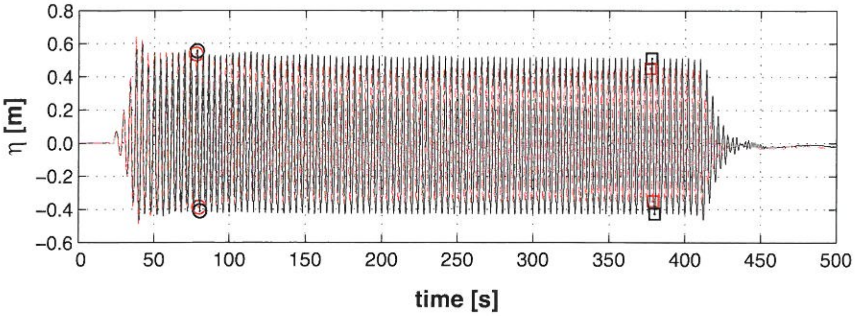

(a)

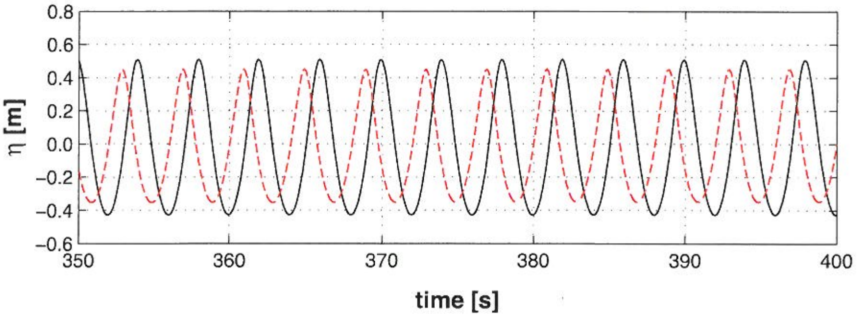

(b)

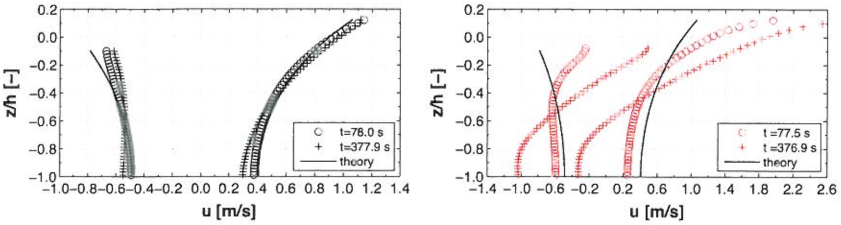

(c) dt=0.03 s

(d) dt=0.015 s

Figure 6.21: Impact of dt on surface elevations and horizontal velocities, shown at $x = x_1$. Total time series (a) and close-up (b) of surface elevations for dt=0.03 s (black solid) and dt=0.015 s (red dashed). Velocity profiles corresponding with the start and end of the wave train for (c) dt=0.03 s and (d) dt=0.015 s. Simulations case 2 with dx=0.1 m, IORDER=1, ALPHA=1, EPSI= $1 * 10^{-3}$, AUTOT=0.

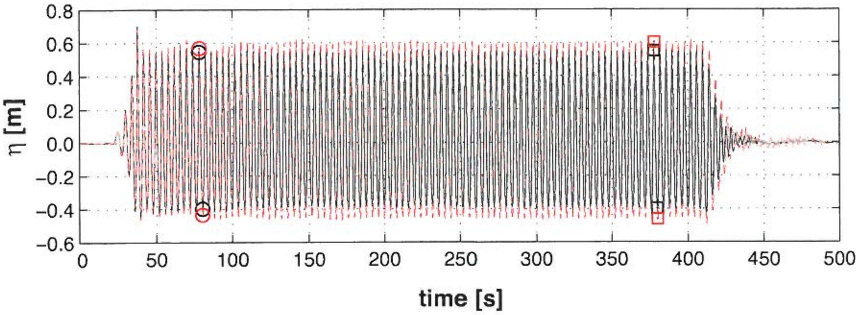

(a)

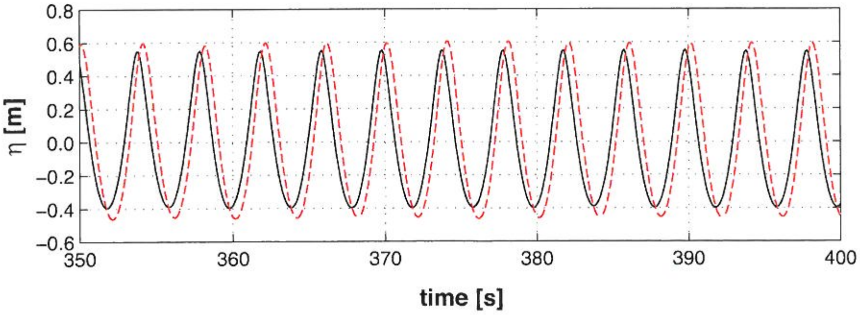

(b)

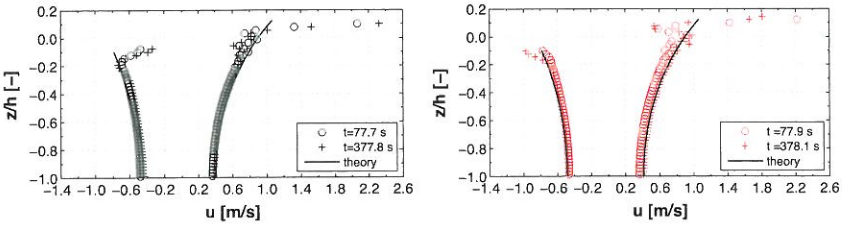

(c) DTMAX=0.015 s (f_s=40 Hz) (d) DTMAX=0.005 s (f_s=100 Hz)

Figure 6.22: Impact of *dt* on surface elevations and horizontal velocities, shown at $x = x_1$. Surface elevations in panel (a) and (b) shown for DTMAX=0.015 s (black solid) and DTMAX=0.005 s (red dashed). Velocity profiles corresponding with the start and end of the wave train for (c) DTMAX=0.015 s and (d) DTMAX=0.005 s. Simulations case 2 with dx=0.1 m, IORDER=2, AUTOT=2, EPSI= $1 * 10^{-3}$.

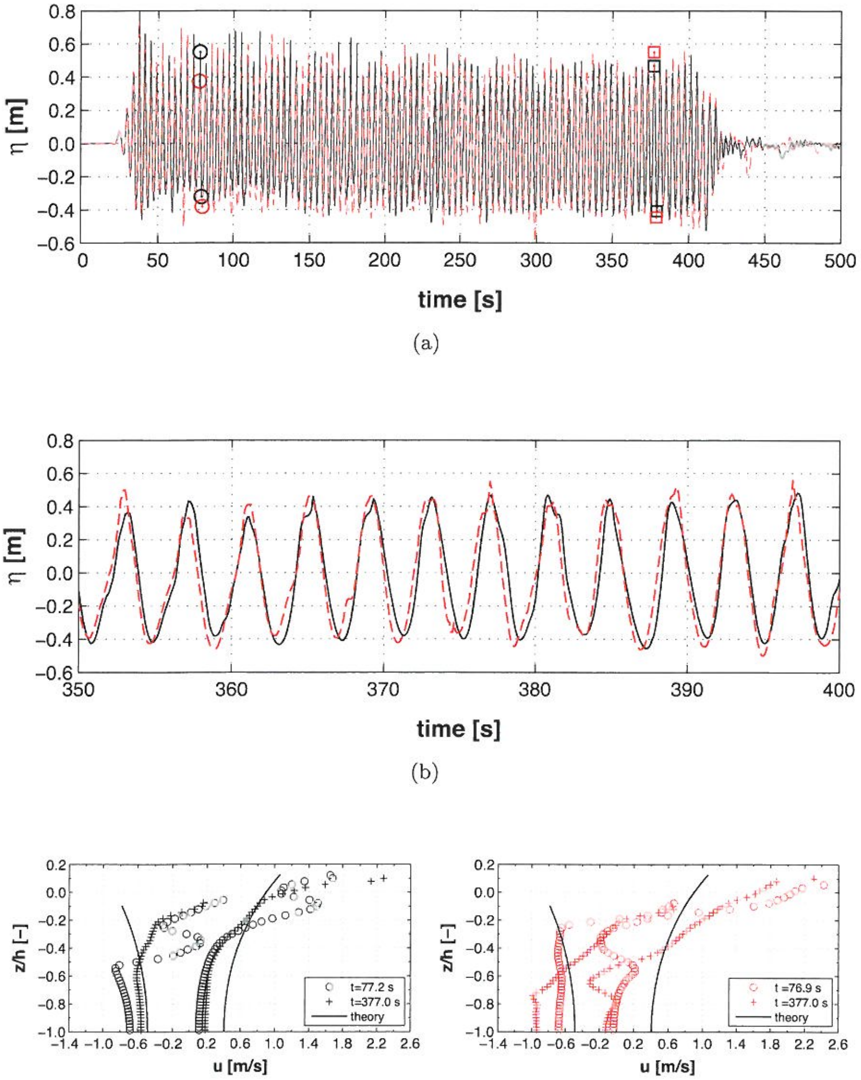

(a)

(b)

(c) DTMAX=0.015 s

(d) DTMAX=0.005 s

Figure 6.23: Impact of *dt* on surface elevations and horizontal velocities, shown at $x = x_1$. Surface elevations in panel (a) and (b) shown for DTMAX=0.015 s (black solid) and DTMAX=0.005 s (red dashed). Velocity profiles corresponding with the start and end of the wave train for (c) DTMAX=0.015 s and (d) DTMAX=0.005 s. Simulations case 2 with dx=0.1 m, IORDER=3, AUTOT=2, EPSI= $1 * 10^{-3}$.

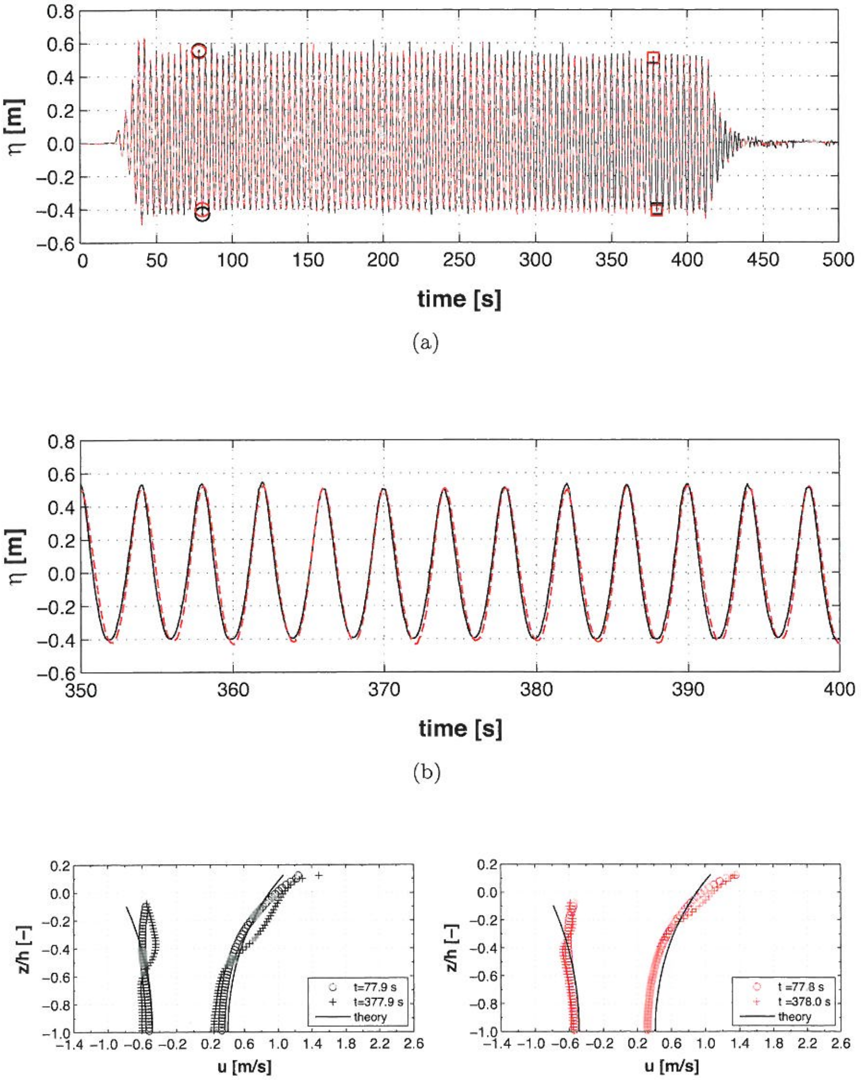

(a)

(b)

(c) ny=2

(d) ny=4

Figure 6.24: Impact of ny on surface elevations and horizontal velocities, shown at $x = x_1$. Surface elevations in panel (a) and (b) shown for ny=2 (black solid) and ny=4 (red dashed). Velocity profiles corresponding with the start and end of the wave train for (c) ny=2 and (d) ny=4. Simulations case 2 with dx=0.1 m, IORDER=1, AUTOT=2, ALPHA=1, DTMAX=0.015 s, EPSI= $1 * 10^{-3}$.

6.4.6 Conclusions

Testing the stability in time of long-duration wave tests with the first-order upwind momentum advection shows a considerable decrease of wave height and nonphysical drift in fluid velocities, when a considerable decrease of time step size occurs, below the stability limits specified in section 5.4.6. A plausible reason for this deficiency is lacking, and simulations with multiple grid cells in the cross direction suggest that mere numerical diffusion is unlikely to be a cause, since the drift is not observed in those cases.

Tests with the second-order scheme do not exhibit the instabilities observed with the first-order upwind scheme. Generally, excellent stability of surface elevations and velocity profiles is obtained, except for the occurrence of spurious velocities near the free surface. The second-order monotonicity-preserving momentum advection scheme yields the poorest results of all three schemes, showing large instabilities in both surface elevation and fluid velocity.

6.5 Validation : active wave absorption

6.5.1 Test setup

The operation of the piston wavemaker was tested in the previous section for sheer wave propagation, i.e. without compensation for reflected waves. In this section, the performance of the active wave absorption system is tested by operating the piston in pure absorption mode. This corresponds to a case where one would expect maximum (100%) reflection from a structure placed within the wave flume.

A piston wavemaker is positioned near the right boundary of the computational domain, with initial position of the left piston face at $x = x_0$, as depicted in Fig. 6.26. The first tree test cases in section 6.3 are used. Case 4 is not modeled, since the spatial variability of velocity profiles due to harmonic generation complicates the proper evaluation of the absorption performance. The piston near the right boundary is a purely generating piston, without active wave absorption. The input control velocity for the generating piston is denoted by $u_{ref,2}$.

Near the left boundary, a piston working in absorbing mode generates the wave that absorbs the incident wave. The initial position of the right face of the absorbing piston equals to $x = x_L$. The piston velocity $u^*_{ref,1}$ is calculated from the superposition of the filtered velocity signals at location $(x_1,\ z_1)$. The parameters defining the FIR filters are given in Table 6.11. By due selection of the filter duration, care is taken that the discrete filter frequencies coincide with the ground frequency of the generated wave train (i.e. 0.25 and 0.125 Hz). Tests are carried out with different piston sample frequencies f_s. The filter frequency f_{sf} is always taken equal to f_s by adjusting the number of filter coefficients.

The length of the wave flume between both pistons is taken as approximately 5 wavelengths, specified in Table 6.12. With the given flume length, the time for the waves to reach the absorbing piston is approximately 20 s for cases 1 and 2, compared to 40 s in case 3. Given the filter duration of 40 s, this implies that the filter is not yet fully operational when the waves reach the piston in cases 1 and 2. However, the test results show that this has no significant effect on the performance of the absorbing piston.

Other numerical parameters defining the model setup are adopted from the basic test setup defined in section 6.3.2. One important exception concerns the specification of the maximum allowable time step size DTMAX. In the case of simple wave generation, no restrictions to DTMAX were needed. When using the active wave absorption this no longer holds, since it is necessary to employ a maximum value of DTMAX equal to the piston time step size $dt_p = f_{sf}^{-1}$. This is due to the fact that the execution of the filter convolution is required at regular times steps f_{sf}^{-1}, which is not guaranteed when dt exceeds $dt_p = f_{sf}^{-1}$. Tests show that the computation becomes unstable when dt exceeds dt_p, leading to excessive fluid motion or even the abortion of the simulation due to a continued time step reduction caused by the piston motion.

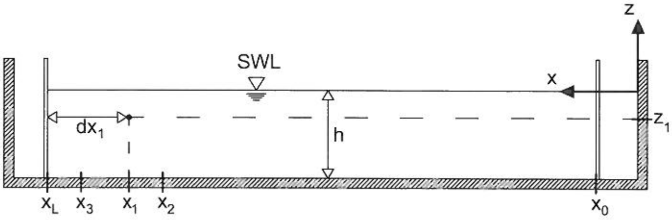

Figure 6.26: Set up of the computational domain for test with absorbing piston.

Table 6.11: Absorbing-piston test: specifications of filter design.

	dx_1 [m]	z_1 [m]	T_{0f} [s]	f_{LC}[Hz]	f_{HC} [Hz]
case 1,2	30	-1.8	40	0.10	0.75
case 3,4	65	-1.8	40	0.045	0.375

The performance of the absorbing piston is verified in 2 ways. The first method computes the amount of wave reflection in front of the piston, which should tend to zero when the left piston is perfectly absorbing the

Table 6.12: Absorbing piston test: specifications of computational domain.

	L[m]	x_0 [m]	x_L[m]	x_1 [m]	x_2 [m]	x_3 [m]
case 1,2	21.58	1.6	109.6	79.6	77.44	82.84
case 3,4	50.62	2.0	255.2	190.2	185.14	197.79

incident waves. The reflection coefficient $CR(f)$ is computed with the 3-gauge-method of Mansard and Funke (1980). Wave gauges locations x_i ($i = 1..3$) are indicated in Table 6.12.

In a second method, the error associated with the absorption of the incident waves is computed as:

$$\epsilon_{abs} = \frac{\overline{u}_{ref,2} - \overline{u}^*_{ref,1}}{\overline{u}_{ref,2}} \tag{6.19}$$

where $\overline{u}^*_{ref,1}$ and $\overline{u}_{ref,2}$ are the mean amplitudes of the control velocities of the left and right piston, respectively. Under perfect absorption, the corrected signal $\overline{u}^*_{ref,1}$ equals the input control signal $\overline{u}_{ref,2}$, and ϵ_{abs} reduces to zero.

6.5.2 Case 1

Simulations are performed with different cell size dx, piston time step dt_p and maximum time step DTMAX, summarized in Table 6.13. The results in Table 6.13 show that satisfactory absorption of the incident waves (e.g. $CR(f)<10\%$ or $|\epsilon_{abs}| < 0.05$) can be achieved already with the largest cell size dx=0.4 m, in case an appropriate piston time step is selected (dt_p=0.025 s). Very little difference is observed between cell sizes 0.1 and 0.05 m. The solution shown in Fig. 6.27 for dx=0.05 m demonstrates that waves are perfectly absorbed by the piston.

As it is noticed in the results in Table 6.13, the choice of dt_p and DTMAX can have a considerable impact on the performance of the absorbing piston. The simulations of progressive waves in section 6.3.3 already showed that reducing dt relatively far below the stability limit size can lead to a drift in the velocity profile when using the first-order upwind scheme. The restriction DTMAX=dt_p may have a similar effect. The incipient value of dt_p causing the drift will depend on the cell size dx. In Table 6.13, it is indicated whether or not the reduction of dt leads to a drift in the velocity profile. Except for the largest cell size $dx = 0.4$ m, this explains why reducing dt_p below a certain limit does not improve the absorption performance.

In addition to the value of dt_p, the specification of DTMAX can have a considerable impact on the obtained wave height, provided that the value is larger than the critical value which leads to a drift in the velocity profile. In the tests, DTMAX was reduced to half the piston time step size dt_p, leading to a significant increase in $H_{m,inc}$ and a reduction of reflection for cell sizes dx 0.1 and 0.05 m. It is noticed that a smaller time step size yields an improved accuracy of the modeled phase, which can explain the improved absorption performance in those cases.

Table 6.13: Performance of the absorbing piston, for test case 1.

dx [m]	dt_p [s]	DTMAX/dt_p	dt [s]	$CR(f)$ [-]	$H_{m,inc}$ [m]	ϵ_{abs} [-]	drift?
0.4	0.10	1	0.09 - 0.10	0.28	0.224	+0.11	y
0.4	0.10	1/2	0.05	0.09	0.238	+0.09	n
0.4	0.05	1	0.05	0.11	0.238	+0.05	n
0.4	0.05	1/2	0.025	0.10	0.239	+0.00	n
0.4	0.025	1	0.025	0.08	0.242	+0.02	n
0.4	0.025	1/2	0.0125	0.08	0.241	+0.01	n
0.2	0.10	1	0.08 - 0.10	0.14	0.249	+0.06	n
0.2	0.10	1/2	0.05	0.11	0.250	-0.02	n
0.2	0.05	1	0.05	0.04	0.247	+0.01	n
0.2	0.05	1/2	0.025	0.12	0.257	-0.05	y
0.2	0.025	1	0.025	0.08	0.250	+0.01	y
0.2	0.025	1/2	0.0125	0.13	0.255	-0.02	y
0.1	0.10	1	0.03 - 0.07	0.12	0.231	-0.01	n
0.1	0.10	1/2	0.025	0.08	0.252	-0.02	n
0.1	0.05	1	0.05	0.05	0.241	+0.06	n
0.1	0.05	1/2	0.025	0.03	0.248	+0.00	n
0.1	0.025	1	0.025	0.08	0.234	+0.06	n
0.1	0.025	1/2	0.0125	0.13	0.249	+0.01	y
0.05	0.10	1/2	0.020 - 0.05	0.07	0.229	+0.03	n
0.05	0.05	1	0.025 - 0.05	0.06	0.229	+0.03	n
0.05	**0.05**	**1/2**	**0.025**	**0.02**	**0.247**	**-0.02**	**n**
0.05	0.025	1	0.023 - 0.025	0.13	0.221	+0.10	n
0.05	0.025	1/2	0.0125	0.07	0.237	+0.02	n
0.05	0.01	1	0.01	0.18	0.217	+0.11	y
0.05	0.01	1/2	0.005	0.08	0.248	+0.02	y

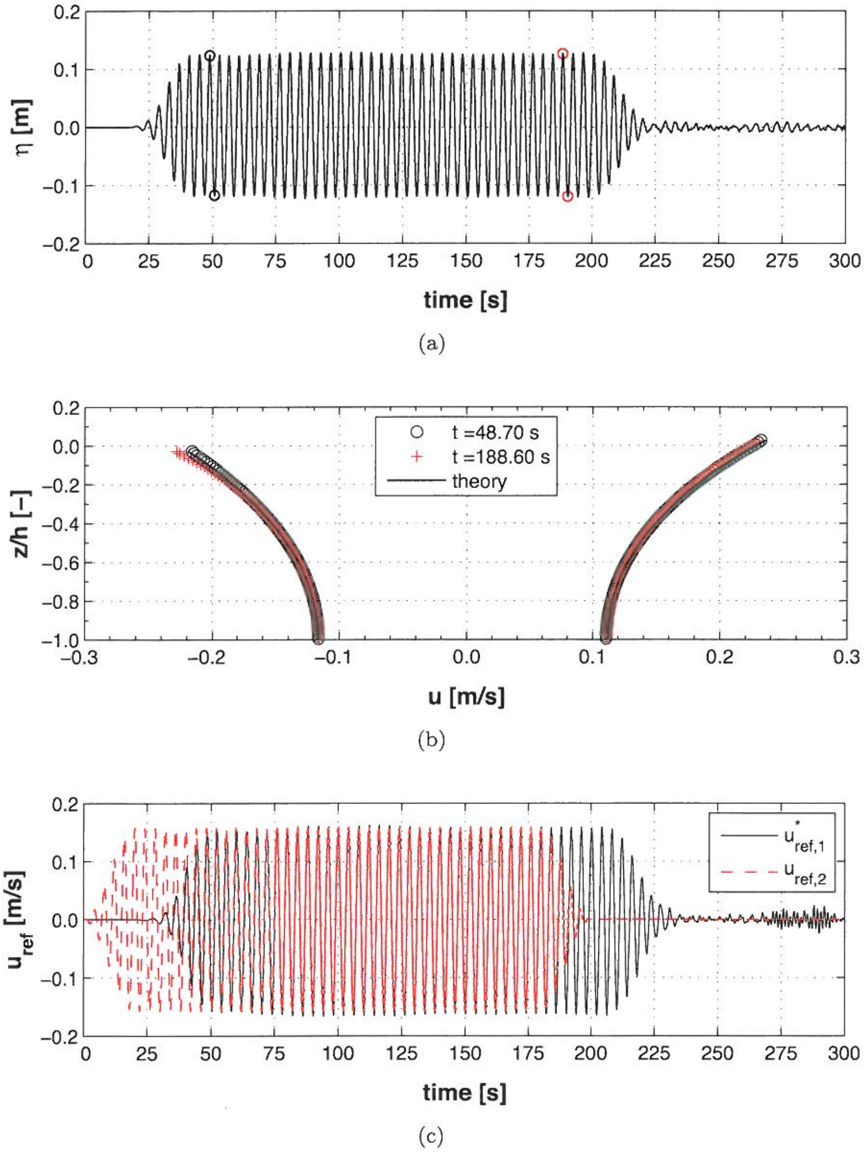

Figure 6.27: Performance of the absorbing piston: (a) time series of surface elevation at $x = x_1$; (b) profile of $u(z)$ at $x = x_1$; and (c) time series of piston control velocities. Simulation case 1 with $dx = 0.05$ m, $dt_p = 0.05$ s and DTMAX$=dt_p/2$.

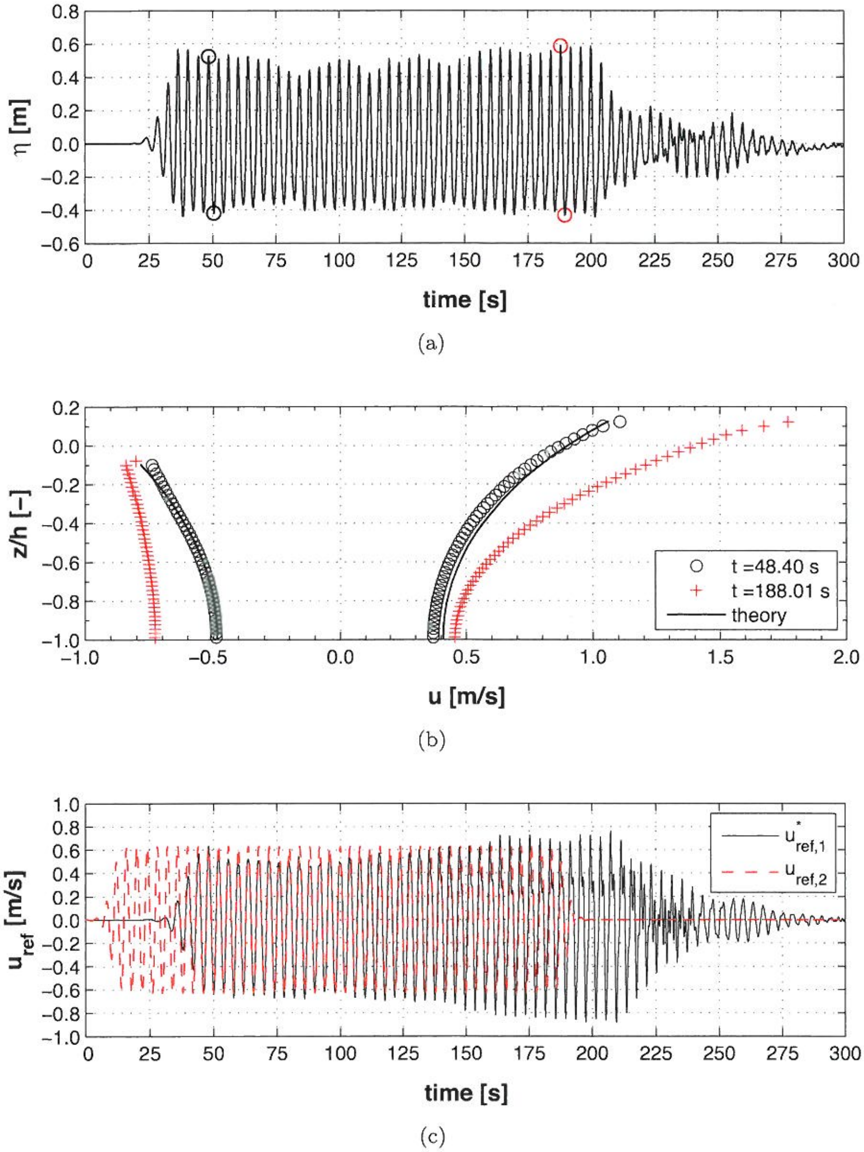

Figure 6.28: Performance of the absorbing piston: (a) time series of surface elevation at $x = x_1$; (b) profile of $u(z)$ at $x = x_1$; and (c) time series of piston control velocities. Simulation case 2 with $dx = 0.10$ m, $dt_p = 0.025$ s and DTMAX$=dt_p$.

6.5.3 Case 2

Table 6.14 shows the simulation results obtained with different values of dx, dt_p and DTMAX. As can be expected, the performance of the absorption piston deteriorates with increasing wave nonlinearity. In optimum conditions, the reflection by the piston can be reduced to approximately 0.20, which is significantly higher than in case 1. An optimal solution is shown in Fig. 6.28. In the time series of surface elevation in Fig. 6.28 (a), the various re-reflections at the generating piston are visible. The stability of surface elevations and velocity profiles in time is not as good as in case 1, but the piston is capable of preventing the simulation to become fully instable due to repeated (re)reflection. Again, it is noticed that selecting a proper value for dt_p and DTMAX can improve the absorbing performance, as long as the occurrence of a drift in fluid velocities is avoided.

Table 6.14: Performance of the absorbing piston, for test case 2.

dx [m]	dt_p [s]	DTMAX/dt_p	dt [s]	$CR(f)$ [-]	$H_{m,inc}$ [m]	ϵ_{abs} [-]	drift?
0.2	0.10	1/2	0.028 - 0.050	0.28	1.043	-0.05	n
0.2	0.05	1	0.015 - 0.050	0.26	1.038	-0.08	n
0.2	0.05	1/2	0.025	0.37	1.049	-0.10	y
0.2	0.025	1	0.015-0.025	0.37	1.038	-0.07	y
0.1	0.10	1/2	0.015 - 0.050	0.30	1.064	-0.11	n
0.1	0.10	1/4	0.015 - 0.025	0.27	1.061	-0.12	n
0.1	0.05	1	0.008 - 0.050	0.32	1.037	-0.10	n
0.1	0.05	1/2	0.012 - 0.025	0.24	1.033	-0.09	n
0.1	**0.025**	**1**	**0.009 - 0.025**	**0.20**	**1.036**	**-0.02**	**n**
0.1	0.025	1/2	0.010 - 0.0125	0.33	1.090	-0.15	y
0.05	0.10	1	0.008 - 0.036	0.24	1.136	+0.01	n
0.05	0.05	1	0.006 - 0.036	0.24	1.072	-0.12	n
0.05	0.025	1	0.005 - 0.025	0.17	1.065	-0.07	n
0.05	0.025	1/2	0.008 - 0.0125	0.17	1.066	-0.05	n
0.05	0.010	1	0.008 - 0.010	0.17	1.053	-0.08	n
0.05	0.010	1/2	0.004 - 0.005	0.31	1.098	-0.15	y

6.5.4 Case 3

Table 6.15 shows the simulation results obtained with different values of dx, dt_p and DTMAX. In optimum conditions, the obtained wave reflection varies between 0.15-0.20, which is considerably larger than in case 1. An optimal solution is shown in Fig. 6.29. As in case 1 and 2, reducing DTMAX improves the absorbing performance in most cases, as long as the occurrence of a drift in the velocity profile is avoided.

Table 6.15: Performance of the absorbing piston, for test case 3.

dx [m]	dt_p [s]	DTMAX/dt_p	dt [s]	$CR(f)$ [-]	$H_{m,inc}$ [m]	ϵ_{abs} [-]	drift?
0.4	0.10	1	0.10	0.16	0.258	-0.00	n
0.4	0.10	1/2	0.05	0.15	0.261	-0.02	n
0.4	0.05	1	0.05	0.15	0.263	-0.01	n
0.4	0.05	1/2	0.025	0.15	0.263	-0.01	n
0.4	0.025	1	0.025	0.15	0.262	-0.01	n
0.4	0.025	1/2	0.0125	0.14	0.265	-0.02	n
0.2	0.10	1	0.081-0.10	0.16	0.261	+0.00	n
0.2	0.10	1/2	0.05	0.15	0.260	+0.01	n
0.2	0.05	1	0.05	0.19	0.234	+0.10	n
0.2	0.05	1/2	0.025	0.18	0.243	+0.07	y
0.1	0.10	1	0.045 - 0.071	0.16	0.253	+0.05	n
0.1	0.10	1/2	0.047 - 0.05	0.17	0.260	+0.02	n
0.1	0.05	1	0.043 - 0.05	0.22	0.224	+0.13	n
0.1	0.05	1/2	0.025	0.20	0.233	+0.11	n
0.1	0.025	1	0.024 - 0.025	0.27	0.200	+0.21	n
0.1	0.025	1/2	0.0125	0.20	0.240	+0.08	y
0.05	0.10	1	0.023 - 0.051	0.17	0.240	+0.09	n
0.05	**0.10**	**1/4**	**0.022 - 0.025**	**0.19**	**0.250**	**+0.05**	**n**
0.05	0.05	1	0.024 - 0.05	0.22	0.215	+0.19	n
0.05	0.05	1/2	0.025	0.22	0.211	+0.19	n
0.05	0.025	1	0.025	0.33	0.182	+0.26	n
0.05	0.025	1/2	0.0125	0.31	0.192	+0.23	n

6.5.5 Optimal time step control

As in the case of purely progressive waves, $dt_p = f_{sf}^{-1}$ should be selected in accordance with the mesh resolution. An important difference however concerns the specification of DTMAX, which has to be limited to dt_p. The previous test cases lead to the following considerations that should be taken into account when specifying dt_p and DTMAX:

1. A maximum piston time step size dt_p in order to limit the difference between dt_p and dt set by the automatic time step control. This avoids the piston control velocities to look like a 'step' signal;

2. A minimum dt_p because of the occurrence of drift of the fluid velocities near the free surface;

3. The stability of velocity profiles and absorption performance improves when the ratio of dt to dt_p decreases. This can be achieved by reducing $dtmax$, however not below the limit which would generate the occurrence of a drift in the velocity profile.

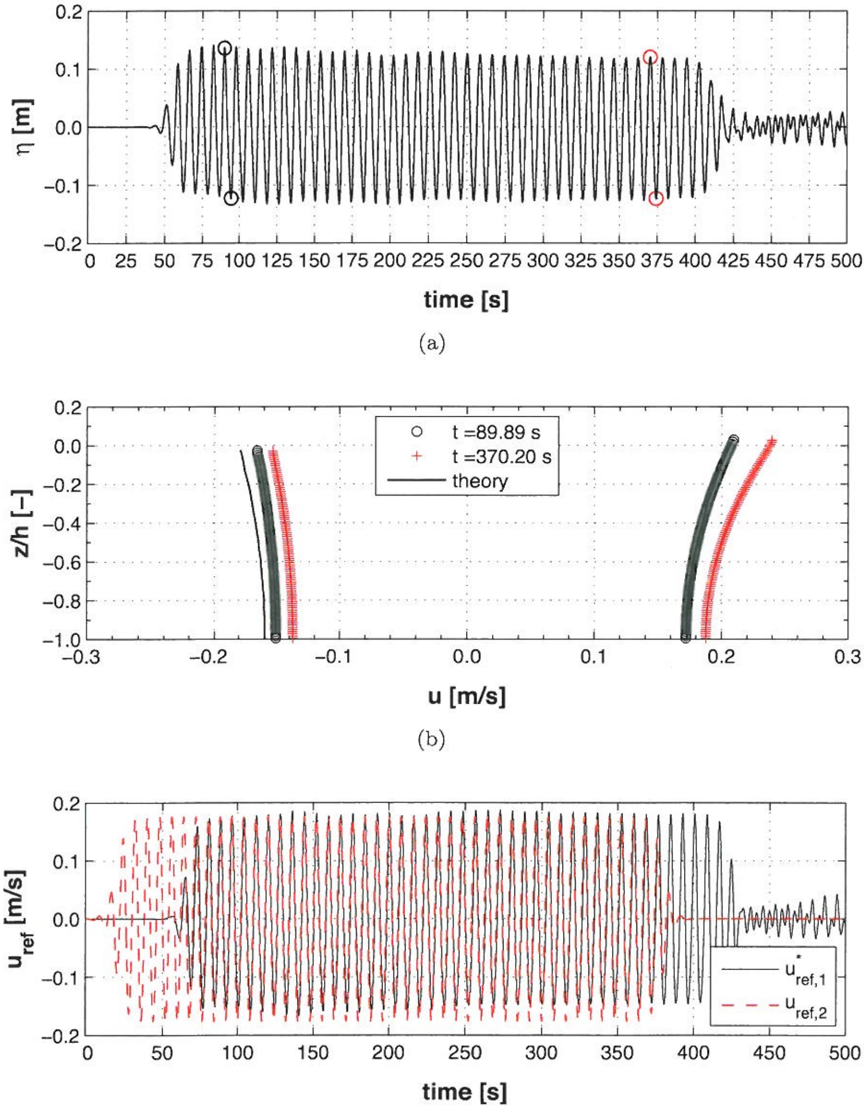

(a)

(b)

(c)

Figure 6.29: Performance of the absorbing piston: (a) time series of surface elevation at $x = x_1$; (b) profile of $u(z)$ at $x = x_1$; and (c) time series of piston control velocities. Simulation case 3 with $dx = 0.05$ m, $dt_p = 0.10$ s and DTMAX=$dt_p/4$.

6.6 Conclusions

A first-order piston wavemaker with active wave absorption has been implemented in FLOW-3D, using the GMO model to represent the piston motion. The operation of the piston has been tested based on a selected number of wave conditions, with varying wave nonlinearity. A basic grid convergence study with purely progressive waves shows that a stable and accurate wave generation and propagation can be achieved with the first-order upwind momentum advection (IORDER=1, ALPHA=1). The accuracy of the solution may vary significantly with changing time step control and specification of the piston time step dt_p. Guidelines to select these numerical parameters are included in section 6.3.

Additional tests with long-duration test series were performed to verify the stability of the generated wave train in time. The first-order upwind scheme proves to be stable, provided the time step size is not reduced below the lower stability limit set by the automatic time step control (AUTOT=1/2). This might be an issue when modeling wave-structure interaction, where a reduction of dt cannot be avoided. A satisfactory explanation for this erroneous behavior is lacking to date. Results obtained with an increased number of grid cells in the cross-direction do not show the deviations associated with the time step reduction. This is an indication that the cause needs to be sought in the numerical implementation. Tests with the second-order scheme do not exhibit the instabilities observed with the first-order upwind scheme.

Finally, the implementation of a linear active wave absorption system has been validated by means of a piston wavemaker in pure absorption mode, for short and long waves with varying wave height. Results show excellent absorption capacity for low-amplitude waves and lower, but still acceptable, performance with larger wave heights. Notwithstanding the active absorption being bound by the limitations of the linear wave absorption system, it seems that its performance is as least as high as in a physical wave flume.

7 Validation with GWK tests

7.1 Introduction

In Chapter 4, large-scale GWK experiments were used to study the wave interaction with a typical breakwater section on an experimental basis. Naturally, the same experiments provide an excellent dataset to validate numerical simulations of wave-induced porous flow, since they contain a large amount of high-precision wave and pressure measurements, a detailed calibration of the porous media properties and a broad variation in wave conditions.

In the following study, the wave interaction with the GWK breakwater model is simulated numerically. After verifying the convergence of the numerical solution, different aspects of the wave-structure interaction are investigated and validated, with the focus on wave-induced porous flow. Hereto, a limited set of wave conditions is selected, in such way that practically the whole range of experimental wave conditions is covered.

7.2 Objectives

The experimental research performed by Muttray (2000) in the GWK flume focuses on a multitude of hydraulic processes taking place in different sections of the breakwater model, summarized in Table 7.1. Not all the hydraulic processes listed in Table 7.1 will be analyzed in detail in the present validation study. A few key processes are selected, which allow to validate the interaction of the waves with the permeable structure. The objectives of the validation study are summarized below:

- verification of the incident wave field in the numerical wave flume, paying special attention to the reflection generated by the breakwater and the formation of a partially-standing wave field in front of the breakwater;
- verification of the wave transmission and evolution of MWL across the breakwater section;

- verification of the spatial distribution of pore pressure height $P(x, z)$ across the breakwater section.

Table 7.1: Sections of the breakwater model with respective hydraulic processes (after Muttray, 2000).

breakwater section	**hydraulic processes**
foreshore	local wave height in the near field (affected by wave reflection and shoaling)
on the seaward slope	wave motion on the slope (wave run-up, water surface elevations and pressure distribution)
under the seaward slope of the breakwater	interaction between external and internal flow: • wave run-up on different breakwater layers • water surface gradients and internal wave braking • pressure distribution and gradients • air entrainment
breakwater core	wave propagation inside the core (wave decay and pressure distribution)
harbour	wave transmission and total wave energy dissipation

7.3 Numerical model setup

7.3.1 Test wave conditions

The full range of GWK test wave conditions is included in Chapter 3. The tests include both regular and irregular waves, limited to nonbreaking and non-overtopping conditions. In the underlying validation study, only regular waves are generated. A wave-by-wave reproduction of irregular wave tests is not possible, since time series of GWK piston motions are not available. As a result, the stochastic nature in wave-structure interaction associated with random waves cannot be included in this validation study. Nonetheless, the experimental results with regular waves still enable a detailed validation of the performance of the numerical model.

A limited number of test conditions is selected, in such way that the total range of wave conditions is covered. It concerns a combination of two different wave heights with two different periods, representing relatively short and long waves. Details on the wave conditions are included in Table 7.2.

Table 7.2: Test wave conditions.

case	test ID GWK	h [m]^1	T [s]	H_0 [m]^2	L [m]^{1,3}	kh [-]^{1,3}
1	310594-01	2.505	4.0	0.25	17.74	0.89
2	020694-03	2.495	4.0	1.00	17.71	0.89
3	010694-02	2.480	8.0	0.25	38.43	0.41
4	200694-02	2.520	8.0	1.00	38.72	0.41

[1] at toe of breakwater
[2] at wave piston
[3] obtained with linear wave theory

7.3.2 Wave flume setup and breakwater materials

The geometry of the numerical wave flume is an exact reproduction of its physical counterpart (see Fig. 3.1), including a horizontal bed in front of the wavemaker, a 1:50 foreshore continuing in a 2 m thick sand layer, on which the breakwater model is placed. At the back of the flume, an impermeable 1:6 slope represents the asphalt dike. The breakwater components are represented as (porous) obstacles, imported in the code by means of STL geometry files which are created from the original plans of GWK tests. Porous media properties of the different materials of the breakwater model are specified in Table 3.1. According to Muttray (2000), the hydraulic properties of the core material were analyzed in Delft Hydraulics by van Gent (1993). The properties of the filter material were derived from laboratory tests in the Leichtweiss Institute by Levsen (1998). No experimental data are available for the Accropode armour. Therefore, Muttray assumed the values of α_F and β_F obtained from a stationary flow test on the filter material to be equally valid. Ranges of Re number for GWK tests, included in Table 3.1, indicate that that the porous media flow in the breakwater core can be classified as fully turbulent, in all cases.

The sandy foreshore is modeled as a (rigid) porous obstacle with its respective resistance properties, although the simulations show that the effect on the wave propagation is seemingly inappreciable, due to the very low permeability of the sand.

Because of the formulation of the viscous stresses, which include fractional areas, all internal obstacles and mesh boundaries are represented as free-slip boundaries. Since it is impossible to apply a no-slip boundary at porous media boundaries, the effect of the surface roughness of the armour elements cannot be directly. Instead, the effect of a specific roughness length is accounted for by the viscous drag term in the porous media flow model.

Grids were generated with uniform square mesh cells, in all cases. An adapted mesh refinement (by using adjacent or nested mesh blocks) could lower the computational cost. Such a technique is however not undertaken in this study, since the use of mesh blocks will inevitably lead to interpolation errors. Using a single mesh block with uniform grid cell thus yields the highest *possible* accuracy. In the grid-convergence study, cell sizes dx between 0.40 and 0.05 m were used.

7.3.3 Wave piston control

The wave piston is modeled as 'dry back', with an initial position corresponding with the position in the GWK flume. The computational domain was extended with an additional space of 2.8 m at the back of the piston to allow its motion.

An optimal setup of the active absorption system has been defined in section 6.5. Table 6.11 contains the parameters which define the filter design, for both wave lengths used in the following tests. The piston wavemaker implemented in FLOW-3D does not possess a upper flap. In addition, the active wave absorption control system is not exactly the same as applied in the GWK wave flume. This can possible produce differences between the physical and numerical wave generation and will be verified in the following tests.

7.3.4 Instrumentation

Naturally, the positions of numerical wave gauges correspond exactly with their physical counterparts. Two sets of wave gauges are available for the analysis of the incident wave field: wave gauges FF1-4 in front of the foreshore slope (far-field) and gauges NF1-5 in front of the breakwater toe (near-field). Transmission gauges (TM1-9) are positioned in front of, inside and behind the breakwater model. 34 pressure gauges correspond with the pressure gauges in the physical model. More details on the position of the instrumentation equipment are provided in Chapter 3 and Appendix A. Pressures and surface elevations are recorded at 40 Hz, unless the numerical time step forces a lower sampling rate. All time series, both experimental and the numerical, were treated with a low pass frequency filter to remove possible noise in the signal.

7.3.5 Computational details

A complete list of computational details is given in Table 7.3. Default values were used for parameters not mentioned in this list. The most important settings include the options for the momentum advection scheme and turbulence.

Simulations with the first-order upwind scheme in Chapter 6 yielded optimal accuracy and stability in surface elevations and velocity profiles. Hence, the same advection scheme will be used again. Simulations are by default performed in 2D, i.e. with the number of cells in transversal direction ny equal to 1. Tests in 6.4 showed that the first-order momentum advection scheme can exceptionally produce unstable results (a drift in velocity profiles) when dt is reduced significantly. Moreover, the velocity drift was found to be connected with a large wave height (cases 2 and 4). To avoid instabilities in those cases, simulations with the first-order upwind scheme are preformed with ny=2.

It can be expected that the simulation of the wave propagation, including the transformation over the foreshore, will not include turbulence due to wave breaking. This is confirmed by Muttray (2000), who reported that instabilities and a light form of wave breaking only occurred for the steepest irregular waves crests. However, the surging waves running up and down the armour slope will certainly generate air entrainment and turbulent dissipation, as can be observed in Fig. A.4 in Appendix A. Preliminary tests with both two-parameter turbulence models included in the code showed an excessive, unphysical turbulent dissipation due to uncontrolled growth of the maximum turbulent dissipation length scale. Since it is difficult to obtain a physical basis for the maximum turbulent dissipation length when no pronounced wave breaking is present, turbulence will be discarded in this study. Since no pronounced wave breaking is expected, and due to the previous simplification, the fluid is modeled as a single phase flow. The consequences of the previous assumptions on the experimental validation will be further discussed when comparing experimental and numerical results in section 7.6. Density and viscosity of the fluid are taken as ρ=1000 kg/m^3 and μ=1.10^{-3} Ns/m^2, respectively.

The numerical time step dt is controlled automatically, based on stability limits. A maximum value $dt = f_s^{-1}$ is applied, due to the fact that the calculation of the filter convolution in the active absorption method is required at regular times steps f_s^{-1}, which is not fulfilled when dt exceeds this value. Since dt is reduced, the pressure convergence criterion is tightened to 0.001, unless the automatic criterion would yield a smaller value for EPSI (see 5.4.4).

Piston sample frequencies f_s are chosen (iteratively) in accordance with the numerical time step resulting from the simulation. Values of 10, 20, 40, 100 and 200 Hz are used, depending on the mesh resolution.

The heaviest computation, with a mesh of 1,650,000 elements, simulation duration of 900 s and dt $\approx$ 0.01 s, takes about 184 hours on a 12 core Intel®Xeon® X5660 2.8 GHz workstation, running *hydr3d* v10.0.3.5.

Table 7.3: FLOW-3D solver parameter settings.

Option	Setting	Parameter
fluid	incompressible	ICMPRS=0
viscosity	Newtonian fluid	IFVISC=1
turbulence	laminar calculation	IFVIS=0
pressure solver	GMRES	IGMRES=1
	convergence	EPSI=0.001
momentum advection	explicit	IMPADV=0
	first-order, upwind	IORDER=1, ALPHA=1
viscous stress	explicit	IMPADV=0
VOF advection	split Lagrangian method	IFVOF=6
F-packing	default	CFPK=1
time step control	automatic (stability)	AUTOT=2
maximum dt	f_s^{-1}	DTMAX

7.4 Incident wave field at breakwater toe

7.4.1 Methodology of analysis

The water depth between far-field and near-field gradually decreases. This has an impact on the kinematics of the progressing waves, manifesting in (i) a reduction in wave length and phase velocity, (ii) a decreasing difference between the wave group velocity (i.e. the velocity at which the wave energy is conveyed) and the wave celerity, (iii) a change in the vertical distribution of pressure and fluid velocities, and (iv) an increase in wave steepness. Additionally, a certain part of the wave energy is dissipated through bottom friction.

After undergoing a transformation on the foreshore, the waves are partially reflected on the breakwater slope. The superposition of the incident and reflected waves creates a partially standing wave field in the near-field of the breakwater, which gradually progresses in time toward the far-field. Nonlinear processes in the wave transformation over the foreshore and wave reflection on the breakwater slope lead to the generation of *secondary waves.* These waves are superposed on the incident and reflected primary waves and create fluctuations in wave field, both in time and space. They are the main source of uncertainty in the determination of the local incident wave field (Muttray, 2000).

In order to describe the hydraulic processes taking place inside and outside the breakwater, an accurate determination of the incident wave height in the near-field is indispensable. In his research, Muttray (2000) performed a reflection analysis in near-field and far-field, and estimated the uncertainty in the determination of the incident wave height $H_{m,inc}$ and reflection coefficient CR. To this purpose, different time windows are defined in the total duration of the wave test (approximately 100 waves), each associated with a specific hydraulic process. The time windows are presented in Table 7.4.

Table 7.4: Time windows and associated hydraulic processes.

Time window	Position in time series	Characteristic hydraulic process
TW1	first waves at foreshore toe	no influence of reflection
TW2	waves 1-10 at breakwater	minimal set-up in breakwater
TW3	first reflected waves at foreshore toe	limited influence of reflected secondary waves
TW4	waves 80-90 at breakwater	constant set-up in breakwater

Comparing the obtained wave height resulting from a reflection analysis in the far-field with the wave height obtained from a simple wave height analysis in TW1 (when no reflection is present) allows to estimate the error in the determination of wave height. Muttray reports an overall standard deviation of 4.4% for a reflection analysis in TW3, increasing to 6.8% in TW4. The larger error in TW4 can be explained by the increased presence of secondary waves, traveling back toward the far-field. A near-field reflection analysis inevitably includes the presence of secondary waves, hence a minimum average error of 6.8% should be taken into account.

Alternatively, the incident wave height in the near field can be computed by transforming the far-field wave height of purely progressing waves, obtained in TW1. Assuming that no reflection is generated by the mild slope (1:50) of the foreshore, the total wave transformation is then composed of shoaling and friction losses. Using a nonlinear shoaling theory (Shuto, 1974) and a theoretical approach for the friction losses (Iwagaki and Tsuchiya, 1966), a relative standard deviation between measured and calculated values of 3.9 % was obtained by Muttray (2000). This suggests that the accuracy of the reflection analysis in the near-field and far-field is comparable, altough it is assumed that the highest accuracy is obtained in the far-field analysis, when the disturbing effect of secondary waves is reduced by selecting a proper time window (TW3) .

Hereafter, a near-field reflection analysis is performed, separating the incident and reflected waves with the 3-gauge-method of Mansard and Funke (1980). The same cut-off frequencies reported by Muttray (2000) are used: $(2.1T)^{-1} \leq f \leq 3.1T^{-1}$. Multiple combinations of wave gauges fulfilling the geometric conditions are considered in the reflection analysis, and the resulting wave parameters are averaged over these combinations. The parameters included in the following discussion are the reflection coefficient $CR(f)$ obtained in frequency domain and the time-domain mean incident wave height $H_{m,inc}$.

In the study of the incident wave field, attention is paid to (i) the time-stability of surface elevations, resulting from a stable operation of the active absorption system, (ii) convergence in the numerical solution and (iii) validation of the incident wave field with experimental results.

7.4.2 Case 1

Time series of experimental and numerical levels of wave crests η_c and troughs η_t in the near-field are shown in Fig. 7.1. Numerical and experimental time series are synchronized at t=0, taking the first wave crest of the wave train in the considered gauge.

Tests with pure wave propagation in water depth h=4.5 m (section 6.3) showed a sufficient accuracy with cell size dx=0.4 m. The case with waves propagating over the foreshore and interacting with the breakwater clearly requires a higher mesh resolution, as can be noticed from the difference between simulations with dx=0.4 and 0.05 m in Fig. 7.1. Envelopes of surface elevation obtained with dx=0.4 m show a relatively large deviation from the experimental ones. Increasing the mesh resolution to dx=0.05 m clearly results in a better agreement between numerical and physical envelopes.

In this case of relatively short and small-amplitude waves, the reflection is limited and quickly stabilizes after a few incident waves. The long-term evolution of the numerical envelopes is similar to the experimental ones, showing that the active absorption is capable of maintaining the stability of the incident wave field in the numerical model.

Fig. 7.2 shows a close-up on surface elevations near the end of the wave train, after about 80 wave cycles. In this figure, wave crests have been synchronized in order to enhance the comparison between experimental and numerical results. A clear increase in surface elevation of wave crests is observed with increasing mesh resolution, due to numerical dissipation generated by the first-order upwind scheme. Tests show very little variation in surface elevations for cell sizes lower than 0.1 m. Spatial variations in surface elevations due to wave reflection are well reproduced by the numerical model, as shown by the comparison between wave gauges NF2 and NF3 in Fig. 7.2.

Fig. 7.3 shows the variation of the incident wave height and reflection coefficient with cell size dx, obtained with a near-field reflection analysis. Slight variations in $H_{m,inc}$ are noticed between time windows TW2 and TW4. Values of $H_{m,inc}$ increase with increasing mesh resolution, and do not level off yet at the highest mesh resolution (dx=0.05 m). In that case, the theoretical value of the target wave height H_0=0.25 m is reached. Further increasing the mesh resolution is not likely to yield a significant increase in wave height and is not tested. Numerical values of $H_{m,inc}$ obtained with the highest mesh resolution exceed the experimental values. The absence of

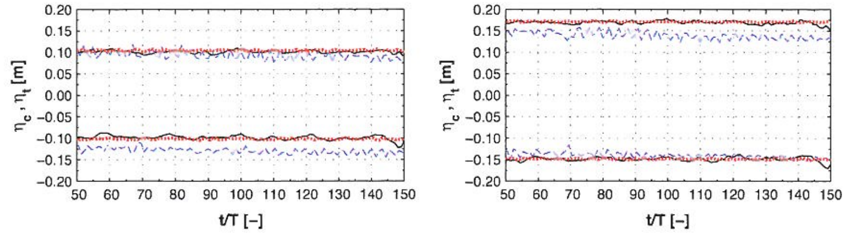

(a) NF2 (b) NF3

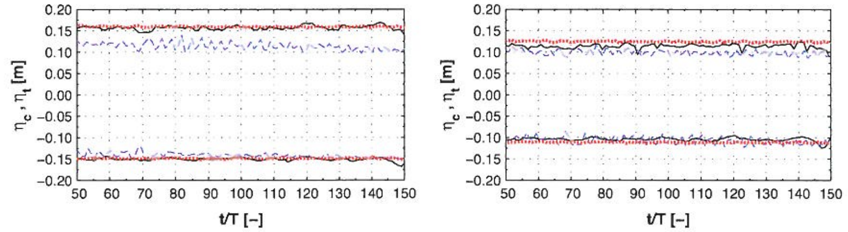

(c) NF4 (d) NF5

Figure 7.1: Near-field time series of wave crests η_c and troughs η_t, case 1. Comparison between experimental measurements (black solid) and numerical simulations: dx=0.40 m, f_s=10 Hz (blue dashed) and dx=0.05 m, f_s=40 Hz (red dotted).

wall and bottom friction in the numerical model, or a mechanical transfer loss associated with the physical wave generation are mentioned as possible factors for this difference. It is noticed that different values of piston time step size dt_p result in (very) small different values of $H_{m,inc}$. Generally, $H_{m,inc}$ increases with increasing f_s.

The reflection coefficient $CR(f)$ is defined as the ratio of the 0^{th}-order moment of the variance of reflected and incident spectral densities. Fig. 7.3(c,d) show very limited differences between the analysis in time windows TW2 and TW4, respectively. Values of $CR(f)$ increase with with increasing mesh resolution, in close agreement with the experimental value.

The influence of the piston time step size $dt_p = f_s^{-1}$ and realized time step size dt on the numerical phase velocity is further explored hereafter. To this purpose, the phase difference between the experimental and numerical wave crests is defined as:

$$\Delta\varphi_c = \varphi_{c,GWK} - \varphi_{c,num} \tag{7.1}$$

where φ_c is the phase at a wave crest. Subscripts 'GWK' and 'num' refer to the experimental and numerical results, respectively.

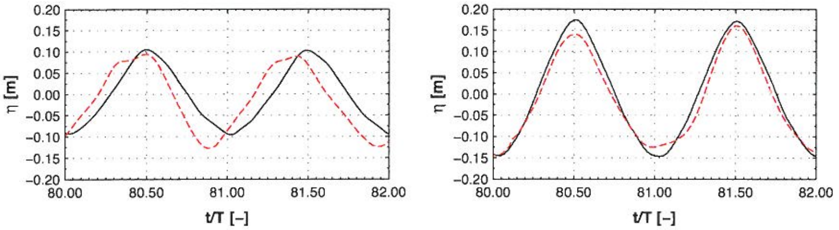

(a) NF2 (b) NF3

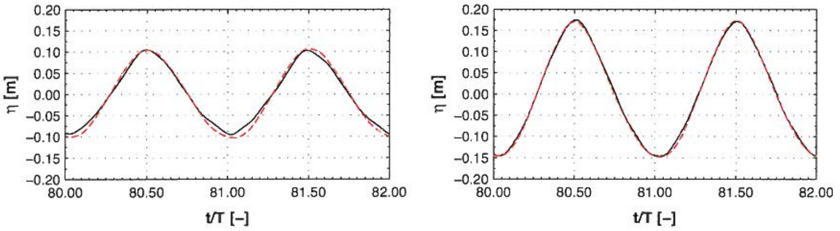

(c) NF2 (d) NF3

Figure 7.2: Detailed comparison of η in near-field near the end of the wave train, case 1. GWK measurements (solid) and numerical simulations (dashed) obtained with dx=0.40 m (a) & (b) and dx=0.05 m (c) & (d).

Fig. 7.4 shows the time evolution of phase difference in a location in the far-field (FF2) and near-field (NF1). In this graph, t=0 corresponds with the first wave crest in the experimental far-field gauge (FF2). Results are shown for two different values of f_s, with a mesh resolution of dx=0.05 m. A phase lag is observed for the numerical model. $\Delta\varphi_c$ steadily decreases at a rate of 0.15-0.25 % per wave cycle. Increasing the piston sample frequency causes smaller values of numerical time step dt, resulting in a slight reduction of phase lag.

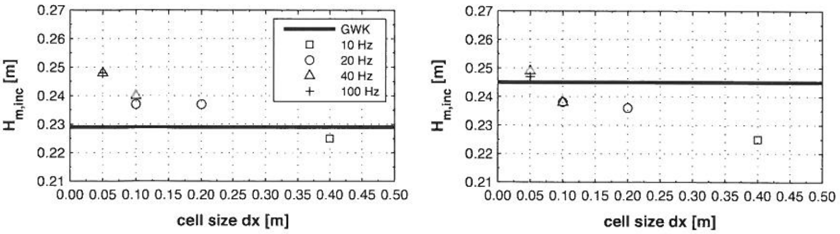

(a) TW2 (b) TW4

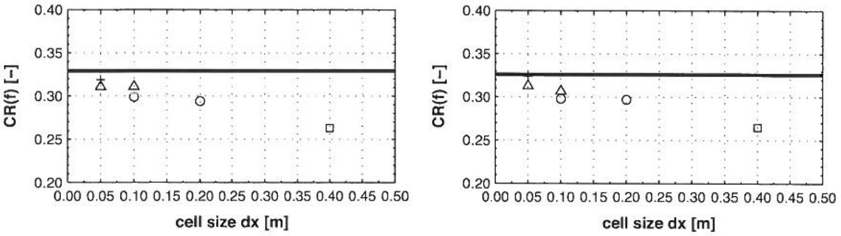

(c) TW2 (d) TW4

Figure 7.3: Variation of incident wave height $H_{m,inc}$ and reflection coefficient $CR(f)$ with cell size dx, resulting from a near-field reflection analysis in TW2 and TW4, case 1. Black solid lines indicate target GWK values.

7.4.3 Case 2

Fig. 7.5 shows the time series of experimental and numerical wave crests and troughs in 4 wave gauges in the near-field. Numerical values of η_c and η_t are found to be stable in time and similar to the experimental measurements, proving the performance of the active wave absorption. The partially standing wave field, created by wave reflection on the breakwater slope, is characterized by spatial variations in wave amplitude (η_c-η_t), which are well preserved in the numerical simulation.

Compared to case 1 however, the time evolution of wave crests and troughs is clearly marked by low-frequency variations, both in the experimental and numerical time series. As suggested by Muttray (2000), this could be attributed to a resonant behavior of the total water mass in the wave flume, with eigenfrequencies according to :

$$f_N = N\frac{\sqrt{gh_m}}{2l_{SWL}}\ ,\ N = 1, 2, 3, ... \tag{7.2}$$

where h_m is the averaged water depth in the wave flume, considering the

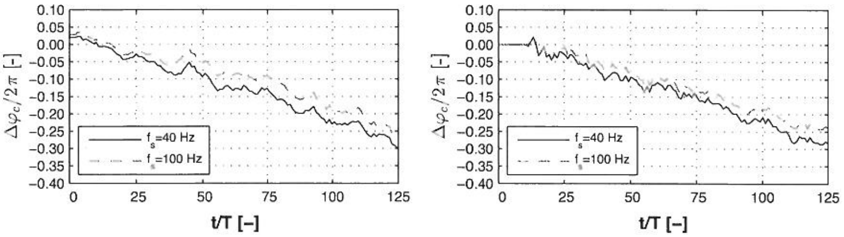

(a) FF2

(b) NF1

Figure 7.4: Evolution of phase difference $\Delta\varphi_c$ between experimental and numerical wave crests, measured in (a) far-field and (b) near-field, case 1. Numerical simulation with dx=0.05 m.

bed profile, and l_{SWL} the length of the water line along the SWL. With a distance l_{SWL} of 248 m between the piston and the breakwater, a water depth h=4.5 m and mean water depth h_m=4.10 m, eq. (7.2) yields an eigenperiod of 78 s (Muttray, 2000), in close agreement with a return period of approximately $20T$, clearly observed in Fig. 7.5(d).

Low-frequency oscillations are hard to absorb by the active absorption control. As long waves travel back and forth in the wave flume, they develop as a standing wave pattern and cause spatial modulations in wave height. This statement is supported by the differences observed in η_c and η_t between different locations in Fig. 7.5. In the far-field (Fig. 7.6) low-frequency variations are even more pronounced, probably due to the diminished influence of secondary nonlinear interactions.

As observed in Figs. 7.5 and 7.6, low-frequency variations exist in both numerical and physical tests, but show differences in amplitude and phase. A detailed comparison of η is given in Fig. 7.7, at an instant were numerical and experimental long waves are in phase. Clearly, the numerical model is shown to correctly represent the instantaneous η variation. In addition, the spatial variation in η between NF2 and NF3 shows that wave reflection is well represented by the numerical model.

Results of the near-field reflection analysis are shown in Fig. 7.8. The target incident wave height is well matched by the simulation with the largest mesh resolution, for the analysis in both time windows. Slightly lower values of $H_{m,inc}$ are observed in TW4 compared to TW2, in both the experiment and numerical simulations. Values of reflection coefficients $CR(f)$ shown in Fig. 7.8 (c,d) converge toward the experimental value in TW4.

The phase lag $\Delta\varphi_c$ in the far-field in Fig. 7.9(a) is approximately constant for the first 50 waves, followed by a steady decrease, similar to

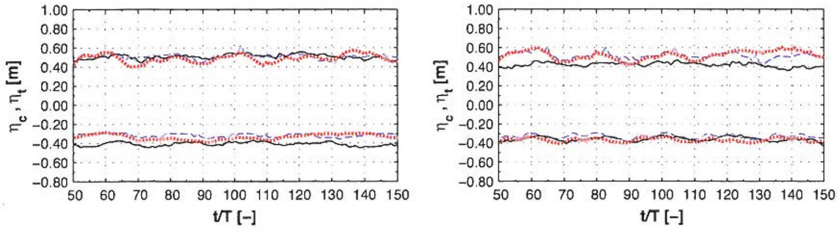

(a) NF1 (b) NF2

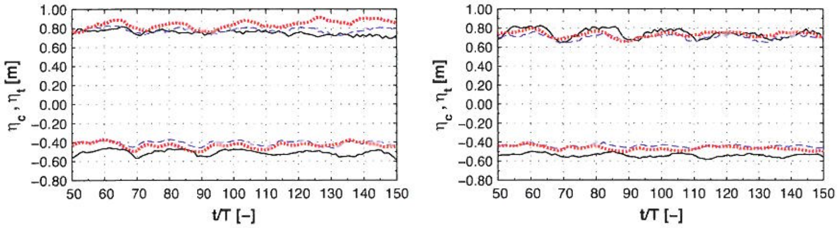

(c) NF3 (d) NF4

Figure 7.5: Near-field time series of wave crests η_c and troughs η_t, case 2. Comparison between experimental measurements (black solid) and numerical simulations: dx=0.20 m, f_s=40 Hz (blue dashed) and dx=0.05 m, f_s=100 Hz (red dotted).

case 1. In the near-field (Fig. 7.9(b)) a similar evolution is observed, but also clearly larger low-frequency oscillations in $\Delta\varphi_c$. The periodicity of the low-frequency variations resembles the one of surface elevations in Fig. 7.6. The cause for the long-term phase fluctuations is however unclear. The difference between near-field and far-field however suggest that nonlinear effects might play a role in this matter. The influence of the resulting numerical time step size on the phase difference, induced by f_s, is limited.

7.4.4 Case 3

Fig. 7.10 shows a comparison between experimental and numerical time series of wave crest and wave trough in the near-field. Levels of η_c clearly exceed experimental values, in all locations. In general, levels of η_t are in closer correspondence with the experimental measurements. The plausible factors explaining for the observed discrepancies in η_c levels in Fig. 7.10 include:

- a 'mechanical' transfer effect related to the operation of the wave paddle

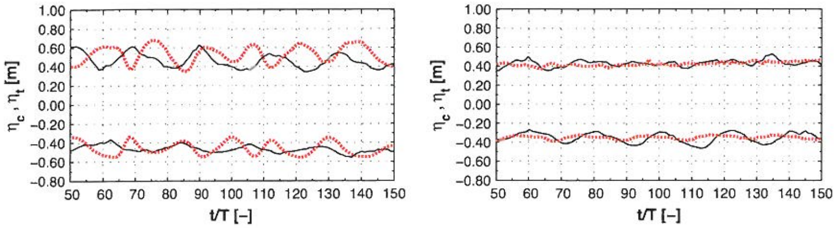

(a) FF1 (b) FF2

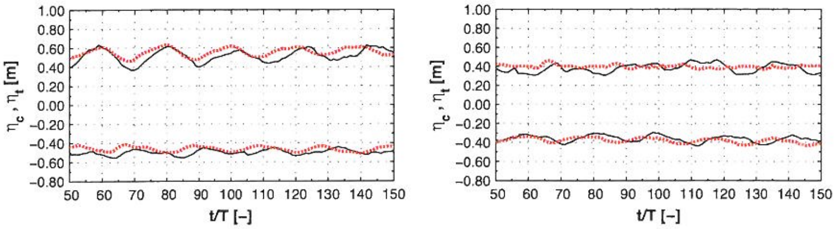

(c) FF3 (d) FF4

Figure 7.6: Far-field time series of wave crests η_c and troughs η_t, case 2. Comparison between experimental measurements (black solid) and numerical simulation dx=0.05 m, f_s=100 Hz (red dotted).

in the GWK flume;

- bottom and wall friction in the GWK flume, which is not included in the numerical model. The amount of friction however is assumed to be negligible, in agreement with the findings of Muttray (2000);
- differences in wave transformation (shoaling) over the foreshore;
- harmonic generation due to application of linear wave generation in nonlinear conditions. In the far-field, the effect is neglible (section 6.3), but can become significant in shallow water. The spatial variations due to harmonic generation affect the performance of the active absorption. It is difficult however, if not impossible, to determine the amount of harmonic generation in a partially standing wave field with a considerable spatial amplitude modulation;
- a difference in wave reflection due to deviations in the modeled structural response (run-up, inflow/outflow through the breakwater slope).

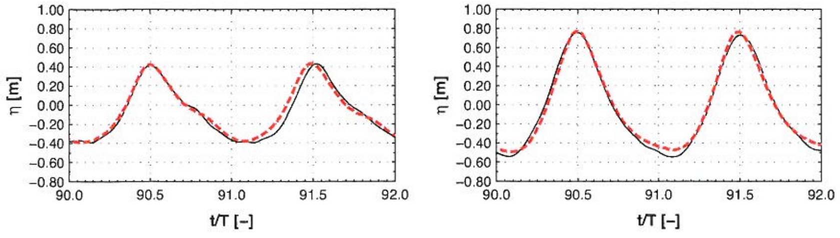

(a) NF2 (b) NF3

Figure 7.7: Detailed comparison of η in near-field, case 2. Comparison between experimental measurements (solid) and numerical simulation (dashed): dx=0.05 m, f_s=100 Hz.

Deviation in far-field

Possible effects related to the operation of the GWK wave paddle are verified by comparing progressive waves in the far-field (FF1-4). When considering a time window (TW1) in the start of the wave train, the influence of wave reflection is excluded. Moreover, the possible influence of harmonic generation is deemed inappreciable in the far-field, due to limited wave nonlinearity (H_0=0.25 m).

In Fig. 7.11, experimental crest and trough elevations are clearly below theoretical values. Numerical η_c and η_t levels are in better agreement with the theoretical value. The wave amplitude (η_c - η_t) is very similar. The discrepancy with the theory is likely caused by the operation of the GWK paddle itself. The empirical correction in the piston control (section 7.3.3) or other 'mechanical' effects, due to the specific construction of the piston paddle or drive, are mentioned as possible influences affecting the generated wave train. It is moreover likely that the mechanical behavior changes with relative water depth, since the observed deviation in Fig. 7.11 is absent in case 1 and 2.

Adjusting H_0

The difference between experimental and numerical levels of η_c and η_t, complicate a further detailed validation of the porous flow field within the structure. Regardless of the exact nature for the observed deviation, a practical 'ad hoc' solution is found in adjusting the piston control wave height H_0, which is used to compute the piston control velocities. By iteratively modifying H_0, the experimental η_c and η_t levels are matched as far as possible. This is justified, since in the further description of the porous flow field, relevant length scale parameters will be referenced with

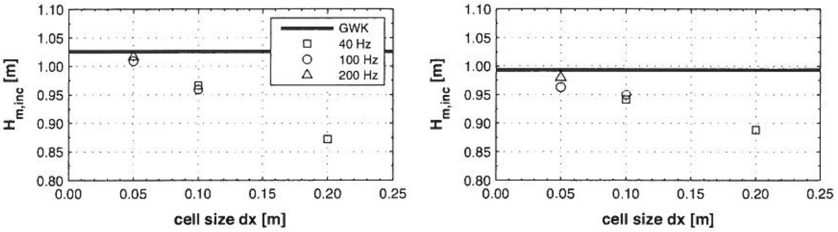

(a) TW2 (b) TW4

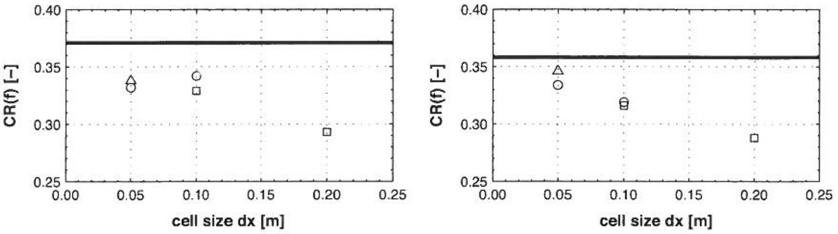

(c) TW2 (d) TW4

Figure 7.8: Variation of incident wave height $H_{m,inc}$ and reflection coefficient $CR(f)$ with cell size dx, resulting from a near-field reflection analysis in TW2 and TW4, case 2. Black solid lines indicate target GWK values.

the obtained incident wave height.

Fig. 7.12 shows the comparison with the experiments of numerical time series of η_c and η_t obtained with a value for H_0 of 0.20 and 0.25 m. The agreement between numerical and experimental wave crests clearly improves for H_0=0.20 m, in all shown positions in the near-field. Due to the smaller value of H_0, levels of η_t slightly increase.

Fig. 7.13 shows a close-up of the surface elevations at the end of the wave train. Relatively large spatial wave amplitude variations are observed between adjacent wave gauges, due to the increased wave reflection resulting from a smaller wave steepness. The wave profile in NF3 and NF4 is characterized by significant secondary wave crests. In general, the reflection pattern seems to be well conserved in the numerical model.

Fig. 7.14 shows the results of a near-field reflection analysis in TW2 and TW4. Little variation is observed between different mesh resolutions, showing that convergence has been achieved. Numerical values of $H_{m,inc}$ are clearly smaller than experimental values ($<$0.04 m), larger than what may be expected from the correspondence in Fig. 7.13. A much better agreement is observed for the reflection coefficient in Fig. 7.14(c,d).

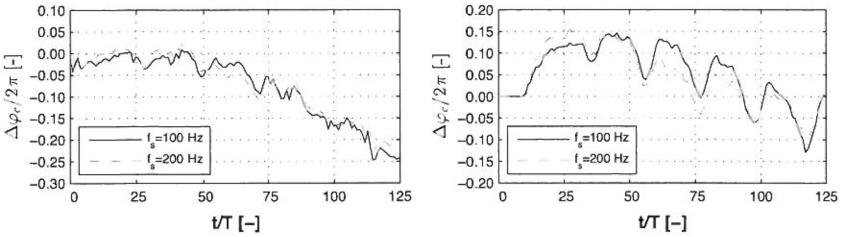

(a) FF2 (b) NF1

Figure 7.9: Evolution of phase difference $\Delta\varphi_c$ between experimental and numerical wave crests, measured in (a) far-field and (b) near-field, case 2. Numerical simulation with dx=0.05 m.

The results of the reflection analysis are further explored, since it is important to obtain an accurate value of $H_{m,inc}$ for further use. Fig. 7.15 therefore shows the amplitude a and phase φ components of the obtained incident wave spectrum, after separation with the 3-gauge method (in this case: NF1-3-5). Only the first two harmonics show a significant level of energy and generally compare well (Fig. 7.15(a)). In addition, the phase spectrum (Fig. 7.15(b)) compares relatively well, what is confirmed by the correspondence in wave amplitude variations between different locations in Fig. 7.13. It can be concluded that the results of the reflection analysis are reliable, in spite of the large difference in $H_{m,inc}$ in Fig. 7.14.

An alternative approach to obtain $H_{m,inc}$ consists of computing the incident wave height as the transformation of the wave height of purely progressive far-field waves, see section 7.4.1. Using the nonlinear shoaling method of Shuto (1974) and Goda (2000), values of $H_{m,inc}$ for different mesh resolutions are compared with the experimental values, shown in Fig. 7.16.

Table 7.5 contains a comparison between incident wave parameters obtained with both methods. The ratio between experimental and numerical wave height in frequency and time domain is consistent, showing that the mean incident wave height $H_{m,inc}$ resulting from the reflection analysis is a reliable measure for further use. The ratio between transformed wave height $H_{m,inc}^{shoal}$ is slightly larger. In the further analysis, the value of $H_{m,inc}$ obtained from the reflection analysis in TW4 will be employed.

The evolution of the phase lag $\Delta\varphi_c$ with time (Fig. 7.17) shows a consistent negatively increasing trend, similar in far-field and near-field. The growth rate of the phase error is comparable to the previous cases.

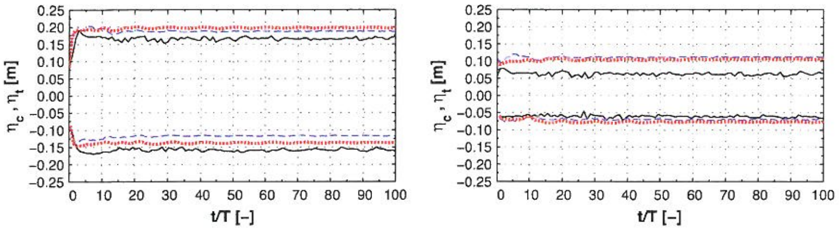

(a) NF1 (b) NF3

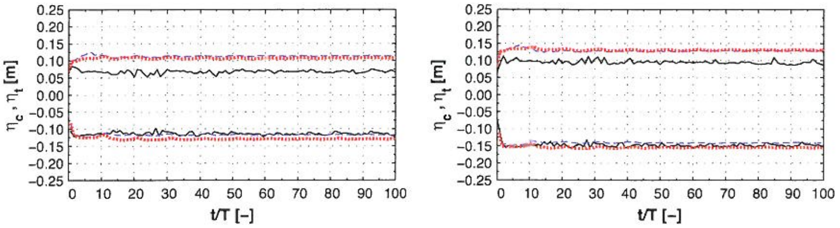

(c) NF4 (d) NF5

Figure 7.10: Near-field time series of wave crests η_c and troughs η_t, case 3. Comparison between experimental measurements (black solid) and numerical simulations: dx=0.40 m, f_s=10 Hz (blue dashed) and dx=0.05 m, f_s=100 Hz (red dotted).

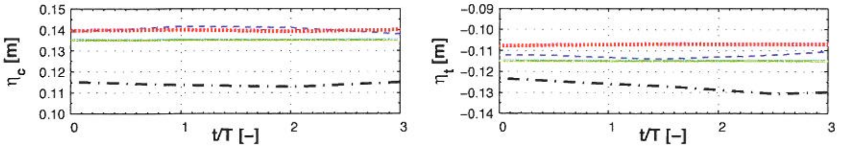

(a) FF1 (b) FF1

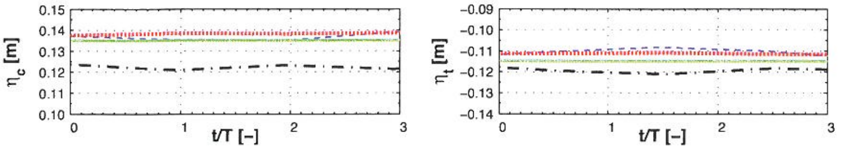

(c) FF4 (d) FF4

Figure 7.11: Time series of wave crests η_c and troughs η_t in far-field, TW1, case 3. Comparison between theoretical value (green solid), experimental measurements (black dash dot) and numerical simulations: dx=0.40 m, f_s=10 Hz (blue dashed) and dx=0.05 m, f_s=100 Hz (red dotted).

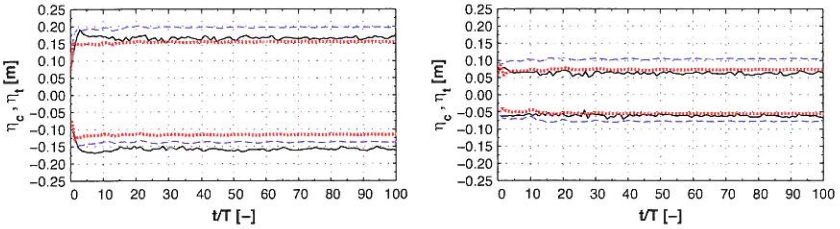

(a) NF1 (b) NF3

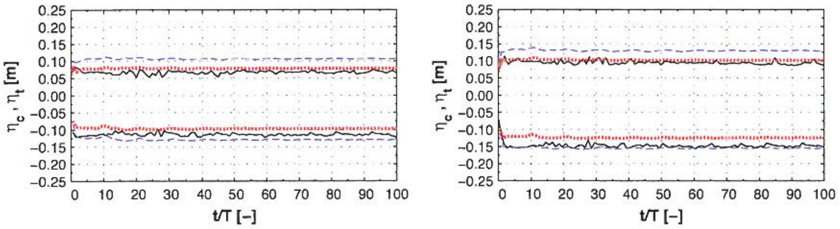

(c) NF4 (d) NF5

Figure 7.12: Near-field time series of wave crests η_c and troughs η_t, case 3. Comparison between experimental measurements (black solid) and numerical simulations: H_0=0.25 m (blue dashed) and H_0=0.20 m (red dotted). Both runs are with dx=0.05 m, f_s=100 Hz.

Table 7.5: Ratio of incident wave energy between experimental and numerical model, case 3.

	$H_{m0,inc}$ $[m]$[1]	$H_{m,inc}$ $[m]$[2]	$H_{m,inc}^{shoal}$ $[m]$[3]
GWK	0.372	0.269	0.248
num (dx=0.05 m)	0.314	0.228	0.203
GWK/num	1.19	1.18	1.22

[1] frequency domain analysis, TW4

[2] time domain analysis, TW4

[3] transformed $H_{m,inc}$ obtained in far-field, TW1

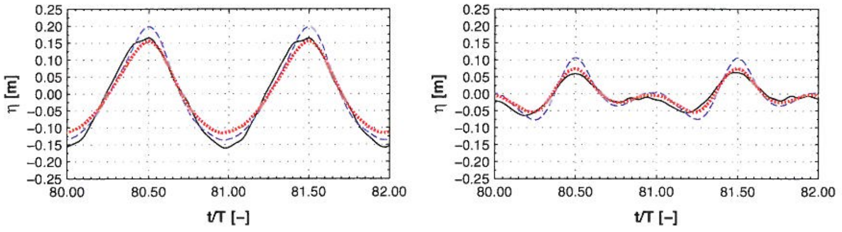

(a) NF1 (b) NF3

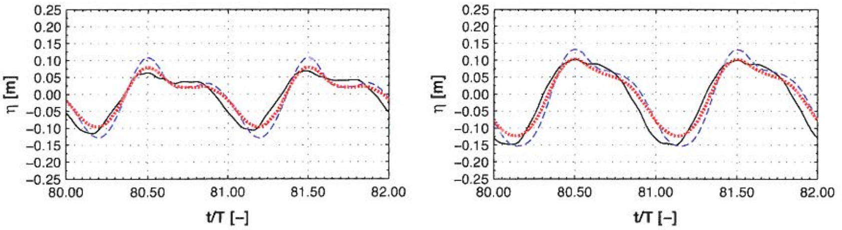

(c) NF4 (d) NF5

Figure 7.13: Detailed comparison of η in near-field, case 3. Comparison between experimental measurements (black solid) and numerical simulations: H_0=0.25 m (blue dashed) and H_0=0.20 m (red dotted). Both runs are with dx=0.05 m, f_s=100 Hz.

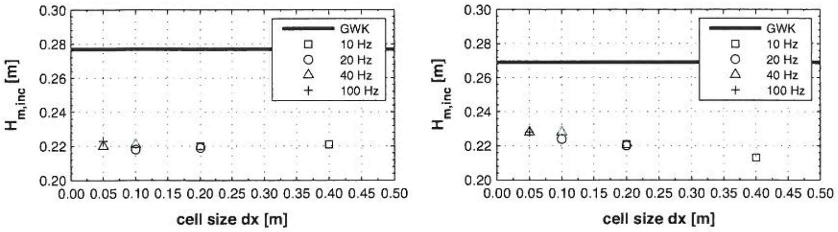

(a) TW2 (b) TW4

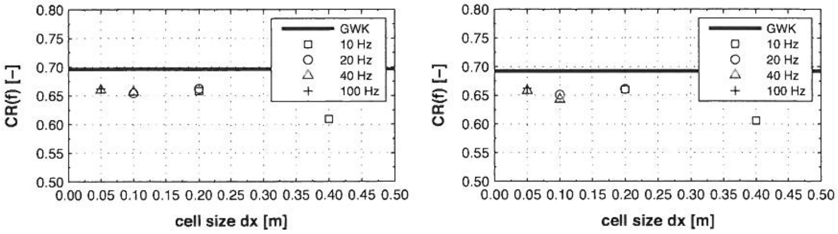

(c) TW2 (d) TW4

Figure 7.14: Variation of incident wave height $H_{m,inc}$ and reflection coefficient $CR(f)$ with cell size dx, resulting from a reflection analysis in TW2 and TW4, case 3. Black solid lines indicate target GWK values.

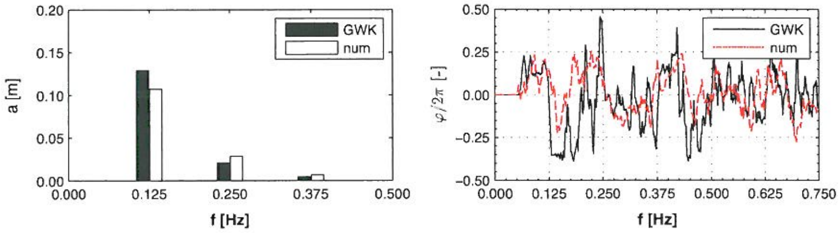

(a) (b)

Figure 7.15: Incident wave spectrum resulting from near-field reflection analysis, case 3: (a) amplitude of spectral components and (b) phase spectrum. Numerical simulation with dx=0.05 m, f_s=100 Hz.

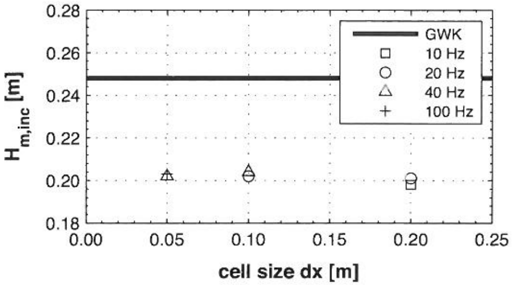

Figure 7.16: Variation of incident wave height $H_{m,inc}$ with cell size dx, case 3. Numerical and experimental values computed $H_{m,inc}$ computed with nonlinear shoaling method. The black solid line indicates the target GWK value.

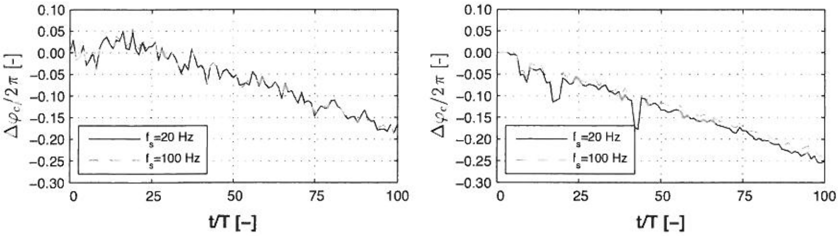

(a) FF2

(b) NF1

Figure 7.17: Evolution of phase difference $\Delta\varphi_c$ between experimental and numerical wave crests, measured in (a) far-field and (b) near-field, case 3. Numerical simulations with dx=0.10 m, f_s=20 Hz and dx=0.05 m, f_s=100 Hz.

7.4.5 Case 4

Similar as with case 3, a close-up on the progressive far-field waves in Fig. 7.18 points to the existence of a 'mechanical transfer' effect which is caused by the operation of the physical wavemaker. Experimental values of crests and troughs are clearly below theoretical values. The total wave amplitude (η_c - η_t) seems to be in close agreement with the theoretical value of 1 m. In the numerical simulation, the wave amplitude generated with H_0=1.0 m clearly exceeds the theoretical value, probably due to the absence of wall and bottom friction losses in the numerical model. Another potential factor for the observed deviation is the occurrence of harmonic generation resulting in spatial wave amplitude modulation. Tests with progressive waves in the same conditions (section 6.3) clearly confirmed the presence of harmonic generation, due to the linear wavemaker theory.

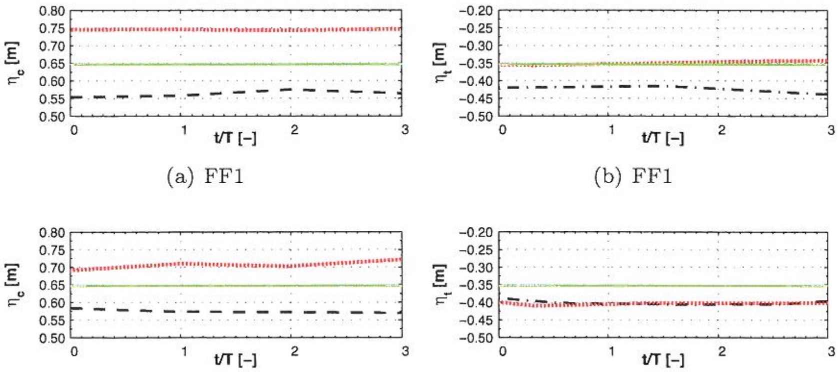

(a) FF1 (b) FF1

(c) FF4 (d) FF4

Figure 7.18: Time series of wave crests η_c and troughs η_t in far-field, TW1, case 4. Comparison between theoretical value (green solid), experimental measurements (black dashed) and numerical simulation with dx=0.10 m, f_s=100 Hz (red dotted).

The time evolution of η_c in Fig. 7.19 shows that wave crest levels generated with H_0=1.0 m are significantly larger than experimental values, more than 0.2 m on average. The higher wave crests are systematically observed at each location of measurement. Observed deviations in wave troughs are much more limited. Reducing H_0 to 0.85 m clearly improves the correspondence between experimental and numerical levels of η_c. It is noticed that the reduction of H_0 has a major impact on η_c, whereas the impact on η_t levels is almost inappreciable. Opposite to case 2, no significant low-frequency amplitude variations are noticed, which could result from a resonant behavior of the water mass in the wave flume.

The observed deviation in wave crest levels η_c is similar to case 3, albeit much more pronounced in this case. In this list of factors in section 7.4.4, the effect of harmonic generation will most likely gain importance and affect the performance of the active absorption. Due to the lacking of GWK paddle displacements however, the behavior of the active absorption in the physical wave flume cannot be determined. Therefore, the questions remain unanswered how the behavior of the active absorption compares between the physical and numerical model and to which extent the harmonic generation affects the wave generation.

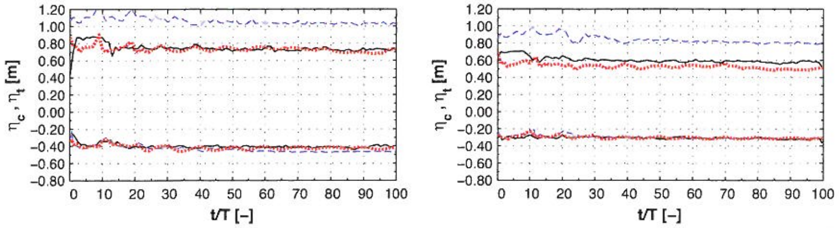

(a) NF1 (b) NF2

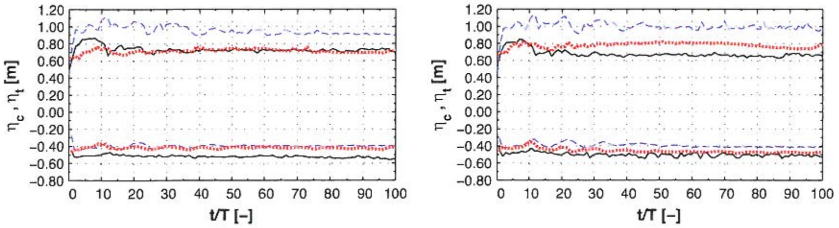

(c) NF4 (d) NF5

Figure 7.19: Near-field time series of wave crests η_c and troughs η_t, case 4. Comparison between experimental measurements (black solid) and numerical simulations: H_0=1.0 m (blue dashed) and H_0=0.85 m (red dotted). Numerical simulations with dx=0.05 m and f_s=100 Hz.

A detailed comparison of the wave profile between numerical and physical model in Fig. 7.20 reveals a significant difference in the shape of the wave trough. This is most probably induced by phase differences between numerical and experimental incident and reflected waves. This is further explored in Fig. 7.21, showing the amplitude a and phase φ components of the obtained incident wave spectrum. The first three harmonics in Fig. 7.21(a) contain a significant amount of energy and generally compare well. Much larger discrepancies are observed in the phase spectrum in

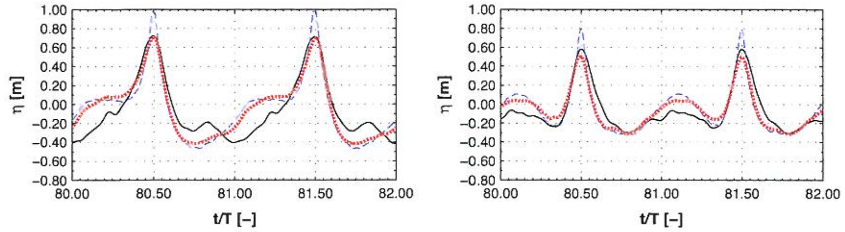

(a) NF1 (b) NF2

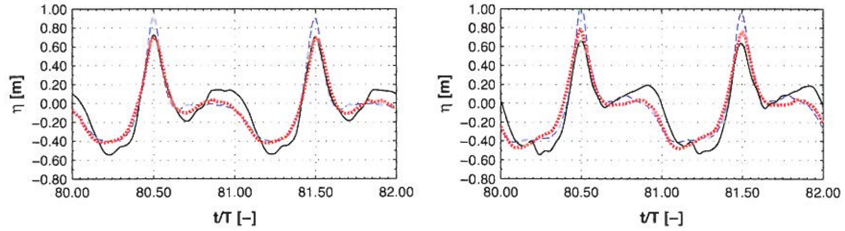

(c) NF4 (d) NF5

Figure 7.20: Detailed comparison of η in near-field, case 4. Comparison between experimental measurements (black solid) and numerical simulations: H_0=1.0 m (dx=0.10 m, blue dashed) and H_0=0.85 m (dx=0.05 m, red dotted).

Fig. 7.21(b), where a significant phase difference is noticed in the first harmonics.

The differences in phase spectrum cause differences in the incident wave time series η_{inc}, obtained by inverse Fourier transformation. A comparison in Fig. 7.21(c) shows a clear deviation in the wave trough evolution, resulting in a large difference between the experimental and numerical value of $H_{m,inc}$ in time domain. This is confirmed by the large deviation ($>$0.20 m) in $H_{m,inc}$ in Fig. 7.22. It is concluded that $H_{m,inc}$ resulting from a time domain analysis will not accurately represent the relative amount of incident wave energy between the experiment and the numerical model. The correspondence between extrema in η_c and η_t in Fig. 7.20 suggests a much closer agreement between values of $H_{m,inc}$.

Alternatively, the incident wave height is computed by transformation of the far-field wave height. A more consistent result is obtained with this approach, yielding smaller values of $H_{m,inc}$ compared to the experimental value (Fig. 7.23), due to the smaller value of H_0 in the numerical model.

Table 7.6 contains the ratio between experimental and numerical wave height in frequency and time domain. The numerical $H_{m,inc}$ is not reliable,

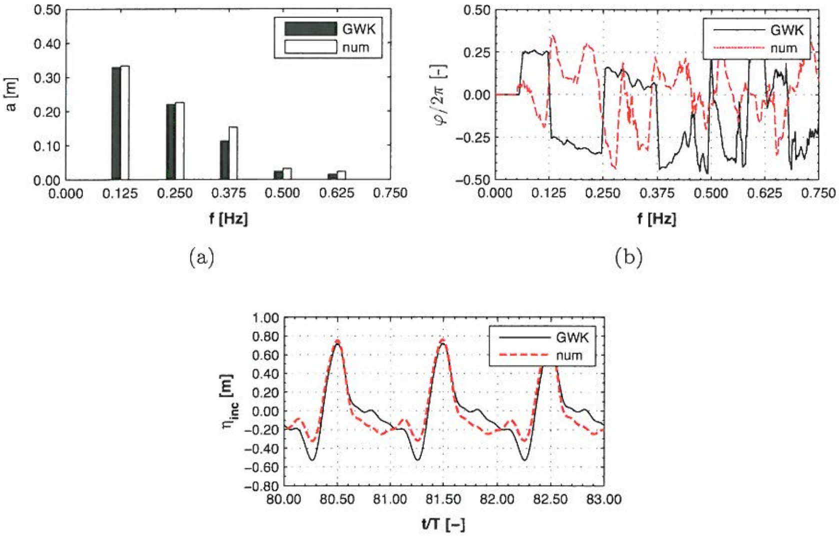

(a) (b)

(c)

Figure 7.21: Near-field reflection analysis, case 4: (a) incident wave amplitude spectral components, (b) incident phase spectrum and (c) reconstructed time series of incident waves. Numerical simulation with dx=0.05 m, f_s=100 Hz.

as discussed previously. The ratio between transformed wave heights $H_{m,inc}^{shoal}$ is consistent with the spectral value H_{m0}, as can be expected from the observed correspondence between numerical and experimental spectral amplitudes (see Fig. 7.21(a)). In the further analysis, the value of $H_{m,inc}^{shoal}$ will be employed as a reference.

The evolution of the phase lag $\Delta\varphi_c$ with time (Fig. 7.24) shows a consistent negatively increasing trend, similar in far-field and near-field. The growth rate of the phase error is comparable to the previous cases. No significant low-frequency oscillations are noticed in Fig. 7.9(b), as in case 2.

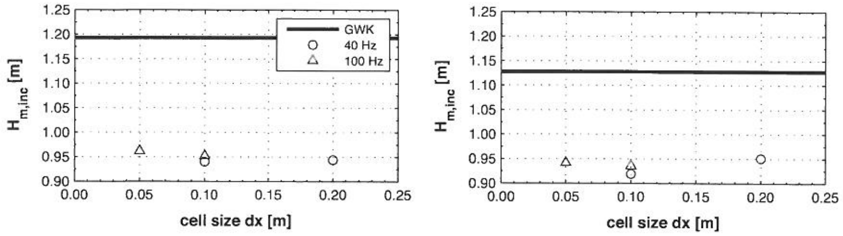

(a) TW2 (b) TW4

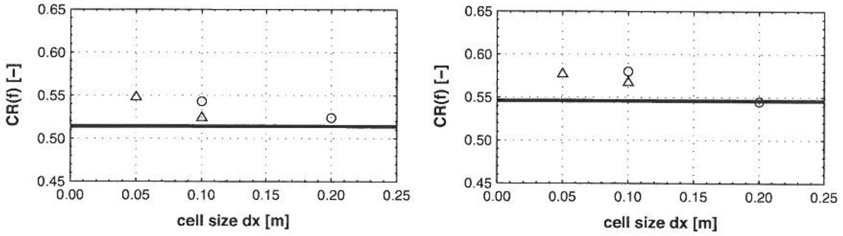

(c) TW2 (d) TW4

Figure 7.22: Variation of incident wave height $H_{m,inc}$ and reflection coefficient $CR(f)$ with cell size dx, resulting from a reflection analysis in TW2 and TW4, case 4. Black solid lines indicate target GWK values.

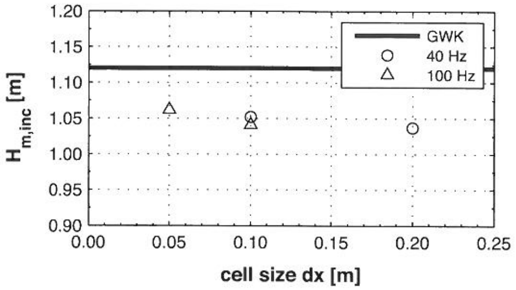

Figure 7.23: Variation of incident wave height $H_{m,inc}$ with cell size dx, case 4. Numerical and experimental values computed $H_{m,inc}$ computed with nonlinear shoaling method. The black solid line indicates the target GWK value.

Table 7.6: Ratio of incident wave energy between experimental and numerical model, case 4.

	$H_{m0,inc}$ $[m]$[1]	$H_{m,inc}$ $[m]$[2]	$H_{m,inc}^{shoal}$ $[m]$[3]
GWK	1.298	1.128	1.120
num (dx=0.05 m)	1.235	0.942	1.062
GWK/num	1.05	1.20	1.06

[1] frequency domain analysis, TW4
[2] time domain analysis, TW4
[3] transformed $H_{m,inc}$ obtained in far-field, TW1

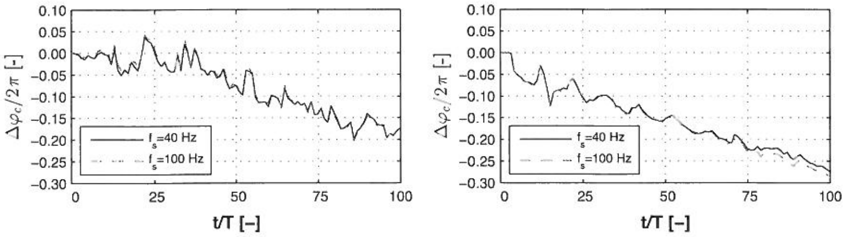

(a) FF2

(b) NF1

Figure 7.24: Evolution of phase difference $\Delta\varphi_c$ between experimental and numerical wave crests, measured in (a) far-field and (b) near-field, case 4. Numerical simulation with dx=0.10 m, f_s=40 Hz and dx=0.05 m, f_s=100 Hz.

7.5 Wave transmission and MWL evolution

In the following, wave transmission through the breakwater section and set-up of MWL inside the breakwater are discussed. A detailed view on the wave interaction with the breakwater model is shown in Fig. D.1 in Appendix D, where the velocity field at different instants during one wave cycle is shown, for case 2.

7.5.1 Case 1

The variation of the wave envelope across the breakwater section, normalized by $H_{m,inc}$, is shown in Fig. 7.25. The same frame of reference is adopted from Fig 4.5.

The envelopes $\overline{\eta}_{c(t)}$ are time-averaged crest and trough surface elevations, defined in TW4, when the set-up in the breakwater core is fully established. Good agreement is observed between experimental and numerical $\overline{\eta}_{c(t)}$, showing that the different interaction processes (wave reflection and transmission, wave run-up and run-down, in-and outflow) are correctly represented in the numerical model. Numerical results are shown for dx=0.05 m, very limited impact of the mesh resolution on the accuracy of the solution is noticed however.

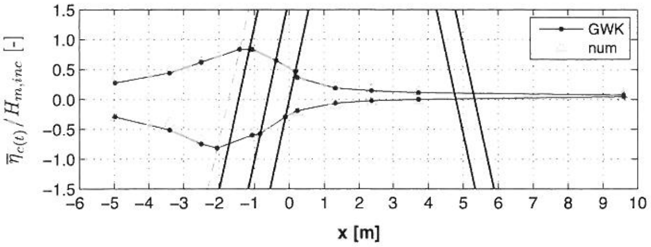

Figure 7.25: Comparison between experimental and numerical envelope of relative free surface elevation $\overline{\eta}_{c(t)}/H_{m,inc}$ across the breakwater section, case 1. Indication of breakwater contours (solid) and run-up gauges (dashed). Numerical simulation with dx=0.05 m and f_s=40 Hz.

A detailed picture of the evolution of MWL $\overline{\eta}$ across the breakwater section is given in Fig. 7.26. Experimental measurements are compared with results from numerical simulations using two different mesh resolutions; dx=0.20 m (f_s=20 Hz) and dx=0.05 m (f_s=40 Hz). Wave gauges TM2 and TM3 in front of the structure register a set-down of MWL. A maximum relative set-down $\overline{\eta}/H_{m,inc}$ of approximately 0.04 is measured in the physical model, which is well matched by the numerical simulations. Much larger low-frequency $\overline{\eta}$ variations are noticed however in the physical model, presumably caused by a difference in wave reflection and/or run-up and run-down processes. Nonetheless, the overall trend in the MWL evolution is well predicted by the numerical model.

The relative set-up inside the breakwater core (gauges TM4, TM5 and TM7) is relatively well matched by the numerical model. Again, low-frequency $\overline{\eta}$ oscillations tend to be more pronounced in the physical model. The relative set-up in the basin behind the breakwater (gauge TM9) is about 0.06 in the physical model, compared to 0.04 numerically.

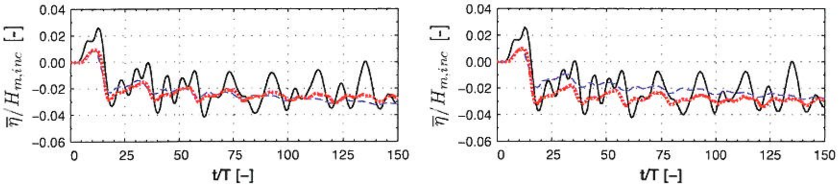

(a) TM2 (b) TM3

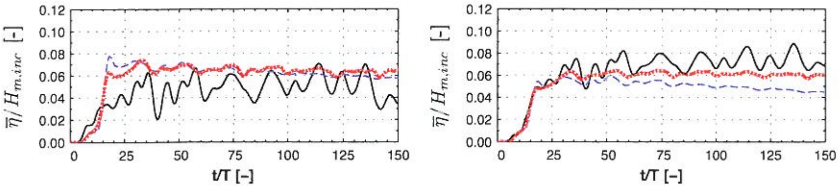

(c) TM4 (d) TM5

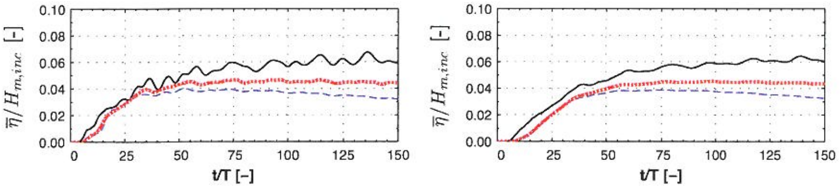

(e) TM7 (f) TM9

Figure 7.26: Evolution of relative mean surface elevation $\overline{\eta}/H_{m,inc}$ across the breakwater section, case 1. Set-down in front of the breakwater (a, b), set-up inside the core (c, d, e) and set-up behind the breakwater (f). Comparison between experimental measurements (black solid) and numerical simulation: dx=0.20 m (blue dashed) and dx=0.05 m (red dotted).

7.5.2 Case 2

Likewise to case 1, good correspondence is generally observed between physical and numerical envelopes of relative wave motion across the breakwater section, presented in Fig. 7.27. The point of highest $\overline{\eta}_c$ measured by TM6 (the 6th point of measurement of $\overline{\eta}_c$ from the left) in the numerical model seems to be somewhat higher than measured experimentally, pointing to a larger hydraulic resistance in the experiments than in the numerical model. Effects of air entrainment are the most likely to explain for this observation (see further).

A detailed view on MWL levels is given in Fig. 7.28. Experimental measurements are compared with results from numerical simulations using two different mesh resolutions: dx=0.20 m (f_s=40 Hz) and dx=0.05 m (f_s=200 Hz). Compared to case 1 (Fig. 7.26), the accuracy of the solution is clearly more dependent on the mesh resolution. Experimental levels of set-down and set-up are well matched by the numerical model. In addition, an improved correspondence is observed between low-frequency $\overline{\eta}$ variations.

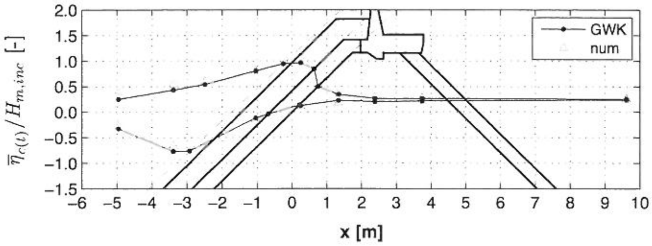

Figure 7.27: Comparison between experimental and numerical envelope of relative free surface elevation $\overline{\eta}_{c(t)}/H_{m,inc}$ across the breakwater section, case 2. Indication of breakwater contours (solid) and run-up gauges (dashed). Numerical simulation with dx=0.05 m and f_s=200 Hz.

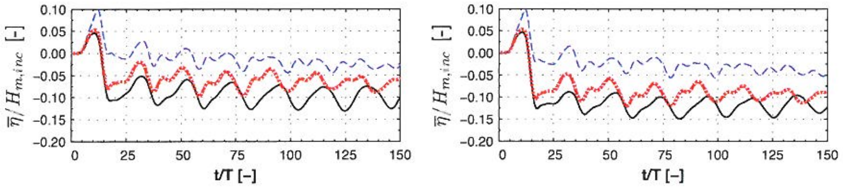

(a) TM1 (b) TM2

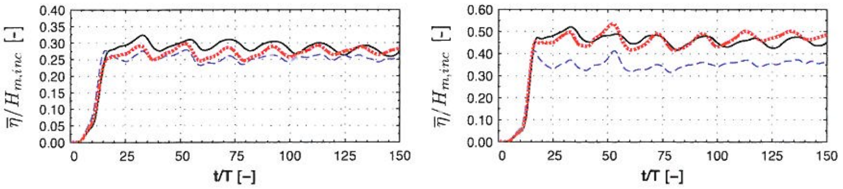

(c) TM4 (d) TM5

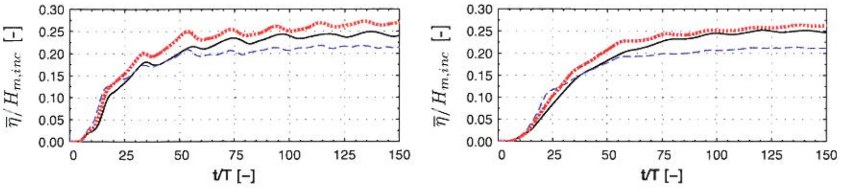

(e) TM7 (f) TM9

Figure 7.28: Evolution of relative mean surface elevation $\overline{\eta}/H_{m,inc}$ across the breakwater section, case 2. Set-down in front of the breakwater (a, b), set-up inside the core (c, d, e) and set-up behind the breakwater (f). Comparison between experimental measurements (black solid) and numerical simulation: dx=0.20 m (blue dashed) and dx=0.05 m (red dotted).

7.5.3 Case 3

The comparison between physical and numerical envelopes of relative wave motion (Fig. 7.29) again shows good overall correspondence between physical and numerical model tests. Due to the longer wave period, run-up and penetration are more pronounced (compared to case 1). The effect is well captured by the numerical model. The highest numerical level of η_c exceeds the physical value, indicating a lack of modeled hydraulic resistance in the armour layer.

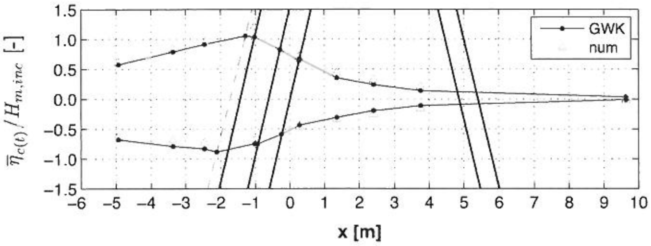

Figure 7.29: Comparison between experimental and numerical envelope of relative free surface elevation $\overline{\eta}_{c(t)}/H_{m,inc}$ across the breakwater section, case 3. Indication of breakwater contours (solid) and run-up gauges (dashed). Numerical simulation with dx=0.05 m and f_s=100 Hz.

A detailed view on MWL levels is given in Fig. 7.30. Experimental measurements are compared with results from numerical simulations using two different mesh resolutions: dx=0.20 m (f_s=20 Hz) and dx=0.05 m (f_s=100 Hz). Relative set-down measured by TM1 and TM3 is very limited (≈ 0.02). Differences between numerical resolutions are very small and results are clearly convergent. Numerical values of set-down do not reach the level of the experimental values. It is noticed however that the set-down is very limited and the measurements therefore present a larger relative error.

The comparison between set-up levels inside the core (Fig. 7.30 (c)-(e)) show that the position of maximum set-up in the numerical model is shifted more toward the seaward side. The maximum experimental value is slightly larger than the numerical value. Behind the breakwater, again a larger set-up is measured in the physical model. Measured values are however very small and thus prone to a larger relative measurement error. It is remarked that the maximum set-up value behind the breakwater (TM9) is considerably smaller compared to case 1. Since case 3 waves have a longer wave period and it is expected that this will lead to a longer penetration depth of the wave motion, this particular outcome is somewhat surprising.

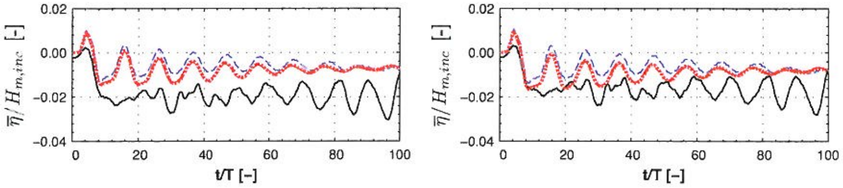

(a) TM1 (b) TM3

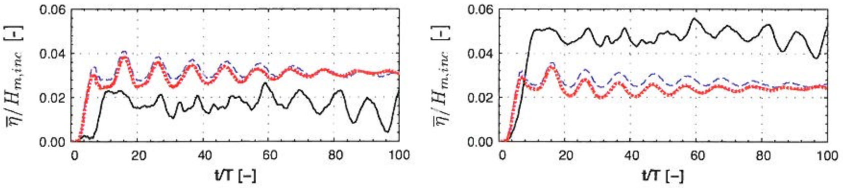

(c) TM4 (d) TM5

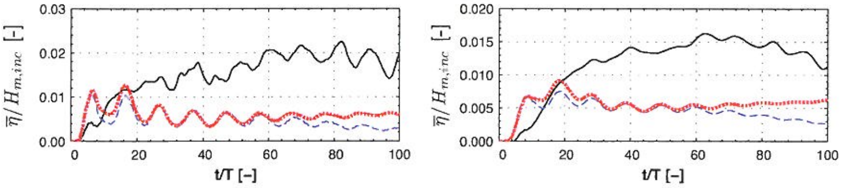

(e) TM7 (f) TM9

Figure 7.30: Evolution of mean surface elevation $\overline{\eta}/H_{m,inc}$ across the breakwater section, case 3. Set-down in front of the breakwater (a, b), set-up inside the core (c, d, e) and set-up behind the breakwater (f). Comparison between experimental measurements (black solid) and numerical simulation: dx=0.20 m (blue dashed) and dx=0.05 m (red dotted).

7.5.4 Case 4

As in the previous cases, the overall image of numerical wave envelopes corresponds well with the experimental measurements, see Fig. 7.31. Slightly higer values of wave crests are observed, which can be partially generated by the uncertainty on the determination of $H_{m,inc}$. The proper operation of wave gauge TM7 in this particular wave test was found to be highly questionable. Hence, this wave gauge has been removed from the analysis.

A detailed view on MWL levels is given in Fig. 7.32. Experimental measurements are compared with results from numerical simulations using two different mesh resolutions; dx=0.20 m (f_s=40 Hz) and dx=0.05 m (f_s=100 Hz). Levels of set-down and set-up generally agree well, with results converging toward the experimental values for increasing mesh resolution. Numerical time series of set-down (TM1 and TM2) show moderate low-frequency $\overline{\eta}$ variations, opposite to the physical results. Apart from a transient effect in the start of the physical wave train, which is not captured in the numerical model, low-frequency $\overline{\eta}$ oscillations are practically zero inside the breakwater.

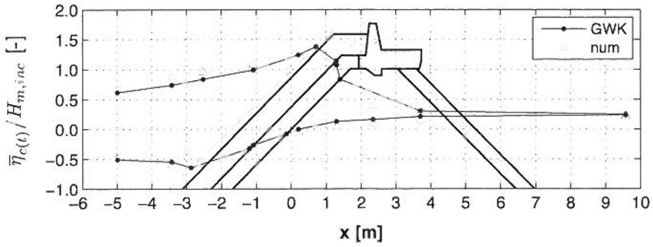

Figure 7.31: Comparison between experimental and numerical envelope of relative free surface elevation $\overline{\eta}_{c(t)}/H_{m,inc}$ across the breakwater section, case 4. Indication of breakwater contours (solid) and run-up gauges (dashed). Numerical simulation with dx=0.05 m and f_s=100 Hz.

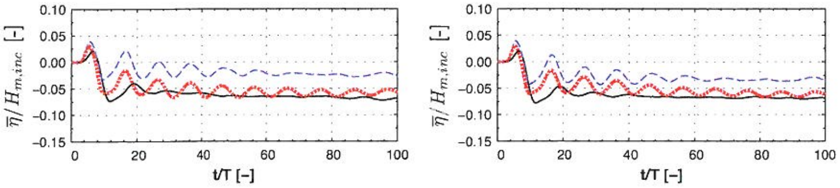

(a) TM1

(b) TM2

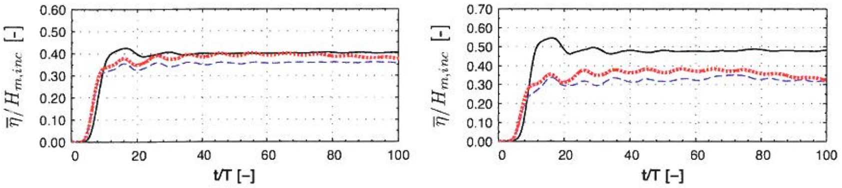

(c) TM5

(d) TM6

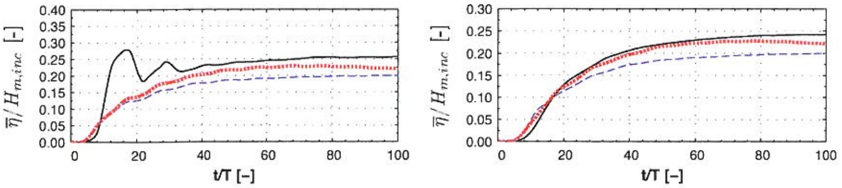

(e) TM8

(f) TM9

Figure 7.32: Evolution of relative mean surface elevation $\overline{\eta}/H_{m,inc}$ across the breakwater section, case 4. Set-down in front of the breakwater (a, b), set-up inside the core (c, d, e) and set-up behind the breakwater (f). Comparison between experimental measurements (black solid) and numerical simulation: dx=0.20 m (blue dashed) and dx=0.05 m (red dotted).

7.6 Pore pressures

The graphs included in this section show the distribution of pore pressure height along the armour, filter and core slope and three sections of pressure gauges inside the breakwater core (see Fig. 3.2). Pressure gauges close to the free surface which are running dry are excluded from the comparison. Values of mean pore pressure height P_m (i.e. the amplitude of pressure oscillations) are obtained in time window TW4, when the set-up in the breakwater core is fully established. Numerical results are presented for two different mesh resolutions: dx=0.20 m and 0.05 m. The results presented hereafter show a limited sensitivity to the mesh resolution, in agreement with the averaging approach used to model porous flow.

7.6.1 Case 1

Distributions of P_m along the armour, filter and core slope are shown in Fig. 7.33(a,b,c). The numerical model seems to capture the flow resistance through the multiple layers fairly accurately. Near the free surface, a larger discrepancy between numerical and experimental results is noticed.

Fig. 7.33(d,e,f) present the pressure height attenuation in function of the horizontal distance x' along the bottom, middle and top section of pressure gauges respectively, measured from the first gauge positioned on the core slope. In the lower and middle section, the attenuation of pore pressure height predicted by the numerical model closely agrees with the experimental one, although a slightly consistent overestimation of the experimental values is noticed, with a relative standard deviation $\sigma' \approx 0.10$. This can be caused by the absence of the inertia term in the modeled porous flow model, however the effect is considered to be small. Along the top section, the deviation from the measured P_m becomes larger ($\sigma' = 0.25$).

The larger discrepancies between experimental and numerical P_m near the free surface are likely caused by air entrainment, which is not accounted for by the present simulation of single-fluid flow. The air entrainment in a confined region near the free surface affects the pressure (i) through a reduction of the air-water mixture density and (ii) by increasing the porous media flow resistance (Hannoura and McCorquodale, 1985). The presence of air entrainment in the GWK model has been studied by Muttray (2000), through comparison of η measured by wave gauges and computed from pressure measurements near the free surface. Air volume fractions could be correlated with the wave run-up on the armour slope, ranging between 20 to 60 %.

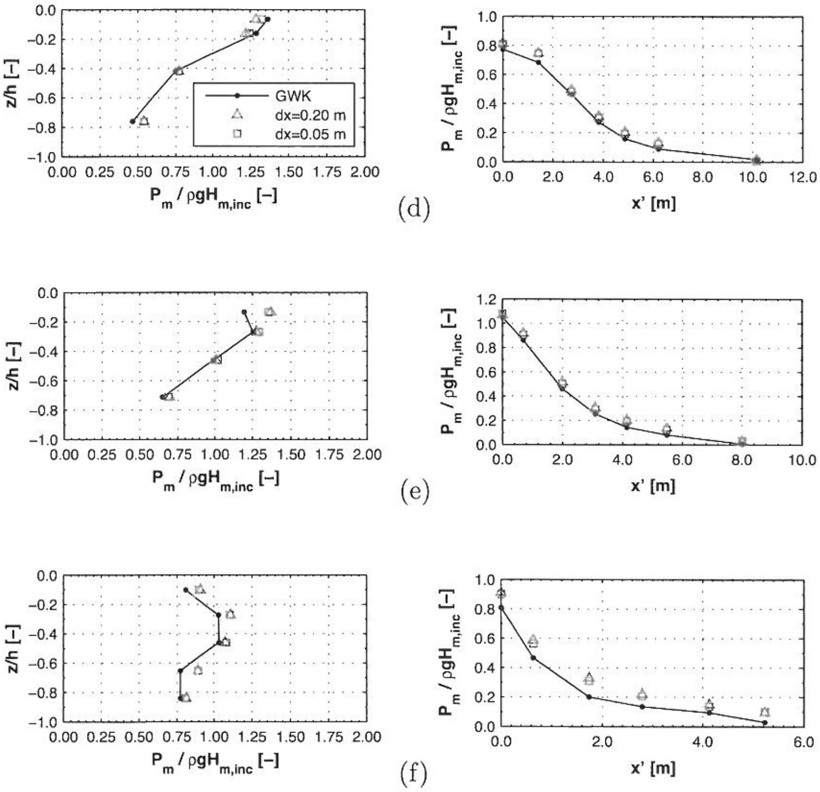

(a) (d)

(b) (e)

(c) (f)

Figure 7.33: Case 1 comparison between experimental and numerical relative pore pressure height along (a) armour slope, (b) filter slope, (c) core slope; (d) bottom section, (e) middle section and (f) top section of pressure gauges.

7.6.2 Case 2

Similar plots of spatial pressure distribution for case 2 are presented in Fig. 7.34. Compared to case 1, larger deviations between numerical and experimental values of P_m near the free surface are observed (σ'=0.35). In particular along the filter and core slope in Fig. 7.34(b,c), the deviation is more pronounced for a longer part of the slope. The larger amount of air entrainment due to the larger wave height is assumed to be the main cause for this observation.

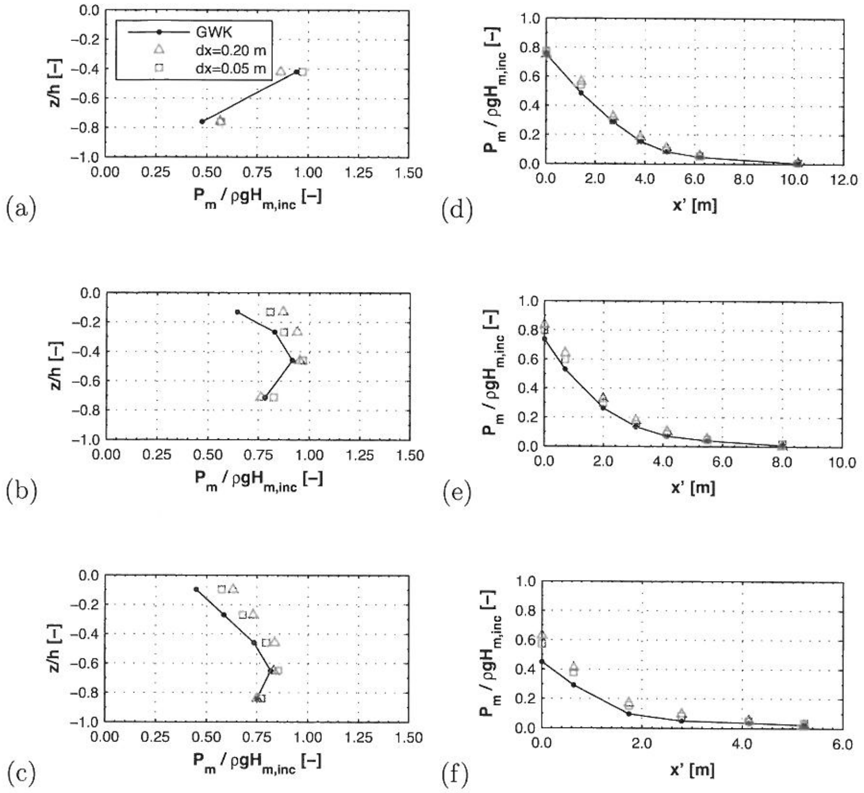

Figure 7.34: Case 2 comparison between experimental and numerical relative pore pressure height along (a) armour slope, (b) filter slope, (c) core slope; (d) bottom section, (e) middle section and (f) top section of pressure gauges.

7.6.3 Case 3

Case 3 presents the results of long small-amplitude waves. The relative pressure height along the armour, filter and core slope is clearly different from the previous cases, due to the effect of the reduced relative water depth (see Chapter 4). This effect seems to be well captured by the numerical model. Again, deviations are larger near the free surface due to air entrainment.

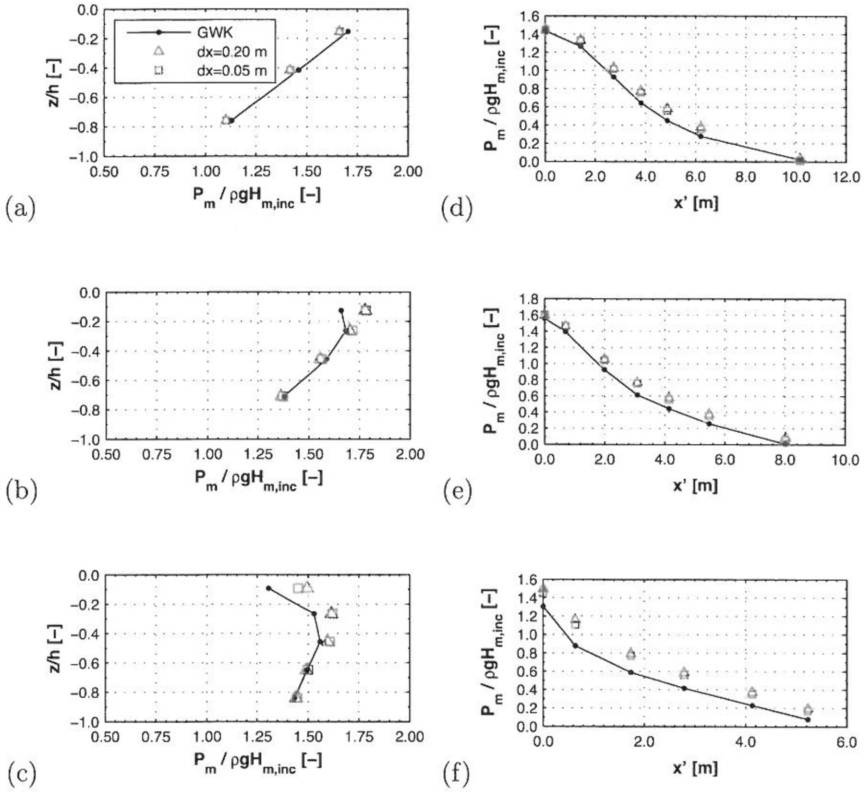

Figure 7.35: Case 3 comparison between experimental and numerical relative pore pressure height along (a) armour slope, (b) filter slope, (c) core slope; (d) bottom section, (e) middle section and (f) top section of pressure gauges.

7.6.4 Case 4

Similar observations as in the previous cases are made for case 4, see Fig. 7.36. The effect of the longer waves, causing a considerably larger wave run-up, is noticed in larger values of the relative pressure height along the interfaces of filter and core. It can be expected that a larger amount of air is entrained in the physical model in this case, due to the larger run-up and penetration depth of wave motion inside the core. This is confirmed by a larger discrepancy (σ'=0.31) between numerical and experimental pressure heights in Fig. 7.36(f).

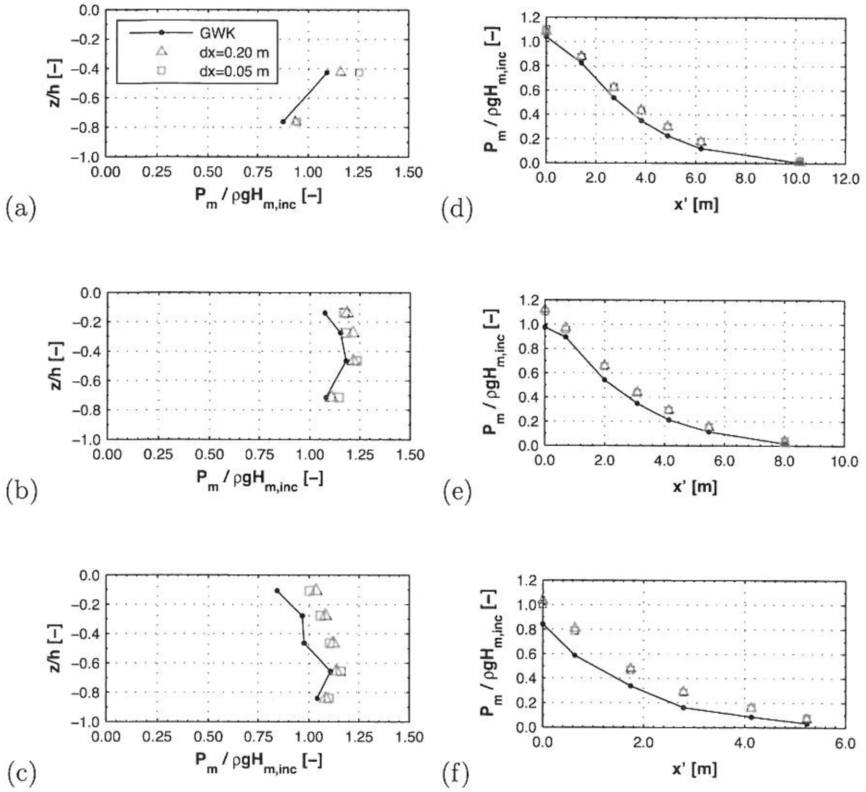

Figure 7.36: Case 4 comparison between experimental and numerical relative pore pressure height along (a) armour slope, (b) filter slope, (c) core slope; (d) bottom section, (e) middle section and (f) top section of pressure gauges.

7.7 Conclusions

A selected number of GWK regular wave tests have been simulated with the numerical model, covering a wide range of relative water depth and wave height. Due to the nature of the studied problem (nonbreaking waves), the problem has been simplified to two dimensions, without applying a turbulence model in the clear-fluid region.

A first step in the validation consisted of a thorough comparison of both incident wave fields. In general, the numerical model is capable of maintaining the long-term stability of the generated wave train. Time evolutions of wave crest and trough levels resemble well, pointing to an effective performance of the active absorption. Results from a reflection analysis in the vicinity of the breakwater show good agreement in terms of incident wave height and reflection coefficient. In case of a larger wave period however, an additional calibration of the piston movements was necessary to match the experimental measurements, probably caused by differences in the operation of the physical wavemaker and nonlinear effects.

The numerical model has shown to accurately predict the transmission of free surface elevation throughout the breakwater cross-section. In addition, the correspondence between measured and simulated values of set-down and set-up proves that the numerical model properly resolves the repetitive succession of inflow and outflow processes through the breakwater slope, thereby confirming the effectiveness of the porous flow model, in spite of its simplifications (cfr. Chapter 5).

Finally, the experimental and numerical spatial distribution of pore pressures along the interfaces of the breakwater front layers and within the core have been compared, revealing good accuracy of predicted values of pressure height, particularly in the absence of air entrainment. Increased discrepancies between experimental and numerical results in a limited zone near the free surface can be attributed to the effect of air entrainment, which has not been taken into account in the present study. The incorporation of two-phase flow with air entrainment, either by incorporation in the porous media model or simulated by a turbulence model, reveals a particular challenge for future work.

8 Conclusions and recommendations

8.1 Conclusions

The importance of the part of porous flow in the structural behavior of permeable coastal structures has been explained in Chapter 1. The present work fits within the scope of improving the understanding of the hydraulic processes involved in wave-induced porous flow and the impact of these processes on the design of permeable coastal structures. To this end, experimental and numerical research are combined in an integrated study.

In the first part of this research, the accuracy of the existing practical calculation model (Burcharth et al., 1999; Troch, 2000) for the attenuation of pore pressure height within the core of a typical RMB section has been verified against an extensive dataset of large-scale model pore pressure measurements (Muttray, 2000). The results point to oversimplifications in the current model, affecting the predictive accuracy under varying wave conditions. Therefore, improvements to the calculation model have been proposed.

The model equations in the improved calculation method were derived from a nonlinear regression analysis and relate the wave-induced pore pressure height to a sea state defined by the relative water depth kh and wave height H_{inc}/h, corresponding with non-overtopping and nonbreaking wave conditions. The dimensionless regression parameters appearing in the model equations are considered to be dependent to a certain extent on the breakwater geometry (slope angle, layer thickness) and the specific material properties affecting the porous flow resistance.

Pore pressure measurements on a small-scale breakwater model have been applied to the newly-derived calculation model, in order to provide insight into the general applicability of the model regression parameters. The small-scale model tests consider similar wave conditions as in large-scale tests and moreover present an equal armour slope. In an effort to maintain Froude scale similarity of the porous flow in the small-scale model, the core material has been determined using a scaling procedure. The validation with the small-scale data proves that the model equations are capable of describing the variation of pressure height under varying wave conditions, but also reveals differences in the model parameters to a certain extent. More specifically, the comparison between both models learns that the regression parameters in the model equation for the reference pressures (along the interface between underlayer and core) are least susceptible to a change in layer thickness or material properties of the armour or filter layer. This can be explained considering that the mean value of the reference pressures along the core slope is determined to a large extent by the wave run-up on the breakwater slope. This phenomenon is implicitly captured by the incorporation of the relative incident wave parameters in the model equation. When moving inside the breakwater core, the influence of the hydraulic resistance of the core material on the pressure height attenuation increases. Consequently, an increased dependency of the model parameters on the specific material properties may be expected.

The improvement in accuracy achieved with the new calculation method has been demonstrated by comparison with the existing method on a selected number of cases. A particular application of the improved method may be found in the scaling procedure of finer core material in reduced scale models (Appendix C), making the procedure more reliable in varying wave conditions.

The second part of this PhD research explores the application of CFD modeling based on the Navier-Stokes equations to the interaction of water waves with permeable coastal structures. The principal goal is to validate the capabilities of such a numerical model, specifically aiming to use a realistic large-scale validation case and consider long-term transient effects in the wave-structure interaction.

Prerequisites to the applied model are an efficient simulation of free surface and porous media flow, two main characteristics dominating the problem of interest. The CFD model FLOW-3D has been selected for this purpose, which is a commercial state-of-the-art model.

FLOW-3D has no standard wave boundary with active wave absorption, which is crucial to simulate realistic long-duration wave tests resembling those in a physical wave flume. For that reason, a linear piston wavemaker has been implemented in the code, based on the GMO moving-object model. In order to prescribe piston control velocities and computing the correction signal in the active wave absorption procedure, existing technology from piston wavemakers operated in the laboratory has been used.

The generation and absorption capacities of the implemented piston wavemaker have been thoroughly validated. The simulation of purely progressive waves have shown that the best results in terms of accuracy and stability are obtained with the first-order upwind momentum scheme. Another important factor concerns the specification of the piston sample frequencies, which need to be in accordance with the numerical time step and are thus governed by the mesh resolution. Guidelines to define optimal settings for different numerical parameters were established. The implementation of a linear active wave absorption system has been validated by means of a purely absorbing wavemaker. Results show excellent absorption capacity for low-amplitude waves and lower, but still acceptable performance with larger wave heights. It appears that the performance of the active absorption is at least as high as in the physical wave flume, however bound by the limitations of the linear wave absorption system.

Finally, a realistic validation case of wave interaction has been carried out, using GWK model tests. Due to the nature of the studied problem (nonbreaking waves), the problem has been simplified to two-dimensional laminar single-fluid flow in the clear-fluid region. A selected number of regular wave cases were used, covering a wide range of relative water depth and wave height.

A first step of the validation consisted of a detailed comparison between numerical and experimental incident wave fields. The analysis on the wave-induced flow features learns that the numerical model predicts well the transmission of free surface elevation throughout the breakwater cross-section, and proves to capture the long-term transient effects of the fluid flow under cyclic wave loading. Finally, comparing the experimental and numerical spatial distribution of wave-induced pore pressures, the model was found to accurately predict the pore pressure height, provided the flow is not affected by air entrainment. Due to the latter effect, larger discrepancies in pore pressures were noticed in a (limited) zone near the free surface in the core and on the breakwater slope.

In summary, the overall predictive accuracy obtained with this model, considering all the simplifications in the present validation study, proves its value as a design tool in support of the coastal engineer.

8.2 Recommendations for further research

The importance of 'rediscovering' the large-scale GWK dataset to the end of this PhD research cannot be stressed enough. However, its possibilities have not been fully exhausted yet. The dataset contains more tests performed with overtopping waves, with measured forces on the front face and below the crest wall. It would be useful to analyze the tests with overtopping wave conditions and study the impact on the pore pressure distribution due to large wave infiltration from the breakwater crest, verify the newly derived calculation model and make adjustments, if necessary. The largest uncertainty in the use of the improved calculation model may be found in the susceptibility of the regression parameters to changes in breakwater geometry and material properties. The best way to investigate this is probably by performing additional experimental research. However, given the value of the numerical model, a logical step would be to firstly perform a numerical study on this topic, since it is much more efficient to apply changes in geometry and material properties in a numerical model than in a physical model, certainly at large scale.

Secondly, the comparison between experimental and numerical wave-induced pore pressures near the free surface suggests improvements are to be found in considering two-phase flow with air entrainment. A first approach may be found in the application of turbulence models in two-phase porous media flow, in order to model air entrainment and related turbulent flow losses and loss of hydraulic conductivity. However, little information is available on the application of such models in coarse granular porous media. To the author's knowledge, detailed validation studies in coastal engineering are lacking. Moreover, the application of such turbulence models in combination with the seepage velocity concept or Forchheimer drag model is not well validated. In an alternative approach without considering turbulence modeling inside porous media (as in the model presented in this work), the increase of porous flow drag in the area affected by air entrainment could be modeled by considering spatially-varying resistance characteristics, based on an approach similar to Hannoura and McCorquodale (1985). However, a simulation of two-phase flow would still be required in such case.

A third path for further research concerns the implementation of higher-order wavemaker theories to improve the accuracy and stability in the generation of nonlinear waves. Naturally, the method should include active wave absorption. An interesting approach in this respect is the use of a force-control feedback instead of a position-controlled piston, see e.g. Spinneken and Swan (2009).

Finally, as mentioned in the literature review on porous media flow (Chapter 2), it is noticed that for large porous materials (e.g. concrete armor units or large rock) virtually no data are available concerning porous flow characteristics. As it turns out to be difficult to perform such large-scale permeameter flow tests, the simulation of specifically designed tests in a CFD model could make a particular contribution to this problem. With the contemporary computational power generated by cluster computing, the direct simulation of a porous flow field in such materials should be possible, yielding a better knowledge of porous flow drag parameters to be applied in a conventional porous media flow model.

A GWK model specifications

Table A.1: Positions of pressure and wave gauges in the GWK breakwater model.

Gauge	x [m][1]	z' [m][2]	Gauge	x [m]	z' [m]
DMD1	247.49	2.40	DMD27	248.73	4.17
DMD2	248.92	2.40	DMD28	249.94	4.98
DMD3	250.21	2.40	DMD29	244.85	2.60
DMD4	251.31	2.40	DMD30	246.55	3.45
DMD5	252.36	2.40	DMD31	247.53	4.10
DMD6	253.70	2.40	DMD32	247.89	4.34
DMD7	257.65	2.40	DMD33	248.83	4.97
DMD8	248.92	3.35	DMD34	250.21	5.89
DMD9	250.21	3.35	FF1	82.18	
DMD10	251.31	3.35	FF2	84.37	
DMD11	252.36	3.35	FF3	88.03	
DMD12	253.70	3.35	FF4	94.82	
DMD13	256.23	3.35	NF1	235.00	
DMD14	250.21	4.27	NF2	237.69	
DMD15	251.31	4.28	NF3	239.97	
DMD16	252.36	4.24	NF4	241.83	
DMD17	253.70	4.30	NF5	243.47	
DMD18	254.80	4.30	TM1	244.98	
DMD19	247.49	2.87	TM2	246.55	
DMD20	248.22	3.35	TM3	247.45	
DMD21	248.92	3.82	TM4	248.89	
DMD22	249.57	4.25	TM5	250.18	
DMD23	250.24	4.70	TM6	251.27	
DMD24	246.55	2.72	TM7	252.32	
DMD25	247.49	3.35	TM8	253.67	
DMD26	248.21	3.83	TM9	259.55	

[1] horizontal distance from right paddle face at initial position
[2] vertical distance from flume bottom

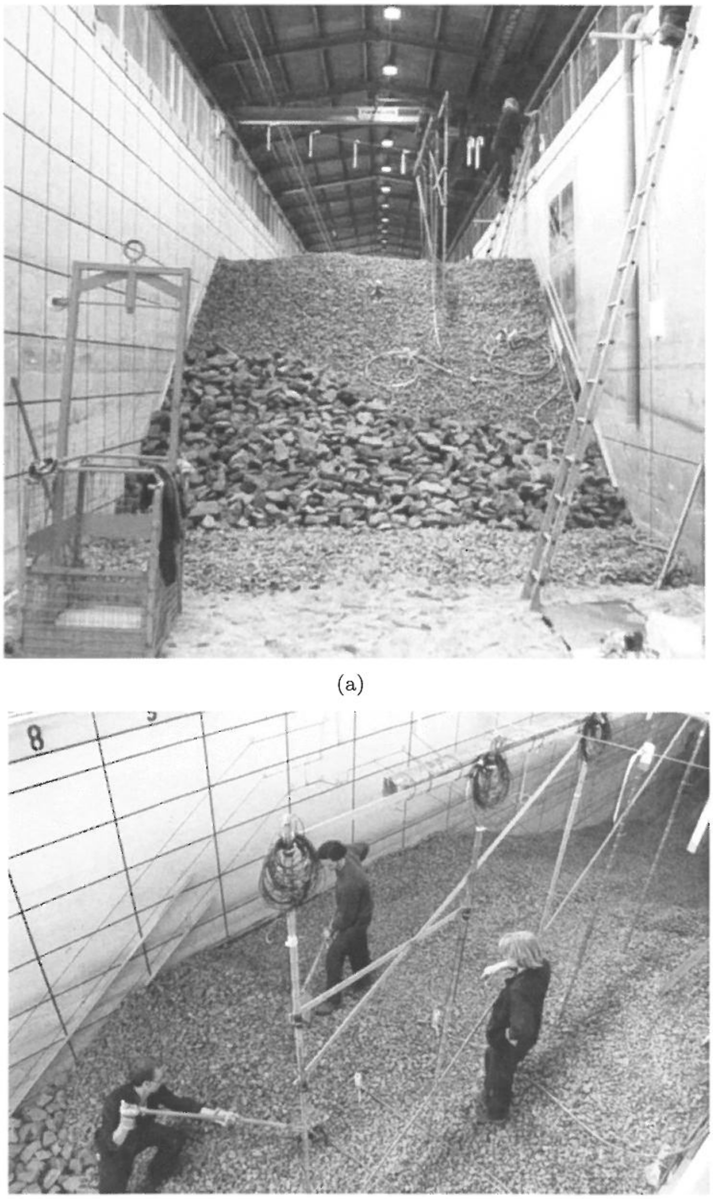

(a)

(b)

Figure A.1: Photographs of the GWK model: (a) construction of the filter layer on the breakwater core; (b) view on pressure and wave transmission gauges in the core. Photo's courtesy of Markus Muttray.

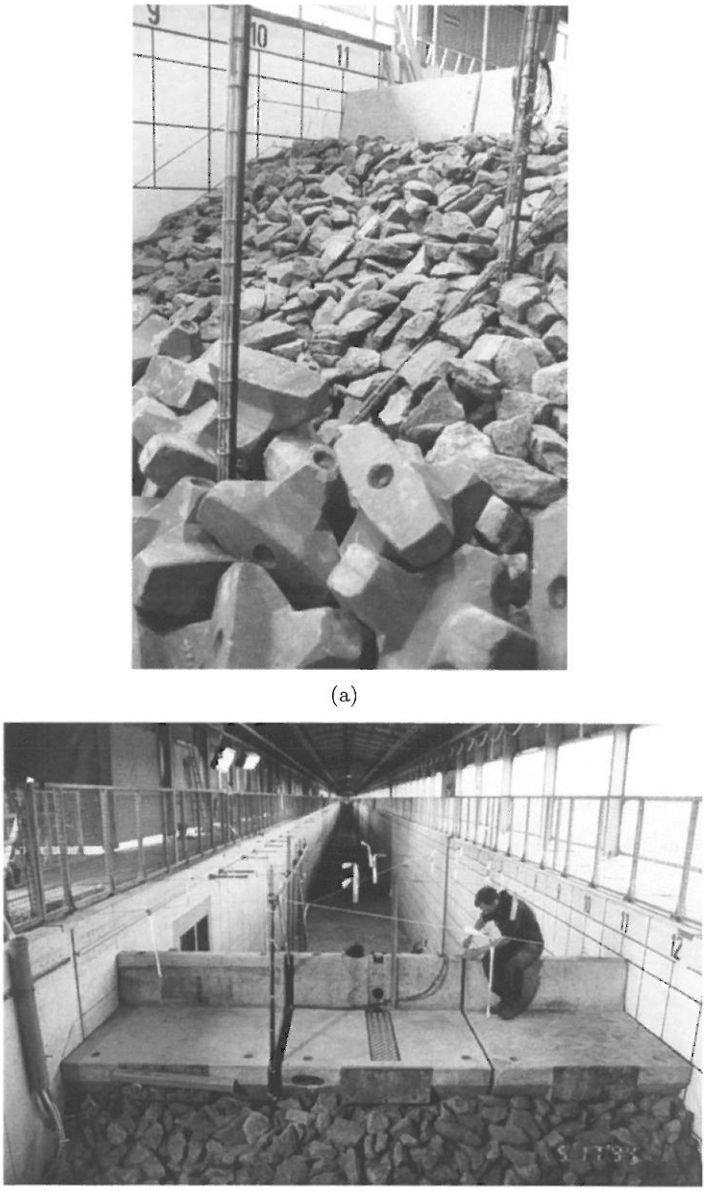

(a)

(b)

Figure A.2: Photographs of the GWK model: (a) view on wave run-up gauge and wave gauge with protection cage in the partially constructed armour layer; (b) crest element (seen in direction of wavemaker). Photo's courtesy of Markus Muttray.

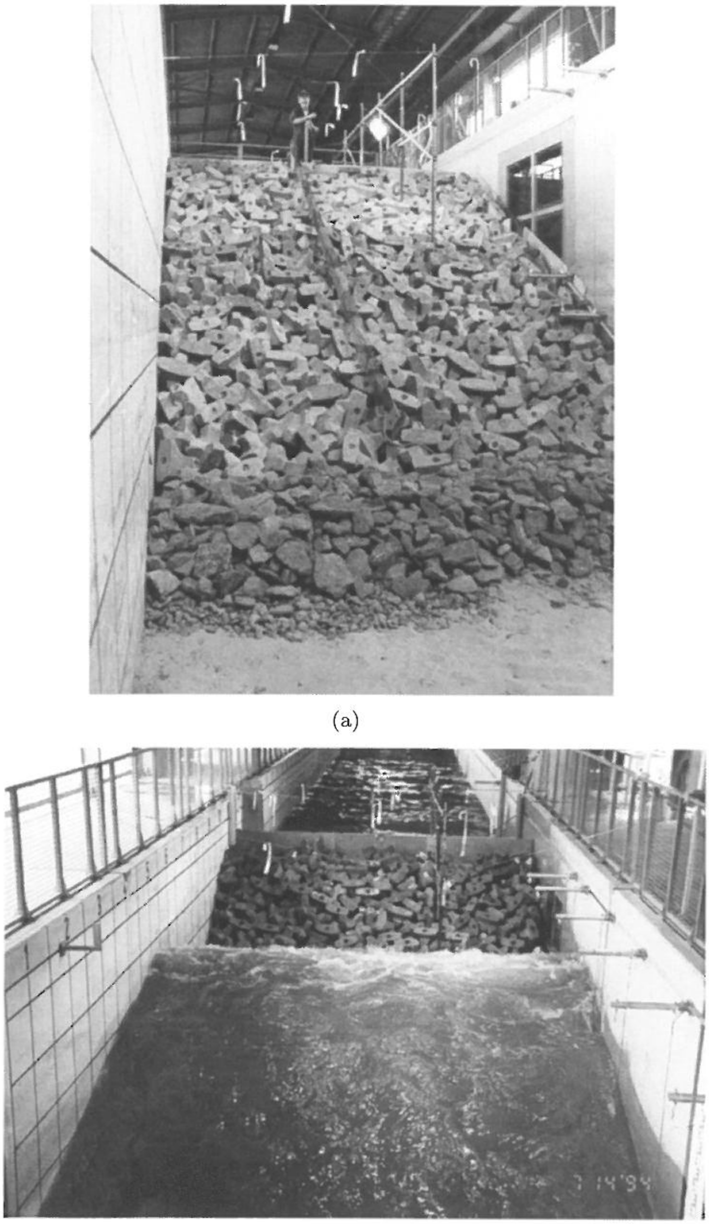

(a)

(b)

Figure A.3: Photographs of the GWK model: (a) view on Accropode armour layer and breakwater toe (with wave run-up gauge near the right flume wall, wave transmission gauges in the middle right side and protection cage for pressure gauges on the middle of the armour layer); (b) wave approaching the breakwater, at the start of wave run-up . Photo's courtesy of Markus Muttray.

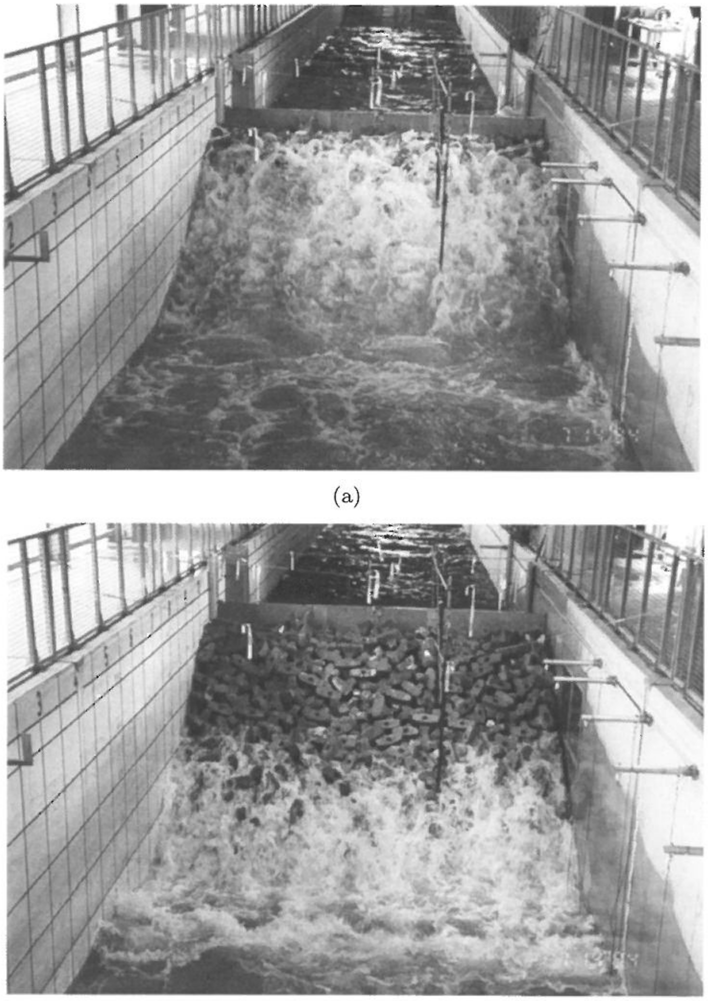

(a)

(b)

Figure A.4: Photographs of the GWK model: (a) maximum wave run-up on the armour slope and (b) wave run-down on the armour slope. Photo's courtesy of Markus Muttray.

B UG model specifications

Table B.1: Positions of pressure and wave gauges in the UG breakwater model.

Gauge	x [m][1]	z' [m][2]	Gauge	x [m]	z' [m]
P1	21.094	0.390	P15	21.520	0.490
P2	21.244	0.490	P16	21.670	0.490
P3	21.394	0.590	P17	21.820	0.490
P4	21.469	0.640	P18	21.970	0.490
P5	21.220	0.390	P19	22.120	0.490
P6	21.370	0.490	P20	22.420	0.490
P7	21.520	0.590	P21	21.670	0.590
P8	21.597	0.640	P22	21.820	0.590
P9	21.370	0.390	P23	21.835	0.590
P10	21.520	0.390	P24	22.135	0.590
P11	21.597	0.390	WG1	21.670	
P12	21.970	0.390	WG2	21.960	
P13	22.270	0.390	WG3	22.250	
P14	22.570	0.390	WG4	23.370	

[1] horizontal distance from right flume wall
[2] vertical distance from flume bottom

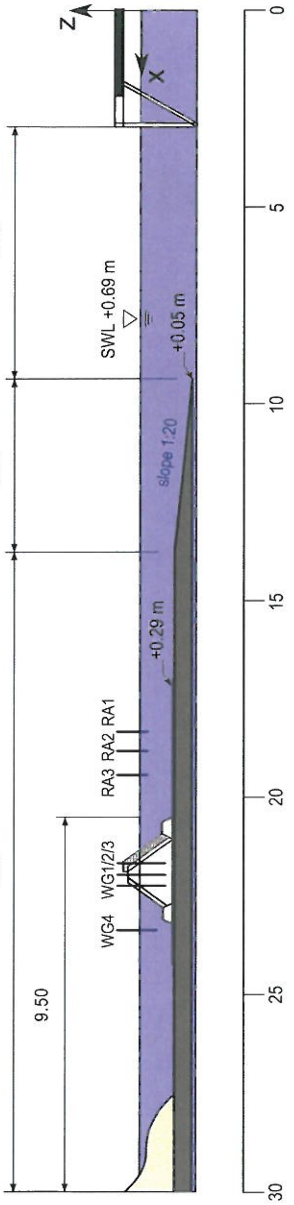

Figure B.1: Layout of the UG flume with indication of gauges for reflection analysis (RAx) and wave transmission (WGx). Dimensions in m (stretched in vertical direction).

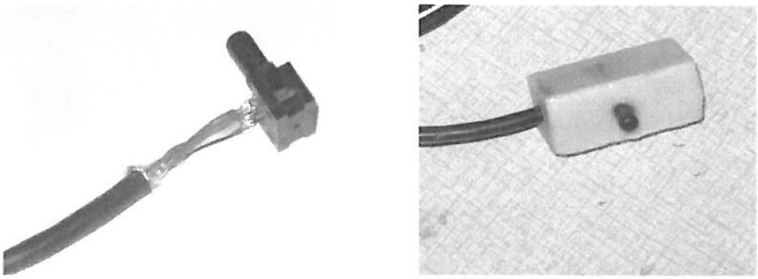

Figure B.2: Detail of 'naked' pressure gauge (left) and gauge covered with epoxy coating (right)

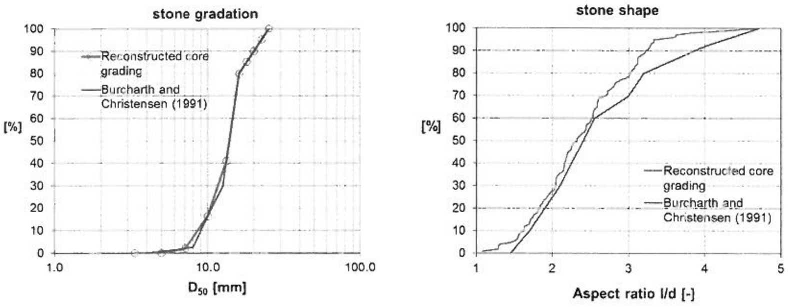

(a) (b)

Figure B.3: Grading (a) and stone shape l/d (b) of original and reconstructed core material in UG tests.

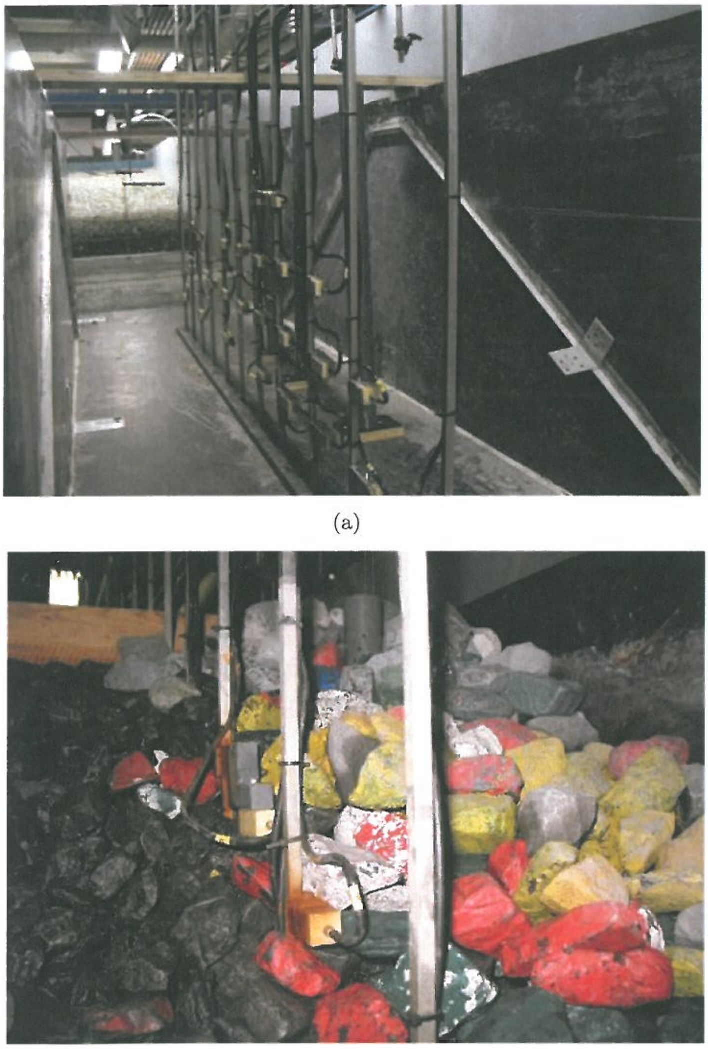

(a)

(b)

Figure B.4: Photographs of the UG model: (a) pressure gauges installed on frame; (b) detail of pressure sensors between core and filter layer.

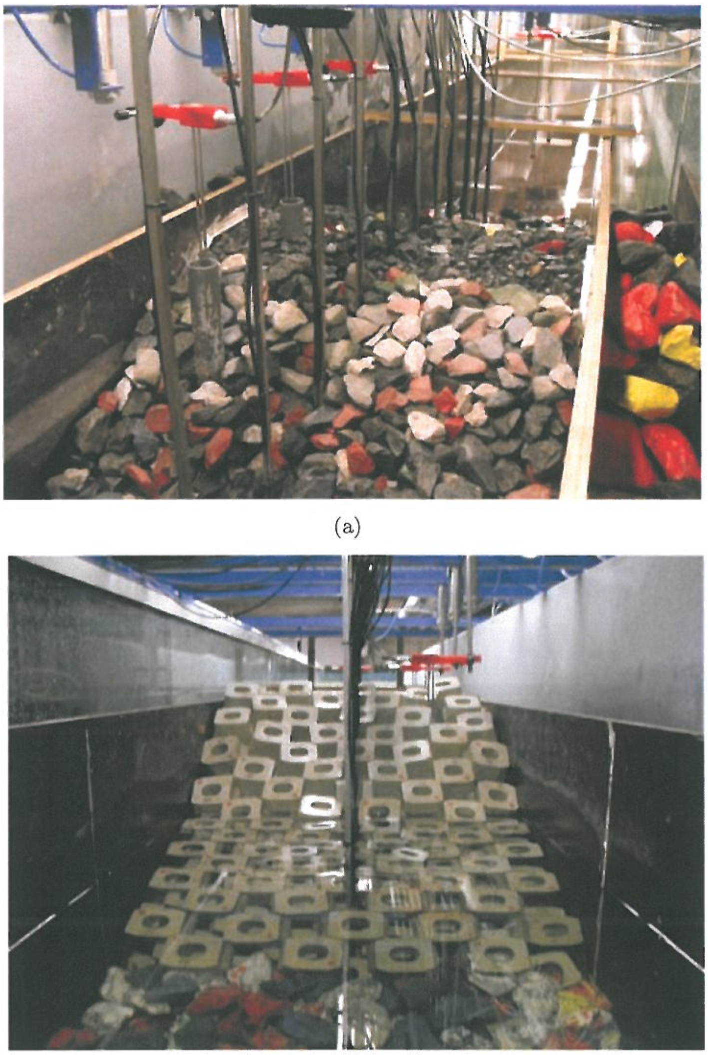
(a)

(b)

Figure B.5: Photographs of the UG model: (a) wave gauges in perforated tubes and (b) view on armour layer with HARO units.

C Application of scaling procedure

In this section, a scaling procedure to determine the dimension of the core material in a small-scale breakwater model is presented. The procedure is nearly identical to the method proposed by Burcharth et al. (1999), which yields the distorted average diameter D_{50} of the core material in a physical model, scaled $1 : \lambda_L$. In this method, the core material is scaled in such way that the Froude scale law holds for a characteristic filter velocity $\overline{u}^f$ inside the porous core. This characteristic filter velocity is averaged over time (one wave period) and space. In the original method, the characteristic velocity is obtained by taking the average of the velocities from 6 locations in the front part of the core, which is most affected with respect to porous flow. The locations are distributed over two sections at $z = 0$ and $z = -H_{m0,inc}$. Here, slightly different positions of these characteristic locations are proposed, indicated in Figure C.1. The three top locations are positioned with sufficient distance below SWL, considering that applying the model equations at SWL ($z = 0$) for waves with finite amplitude would be be unrealistic. In total, 6 locations on two sections are considered, at $z/h = -0.15$ and $z/h = -0.5$.

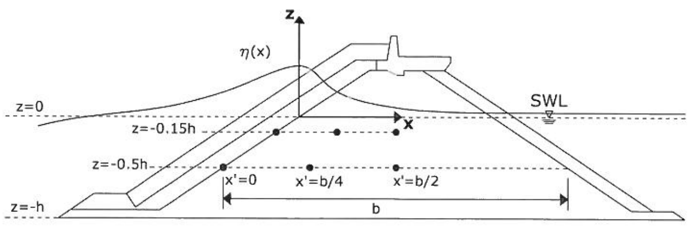

Figure C.1: Location of calculation points for the characteristic filter velocity.

In order to obtain the characteristic filter velocity, use is made of equation (2.3), which relates the filter velocity u^f with the hydraulic gradient I_P in the core. The variation of the instantaneous pore pressure $p(x, z, t)$ in the core with respect to time and space is approximated by:

$$p(x, z, t) = P(x, z) cos(k'x + \omega t) \tag{C.1}$$

where $\omega = 2\pi/T$ is the pulsation frequency and $P(x, z)$ the local pressure height, given by eq. (4.4) for $x \leq x_s$ and eq. (4.6) for $x > x_s$. After introduction of a local x'-axis ($x' = x - zcotan\alpha$), the pressure gradient I_P(z) can be written as follows:

$$\begin{aligned} I_P(z) &= I_{P,1}(z) cos(k'x' + \omega t) \\ &\quad + k' \left(\tfrac{P_{0,m0}(z)}{\rho g} - x' I_{P,1}(z) \right) sin(k'x' + \omega t) \ ; \ x(z) \leq x_s(z) \qquad \text{(C.2a)} \\ I_P(z) &= \tfrac{P_s(z)}{\rho g} exp\left[-\delta'(z) k (x' - x'_s)\right] * \\ &\quad \left[\delta'(z) k cos(k'x' + \omega t) + k' sin(k'x' + \omega t)\right] \ ; \ x(z) > x_s(z) \qquad \text{(C.2b)} \end{aligned}$$

The internal wave number k' is unknown in eqs. (C.2). In Burcharth et al. (1999), it is approximated as $k' = k\sqrt{1.4}$. The same assumption will be used here.

For the sake of simplicity, using (2.3) for stationary flow has been used. This is justified, since it may be expected that the effect of inertia is generally small compared to the other contributions in the total hydraulic resistance and will have a very limited impact on the outcome of the procedure. Accordingly, eq. (2.23) is used to obtain the hydraulic gradient:

$$I_P(z) = \alpha_F \frac{(1-n)^2}{n^3} \frac{\nu}{g D_{50}^2} u^f + \beta_F \frac{1-n}{n^3} \frac{1}{g D_{50}} u^f |u^f| \tag{C.3}$$

The application of the scaling procedure is proceeded iteratively, since the choice of the grain size (D_{50}) and related hydraulic resistance properties are influenced by the flow regime, which cannot be determined in advance:

- firstly, the characteristic prototype filter velocity $\overline{u}_p^f$ is computed by equating eq. (C.2a) or (C.2b) with (C.3) and taking the average over time (one wave period) and space (the six locations in Figure C.1). In eqs. (C.2a) and (C.2b), the GWK piecewise linear approximations are used to compute the model parameters $c_{k,i}(z)$ in the model equations yielding $x_s(z)$, $I_{P,1}(z)$, $P_{0,m0}(z)$, $P_s(z)$ and $\delta'(z)$. Eq. (C.3) requires the input of the hydraulic resistance properties (n, D_{50}, α_F and β_F) of the prototype core material. It is verified whether the flow conditions in prototype are in accordance with the flow regime which applies for the specific shape coefficients used in the computation[1]. Ultimately, the target value for the characteristic filter velocity in the model is computed as $\overline{u}_p^f/\sqrt{\lambda_L}$;

- the next step consists of selecting the core material for the scale model, with known hydraulic resistance parameters. A first guess can be based on the geometric model scale λ_L. The characteristic filter velocity $\overline{u}_m^f$ is then computed by equating equations (C.2a) or (C.2a) with (C.3), in a similar way as in the previous step;
- in a last step, the resulting $\overline{u}_m^f$ is compared with the target value obtained in the first step. If necessary, the previous step is repeated until $\overline{u}_m^f$ reaches the target value. In each iteration, it is verified whether the resulting flow regime is in agreement with the choice of the shape coefficients α_F and β_F.

---

[1] Most probably, flow conditions in prototype will be fully turbulent.

D Velocity field case 2

Fig. D.1 presented hereafter shows the velocity field under the interaction of case 2 waves during one wave cycle, at four time instants. Note that the represented velocity inside the breakwater is the seepage velocity.

In Fig. D.1(a), an instant corresponding with maximum run-down on the breakwater slope is shown. Water is flowing out of the breakwater towards the seaward side, where an incident wave approaches the breakwater.

Fig. D.1(b) corresponds with an instant just before maximum wave run-up on the breakwater slope, when maximum velocities are found in the water mass running up.

Fig. D.1(c) corresponds with an close to maximum wave run-up.

Fig. D.1(d) shows an image between to maximum wave run-up and run-down, where the down-rush of water on the breakwater slope can be observed.

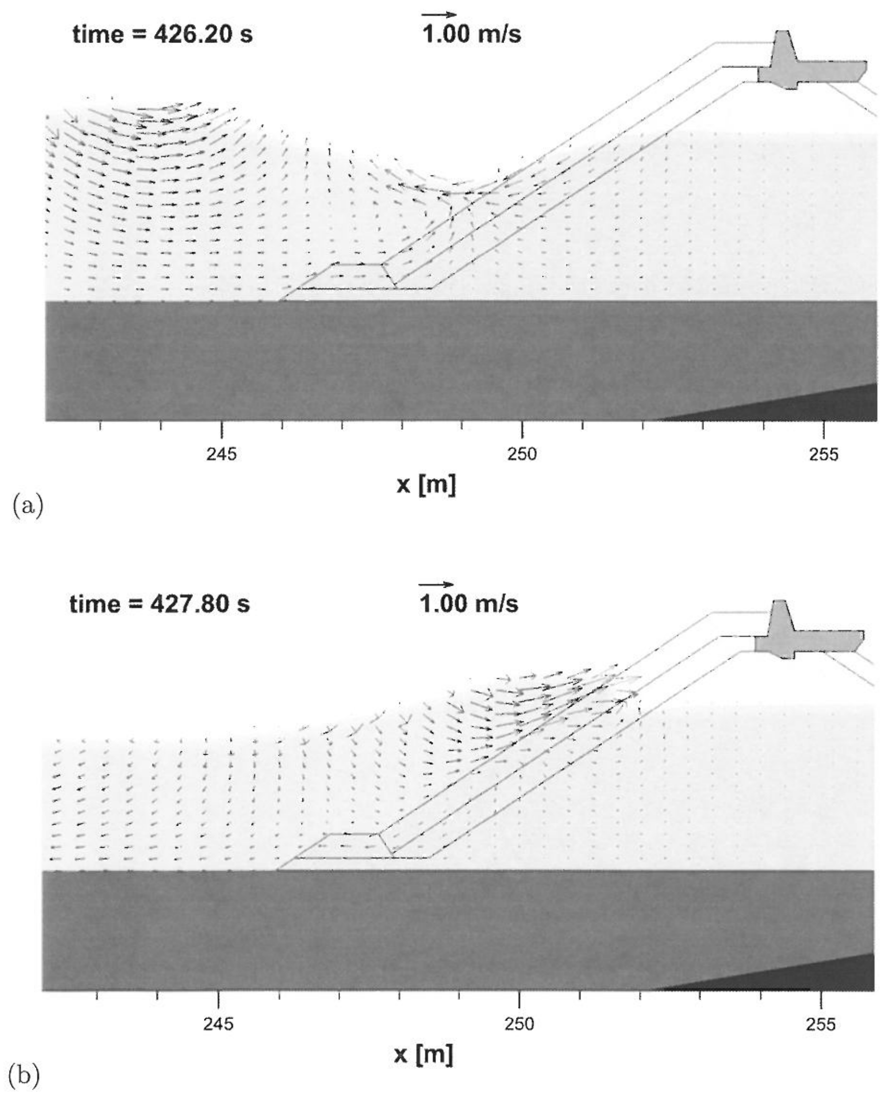

Figure D.1: Velocity field at (a) maximum run-down and (b) maximum velocity in water running up the breakwater slope.

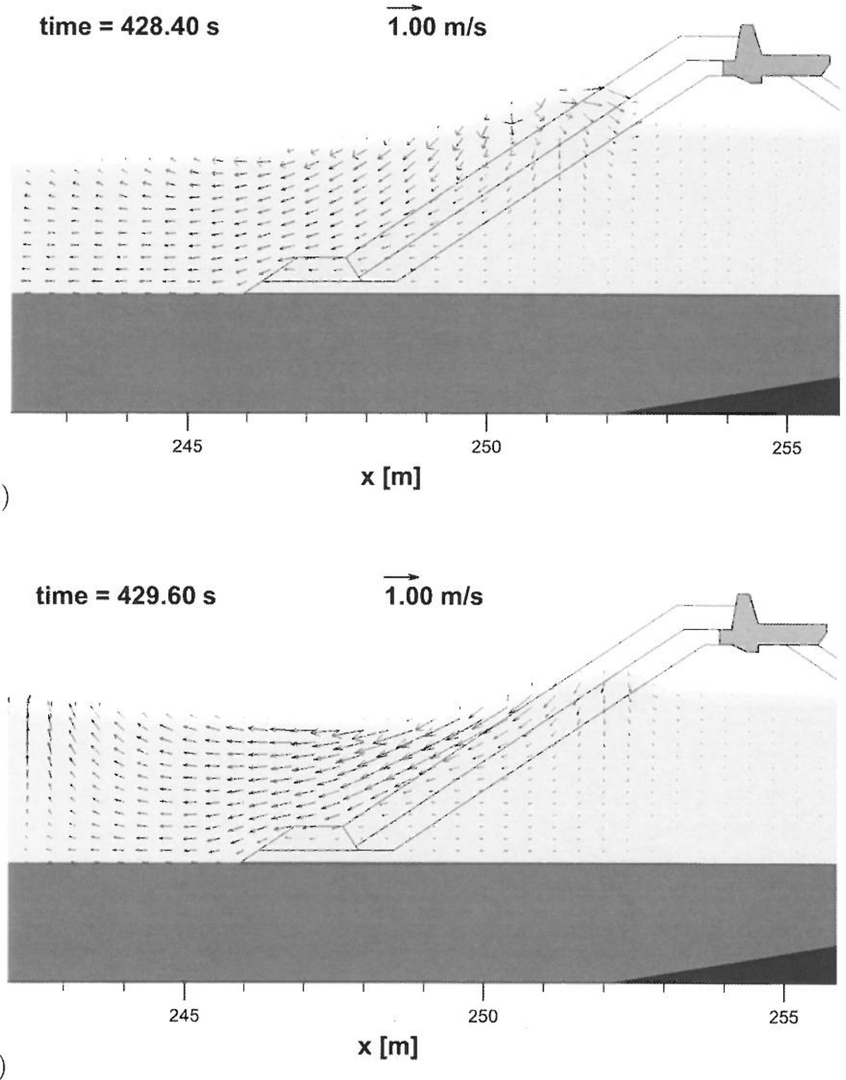

(c)

(d)

Figure D.1: Velocity field at (c) maximum run-up and (d) between maximum run-up and run-down.

References

Austin, D.I., Schlueter, R.S., 1982. A numerical model of wave breaking/breakwater interactions, in: Proc. of the International Conference on Coastal Engineering, ASCE, Cape Town (Republic of South Africa). pp. 2079–2096.

Barends, F.B.J., 1980. Nonlinearity in groundwater flow. Ph.D. thesis. Delft University of Technology, Delft (The Netherlands).

Barkhudarov, M.R., 2004. Lagrangian VOF advection Method for FLOW-3D. Technical Report FSI-03-TN63-R. Flow Science, Inc. (USA).

Barkhudarov, M.R., 2012. Private communication.

Bear, J., 1972. Dynamics of fluids in porous media. American Elsevier.

Biesel, F., 1950. Equations de l'écoulement non lent en milieu perméable. La Houille Blanche 2, 157–160.

Biesel, F., Suquet, F., 1951. Étude théorique d'un type d'appareil à la houle. La Houille Blanche 6^e Ann., nr.2, 152–165.

Boussinesq, J., 1877. "Essai sur la théorie des eaux courantes", Mémoires présentés par divers savants à l'Académie des Sciences 23 (1), Paris (France).

Brethour, J.M., 2009. Improved Generalized Minimal Residual (GMRES) Solver in FLOW-3D - How it works and when to use it. FLOW-3D Technical Note FSI-09-TN82. Flow Science, Inc. (USA).

Bronisz, C.L., Hirt, C.W., 1991. Flows with density stratification: an illustration of higher-order scalar transport. Technical Report FSI-91-TN32. Flow Science, Inc. (USA).

Burcharth, H.F., Andersen, O.K., 1995. On the one-dimensional steady and unsteady porous flow equations. Coastal Engineering 24(3-4), 233–257.

Burcharth, H.F., Christensen, C., 1991. On stationary and non-stationary porous flow in coarse granular materials. Technical Report MAST G6-S Project I, Wave action on and in coastal structures. Deptartment of Civil Engineering, Aalborg University, Aalborg (Denmark).

Burcharth, H.F., Liu, Z., Troch, P., 1999. Scaling of core material in rubble mound breakwater model tests, in: Proc. of the International Conference on Coastal and Port Engineering in Developing Countries (COPEDEC), Cape Town (Republic of South Africa).

Bürger, W., Oumeraci, H., Partenscky, H.W., 1988. Geohydraulic investigations of rubble mound breakwaters, in: Proc. of the International Conference on Coastal Engineering, ASCE, Torremolinos (Spain). pp. 2242–2256.

CECW-EH, 2011. Coastal Engineering Manual, EM 1110-2-1100, part V and VI. US Army Corps of Engineers. Washington, DC (USA).

Chorin, A.J., 1968. Numerical solution of the Navier-Stokes equations. Math. Comp. 22, 745–762.

CIRIA, CUR, CETMEF, 2007. The Rock Manual. The use of rock in hydraulic engineering (2nd edition). C683, CIRIA, London (UK).

Dalrymple, R., Rogers, B., 2006. Numerical modeling of water waves with the SPH method. Coastal Engineering 53, 141 – 147.

Darcy, H., 1856. Les fontaines publiques de la ville de Dijon. Dalmont, Paris (France).

De Groot, M.B., Yamazaki, H., van Gent, M.R.A., Kheyruri, Z., 1994. Pore pressures in rubble mound breakwaters, in: Proc. of the International Conference on Coastal Engineering, ASCE, Kobe (Japan). pp. 1727–1738.

Dean, R.G., Dalrymple, R.A., 1991. Water wave mechanics for engineers and scientists. volume 2 of *Advanced series on ocean engineering*. World Scientific Publishing Co., Singapore.

Dybbs, A., Edwards, R.V., 1984. A new look at porous media fluid mechanics - Darcy to turbulent. Martinus Nijhoff Publishers, Dordrecht (The Netherlands). chapter A new look at porous media fluid mechanics. pp. 199–256.

EurOtop, 2007. EurOtop, wave overtopping of sea defences and related structures: assessment manual. Technical Report. Environment Agency, UK / ENW Expertise Netwerk Waterkeren, NL / KFKI Kuratorium für Forschung im Küsteningenieurswesen, DE / Pullen, T. / Allsop; N.W.H., Bruce, T. / Kortenhaus, A. / Schüttrumpf, H. / van der Meer, J.W.. http://www.overtopping-manual.com.

Fand, R.M., Kim, B.Y.K., Lam, A.C.C., Phan, R.T., 1987. Resistance to the flow of fluids through simple and complex porous media whose matrices are composed of randomly packed spheres. Fluids Eng. (ASME) 109, 268–274.

Fenton, J.D., 1988. The numerical solution of steady water wave problems. Computers and Geosciences 14, 357–368.

Fenton, J.D., 2012. Steadily-progressing wave problem, solution using program Fourier. http://johndfenton.com/Steady-waves/Fourier.html.

Flow Science, 2011. Flow-3D User Manual Version 10.0. Flow Science, Inc. (USA). 683 Harkle Road, Suite A Santa Fe, NM 87505 (USA).

Flow Science, I., 2012. CFD-101: The basics of computational fluid dynamics modeling (www.flow3d.com).

Forchheimer, P., 1901. Wasserbewegung durch bodem. Z. Ver. Deutsch. Ing. 48, 1782–1788.

Frigaard, P., Christensen, M., 1994. An absorbing wave maker based on digital filters, in: Proc. of the International Conference on Coastal Engineering, ASCE. pp. 168–180.

Frigaard, P., Hgedal, M., Christensen, M., 1993. Wave generation theory. Hydraulics and Coastal Engineering Laboratory, Dept. of Civil Engineering, Aalborg University, Aalborg (Denmark).

van Gent, M.R.A., 1992. Formulae to describe porous flow. Communications on hydraulic and geotechnical engineering, Rep. No. 92-2. Technical Report. Delft University of Technology, Delft (The Netherlands).

van Gent, M.R.A., 1993. Stationary and oscillatory flow through coarse porous media. Communications on hydraulic and geotechnical engineering, Rep. No. 93-9. Communications on Hydraulic and Geotechnical Engineering No. 93-9. Faculty of Engineering, Delft University, Delft (The Netherlands).

Goda, Y., 2000. Random seas and design of maritime structures. volume 15 of *Advanced Series on Ocean Engineering*. World Scientific. 2nd edition.

Gu, Z., Wang, H., 1991. Gravity waves over porous bottoms. Coastal Engineering 15, 497 – 524.

Guanche, R., Losada, I.J., Lara, J.L., 2009. Numerical analysis of wave loads for coastal structure stability. Coastal Engineering 56, 543 – 558.

Hall, K.R., 1991. Trends in phreatic surface motion in rubble-mound breakwaters. Waterway, Port, Coastal, and Ocean Engineering 117(2), 179–187.

Hall, K.R., 1992. Hydrodynamic pressure changes in rubble mound breakwater armour layers., in: Proc. of the International symposium: Waves - physical and numerical modelling, IAHR, Vancouver (Canada). pp. 1394–1403.

Hannoura, A.A., McCorquodale, J.A., 1978. Air-water flow in coarse granular media. Journal of Hydraulics Division, ASCE 104(7), 1001–1010.

Hannoura, A.A., McCorquodale, J.A., 1985. Rubble mounds: hydraulic conductivity equation. Waterway, Port, Coastal and Ocean Engineering 111(5), 783–799.

Harlow, E.H., 1980. Large rubble-mound breakwater failures. Waterway, Port, Coastal and Ocean Division (ASCE) 106, 275–278.

Harlow, F.H., Nakayama, P.I., 1967. Turbulence transport equations. Physics of Fluids 10, 2323.

Harlow, F.H., Welch, J.E., 1965. Numerical calculation of time dependent viscous incompressible flow of fluid with free surface. Phys. Fluids 8.

Hasselmann, K., P, B.T., Bouws, E., Carlson, H., Cartwright, D., Enke, K., Ewing, J., Gienapp, H., Hasselmann, D., Kruseman, P., Meerburg, A., Mller, P., Olbers, D., Richter, K., Sell, W., Walden, H., 1973. Measurements of wind-wave growth and swell decay during the Joint North Sea Wave Project (JONSWAP). Deutsche Hydrographische Zeitschrift, Ergänzungsheft Reihe A(8) 12, 95 pp.

Hasselmann, K., Ross, B., Müller, P., Sell, W., 1976. A parametric wave prediction model. Physical Oceanography 6, 200–228.

Higuera, P., Lara, J.L., Losada, I.J., 2013. Realistic wave generation and active wave absorption for Navier-Stokes models: Application to OpenFOAM®. Coastal Engineering 71, 102 – 118.

Hirt, C.W., Cook, J.L., Butler, T.D., 1970. A Lagrangian method for calculating the dynamics of an incompressible fluid with free surface. Computational Physics 5, 103 – 124.

Hirt, C.W., Nichols, B.D., 1981. Volume of fluid (VOF) method for the dynamics of free boundaries. Computational Physics 39, 201–225.

Hirt, C.W., Sicilian, J.M., 1985. A porosity technique for the definition of obstacles in rectangular cell meshes, in: Proc. of the Fourth International Conference of Ship Hydrodynamics, National Academy of Science, Washington D.C. (USA).

Hsu, T.J., Sakakiyama, T., Liu, P.L.F., 2002. A numerical model for wave motions and turbulence flows in front of a composite breakwater. Coastal Engineering 46, 25 – 50.

Hughes, S.A., 1984. The TMA shallow-water spectrum, description and applications. Technical Report CERC-84-7. Technical Report. US Army Engineer Research Station, Vicksburg, Mississippi (USA).

Hur, D.S., Lee, K.H., Yeom, G.S., 2008. The phase difference effects on 3-D structure of wave pressure acting on a composite breakwater. Ocean Engineering 35, 1826 – 1841.

Isfahani, A.H.G., Brethour, J.M., 2009. On the implementation of two-equation turbulence models in FLOW-3D. FLOW-3D Technical Note FSI-09-TN86. Flow Science, Inc. (USA).

Iwagaki, Y., Tsuchiya, Y., 1966. Laminar damping of oscillatory waves due to bottom friction, in: Proc. of the International Conference on Coastal Engineering, ASCE, Tokyo (Japan). pp. 149–174.

del Jesus, M., 2011. Three-dimensional interaction of water waves with coastal structures. Ph.D. thesis. Universidad de Cantabria, Santander (Spain).

del Jesus, M., Lara, J.L., Losada, I.J., 2012. Three-dimensional interaction of waves and porous coastal structures: Part I: Numerical model formulation. Coastal Engineering 64, 57 – 72.

Kothe, D.B., Mjolsness, R.C., Torrey, M.D., 1994. RIPPLE: A Computer Program for Incompressible Flows with Free Surfaces. Technical Report LA-12007-MS. Los Alamos National Laboratory, New Mexico (USA).

Lara, J., Losada, I., Guanche, R., 2008. Wave interaction with low-mound breakwaters using a RANS model. Ocean Engineering 35, 1388 – 1400.

Launder, B.E., Spalding, D.B., 1974. The numerical computation of turbulent flows. Comput. Methods Appl. Mech. Eng. 3, 269–289.

Le Méhauté, B., 1957. Perméabilité des digues en enrochements aux ondes de gravité périodiques. La Houille Blanche 6, 903–919.

Le Méhauté, B., 1958. Perméabilité des digues en enrochements aux ondes de gravité périodiques (suite). La Houille Blanche 2, 148–178.

Le Méhauté, B., 1976. An introduction to Hydrodynamics and water waves. Springer-Verlag, New York (USA).

de Lemos, M.J.S., 2006. Turbulence in porous media. Modeling and applications. Elsevier.

de Lemos, M.J.S., Pedras, M.H.J., 2001. Recent mathematical models for turbulent flow in saturated rigid porous media. J. Fluids Eng. 123, 935–940.

Levsen, A., 1998. Untersuchung der hydraulischen Eigenschaften eines grobkörnigen porösen Mediums bei stationärer Strömung. Studienarbeit. Master's thesis. Institut für Grundbau and Bodenmechanik,Technische Universität Braunschweig, Braunschweig (Germany).

Liu, P.L.F., Lin, P., 1997. A numerical model for breaking waves: the volume of fluid method. Research Report CACR-97-02. Center for Applied Coastal Research, University of Delaware, Newark, Delaware (USA).

Liu, P.L.F., Lin, P., Hsu, T.J., Chang, K.A., Losada, I.J., Vidal, C., Sakakiyama, T., 1999. A reynolds-averaged navies stokes equation model for nonlinear water wave and structure interaction, in: Proc. Coastal Structures 99, JSCE. pp. 169–174.

Losada, I.J., Lara, J.L., Guanche, R., Gonzalez-Ondina, J.M., 2008. Numerical analysis of wave overtopping of rubble mound breakwaters. Coastal Engineering 55, 47 – 62.

Lumley, J.L., 1975. Modeling turbulent flux of passive scalar quantities in inhomogeneous flows. Physics of Fluids 18, 619–621.

Madsen, O.S., 1974. Wave transmission through porous structures. Waterways, Harbors and Coastal Engineering Division 100, 169–188.

Madsen, P.A., Sørensen, O.R., 1993. Bound waves and triad interactions in shallow water. Ocean Engineering 20, 359 – 388.

Mansard, E.P.D., Funke, E.R., 1980. The measurement of incident and reflected spectra using a least squares method, in: Proc. of the International Conference on Coastal Engineering, ASCE. pp. 154–172.

Menter, F., 1994. Two-equation eddy-viscosity turbulence models for engineering applications. American Institute of Aeronautics and Astronautics (AIAA) 32(8), 1598–1605.

Monaghan, J., 1994. Simulating free surface flows with SPH. Journal of Computational Physics 110, 399 – 406.

Muttray, M., 2000. Wellenbewegung an und in einem geschütteten Wellenbrecher-Laborexperimente im Grossmassstab und theoretische Untersuchungen. Ph.D. thesis. Technical University Braunschweig, Braunschweig (Germany).

Muttray, M., Oumeraci, H., 2005. Theoretical and experimental study on wave damping inside a rubble mound breakwater. Coastal Engineering 52(8), 709–725.

Muttray, M., Oumeraci, H., Zimmerman, C., 1995. Wave-induced flow in a rubble mound breakwater, in: Proc. of the International Conference on Coastal and Port Engineering in Developing Countries (COPEDEC), Rio de Janeiro, Brasil. pp. 1219–1231.

Muttray, M., Oumeraci, H., Zimmerman, C., Partenscky, H.W., 1992. Wave energy dissipation on and in rubble mound breakwaters, in: Proc. of the International Conference on Coastal Engineering, ASCE, Venice (Italy). pp. 1434–1447.

Nakayama, A., Kuwahara, F., 1999. A macroscopic turbulence model for flow in a porous medium. Journal of Fluids Engineering 121, 427.

Nicholls, R.J., Wong, P.P., Burkett, V.R., O, C.J., Hay, J.E., McLean, R.F., Ragoonaden, S., Woodroffe, C.D., 2007. Climate Change 2007: Impacts, Adaptation and Vulnerability. Contribution of Working Group II to the Fourth Assessment Report of the Intergovernmental Panel on Climate Change. Cambridge University Press, Cambridge (UK). chapter Coastal systems and low-lying areas. pp. 315–356.

Nichols, B.D., Hirt, C.W., Hotchkiss, R.S., 1980. SOLA-VOF: A Solution Algorithm for Transient Fluid Flow with Multiple Free Boundaries. Technical Report LA-8355. Los Alamos National Laboratory, New Mexico (USA).

Oñate, E., Idelsohn, S.R., Del Pin, F., Aubry, R., 2004. The particle finite element method. an overview. International Journal of Computational Methods 1, 267–307.

Oumeraci, H., Partenscky, H.W., 1990. Wave-induced pore pressure in rubble mound breakwaters, in: Proc. of the International Conference on Coastal Engineering, ASCE, Delft (The Netherlands). pp. 1334–1347.

Pierson, W.J., Moskowitz, L., 1964. A proposed spectral form for fully-developed wind sea based on the similarity law of S. A. Kitaigorodoskii. Journal of Geophysical Research 69, 5181–5203.

Polubarinova-Kochina, P., 1962. Theory of groundwater movement. Princeton University Press, Princeton, New Jersey (USA).

Pope, S.B., 2000. Turbulent flows. Cambridge University Press, Cambridge (UK).

Rauwoens, P., 2008. Pressure-Correction Algorithms for General Fluids at Low Speeds, Applied to Non-Premixed Flame Simulations. Ph.D. thesis. Faculty of Engineering and Architecture, Ghent University, Ghent (Belgium).

Rienecker, M.M., Fenton, J.D., 1981. A fourier approximation method for steady water waves. Fluid Mechanics 104, 119–137.

Schäffer, H.A., 1996. Second-order wavemaker theory for irregular waves. Ocean Engineering 23, 47–88.

Schmidt-Koppenhagen, R., Gerdes, M., Tautenhain, E., Grüne, J., 1997. Online absorption control system for wave generation, in: Edge, B., Hemsley, J. (Eds.), Proc. of the 3rd Int. Symp. on Ocean Wave Measurements and Analysis (WAVES'97), ASCE, Virginia Beach, Virginia (USA). pp. 1295–1305.

Shao, S., 2010. Incompressible SPH flow model for wave interactions with porous media. Coastal Engineering 57, 304 – 316.

Shirani, E., Jafari, A., Ashgriz, N., 2006. Turbulence models for flows with free surfaces and interfaces. American Institute of Aeronautics and Astronautics (AIAA) 44 (7), 1454–1462.

Shuto, N., 1974. Nonlinear long waves in a channel of variable section, in: Coastal Engineering in Japan, JSCE, Tokyo (Japan). pp. 1–12.

Slattery, J.C., 1999. Advanced transport phenomena. Cambridge University Press, Cambridge (UK).

Sollit, C.K., Cross, R.H., 1972. Wave transmission through permeable breakwaters, in: Proc. of the International Conference on Coastal Engineering, ASCE. pp. 1827–1846.

Sollit, C.K., Cross, R.H., 1976. Wave reflection and transmission at permeable breakwaters. Technical Report. Defense Technical Information Center, U.S. Army Corps of Engineers (USA).

Spinneken, J., Swan, C., 2009. Second-order wave maker theory using force-feedback control. part I: A new theory for regular wave generation. Ocean Engineering 36, 539 – 548.

Torres-Freyermuth, A., Lara, J.L., Losada, I.J., 2010. Numerical modelling of short- and long-wave transformation on a barred beach. Coastal Engineering 57, 317 – 330.

Troch, P., 2000. Experimentele studie en numerieke modellering van golfinteractie met stortsteengolfbrekers. Ph.D. thesis. Faculty of Engineering and Architecture, Ghent University, Ghent (Belgium).

Troch, P., De Rouck, J., 1999. An active wave generating-absorbing boundary condition for VOF type numerical model. Coastal Engineering 38, 223–247.

Troch, P., De Rouck, J., Burcharth, H.F., 2002. Experimental study and numerical modeling of wave induced pore pressure attenuation inside a rubble mound breakwater, in: Proc. of the International Conference on Coastal Engineering, ASCE, Cardiff (UK). pp. 1607–1619.

Troch, P., De Rouck, J., Van Damme, L., 1998. Instrumentation and prototype measurements at the Zeebrugge rubble mound breakwater. Coastal Engineering 35(1-2), 141–166.

Tuah, H., Hudspeth, R.T., 1982. Comparisons of numerical random sea simulations. Waterway, Port, Coastal and Ocean Division 108, 569–584.

van Gent, M.R.A., 1995. Wave interaction with permeable coastal structures. Ph.D. thesis. Delft Technical University, Delft (The Netherlands).

Van Leer, B., 1977. Towards the ultimate conservative difference scheme. IV. a new approach to numerical convection. Comput. Phys. 23, 276–299.

Vanneste, D., Troch, P., 2010. Experimental research on pore pressure attenuation in rubble-mound breakwaters, in: Proc. of the International Conference on Coastal Engineering, ASCE, Shanghai (China).

Vanneste, D., Troch, P., 2012. An improved calculation model for the wave-induced pore pressure distribution in a rubble-mound breakwater core. Coastal Engineering 66, 8 – 23.

Versteeg, H.K., Malalasekera, W., 1995. Computational Fluid Dynamics : The Finite Volume Method. Longman Scientific & Technical, Essex (UK).

Yakhot, V., Orszag, S.A., Thangam, S., Gatski, T.B., Speziale, C.G., 1992. Development of turbulence models for shear flows by a double expansion technique. Physics of Fluids 4, 1510–1520.

Yao, G.F., 2004. Development of new pressure-velocity solvers in FLOW-3D. FLOW-3D Technical Note FSI-04-TN68. Flow Science, Inc. (USA).